National Technical University of Athens
School of Electrical and Computer Engineering
Division of Information Transmission Systems and Material Technology

System Development of Silicon Photonics Transceivers for Future Upgrades of High Energy Physics Experiments at CERN

PhD Thesis

of

THEONI G. PROUSALIDI

CERN-THESIS-2024-056
24/04/2024

Athens, April 2024

National Technical University of Athens
School of Electrical and Computer Engineering
Division of Information Transmission Systems and Material Technology

System Development of Silicon Photonics Transceivers for Future Upgrades of High Energy Physics Experiments at CERN

PhD Thesis

of

THEONI G. PROUSALIDI

Advisory Committee : Hercules Avramopoulos
Dimitrios Soudris
Jan Troska

Approved by the examination committee on 24th April 2024.

.....	.....	.....
Hercules Avramopoulos	Dimitrios Soudris	Jan Troska
NTUA Professor	NTUA Professor	CERN Researcher
.....	.....	.....
Athanasios Panagopoulos	Elias Glytsis	Nikos Pleros
NTUA Professor	NTUA Professor	AUTH Professor

.....
Nikolaos Uzunoglu
NTUA Professor Emeritus

Athens, April 2024

National Technical University of Athens
School of Electrical and Computer Engineering
Division of Information Transmission Systems and Material Technology

Copyright © – All rights reserved.
Theoni G. Prousalidi, 2024.

The copying, storage and distribution of this PhD thesis, exall or part of it, is prohibited for commercial purposes. Reprinting, storage and distribution for non - profit, educational or of a research nature is allowed, provided that the source is indicated and that this message is retained.

The content of this thesis does not necessarily reflect the views of the Department, the Supervisor, or the committee that approved it.

DISCLAIMER ON ACADEMIC ETHICS AND INTELLECTUAL PROPERTY RIGHTS

Being fully aware of the implications of copyright laws, I expressly state that this PhD thesis, as well as the electronic files and source codes developed or modified in the course of this thesis, are solely the product of my personal work and do not infringe any rights of intellectual property, personality and personal data of third parties, do not contain work / contributions of third parties for which the permission of the authors / beneficiaries is required and are not a product of partial or complete plagiarism, while the sources used are limited to the bibliographic references only and meet the rules of scientific citing. The points where I have used ideas, text, files and / or sources of other authors are clearly mentioned in the text with the appropriate citation and the relevant complete reference is included in the bibliographic references section. I fully, individually and personally undertake all legal and administrative consequences that may arise in the event that it is proven, in the course of time, that this thesis or part of it does not belong to me because it is a product of plagiarism.

(Signature)

.....
Theoni G. Prousalidi
PhD of School of Electrical and Computer Engineering, NTUA
24th April 2024

Στην οικογένειά μου

Abstract

In the coming years, various upgrades will take place in CERN's detectors and experiments. The first one of these, called the high luminosity LHC project, is already underway and foresees the starting of the operation of the upgraded systems in 2026. Starting at the end of the HL-LHC era, the high radiation levels and increased data rates due to the increased luminosity of the accelerator will impose the need for a new generation of optical links, able to withstand the extreme condition in the detectors, and support the data rates. The currently available optical transceivers will not be able to survive in the innermost regions of some of the detectors due to their limited radiation tolerance. It is therefore evident that a new generation of optical links will be required in future upgrades of experiments at CERN. SiPh has been identified as the perfect candidate for this upgrade, since it combines all the advantages that are required for such an application.

In recent years CERN has taken an interest in the SiPh technology for the aforementioned reason. An extensive effort has been taking place the past years within the EP-ESE group at CERN that focuses on the modelling and development of SiPh transceivers for HEP application. This effort includes the simulation, design and fabrication of SiPh PICs for the development of the necessary building blocks that can be combined to realize radiation-hard SiPh transceivers. At the same time, this effort includes the testing and characterization of the designed structures as part of the feedback process that is required to make design, technology and architecture choices regarding the target system. An indispensable side of the development of radiation-hard SiPh based links is also the extensive study and validation of the radiation tolerance of the developed components and circuits. Without this study, the integration of SiPh based TRx is CERN experiments will not be possible.

Within the CERN collaboration, various SiPh test chips have been designed and characterized. Relevant to the work described in this thesis is the second chip that was designed at CERN in 2019 and was fabricated by imec's multi project wafer (MPW) in 2020, namely PICv2. This test chip includes IP blocks designed at CERN or made available by the foundry's libraries, combined to form structures for data transmission demonstrations. More specifically, the PIC includes various versions of RMs, Mach-Zehnder modulators (MZMs), Ge PDs, optical multiplexers, interferometers for polarization recovery studies, as well as a WDM circuit with four cascaded RMs connected in series.

This PIC serves first of all as a test vehicle for the characterization of the individual components, the implementation of radiation tests and the comparison of the different versions of the components in terms of performance and radiation hardness. At the same time, the building blocks that are available from the PIC can be combined and utilized for the assembly of a first version of transmitters and receivers, allowing higher level testing and characterization.

On a system level, the development and operation of SiPh based transceivers involves many challenges. On the transmitter side, a very important challenge is the wavelength stabilization of the RMs. This is necessary to achieve their stable operation at the desired wavelength of operation irrespective of variations in the environmental conditions (e.g.

temperature, external laser wavelength variation). Another important challenge is the polarization management. This is required due to the unique architecture of such a link that imposes the placement of the optical sources in the back-end, away for the SiPh PICs, and their connection with SMFs that do not maintain the polarization. The same problem exists also on the receiver side, since the SiPh Rx will be connected to the BE Tx through long SMFs. Especially in the case of a WDM implementation, the architecture of the whole link, including the SiPh circuit, the power supplies and the polarization management and thermal tuning, becomes more complex and requires extra effort and problems to be addressed.

The scope of this thesis, that also reflects the work that the writer carried out during the past three years, evolves around the development of a SiPh Tx and Rx based on the components provided by PICv2. It also concerns the addressing of the challenges that are involved in the development of such a SiPh TRx, from a system point of view. The aforementioned objectives target the advancing towards a first demonstration of SiPh TRx for HEP experiments.

Keywords

Silicon Photonics, Silicon, Photonic Integrated Circuit, Transmitter, Receiver, Transceiver, CERN, optical links, Ring Modulator, Germanium Photodiode, Thermal Tuning, Polarization Management, PIC design, radiation tolerance, High Energy Physics

Περίληψη

Στις επόμενες δεκαετίες, διάφορες αναβαθμίσεις θα λάνουν χώρα στους ανιχνευτές και στα πειράματα του CERN. Η πρώτη από αυτές ονομάζεται high luminosity LHC βρίσκεται ήδη σε εξέλιξη και προβλέπει την λειτουργία των αναβαθμισμένων συστημάτων από το 2026. Ξεκινώντας από το τέλος της εποχής του HL-LHC, τα υψηλά επίπεδα ακτινοβολίας και οι αυξημένοι ρυθμοί δεδομένων λόγω της αυξημένης φωτεινότητας του επιταχυντή θα επιβάλουν την ανάγκη για μια νέα γενιά οπτικών ζεύξεων, ικανών να αντέξουν τις ακραίες συνθήκες στους ανιχνευτές και να υποστηρίξουν τους ρυθμούς δεδομένων. Οι διαθέσιμοι σήμερα οπτικοί πομποδέκτες δεν θα είναι σε θέση να επιβιώσουν στις ενδότερες περιοχές ορισμένων ανιχνευτών λόγω της περιορισμένης ανθεκτικότητάς τους στην ακτινοβολία. Είναι εμφανές λοιπόν ότι μια νέα γενιά οπτικών ζεύξεων μεταφοράς δεδομένων θα απαιτηθεί για τις μελλοντικές αναβαθμίσεις των πειραμάτων στο CERN. Η τεχνολογία των φωτονικών συστημάτων πυριτίου (SiPh) έχει αναγνωριστεί ως ο τέλειος υποψήφιος για αυτή την αναβάθμιση, καθώς συνδυάζει όλα τα πλεονεκτήματα που απαιτούνται για μια τέτοια εφαρμογή.

Τα τελευταία χρόνια το CERN έχει ενδιαφερθεί για την τεχνολογία SiPh για τον προαναφερθέντα λόγο. Μια εκτεταμένη προσπάθεια έχει λάβει χώρα στο πλαίσιο της ομάδας EP-ESE του CERN που επικεντρώνεται στη μοντελοποίηση και την ανάπτυξη πομποδεκτών SiPh για εφαρμογή σε πειράματα φυσικής υψηλών ενεργειών. Η προσπάθεια αυτή περιλαμβάνει την προσομοίωση, το σχεδιασμό και την κατασκευή ολοκληρωμένβν κυκλωμάτων SiPh για την ανάπτυξη των απαραίτητων δομικών στοιχείων που μπορούν να συνδυαστούν για την υλοποίηση πομποδεκτών SiPh ανθεκτικών στην ακτινοβολία. Ταυτόχρονα, μέρος αυτής της προσπάθειας αποτελεί και η δοκιμή και ο χαρακτηρισμός των δομών που σχεδιάστηκαν ως μέρος της διαδικασίας ανατροφοδότησης που απαιτείται για τη λήψη αποφάσεων σχεδιασμού, τεχνολογίας και αρχιτεκτονικής όσον αφορά το σύστημα-στόχο. Απαραίτητη πλευρά της ανάπτυξης οπτικών ζεύξεων με βάση τα SiPh για χρήση στο CERN είναι επίσης η εκτεταμένη μελέτη και επικύρωση της ανοχής στην ακτινοβολία των εξαρτημάτων και των κυκλωμάτων που αναπτύχθηκαν. Χωρίς αυτή τη μελέτη, η ενσωμάτωση των SiPh TRx δεν θα είναι δυνατή σε πειράματα του CERN.

Στο πλαίσιο της συνεργασίας του CERN, έχουν σχεδιαστεί και χαρακτηριστεί διάφορα δοκιμαστικά τσιπ SiPh. Σχετικό με την παρούσα διατριβή είναι το δεύτερο τσιπ που σχεδιάστηκε στο CERN το 2019 και κατασκευάστηκε από το multi project wafer (MPW) της imec το 2020, δηλαδή το PICv2. Αυτό το δοκιμαστικό PIC περιλαμβάνει IP μπλοκ που σχεδιάστηκαν στο CERN ή διατέθηκαν από τις βιβλιοθήκες του fab, τα οποία συνδυάζονται για να σχηματίσουν δομές για επιδείξεις μετάδοσης δεδομένων. Πιο συγκεκριμένα, το PIC περιλαμβάνει διάφορες παραλλαγές διαμορφωτών δακτυλίου, διαμορφωτές Mach-Zehnder (MZMs), φωτοδιόδους Γερμανίου, οπτικούς πολυπλέκτες, συμβολόμετρα για μελέτες ανάκτησης πόλωσης, καθώς και ένα κύκλωμα WDM με τέσσερεις διαμορφωτές δακτυλίου συνδεδεμένους σειριακά. Αυτό το PIC χρησίμευσε καταρχάς ως όχημα δοκιμών για τον χαρακτηρισμό των επιμέρους στοιχείων, την υλοποίηση test ακτινοβολίας και τη σύγκριση των διαφόρων παραλλαγών των στοιχείων όσον αφορά την απόδοση και την ανθεκτικότητα στην ακτινοβολία. Ταυτόχρονα, τα δομικά στοιχεία που είναι διαθέσιμα από το PIC μπορεσαν να συνδυαστούν και να χρησιμοποιηθούν για τη συναρμολόγηση μιας πρώτης υλοποίησης πομπών και δεκτών, επιτρέποντας

δοκιμές και χαρακτηρισμό υψηλότερου επιπέδου.

Σε επίπεδο συστήματος, η ανάπτυξη και λειτουργία πομποδεκτών πυριτίου περιλαμβάνει πολλές προκλήσεις. Από την πλευρά του πομπού, μια πολύ σημαντική πρόκληση είναι η σταθεροποίηση του μήκους κύματος των διαμορφωτών δακτυλίου. Αυτό είναι απαραίτητο για να επιτευχθεί η σταθερή λειτουργία τους στο επιθυμητό μήκος κύματος λειτουργίας ανεξάρτητα από τις μεταβολές των περιβαλλοντικών συνθηκών (π.χ. θερμοκρασία, μεταβολή του μήκους κύματος του εξωτερικού λέιζερ). Μια άλλη σημαντική πρόκληση είναι η διαχείριση της πόλωσης. Αυτό απαιτείται λόγω της μοναδικής αρχιτεκτονικής μιας τέτοιας ζεύξης που επιβάλλει την τοποθέτηση των οπτικών πηγών στο back-end, μακριά από τα SiPh PICs, και τη σύνδεσή τους με οπτικές ίνες που δεν διατηρούν την πόλωση. Το ίδιο πρόβλημα υπάρχει και στην πλευρά του δέκτη, δεδομένου ότι ο SiPh δέκτης θα συνδεθεί με τον BE πομπό μέσω οπτικών ινών. Ειδικά στην περίπτωση μιας υλοποίησης πολυπλεξίας μηκών κύματος, ολόκληρη η αρχιτεκτονική της ζεύξης, συμπεριλαμβανομένου του κυκλώματος SiPh, των laser και της διαχείρισης της πόλωσης και του θερμικού συντονισμού, γίνεται πιο πολύπλοκη και απαιτεί επιπλέον προσπάθεια και προκλησεις προς αντιμετώπιση.

Το αντικείμενο αυτής της διατριβής, που αντικατοπτρίζει επίσης την δουλειά που πραγματοποίησε η συγγραφέας τα τελευταία τρία χρόνια, αφορά στην ανάπτυξη ενός SiPh πομπού και δέκτη με βάση τα εξαρτήματα που παρέχονται από το PICv2. Αφορά επίσης την αντιμετώπιση των προκλήσεων που συνεπάγεται η ανάπτυξη ενός τέτοιου SiPh πομποδέκτη σε επίπεδο συστήματος. Αυτοί οι στόχοι στοχεύουν στην πρόοδο προς μια πρώτη υλοποίηση ενός SiPh πομποδέκτη για πειράματα φυσικής υψηλών ενεργειών.

Λέξεις-κλειδιά

Φωτονικά Συστήματα Πυριτίου, Πυρίτιο, Ολοκληρωμένο φωτονικό Κύκλωμα, Πομπός, Δέκτης, Πομποδέκτης, CERN, οπτικές ζεύξεις, διαμορφωτής δακτυλίου, φωτοδίοδος Γερμανίου, Θερμικός Έλεγχος, πόλωση, σχεδιασμός PIC, ανεκτικότητα στην ακτινοβολία, Φυσική Υψηλών Ενεργειών

Ευχαριστίες - Acknowledgments

Το ταξίδι μου ως υποψήφια διδάκτορας είναι ένα περίεργο ταξίδι... Η ιδέα του ξεκίνησε από μία τυχαία συζήτηση στον διάδρομο του κτηρίου 598 του CERN με την Στέλλα και συνεχίστηκε με κάποιες - όχι τόσο τυχαίες αυτή τη φορά - συζητήσεις με τον Παναγιώτη και τον Γιάννη έξω από μία συνέλευση στο αμφιθέατρο 1 της σχολής ΗΜΜΥ, για να πάρει σάρκα και οστά στο γραφείο του κ. Αβραμόπουλου κάποια στιγμή το φθινόπωρο του 2019. Ακολούθησαν πολλά επεισόδια μεταξύ Ελλάδας κι Ελβετίας. Τώρα φτάνει στο τέλος του και μου φαίνεται πολύ ταιριαστό που αυτό συμβαίνει στην Ελλάδα. Παρότι ξεκίνησε κάπως τυχαία και τα πρώτα βήματά του ήταν αναγνωριστικά μιάς και ιδέα δεν είχα τι ήταν τα Silicon Photonics, στην πορεία του έγινε μια συνειδητή επιλογή και κυρίως με οδήγησε στο να κατανοήσω και να εκτίμησω την αξία των επιλογών μου. Ξεκινώντας, λοιπόν, από την αρχή και φτάνοντας μέχρι το τέλος, θα ήθελα να ευχαριστήσω όλους τους ανθρώπους που βρέθηκαν δίπλα μου σε αυτό το ταξίδι.

Starting for the CERN era, I would first like to thank Stella Orfanelli. For this chat we had when I was leaving CERN the first time at the end of my internship, when she asked what I was planning to do next and I said I would consider doing a PhD. And for all the help to make this happen and introduce me to the opto-team at CERN, and all the support throughout the duration of the PhD. Σε ευχαριστώ πολύ Στέλλα, η βοήθεια σου ήταν πολύτιμη και στάθηκε η αφορμή για αυτό το όμορφο ταξίδι! Alongside Stella, I would also like to thank Duccio Abbaneo. His contribution to making this PhD happen was invaluable and he was always there to offer his help and support. I really appreciate everything you have done for me.

Moving on to the EP-ESE-BE section opto-team, that became my work family for the past 3 years, I would like to thank all of its members for making everyday fun in the numerous coffee brakes we had, and all the discussions that accompanied them. I feel very lucky to have had such wonderful co-workers, it helped me enjoy every day at work! Christophe Sigaud, Stephan Detraz, Lauri Olantera, and Csaba Soos, thank you for all the help that you offered when needed, you are all unique and funny in your own way and I am glad to have met you. I would also like to thank the younger members of the team, Milana Lalovic, Daisy Bergin, Ulrik Sandven, Aalia Ahmad, Leonardo Marcon, Awanish Pandey and Antonio Cassese. I met you in different periods during my PhD at CERN but you were all excellent co-workers and fun people, and we have shared some very nice moments! I would like to especially thanks Daniele Alfiero, whom I unfortunately met only at the end of my PhD, but I had the chance to share the office with him for a few months. Although at first the idea of sharing the office was annoying, you turned out to be the best office mate I could have asked for! I am really sad I only met you at the end, because I am sure we would have had a great time and I would have loved working with you. However, I am happy to call you my friend, you are the most well organized plant whisperer I have ever met, and I hope we will cross paths again.

At this point, I would like to thank Jan Troska, the leader of the opto-team. Although we did not spend much time working together, your guidance and perspective were precious. Thank you for the opportunities you have given me, and for always taking the time to help

and support me when it was needed. The discussions we had helped me a lot. I have promised myself to finish "What color is your parachute" with the first chance.. Of course, I would also like to thank from the bottom of my heart my supervisor, Carmelo Scarcella. I honestly believe you were the best supervisor I could have had. You are one of the smartest and most capable and hard-working people I have met. I have learned so much for you. I am grateful for all the knowledge you have shared, and your patience in helping me and answering all my questions, again and again. You always found the time to offer your help and support, and knew when to encourage me to find my own answers. It has been an honor to work with you and I am proud of the work we have achieved together. You have truly been an inspiration! Last but not least, a big thank you the rest of the members of the EP-ESE group, and especially to Sophie Baron, Daniel Hernandez and Paschalis Vichoudis. That you for the collaboration and I wish you all the best!

Σε αυτό το μεταβατικό σημείο, πριν επιστρέψω στην Ελλάδα, θα ήθελα να ευχαριστήσω πραγματικά όλους τους φίλους που γνώρισα ή συνάντησα ξανά στο CERN, και οι οποίοι έκαναν την δύσκολη καθημερινότητα ευχάριστη. Θέλω να ευχαριστήσω τον Μάνο, τον Χρήστο, την Μάγκυ, την Όλγα, την Tiona, τον Kacper, την Ναταλία, τον Κώστα, τον Μιχάλη, τον Felix και όλους τους υπόλοιπους. Οι δρόμοι μας συναντήθηκαν για λιγότερο ή περισσότερο, ωστόσο όλοι με βοηθήσατε να νιώσω το μέρος πιο φιλόξενο και οικείο. Έχω πολύ όμορφες αναμνήσεις μαζί σας. Χωρίς εσάς δεν θα τα είχα καταφέρει. Τέλος, θέλω να ευχαριστήσω ιδιαιτέρως τον Tirsi. Μαζί από την αρχή σε αυτό το ταξίδι, με βοήθησες σε κάθε στάδιο, και η παρουσία σου ήταν πάντα ανεκίμητη.

Συνεχίζοντας στον τελικό προορισμό του ταξιδιού, την Ελλάδα και το Εργαστήριο Φωτονικών Επικοινωνιών (ΕΦΕ) θα ήθελα να ξεκινήσω λέγοντας ένα τεράστιο ευχαριστώ στον καθηγητή μου, τον κ. Ηρακλή Αβραμόπουλο. Σας ευχαριστώ ειλικρινά που μου δώσατε την ευκαιρία να γίνω μέλος του εργαστηρίου και να κάνω το διδακτορικό μου μαζί σας. Από την αρχή της προσπάθειας υπήρξατε ιδιαίτερα βοηθητικός να ξεκινήσει αυτή η συνεργασία με το CERN, εν μέσω δύσκολων και απαιτητικών συνθηκών. Κυρίως όμως, συντελέσατε στο να γίνει αυτή η συνεργασία, που συνήθως είναι τυπική, πραγματική και ουσιαστική. Η συνεχής επικοινωνία, καθοδήγηση και προσπάθεια απο τη μεριά σας να βρεθούν σημεία τομής μεταξύ των ερευνητιών ομάδων του CERN και του ΕΦΕ, και να με υποστηρίξετε στην εκπόνηση του διδακτορικού, ήταν καθοριστικές. Έμαθα πάρα πολλά από την συνεργασία μου μαζί σας τόσο σε θεωρητικό όσο και σε πρακτικό επίπεδο μέσα από τις συχνές επισκέψεις στο εργαστήριο. Όλα αυτά είχαν ουσιαστική επίδραση στην ποιήτητα της έρευνας της διδακτορικής μου διατριβής, αφού πολλά κομμάτια της δεν θα είχαν γίνει αν δεν είχα τη βοήθεια σας. Ταυτόχρονα, οι συμβουλές σας ήταν πολύτιμες και σε προσωπικό επίπεδο. Χαίρομαι διαιτέρως που αυτά τα λόγια τα γράφω σαν πραγματικό μέλος του ΕΦΕ πλέον, έχοντας γυρίσει στην Ελλάδα. Αυτό για εμένα αποδεικνύει πόσο ουσιαστικά με βοηθήσατε και στην αρχή και στο τέλος του διδακτορικού, στα επόμενα βήματα. Έχετε στήσει ένα εξαιρετικό εργαστήριο, και η ύπαρξη του στην Ελλάδα, σαν μέρος του Δημόσιου Πανεπιστημίου, είναι πολύτιμη.

Συνεχίζοντας με τα μέλη του ΕΦΕ, στην διάρκεια του διδακτορικού μου, καθοριστική ήταν η βοήθεια του Γιάννη Πουλόπουλου, ο οποίος υπήρξε αφορμή και έμπνευση για να ασχοληθώ με τις προσομοιώσεις και τον σχεδιασμό ολοκληρωμενων φωτονικών κυκλωμάτων. Ένα σημαντικό κομμάτι του διδακτορικού μου αλλά και η μετέπειτα πορεία μου καθώς και το πρώτο

paper που έστειλα σε συνέδριο οφείλονται στην βοήθεια του. Ευχαριστώ επίσης πολύ τον Χάρη Ζερβό, που από την αρχή αλλά και στο τέλος με καλωσόρισε στην ομάδα του και βοήθησε σε όλα τα στάδιο στην οργάνωση και την ομαλή έκβαση της συνεργασίας μας (κυρίως με τα αστεία του). Θα ήθελα να ευχαριστήσω παράλληλα και τα υπόλοιπα μάλη του εργασητρίου, για την άψογη συνεργασία τους όλα αυτά τα χρόνια αλλά και για τις πολύ όμορφες στιγμές που περάσαμε στις επισκέψεις μου, τις βόλτες και τα ποτά, που αν και σύντομα αποτέλεσαν αφορμή να βρίσκομαι σήμερα στο ΕΦΕ. Τον Γιώργο Συριόπουλο για τις συζητήσεις, τις βόλτες, τα πρώτα πειράματα στο εργασήριο και τις αμίμητες ατάκες του, τις οποίες βέβαια σπάνια καταλαβαίνω ειδικά όταν συνδυάζονται με αυτές του Πουλόπουλου. Την Ευρυδίκη Κυριαζή, τον Παναγιώτη Τουμάση, τον Γιώργο Μπρέστα, τον Αργύρη Ντάνο, την Έλενα Μαριανίδου, τον Άρη Στάθη, τον Γιάννη Κανάκη για όλες τις όμορφες στιγμές και το γεγονός ότι έκαναν την παρουσία μου στο ΕΦΕ πολύ διασκεδαστική. Την Κωνσταντίνα Καντά, καλή μου φίλη από παλιά που την ξανασυνάντησα στο ΕΦΕ και της εύχομαι καλή τύχη στα επόμενα βήματα της. Ευχαριστώ επίσης του πιο μεγάλους του εργαστηρίου, τον Δημήτρη Αποστολόπουλο, τον Γιάννη Γιαννούλη και την Μαριλή Σπυροπούλου για την καθοδήγησή τους, κι ελπίζω να έχουμε την ευκαρία για συνεργαστούμε περισσότερο στο μέλλον. Ευχαριστώ την Βάσια Λαμπροπούλου και την Πόλυ Βλάση για την πολύτιμη βοήθειά τους. Τέλος ευχαιρστώ τον Λευτέρη Γουναρίδη, τον Πάνο Γκρούμα, τον Αδάμ Ραπτάκη, τον Στάθη Ανδριανόπουλο, τον Χρήστο Τσώκο, τον Νίκο Λύρα και τον Χρήστο Κουλουμέντα. Αν και δεν δουέψαμε μαζί ως τώρα, κάναμε όμορφες συζητήσεσι κατά τις επισκέψεις μου στο ΕΦΕ που με βοήθησαν να καταλάβω και να εκτιμήσω την πολύπλευρη έρευνα που λαμβάνει χώρα εκεί. Χάρη σε όλους εσάς το τελείωμα του διδακτορικού σηματοδοτεί ταυτόχρονα και μια νέα αρχή για εμένα, σαν μέλος του ΕΦΕ, εντός έδρας αυτή τη φορά.

Ολοκλήρώνοντας τις ευχαριστίες, θα ήθελα να αναφερθώ στους συγγενείς και φίλους που υπήρξαν στο πλάι μου όλα αυτά τα χρόνια, συνοδοιπόροι στη ζωή. Ευχαριστώ ολόψυχα την οικογένεια μου, την μαμά μου Ελίζα, τον μπαμπά μου Γιώργο και τα αδέρφια μου Ντίνο και Βασίλη. Τους ευχαριστώ για την άνευ όρων αγάπη και υποστήριξή τους σε κάθε βήμα της ζωής μου. Τους ευχαριστώ επίσης που με βοήθησαν να γίνω ο άνθρωπος που είμαι, και να βρίσκομαι στην σωστή πλευρά της ιστορίας, όπως την αναλαμβάνομαι. Τους εύχομαι να είναι πάντα ευτυχισμένοι και χαρούμενοι, και να μην ξεχνάνε ποιά είναι τα σημαντικά σε αυτή την ζωή. Ευχαριστώ την Άνθια. Έχουμε περάσει πολλά, όμορφα και δύσκολα, και είναι πάντα εκεί σε όλα, πργματική φίλη και υπέροχος άνθρωπος. Ευχαριστώ την Έλια, την Εμμανουέλα, την Ιόλη, τον Γιώργο, τον Χρήστο, τον Νίκο, την Κατερίνα. Η ζωή είναι πιο ωραία μαζί σας! Ευχαριστώ την Λένα, την Αφροδίτη, τον Θοδωρή, τον Γρηγόρη, τον Χρήστο και την Μάρθα για την παρουσία τους και το παράδειγμά τους όλα αυτά τα χρόνια. Ευχαριστώ επίσης όλους τους ΄δασκάλους' μου, και ειδικά τον κ. Γιαμούρη, για την έμπνευση και την αγάπη μου με μετέδωσαν για την γνώση. Τελος, θα ήθελα να ευχαριστήσω τον Α.Κ. για πουλλά. Για την συντροφιά, την υποστήριξη και όλες τις υπέροχες στιγμές που έχουμε μοιραστεί. Είσαι ένας μοναδικός άνθρωπος και έδωσες με την αγαπημένη παρουσία σου ιδιαίτερη διάσταση στην ζωή. Εύχομαι να είσαι πάντα ευτυχισμένος και να βρεις αυτά που ψάχνεις.

Απρίλιος 2024,

Θένια

Contents

Εκτεταμένη Περίληψη

Στις επόμενες δεκαετίες, διάφορες αναβαθμίσεις θα λάνουν χώρα στους ανιχνευτές και στα πειράματα του CERN. Η πρώτη από αυτές ονομάζεται high luminosity LHC βρίσκεται ήδη σε εξέλιξη και προβλέπει την λειτουργία των αναβαθμισμένων συστημάτων από το 2026. Ξεκινώντας από το τέλος της εποχής του HL-LHC, τα υψηλά επίπεδα ακτινοβολίας και οι αυξημένοι ρυθμοί δεδομένων λόγω της αυξημένης φωτεινότητας του επιταχυντή θα επιβάλουν την ανάγκη για μια νέα γενιά οπτικών ζεύξεων, ικανών να αντέξουν τις ακραίες συνθήκες στους ανιχνευτές και να υποστηρίξουν τους ρυθμούς δεδομένων. Οι διαθέσιμοι σήμερα οπτικοί πομποδέκτες που βασίζονται σε διακριτές φωτοδιόδους InGaAs και VCSEL δεν θα είναι σε θέση να επιβιώσουν στις ενδότερες περιοχές ορισμένων ανιχνευτών. Είναι εμφανές λοιπό ότι μια νέα γενιά οπτικών ζεύξεων μεταφοράς δεδομένων θα απαιτηθεί για τις μελλοντικές αναβαθμίσεις των πειραμάτων στο CERN. Η τεχνολογία φωτονικών συστημάτων πυριτίου (SiPh) έχει αναγνωριστεί ως ο τέλειος υποψήφιος για αυτή την αναβάθμιση, καθώς συνδυάζει όλα τα πλεονεκτήματα που απαιτούνται για μια τέτοια εφαρμογή.

Τα τελευταία χρόνια το CERN έχει ενδιαφερθεί για την τεχνολογία SiPh για τον προαναφερθέντα λόγο. Μια εκτεταμένη προσπάθεια έχει λάβει χώρα στο πλαίσιο της ομάδας EP-ESE του CERN που επικεντρώνεται στη μοντελοποίηση και την ανάπτυξη πομποδεκτών SiPh για εφαρμογή σε πειράματα φυσικής υψηλών ενεργειών. Η προσπάθεια αυτή περιλαμβάνει την προσομοίωση, το σχεδιασμό και την κατασκευή SiPh PICs για την ανάπτυξη των απαραίτητων δομικών στοιχείων που μπορούν να συνδυαστούν για την υλοποίηση πομποδεκτών SiPh ανθεκτικών στην ακτινοβολία. Ταυτόχρονα, μέρος αυτής της προσπάθειας αποτελεί και η δοκιμή και ο χαρακτηρισμός των δομών που σχεδιάστηκαν ως μέρος της διαδικασίας ανατροφοδότησης που απαιτείται για τη λήψη επιλογών σχεδιασμού, τεχνολογίας και αρχιτεκτονικής όσον αφορά το σύστημα-στόχο. Απαραίτητη πλευρά της ανάπτυξης οπτικών ζεύξεων με βάση τα SiPh για χρήση στο CERN είναι επίσης η εκτεταμένη μελέτη και επικύρωση της ανοχής στην ακτινοβολία των εξαρτημάτων και των κυκλωμάτων που αναπτύχθηκαν. Χωρίς αυτή τη μελέτη, η ενσωμάτωση των SiPh TRx δεν θα είναι δυνατή σε πειράματα του CERN.

Στο πλαίσιο της συνεργασίας του CERN, έχουν σχεδιαστεί και χαρακτηριστεί διάφορα δοκιμαστικά τσιπ SiPh. Σχετικό με την παρούσα διατριβή είναι το δεύτερο τσιπ που σχεδιάστηκε στο CERN το 2019 και κατασκευάστηκε από το multi project wafer (MPW) της imec το 2020, δηλαδή το PICv2. Αυτό το δοκιμαστικό τσιπ έχει διαστάσεις 5 mm x 5 mm και περιλαμβάνει IP μπλοκ που σχεδιάστηκαν στο CERN ή διατέθηκαν από τις βιβλιοθήκες του fab, τα οποία συνδυάζονται για να σχηματίσουν δομές για επιδείξεις μετάδοσης δεδομένων. Πιο συγκεκριμένα, το PIC περιλαμβάνει διάφορες παραλλαγές διαμορφωτών δακτυλίου, διαμορφωτές Mach-Zehnder (MZMs), φωτοδιόδους Γερμανίου, οπτικούς πολυπλέκτες, συμβολόμετρα για μελέτες ανάκτησης πόλωσης, καθώς και ένα κύκλωμα WDM με τέσσερεις διαμορφωτές δακτυλίου συνδεδεμένους σειριακά. Αυτό το PIC χρησίμευσε καταρχάς ως όχημα δοκιμών για τον χαρακτηρισμό των επιμέρους στοιχείων, την υλοποίηση test ακτινοβολίας και τη σύγκριση των διαφόρων παραλλαγών των στοιχείων όσον αφορά την απόδοση και την ανθεκτικότητα στην ακτινοβολία. Ταυτόχρονα, τα δομικά στοιχεία που είναι διαθέσιμα από το PIC μπόρεσαν να συνδυαστούν και να χρησιμοποιηθούν για τη συναρμολόγηση μιας πρώτης υλοποίησης πομπών και δεκτών, επιτρέποντας δοκιμές και χαρακτηρισμό υψηλότερου επιπέδου.

Σε επίπεδο συστήματος, η ανάπτυξη και λειτουργία πομποδεκτών με βάση το SiPh περιλαμβάνει πολλές προκλήσεις. Από την πλευρά του πομπού, μια πολύ σημαντική πρόκληση είναι η σταθεροποίηση του μήκους κύματος των διαμορφωτών δακτυλίου. Αυτό είναι απαραίτητο για να επιτευχθεί η σταθερή λειτουργία τους στο επιθυμητό μήκος κύματος λειτουργίας ανεξάρτητα από τις μεταβολές των περιβαλλοντικών συνθηκών (π.χ. θερμοκρασία, μεταβολή του μήκους κύματος του εξωτερικού λέιζερ). Μια άλλη σημαντική πρόκληση είναι η διαχείριση της πόλωσης. Αυτό απαιτείται λόγω της μοναδικής αρχιτεκτονικής μιας τέτοιας ζεύξης που επιβάλλει την τοποθέτηση των οπτικών πηγών στο back-end, μακριά από τα SiPh PICs, και τη σύνδεσή τους με οπτικές ίνες που δεν διατηρούν την πόλωση. Το ίδιο πρόβλημα υπάρχει και στην πλευρά του δέκτη, δεδομένου ότι ο SiPh δέκτης θα συνδεθεί με τον BE πομπό μέσω οπτικών ινών. Ειδικά στην περίπτωση μιας υλοποίησης πολυπλεξίας μηκών κύματος, η αρχιτεκτονική ολόκληρης της ζεύξης, συμπεριλαμβανομένου του κυκλώματος SiPh, των laser και της διαχείρισης της πόλωσης και του θερμικού συντονισμού, γίνεται πιο πολύπλοκη και απαιτεί επιπλέον προσπάθεια και προκλησεις προς αντιμετώπιση.

Το αντικείμενο αυτής της διατριβής, που αντικατοπτρίζει επίσης την δουλειά που πραγματοποίησε η συγγραφέας τα τελευταία τρία χρόνια, εξελίσσεται γύρω από την ανάπτυξη ενός SiPh πομπού και δέκτη με βάση τα εξαρτήματα που παρέχονται από το PICv2. Αφορά επίσης την αντιμετώπιση των προκλήσεων που συνεπάγεται η ανάπτυξη ενός τέτοιου SiPh πομποδέκτη σε επίπεδο συστήματος. Παρακάτω αναλύονται τα βασικά σημεία της έρευνας που διενεργήθει σε αυτά τα πλαίσια κατά τη διάρκεια του διδακτορικού.

Η διατριβή ξεκινάει με μία εισαγωγική περιγραφή του CERN. Το CERN είναι ένα συλλογικό εγχείρημα στο οποία συμμετέχουν επιστήμονες και μηχανικοί από όλο τον κόσμο. Η έρευνα που πραγματοποιείται στο CERN επικεντρώνεται στη σωματιδιακή φυσική και συγκεκριμένα στη μελέτη των μικρότερων σωματιδίων που αποτελούν το σύμπαν και των θεμελιωδών δυνάμεων που τα διέπουν. Η βασικότερη υποδομή του CERN είναι ο LHC, ο μεγάλος επιταχυντής σωματιδίων, ο οποίος αποτελείται από διαφορετικούς επιταχυντές και ανιχνευτές που δουλεύουν μαζί σαν ένα σύνολο. Για την πλήρη αξιοποίηση των φυσικών δυνατοτήτων του LHC, το CERN δημιούργησε το πρόγραμμα HL-LHC που στοχεύει στην αύξηση του ρυθμού σύγκρουσης σωματιδίων κατά τουλάχιστον δέκα φορές. Ο υψηλότερος αριθμός συγκρούσεων θα προκαλέσει σημαντική αύξηση στον ρυθμό παραγωγής και ανάγνωσης δεδομένων, καθώς και αυξημένα επίπεδα ακτινοβολίας στο περιβάλλον του ανιχνευτή. Αυτό με τη σειρά του απαιτεί πιο πολύπλοκο υλικό και λογισμικό που θα είναι σε θέση να διαχειριστεί τον αυξημένο όγκο δεδομένων. Ταυτόχρονα, η αυξημένη φωτεινότητα δημιουργεί την ανάγκη για εξαρτήματα που θα είναι πιο ανθεκτικά στην ακτινοβολία και ικανά να λειτουργήσουν αξιόπιστα στους ανιχνευτές για το απαιτούμενο χρονικό διάστημα. Αυτό σημαίνει ότι η αναβάθμιση του HL-LHC και άλλες μελλοντικές αναβαθμίσεις των πειραμάτων του CERN θα πρέπει να συνοδευτούν από αναβάθμιση των συστημάτων των ανιχνευτών, του υλικού και του λογισμικού, για να αντιμετωπίσουν τους ολοένα αυξανόμενους ρυθμούς παραγωγής δεδομένων και τα επίπεδα ακτινοβολίας. Μια από τις σημαντικότερες προκλήσεις στα πειράματα του CERN είναι η υλοποίηση συνδέσεων για τη μεταφορά των δεδομένων που παράγονται από τους ανιχνευτές στο back-end (BE) για επεξεργασία και αποθήκευση, καθώς και των δεδομένων ρύθμισης και χρονισμού από τον BE στο front-end (FE).

Οι οπτικές ζεύξεις μεταφοράς δεδομένων προτιμώνται ευρέως σε όλα τα πειράματα του

LHC λόγω των πολλών πλεονεκτημάτων που παρέχουν έναντι των λύσεων που βασίζονται στο χαλκό. Κατά τη διάρκεια των τελικών περιόδων λειτουργίας του HL-LHC, τα εξαρτήματα που είναι εγκατεστημένα στις πιο εσωτερικές περιοχές των ανιχνευτών θα πρέπει να αντέξουν μια συνολική ιοντίζουσα δόση (TID) 12 MGy(Si) και μια ισοδύναμη ροή νετρονίων 1 MeV $2.3 \times 10^{16}\,\mathrm{n_{eq}/cm^2}$. Κατά συνέπεια, οι τελικές περίοδοι λειτουργίας του HL-LHC και άλλες μελλοντικές αναβαθμίσεις πρέπει να συνοδεύονται από αναβάθμιση του υλικού των οπτικών ζεύξεων του ανιχνευτή ώστε να μπορεί να χειριστεί τους συνεχώς αυξανόμενους ρυθμούς δεδομένων και τα επίπεδα ακτινοβολίας. Καθίσταται προφανές ότι πρέπει να αναπτυχθεί μια νέα γενιά οπτικών ζεύξεων που θα είναι συμβατές με τις απαιτήσεις των τελικών περιόδων λειτουργίας του HL-LHC και των μελλοντικών αναβαθμίσεων των πειραμάτων του CERN. Οι απαιτήσεις για αυτά τα εξαρτήματα είναι αυξημένη ανθεκτικότητα στην ακτινοβολία, αυξημένο εύρος ζώνης, χαμηλή μάζα και χαμηλή κατανάλωση ενέργειας, χαμηλό κόστος και συμβατότητα με τα εμπορικά διαθέσιμα εξαρτήματα που θα τοποθετηθούν στο BE.

Μεταξύ των διαθέσιμων τεχνολογιών, η φωτονική τεχνολογία πυριτίου (Silicon Photonics - SiPh) έχει αναγνωριστεί ως εξαιρετικός υποψήφιος για την ανάπτυξη της επόμενης γενιάς οπτικών ζεύξεων στο CERN. Τα επιχειρήματα υπέρ αυτής της τεχνολογίας είναι η συμβατότητά της με τις διαδικασίες κατασκευής CMOS, επιτρέποντας χαμηλό κόστος και υψηλή ποιότητα κατασκευής. Το πυρίτιο έχει εξαιρετικές ιδιότητες σαν υλικού που είναι σημαντικές στις φωτονικές διατάξεις. Αυτές περιλαμβάνουν υψηλή θερμική αγωγιμότητα (σχεδόν 10 φορές υψηλότερη από το GaAs), υψηλό κατώφλι οπτικής βλάβης (σχεδόν 10 φορές υψηλότερο από το GaAs) και υψηλές οπτικές μη γραμμικότητες τρίτης τάξης. Το πυρίτιο παρουσιάζει ένα παράθυρο μήκους κύματος χαμηλών απωλειών που εκτείνεται από 1,1 έως σχεδόν 7 μm, καθιστώντας το ιδανικό υλικό για την υλοποίηση οπτικών κυκλωμάτων στα δαταζομ και τελεζομ μήκη κύματος γύρω από τις C και O μπάντες. Συνολικά, η πλατφόρμα SiPh είναι μια πλήρης πλατφόρμα που επιτρέπει την ανάπτυξη όλων των απαραίτητων παθητικών και ενεργών στοιχείων (κυματοδηγοί, ζεύκτες, διαχωριστές ισχύος, διαχωριστές και περιστροφείς πόλωσης, οπτικοί διαμορφωτές, μετατοπιστές φάσης, φωτοανιχνευτές κ.λπ.) που μπορούν να συνδυαστούν για την υλοποίηση ολοκληρωμένων οπτικών ζεύξεων μεταφοράς δεδομένων. Οι πομποί πυριτίου μπορούν να επιτύχουν πολύ υψηλούς ρυθμούς μετάδοσης δεδομένων. Στη βιβλιογραφία έχουν αναφερθεί διαμορφωτές δακτυλίου με BW άνω των 100 GHz, καθιστώντας την πλατφόρμα SiPh συμβατή με εφαρμογές που απαιτούν υψηλές ταχύτητες. Είναι επίσης δυνατή η υλοποίηση συστημάτων πολυπλεξίας μηκών κύματος (WDM) με πομπούς πυριτίου, τα οποία μπορούν να αυξήσουν περαιτέρω τη χωρητικότητα των συνδέσεων. Ένα άλλο πλεονέκτημα της πλατφόρμας SiPh και της συμβατότητάς της με τις διεργασίες κατασκευής CMOS είναι η δυνατότητα επίτευξης υψηλών επιπέδων ολοκλήρωσης μεταξύ των φωτονικών και των ηλεκτρονικών τσιπ. Ωστόσο, το βασικό επιχείρημα υπέρ της συγκεκριμένης τεχνολογίας είναι η υψηλή ανθεκτικότητα στην ακτινοβολία των παθητικών και ενεργών στοιχείων πυριτίου, η οποία αποτέλεσε αντικείμενο εκτεταμένης έρευνας στην κοινότητα φυσικής υψηλών ενεργειών και στο CERN. Διάφορες μελέτες που πραγματοποιήθηκαν τόσο στο CERN όσο και σε άλλες ερευνητικές εγκαταστάσεις έχουν διερευνήσει την ανθεκτικότητα των εξαρτημάτων και συσκευών πυριτίου έναντι βλαβών από ιονίζουσα και μη ιονίζουσα ακτινοβολία.

Λόγω αυτών των πλεονεκτημάτων, η Τεχνολογία SiPh ερευνάται εκτενώς τα τελευταίο χρόνια στο CERN. Μια σειρά chip έχουν σχεδιαστεί που περιλαμβάνουν τα στοιχεία εκείνα

που είναι απαραίτητα για την σύνθεση πομπών και δεκτών πυριτίου. Ο SiPh πομπός αποτελείται από ένα διαμορφωτή δακτυλίου πυριτίου απογύμνωσης φορέων σε ανάστροφη πόλωση που περιλαμβάνει μια δεύτερη θύρα εξόδου (drop-port), με εύρος ζώνης 50 GHz και ακτίνα 5 μm. Μία φωτοδίοδος Γερμανίου συνδεδεμένη στην έξοδο της drop θύρας επιτρέπει την παρακολούθηση της μέσης ισχύος της drop θύρας (P_{avg}). Αυτό το σύστημα είναι χρήσιμο για την υλοποίηση ενός βρόχου ελέγχου θερμικής ρύθμισης που βασίζεται στην παρακολούθηση της μέσης ισχύος στη drop θύρα. Ένας ενσωματωμένος μικροθερμαντήρας βολφραμίου που τοποθετείται πάνω από τον κυματοδηγό του διαμορφωτή δακτυλίου επιτρέπει τον έλεγχο της θερμοκρασίας και του μήκους κύματος συντονισμού (λ_{res}) μέσω του θερμοοπτικού φαινομένου στο πυρίτιο. Αυτό μπορεί να επιτευχθεί με τη ρύθμιση της τάσης που εφαρμόζεται στον θερμαντήρα (V_{heater}) με μια πηγή τάσης. Η διαμόρφωση υψηλής ταχύτητας του διαμορφωτή δακτυλίου μπορεί να επιτευχθεί με την εφαρμογή μιας τάσης διαμόρφωσης υψηλού εύρους ζώνης V_{mod}, που αντιστοιχεί στα ηλεκτρικά δεδομένα, μέσω των ακροδεκτών υψηλού εύρους ζώνης του διαμορφωτή. Στη συνέχεια της διατριβής πραγματοποιείται ο χαρακτηρισμός του διαμορφωτή δακτυλίου, συμπεριλαμβανομένων των μετρήσεων του φάσματος εξόδου του και της εξαγωγής των σημαντικών παραμέτρων του, δηλαδή του ελεύθερου φασματικού εύρους (FSR), του εύρους δέσμης ημίσειας ισχύος (FWHM) και του συντελεστή ποιότητας Q. Οι εξαγόμενες τιμές $FSR = 20\,\text{nm}$ και $Q = 2000$ συμφωνούν καλά με τις αναμενόμενες τιμές με βάση τις σχεδιαστικές παραμέτρους. Στη συνέχεια, παρουσιάζονται οι διάφορες πλακέτες που έχουν συναρμολογηθεί για τον χαρακτηρισμό του πομπού. Περιλαμβάνουν την πλακέτα δοκιμών χαμηλών συχνοτήτων για τον DC χαρακτηρισμό, την πλακέτα για μετρήσεις σε ταχύτητες δεδομένων έως $10\,\text{Gbit}\,\text{s}^{-1}$ και τις πλακέτες $25\,\text{Gbit}\,\text{s}^{-1}$, που επιτρέπουν τον χαρακτηρισμό σε υψηλές συχνότητες που υποστηρίζουν ταχύτητες δεδομένων έως $25\,\text{Gbit}\,\text{s}^{-1}$.

Ο χαρακτηρισμός του πομπού περιλαμβάνει τις στατικές μετρήσεις και τις μετρήσεις με υψηλούς ρυθμούς δεδομένων. Οι στατικές μετρήσεις πραγματοποιούνται μόνο με σήματα συνεχούς ρεύματος και χωρίς οδήγηση υψηλής ταχύτητας. Αποτελούν ένα ισχυρό εργαλείο για τη μέτρηση των περισσότερων χαρακτηριστικών του διαμορφωτή δακτυλίου και του πομπού, δηλαδή του οπτικού πλάτους διαμόρφωσης (OMA), του λόγου αποσβέσεως (ER), των απωλειών εισόδου (IL) και του κόστους μετάδοσης (TP), απλά και χωρίς την ανάγκη οδήγησης υψηλής ταχύτητας. Ως δεύτερο βήμα, τα τεστ σε υψηλούς ρυθμούς δεδομένων επιτρέπουν τις μετρήσεις των διαγραμμάτων οφθαλμού υψηλής ταχύτητας και την επικύρωση της λειτουργίας υψηλής ταχύτητας του πομπού. Η εκτέλεσή τους είναι πιο περίπλοκη, δεδομένου ότι απαιτείται εξοπλισμός που να υποστηρίζει τους απαιτούμενους ρυθμούς δεδομένων τόσο για την οδήγηση των διαμορφωτών δακτυλίου όσο και για την καταγραφή των διαγραμμάτων οφθαλμού. Στην διατριβή αυτή παρουσιάζεται πρώτα ο χαρακτηρισμό DC και στη συνέχεια ο χαρακτηρισμός υψηλής ταχύτητας του πομπού. Αρχικά, ο χαρακτηρισμός DC πραγματοποιείται με χαμηλή ισχύ εισόδου ($< 0.5\,\text{mW}$) για να αποφευχθούν τυχόν φαινόμενα αυτοθέρμανσης (self-heating). Το φάσμα μετάδοσης του PM μετράται μεταβάλλοντας το μήκος κύματος του εξωτερικού λέιζερ (λ_{laser}) για διαφορετικές τάσεις διαμόρφωσης V_{mod}. Η εξαγόμενη απόδοση διαμόρφωσης είναι $40\,\text{pm}\,\text{V}^{-1}$. Από αυτά τα δεδομένα μπορούμε να εξάγουμε τα χαρακτηριστικά που προαναφέρθηκαν (OMA, TP, ER, IL). Ωστόσο, στις εφαρμογές datacom η ισχύς εισόδου πρέπει να είναι υψηλότερη για να είναι συμβατή με τις απαιτήσεις ισχύος των χρησιμοποιούμενων ζεύξεων. Επομένως, οι προηγούμενες μετρήσεις επαναλήφθηκαν για πιο υψηλό P_{in} (μερικά

mW). Σε αυτή την περίπτωση το φαινόμενο αυτοθέρμανσης τροποποιεί την απόκριση του διαμορφωτή. Οι μετρούμενες καμπύλες εμφανίζονται τότε μετατοπισμένες προς μεγαλύτερα μήκη κύματος και δεν είναι πλέον συμμετρικές. Ωστόσο, όπως και στην περίπτωση της χαμηλής ισχύς εισόδου, υπάρχει ένα συγκεκριμένο βέλτιστο μήκος κύματος (λ_{optimal}) κοντά στον σημείο συντονισμού του διαμορφωτή δακτυλίου όπου το OMA μεγιστοποιείται και το TP ελαχιστοποιείται. Αυτό είναι το βέλτιστο σημείο λειτουργίας του διαμορφωτή όπου το άνοιγμα του διαγράμματος οφθαλμού είναι το μεγαλύτερο. Μια χαρακτηριστική τιμή του φωτορεύματος I_{ph}, στην φωτοδίοδο που βρίσκεται στην drop έξοδο του διαμορφωτή, που ονομάζεται setpoint αντιστοιχεί σε αυτό το βέλτιστο σημείο. Για έναν δεδομένο σχεδιασμό του διαμορφωτή αυτό το σημείο ισούται με ένα σταθερό ποσοστό του μέγιστου $\text{I}_{\pi\eta}$ ($I_{ph} = k \cdot I_{ph-max}$). Το k εξαρτάται από τα γεωμετρικά χαρακτηριστικά του διαμορφωτή που προσδιορίζονται κατά τον σχεδιασμό και ο υπολογισμός του επιτρέπει τον εύκολο υπολογισμό του χαρακτηριστικού σημείου. Για τους διαμορφωτές δακτυλίου από το PIC μας, το k μετρήθηκε στο εύρος $0.65 - 0.8$. Ο υπολογισμός του κ και κατά συνέπεια του χαρακτηριστικού σημείου λειτουργίας (βέλτιστο I_{ph}) είναι απαραίτητος, καθώς επιτρέπει τον εύκολο εντοπισμό του βέλτιστου σημείου λειτουργίας του διαμορφωτή κατά τη λειτουργία. Αυτό με τη σειρά του επιτρέπει τον ενεργό έλεγχο και τη θερμική σταθεροποίηση του διαμορφωτή για τη διασφάλιση της σταθερής λειτουργίας του. Η λειτουργία του διαμορφωτή σε αυτό το βέλτιστο σημείο επιτυγχάνεται όταν $\lambda_{\text{laser}} = \lambda_{\text{optimal}}$. Λόγω εξωτερικών μεταβολών (π.χ. μεταβολές της θερμοκρασίας) που επηρεάζουν το μήκος κύματος συντονισμού των διαμορφωτών δακτυλίου, είναι απαραίτητος ο συνεχής ενεργός έλεγχος των συσκευών για να εξασφαλιστεί η σταθερή λειτουργία τους σε αυτό το βέλτιστο σημείο λειτουργίας.

Για να επικυρωθεί η λειτουργία του πομπού σε υψηλούς ρυθμούς δεδομένων, πραγματοποιήθηκαν μετρήσεις διαγράμματος οφθαλμού σε ρυθμούς $25\,\text{Gbit}\,\text{s}^{-1}$. Τα αποτελέσματα δείχνουν διαγράμματα οφθαλμών που είναι ανοικτά και καθαρά, χωρίς τρεμούλιασμα και θόρυβο. Αυτά τα αποτελέσματα αποτελούν ένδειξη της αποτελεσματικής λειτουργίας των SiPh διαμορφωτών δακτυλίου σε υψηλούς ρυθμούς δεδομένων. Ταυτόχρονα, πραγματοποιήθηκε ο χαρακτηρισμός του μικροθερμαντήρα. Αυτό περιελάμβανε τη μέτρηση της βηματικής συνάρτησης απόκρισης και της χρονικής σταθεράς του, η οποία μετρήθηκε ίση με $20\,\mu\text{s}$. Έγινε επίσης ο θερμικός και ηλεκτρικός χαρακτηρισμός. Τα χαρακτηριστικά που εξήχθησαν από τον μικροθερμαντήρα είναι τα ακόλουθα:

$$\frac{d\lambda_{res}}{dT} = 70\,\frac{\text{pm}}{^{\circ}\text{C}}$$

$$\frac{d\lambda_{res}}{dP_{heater}} = 272\,\frac{\text{pm}}{\text{mW}}$$

$$\frac{dT}{dP_{heater}} = 4\,\frac{^{\circ}\text{C}}{\text{mW}}$$

Ο χαρακτηρισμός του πομπού περιλαμβάνει, τέλος, μετρήσεις σχετικά με το φαινόμενο αυτοθέρμανσης και τη θερμο-οπτική συνάρτηση μεταφοράς του διαμορφωτή δακτυλίου.

Στη συνέχεια της διατριβής παρουσιάζονται ορισμένες εκτιμήσεις σχετικά με τον ηλεκτρικό οδηγό και το σχήμα διαμόρφωσης του πομπού, οι οποίες αποσκοπούν στην αιτιολόγηση ορισμένων επιλογών σχεδιασμού και συστήματος που έχουν γίνει καθώς και στη διερεύνηση

πιθανών τρόπων αύξησης του εύτους ζώνης της ζεύξης, όπως η χρήση σχημάτων PAM4 ή WDM.

Το PIC που σχεδιάστηκε στο CERN περιλαμβάνει, εκτός από τους απλούς διαμορφωτές δακτυλίου, κι ένα κύκλωμα πομπού πολυπλεξίας μηκών κύματος (WDM) 4 καναλιών με τέσσερεις διαμορφωτές δακτυλίου συνδεδεμένων σειριακά, που είναι συζευγμένοι σε έναν κοινό κυματοδηγό. Το κύκλωμα σχεδιάστηκε ώστε να είναι συμβατό με το πυκνό πλέγμα μηκών κύματος (DWDM grid). Οι δακτύλιοι έχουν διαφορετικές ακτίνες ($\mathrm{r} = 5\,\mu\mathrm{m}$ με $\Delta\mathrm{r} = 24\,\mathrm{nm}$) που προκαλούν ομοιόμορφα κατανεμημένες κορυφές συντονισμού με απόσταση 5 nm. Κάθε διαμορφωτής έχει τους δικούς του ακροδέκτες υψηλής ταχύτητας, μικροθερμαντήρα και φωτοδιόδου drop θύρας για τη θερμική του ρύθμιση ανεξάρτητα. Για τη λειτουργία αυτού του κυκλώματος μπορεί να χρησιμοποιηθεί ένα εξωτερικό λέιζερ 4 καναλιών με πλέγμα DWDM με απόσταση καναλιών 5 nm.

Όπως και στην περίπτωση του κυκλώματος ενός καναλιού, έτσι κι εδώ η δομή 4 καναλιών χαρακτηρίστηκε και με στατικές μετρήσεις αλλά και μετρήσεις υψηλής ταχύτητας. Ο στατικός χαρακτηρισμός του κυκλώματος 4 καναλιών περιλαμβάνει τη μέτρηση του φάσματος μετάδοσης στην έξοδο του κυκλώματος, μεταβάλλοντας το μήκος κύματος εισόδου. Η μέτρηση αυτή πραγματοποιήθηκε με μια πηγή λέιζερ ρυθμιζόμενου μήκους κύματος και επιβεβαίωσε ότι οι κορυφές συντονισμού έχουν απόσταση 5 nm και ότι το FSR του διαμορφωτή εξακολουθεί να είναι 20 nm. Ο χαρακτηρισμός υψηλής ταχύτητας του κυκλώματος 4 καναλιών περιελάμβανε τη μέτρηση των διαγραμμάτων οφθαλμού υψηλής ταχύτητας και για τους 4 διαμορφωτές στα $25\,\mathrm{Gbit\,s^{-1}}$. Οι μετρήσεις δείχνουν καλή ομοιομορφία μεταξύ των τεσσάρων καναλιών.

Λόγω του υψηλού θερμο-οπτικού συντελεστή του πυριτίου, το λ_{res} των διαμορφωτών δακτυλίου είναι ευαίσθητο στις διακυμάνσεις της θερμοκρασίας (μετρούμενο $\frac{\Delta\lambda res}{\Delta T} = 70\frac{pm}{^\circ\mathrm{C}}$). Επίσης, σφάλματα κατά τη διαδικασία κατασκευής επηρεάζουν τις γεωμετρικές παραμέτρους των διαμορφωτώμ και μπορούν να προκαλέσουν μεταβολές του λ_{res} μερικών nm. Το λ_{laser} μπορεί επίσης να αποκλίνει από την ονομαστική του τιμή λόγω θερμικών μετατοπίσεων ή παραλλαγών στην κατασκευή. Σε όλες αυτές τις περιπτώσεις το λ_{res} αποσυντονίζεται από το λ_{laser} και ο διαμορφωτής δεν λειτουργεί πλέον στο βέλτιστο σημείο μέγιστου OMA. Αυτό μπορεί να έχει ως αποτέλεσμα την υποβάθμιση του διαμορφωμένου οπτικού σήματος ή την πλήρη απώλεια της διαμόρφωσης.

Για να εξασφαλιστεί η σταθερή λειτουργία των διαμορφωτών είναι απαραίτητος ένας μηχανισμός θερμικής ρύθμισης που αντισταθμίζει τις προαναφερθείσες διακυμάνσεις ρυθμίζοντας ενεργά τη θερμοκρασία (και ισοδύναμα το λ_{res}) του διαμορφωτή, εκμεταλλευόμενος το θερμο-οπτικό φαινόμενο. Μετά από εκτενή ανασκόπηση των διαθέσιμων τεχνικών θερμικής ρύθμισης στη βιβλιογραφία, επιλέγεται για την παρούσα εφαρμογή ένας βρόχος ελέγχου ανάδρασης που βασίζεται στην παρακολούθηση της μέσης ισχύος στη drop θύρα του διαμροφωτή. Αυτή η τεχνική απαιτεί ηλεκτρονικά χαμηλής συχνότητας και χαμηλής ισχύος και είναι συμβατή με κυκλώματα WDM. Στα πλαίσια της διατριβής, πραγματοποιείται εκτενής διερεύνηση των απαιτήσεων ενός τέτοιου συστήματος ελέγχου θερμικής ρύθμισης. Η διερεύνηση στοχεύει στον καθορισμό των απαραίτητων στοιχείων του συστήματος, των χαρακτηριστικών αυτών των στοιχείων, καθώς και της καταλληλότητας αυτής της λύσης για την εφαρμογή μας, η οποία επαληθεύεται.

Ο βρόχος ελέγχου ανατροφοδότησης βασίζεται σε μια αρχιτεκτονική αισθητήρα-ελεγκτή-

ενεργοποιητή. Περιλαμβάνει τη drop θύρα με την φωτοδίοδο Γερμανίου, τον PI ελεγκτή και τον μικροθερμαντήρα. Ο ελεγκτής PI παρακολουθεί το σήμα ανάδρασης (drop port I_{ph}) που παράγεται από τη φωτοδίοδο (αισθητήρας) και το συγκρίνει με την τιμή αναφοράς για τον υπολογισμό του σφάλματος. Δεδομένης της τιμής σφάλματος, εφαρμόζεται διόρθωση στον διαμορφωτή με κατάλληλη πόλωση του μικροθερμαντήρα (ενεργοποιητής) για να ρυθμιστεί ενεργά η θερμοκρασία του διαμορφωτή.

Για τη δοκιμή του συστήματος θερμικής ρύθμισης και τον χαρακτηρισμό του πομπού, υλοποιούνται δύο διαφορετικές εκδόσεις του βρόχου ελέγχου θερμικής ρύθμισης, σύμφωνα με τις ανάγκες και τις δυνατότητες των διαφόρων ερευνητικών φάσεων. Μια πρώτη έκδοση του βρόχου ελέγχου κλειστής ανατροφοδότησης συναρμολογήθηκε με σκοπό τη δοκιμή της καταλληλότητας και της απόδοσης του βρόχου ελέγχου παρακολούθησης καθώς και την επαλήθευση της συμβατότητάς του με τους διαμορφωτές του PIC που σχεδιάστηκε στο CERN. Αυτή η πρώτη υλοποίηση βασίστηκε σε όργανα πάγκου για την ανάγνωση του I_{ph} της drop θύρας καθώς και της πόλωσης του μικροθερμαντήρα και είχε ως στόχο τη μελέτη και την αντιστάθμιση αργών περιβαλλοντικών θερμοκρασιακών διαταραχών. Σε δεύτερο χρόνο, για να βελτιστοποιηθεί το μέγεθος και η επεκτασιμότητα της διάταξης δοκιμής θερμικού ελέγχου καθώς και η συχνότητα λειτουργίας της, τα όργανα πάγκου αντικαταστάθηκαν από μια πλακέτα που σχεδιάστηκε στο CERN για αυτόν το σκοπό. Αυτό αύξησε τη συχνότητα λειτουργίας του βρόχου ελέγχου από 2 Hz σε 50 Hz επιτρέποντας ταχύτερη διόρθωση σφαλμάτων, ενώ αποτελεί μια λύση που πιάνει πολύ λιγότερο χώρο σε σύγκριση με τα όργανα πάγκου. Ταυτόχρονα, η χρήση των πλακετών επιτρέπει τον θερμικό έλεγχο του κυκλώματος WDM που περιλαμβάνει 4 διαμορφωτές. Η υλοποίηση του επιλεγμένου μηχανισμού θερμικής ρύθμισης απαιτούσε το σχεδιασμό και τη ρύθμιση του ελεγκτή PI που πραγματοποιήθηκε με το Matlab και το Simulink και προσαρμόστηκε για τις διάφορες εκδόσεις του συστήματος.

Η διαδικασία θερμικής ρύθμισης περιλαμβάνει δύο βήματα. Το πρώτο είναι η διαδικασία εκκίνησης κατά την οποία μετράται η καμπύλη I_{ph}=f(V_{heater}) και προσδιορίζεται το βέλτιστο I_{ph} (setpoint) που αντιστοιχεί στο επιθυμητό σημείο λειτουργίας, με τη βοήθεια της παραμέτρου k. Στη συνέχεια, ως δεύτερο βήμα, ο ελεγκτής PI αναλαμβάνει να κλειδώσει το I_{ph} στην τιμή αναφοράς. Αυτή η υλοποίηση του βρόχου θερμικού ελέγχου εξασφαλίζει τη σταθερή λειτουργία του διαμορφωτή δακτυλίου στο βέλτιστο σημείο του.

Αφού ολοκληρώθηκε η διαδικασία σχεδιασμού, προσομοίωσης, υλοποίησης και επαλήθευσης του βρόχου θερμικού ελέγχου, ο βρόχος δοκιμάστηκε πειραματικά σε λειτουργία ενός καναλιού, σε κλειστό βρόχο. Για να το δοκιμάσουμε έναντι όλων των τύπων διακυμάνσεων μεταβάλλαμε με τη σειρά τόσο τη θερμοκρασία όσο και το μήκος κύματος του laser λlaser. Οι αντίστοιχες παράμετροι του διαγράμματος οφθαλμού καταγράφηκαν κατά τη διάρκεια εκτέλεσης του τεστ. Το OMA και το ER παρουσιάζουν διακυμάνσεις έως και 20% σε ένα εύρος θερμοκρασιών 50 °C. Παρ΄όλα αυτά, αυτές οι διακυμάνσεις δεν ειναι πραγματικές και οφείλονται στη διαδικασία μέτρησης. Πιο συγκεκριμένα εισάγονται λόγω της εξάρτηση της οπτικής σύζευξης από τη θερμοκρασία. Απαιτούνται περισσότερες μελέτες για τη βελτιστοποίηση της διαδικασίας συναρμολόγησης της δοκιμαστικής πλακέτας και την επίτευξη σταθερής και ανεξάρτητης από τη θερμοκρασία σύζευξης μεταξύ των οπτικών ινών και των συζευκτών πλέγματος πυριτίου. Όσον αφορά τη διακύμανση του λ_{laser}, το OMA και το ER είναι σταθερά με διακυμάνσεις μικρότερες από 10% της μέσης τιμής τους για εύρος διακύμανσης 6 nm. Οι

μετρήσεις αυτές επιβεβαιώνουν ότι ο βρόχος θερμικού ελέγχου μπορεί να αντισταθμίσει αποτελεσματικά τόσο τις διακυμάνσεις της θερμοκρασίας όσο και του λ_{laser} εξασφαλίζοντας έτσι τη σταθερή λειτουργία του διαμορφωτή στο βέλτιστο σημείο λειτουργίας του.

Όπως συμβαίνει με το σύστημα ενός καναλιού, το σύστημα WDM απαιτεί επίσης θερμική ρύθμιση. Οι διαμορφωτές στον WDM πομπό δεν είναι ευθυγραμμισμένοι με λ_{laser} στο οποίο είναι σχεδιασμένοι να λειτουργούν. Η ευθυγράμμιση αυτή επιτυγχάνεται με τον βρόχο ελέγχου θερμικής ρύθμισης. Για τα τεστ που διενεργούνται σε αυτό το στάδιο, η αντιστοιχία μεταξύ διαμορφωτή και λ_{laser} μπορεί να επιλεγεί ελεύθερα για λόγους ευκολίας. Ωστόσο, στο τελικό σύστημα κάθε διαμορφωτής πρέπει να λειτουργεί σε ένα συγκεκριμένο μήκος κύματος, για τη διαλειτουργικότητα μεταξύ των frontend και backend καναλιών.

Για να δοκιμαστεί ο βρόχος θερμικού ελέγχου σε πολυκαναλική λειτουργία, πραγματοποιήθηκε σάρωση θερμοκρασίας ενώ ο ελεγκτής λειτουργούσε ταυτόχρονα σε κλειστό βρόχο και για τους τέσσερα διαμορφωτές. Για τον έλεγχο της θερμοκρασίας της πλακέτας δοκιμής χρησιμοποιήθηκε ένας κλιματικός θάλαμος, ενώ καταγράφονταν τα δεδομένα θερμοκρασίας και διαγραμμάτων οφθαλμού. Δεδομένης της διαθεσιμότητας του εξοπλισμού, μόνο δύο διαμορφωτές διαμορφώθηκαν από το σήμα υψηλής ταχύτητας κατά τη διάρκεια της δοκιμής. Το OMA παρέμεινε σταθερό (εντός του 20% της ονομαστικής του τιμής) στην περιοχή θερμοκρασιών από $25\,^{\circ}\text{C}$ έως $-5\,^{\circ}\text{C}$. Ένα πιθναό πρόβλημα για ένα πολυκαναλικό σύστημα θα μπορούσε να είναι ότι η λειτουργία ενός δεδομένου καναλιού επηρεάζει τα γειτονικά κανάλια - μια μορφή παρεμβολής. Δεδομένης της παρατηρούμενης σταθερότητας, μπορούμε να υποθέσουμε ότι η εν λόγω παρεμβολή είναι αμελητέα σε αυτό το σύστημα.

Παρόλο που ο βρόχος ελέγχου θερμικής ρύθμισης δοκιμάστηκε με επιτυχία σε πολυκαναλική λειτουργία, η ανάπτυξή του στο τελικό σύστημα περιλαμβάνει μια σειρά προκλήσεων που η παρούσα διατριβή έχει ως στόχο να αντιμετωπίσει. Η πρώτη αφορά τη διαδικασία θερμικής ρύθμισης. Αυτή καθιστά τον αρχικό μηχανισμό κλειδώματος μήκους κύματος πιο περίπλοκο λόγω της παρουσίας πολλαπλών μηκών κύματος στον κοινό κυματοδηγό. Στα πλαίσια της διατριβής προτείνονται διάφορες λύσεις που βασίζονται στη χρήση φίλτρων στην drop θύρα ή στην υιοθέτηση διαφορετικού μηχανισμού θερμικού συντονισμού ή διαφορετικής αρχιτεκτονικής του συστήματος. Μια άλλη πρόκληση αποτελεί η συναρμολόγηση της πλακέτας δοκιμής WDM. Η πλακέτα δοκιμών αποδείχθηκε πολύ ευαίσθητη στη θερμοκρασία και υπέστη μόνιμη βλάβη όταν η θερμοκρασία σαρώθηκε στο επιθυμητό εύρος από $-30\,^{\circ}\text{C}$ έως $20\,^{\circ}\text{C}$. Παρότι βρέθηκαν προσωρινές λύσεις για την περάτωση των πρώτων δοκιμών που πραγματοποιήθηκαν στο εργαστήριο, το πρόβλημα αυτό βρίσκεται ακόμη υπό διερεύνηση.

Εκτός από την ανάγκη για θερμικό έλεγχο των διαμορφωτών δακτυλίου, άλλη μία πολύ σημαντική πρόκληση που αφορά το σύστημα του πομπού σχετίζεται με την διαχείριση της πόλωσης. Οι κυματοδηγοί πυριτίου παρουσιάζουν πολύ ισχυρή διπλοθλαστικότητα λόγω του μη τετραγωνικού τους σχήματος και της μεγάλης αντίθεσης δεικτών διάθλασης μεταξύ του Si και του SiO_2. Ως αποτέλεσμα, τα φωτονικά στοιχεία πυριτίου είναι εξαιρετικά ευαίσθητα στην πόλωση και συνήθως σχεδιάζονται για λειτουργία είτε σε εγκάρσιο ηλεκτρικό (TE) είτε σε εγκάρσιο μαγνητικό (TM) ρυθμό. Τα τσιπ πυριτίου που διαθέτουμε είναι σχεδιασμένα και βελτιστοποιημένα για πόλωση TE. Ταυτόχρονα, στο συγκεκριμένο σύστημα τα laser θα τοποθετηθούν περίπου $100\,\text{m}$ μακριά από τα τσιπ. Σε αυτή τη διαμόρφωση, ο πομπός πυριτίου θα πρέπει να συνδέεται με τα laser μέσω μονορυθμικών οπτικών ινών. Ωστόσο, οι ίνες

δεν διατηρούν την πόλωση του φωτός. Λόγω της διπλοθλαστικότητα προκαλείται διασπορά ρυθμού διάδοσης και διεύρυνση του οπτικού σήματος. Ταυτόχρονα η πόλωση του φωτός που μεταδίδεται μέσω οπτικών ινών είναι τυχαία και ασταθής. Γίνεται επομένως φανερό ότι για τη σύζευξη του τυχαία πολωμένου φωτός από μια ίνα σε TE πολωμένο φως σε ένα τσιπ πυριτίου καθώς και την αντιστάθμιση της διασποράς ρυθμού διάδοσης απαιτείται ένα σύστημα διαχείρισης της πόλωσης. Αυτό είναι απαραίτητο για να εξασφαλιστεί σταθερή σύζευξη ισχύος στο PIC πυριτίου ανεξάρτητα από την τυχαία περιστροφή της πόλωσης που θα υποστεί το φως στην οπτική ίνα.

Τα συστήματα διαχείρισης της πόλωσης μπορούν να χωριστούν σε δύο κατηγορίες: τις μεθόδους εκτός του chip και τις μεθόδους εντός του chip. Στην πρώτη περίπτωση ο έλεγχος της πόλωσης γίνεται εκτός chip, κατά μήκος της ίνας ή στην έξοδό της, έτσι ώστε το φως να φτάνει στην είσοδο του PIC με τη σωστή TE-ισοδύναμη πόλωση. Τέτοιες λύσεις περιλαμβάνουν τη χρήση ινών που διατηρούν την πόλωση ή ελεγκτών πόλωσης. Στη δεύτερη περίπτωση, το φως φτάνει στο Si PIC με τυχαία πόλωση και η περιστροφή και η αντιστάθμιση της διασποράς συμβαίνουν εντός του chip. Αυτού του τύπου οι μέθοδοι περιλαμβάνουν τη χρήση δισδιάστατων συζευκτών πλέγματος ή ολοκληρωμένων διατάξεων για διαχωρισμό και περιστροφή της πόλωσης. Αν και οι μέθοδοι εκτός chip είναι χρήσιμες για εργαστηριακές δοκιμές, δεν είναι συμβατές με την τελική υλοποίηση του συστήματος. Ως εκ τούτου, στην παρούσα διατριβή διερευνούμε λύσεις για τη διαχείριση της πόλωσης εντός του chip.

Η πρώτη βασίζεται στη χρήση δισδιάστατων συζευκτών πλέγματος (2D grating couplers - 2D-GCs). Οι 2D-GCs διαχωρίζουν και περιστρέφουν ταυτόχρονα την πόλωση με τη σύζευξη καθεμιάς από τις δύο πολώσεις της ίνας σε έναν από τους δύο κυματοδηγούς εξόδου τους αντίστοιχα. Παρόλο που έχουν αρκετά υψηλές απώλειες (IL) στην τεχνολογία που χρησιμοποιούμε, επιτρέπουν τη δημιουργία απλών κυκλωμάτων ελέγχου της πόλωσης εντός του chip. Ένα πλήρες κύκλωμα ανάκτησης της πόλωσης που βασίζεται σε 2D-GCs απαιτεί εκτός από το 2D-GC ένα επιπλέον κύκλωμα για τον ανασυνδυασμό του φωτός από τις δύο εξόδους των 2D-GCs σε έναν ενιαίο κυματοδηγό. Ένα τέτοιο κύκλωμα προτείνεται στην παρούσα διατριβή. Περιλαμβάνει ένα 2D-GC συνδεδεμένο με ένα 2χ2 Mach-Zehnder συμβολόμετρο (MZI) για τον ανασυνδυασμό της ισχύος. Οι κυματοδηγοί εξόδου 2D-GC περιλαμβάνουν μετατοπιστές φάσης (PS). Το 2χ2 MZI χρησιμοποιεί 2χ2 πολυριθμικά συμβολόμετρα (MMI) ως διαχωριστές ισχύος και περιλαμβάνει επίσης PS σε κάθε βραχίονα. Το βασικό δομικό στοιχείο του κυκλώματος MZI είναι το MMI. Η λειτουργικότητά του επαληθεύτηκε με προσομοιώσεις με τη χρήση του Lumerical INTERCONNECT. Με την κατάλληλη ρύθμιση αυτού του κυκλώματος μπορεί να επιτευχθεί ο προσθετικός ανασυνδυασμός της ισχύος σε έναν από τους δύο κυματοδηγούς εξόδου του.

Το πρώτο στάδιο του κυκλώματος (μέχρι το πρώτο MMI) περιλαμβάνεται στο υπό δοκιμή chip. Επαληθεύσαμε πειραματικά ότι αντισταθμίζει με επιτυχία την διασπορά πόλωσης PMD που προκαλείται από τις ίνες. Επικυρώσαμε επίσης τη συμβατότητα αυτής της λύσης με τα σχήματα WDM. Τα αποτελέσματα δείχνουν ότι το προτεινόμενο κύκλωμα θα αποτελέσει μια ολοκληρωμένη λύση για τη διαχείριση της πόλωσης στο chip, ικανή να μετατρέψει οποιαδήποτε τυχαία πόλωση που συνδέεται από την ίνα σε πόλωση TE στο chip, ακόμα και σε πολυκαναλική λειτουργία. Περαιτέρω βελτιώσεις στις διαδικασίες κατασκευής αναμένεται να μειώσουν τις απώλειες του 2D-GC, καθιστώντας τη λύση αυτή ακόμη πιο ελκυστική.

Η δεύτερη τεχνική διαχείρισης πόλωσης στο τσιπ βασίζεται σε διαχωριστές και στροφείς πόλωσης (PSRs). Τα PSRs χωρίζουν τον TE και TM ρυθμό ενός κυματοδηγού πυριτίου και μπορούν επίσης να περιστρέψουν τον TM ρυθμό σε TE. Είναι χρήσιμοι όταν χρησιμοποιούνται σχήματα edge coupling στα τσιπ και το φως κυματοδηγείται στο PIC τόσο με πόλωση TE όσο και με πόλωση TM. Η χρήση των edge couplers και των PSRs είναι ελκυστική, καθώς οι edge couplers παρουσιάζουν πολύ χαμηλότερο IL σε σύγκριση με τα GCs (λιγότερο από 2 dB επί του παρόντος) και είναι πιο κατάλληλοι για την τελική υλοποίηση του συστήματος. Στα πλαίσια της διατριβής, προτείνεται μια ολοκληρωμένη λύση για τη διαχείριση της πόλωσης στο τσιπ με βάση τη χρήση PSRs. Λόγω της μη διαθεσιμότητας των επιθυμητών στοιχείων PSR με τις απαιτούμενες προδιαγραφές, η σχεδίαση και η προσομοίωσή τους πραγματοποιήθηκε στο πλαίσιο της παρούσας διατριβής. Για το σκοπό αυτό προσομοιώσαμε και σχεδιάσαμε δύο διαφορετικά στοιχεία. Το πρώτο είναι ένας θερμικά συντονιζόμενος στροφέας πόλωσης για τη C μπάντα, το οποίο μπορεί να περιστρέψει αποτελεσματικά την TM πόλωση σε TE. Βασίζεται στον υβριδισμό των υποστηριζόμενων ρυθμών και διαμορφώνεται ως κυματοδηγός μονής σκάλας με διπλό βάθος χάραξης. Το δεύτερο στοιχείο είναι ένας ευρυζωνικός PSR για την O μπάντα που βασίζεται στη μετατροπή ρυθμών και την συνθήκη ταιριάσματος φάσης (phase matching) και υλοποιεί τη μετατροπή ρυθμού TM_0-TE_1-TE_0. Η δομή αποτελείται από έναν αδιαβατικό κυματοδηγού μεταβαλλόμενου πλάτους (taper) και έναν ασύμμετρο κατευθυντικό συζεύκτη (ADC) του οποίου ο ένας βραχίονας έχει επίσης μεταβαλλόμενο πλάτος, χρησιμοποιώντας αέρα ως άνω επένδυση. Και τα δύο στοιχεία είναι πλήρως συμβατά με τυπικές διαδικασίες κατασκευής λιθογραφίας DUV και έχουν συμπεριληφθεί σε ένα PIC το οποίο βρίσκεται υπό κατασκευή.

Μέχρι στιγμής έχουμε επικεντρωθεί στην ανάπτυξη και τον χαρακτηρισμό του πομπού πυριτίου, καθώς και στις διάφορες προκλήσεις του συστήματος του πομπού που πρέπει να αντιμετωπιστούν για την αξιόπιστη λειτουργία του (θερμική ρύθμιση και διαχείριση της πόλωσης). Ωστόσο, στα πλαίσια της παρούσας διατριβής πραγματοποιήθηκε επίσης δουλειά που αφορά στην ανάπτυξη και τον χαρακτηρισμό του δέκτη πυριτίου. Ο δέκτης πυριτίου αποτελείται από μία φωτοδίοδο Γερμανίου με εύρος ζώνης 50 GHz και αποκρισιμότητα $0.8\,\mathrm{A\,W^{-1}}$. Η φωτοδίοδος λειτουργεί ως φωτοανιχνευτής και είναι υπεύθυνη για τη μετατροπή των οπτικών δεδομένων (δεδομένα ρύθμισης, triggering και χρονισμού στην περίπτωσή μας) που λαμβάνονται από το BE, σε ηλεκτρικά, πριν αυτά στη συνέχεια μεταδοθούν στα ηλεκτρονικά του FE. Η έξοδος της φωτοδιόδου είναι ένα φωτορεύμα (I_{PD}) του οποίου η τιμή είναι ανάλογη της οπτικής ισχύος εισόδου, σύμφωνα με την αποκρισιμότητα της. Το I_{PD} απαιτεί στη συνέχεια ενίσχυση, η οποία συνήθως επιτυγχάνεται με τη βοήθεια ενός transimpedence ενισχυτή (TIA). Το TIA μετατρέπει επίσης το φωτορεύμα σε ψηφιακό σήμα τάσης με κατάλληλες στάθμες που είναι συμβατές με τις απαιτήσεις εισόδου των ηλεκτρονικών στο FE. Για τη διασύνδεση του δέκτη πυριτίου με τις οπτική ίνα χρησιμοποιείται ένας 2D-GC που δεν είναι ευαίσθητος στην πόλωση. Στο πλαίσιο συνεργασιών του CERN έχουν αναπτυχθεί δύο διαφορετικές εκδόσεις TIA με ανοχή στην ακτινοβολία, το GBTIA και το lpGBTIA. Το GBTIA υλοποιείται σε 130 nm CMOS τεχνολογία, απαιτεί τάση τροφοδοσίας 2.5 V και λειτουργεί σε ρυθμούς δεδομένων έως και 5 Gb/s. Το lpGBTIA υλοποιείται σε 65 nm CMOS τεχνολογία, απαιτεί τάση τροφοδοσίας 1.2 volt και λειτουργεί στα 2.56 Gb/s. Και τα δύο ASIC δοκιμάστηκαν με τη φωτοδίοδο. Παρότι το GBTIA και το lpGBTIA δεν αντέχουν τα επίπεδα ακτινοβολίας των

εσωτερικών περιοχών του HL-LHC και τελικά θα πρέπει να αντικατασταθούν από ένα πιο ανθεκτικό στην ακτινοβολία TIA, η χρήση τους επιτρέπει την δοκιμή κι επίδειξη της ιδέας του SiPh δέκτη.

Στα πλαίσια της διατριβής αυτής, συναρμολογήθηκαν δύο διαφορετικές πλακέτες δοκιμής του δέκτη που περιλαμβάνουν διαφορετικές παραλλαγές της φωτοδιόδου, του TIA και του σχήματος οπτικής σύζευξης μεταξύ PIC και ίνας. Και οι δύο δοκιμαστικές πλακέτες αξιολογήθηκαν πειραματικά. Ο χαρακτηρισμός του δέκτη σε επίπεδο συστήματος περιελάμβανε δύο τύπους μετρήσεων: τις μετρήσεις διαγραμμάτων οφθαλμού υψηλής ταχύτητας για την αξιολόγηση της ποιότητας του σήματος εξόδου και την επαλήθευση της συμβατότητας της φωτοδιόδου με το GBTIA και το lpGBTIA, καθώς και τις μετρήσεις του ρυθμού σφαλμάτων bit (BER) για τον υπολογισμό του περιθωρίου του συστήματος για μετάδοση χωρίς σφάλματα. Η λειτουργία υψηλών ταχυτήτων των φωτοδιόδων επαληθεύτηκε με τις μετρήσεις διαγράμματος οφθαλμού που καταγράφηκαν σε $5.12\,\mathrm{Gbit\,s^{-1}}$. Το διάγραμμα οφθαλμού μου μετρήθηκε είναι ανοικτό με χαμηλό θόρυβο και jitter. Αυτή η μέτρηση αναδεικνύει επίσης τη συμβατότητα της φωτοδιόδου με το διαθέσιμο TIA. Οι μετρήσεις BER έδειξαν ότι ο δέκτης έχει και για τις δύο εκδοχές του συστήματος (GBTIA, lpGBTIA) ευαισθησία περίπου $-11\,\mathrm{dBm}$. Η τιμή αυτή ταιριάζει με την εκτιμώμενη ευαισθησία και αποτελεί ένα πολύ καλό αποτέλεσμα για τον δέκτη που παρέχει αρκετά περιθώρια για το σύστημα. Οι απώλειες τη ζεύξης δεν θα είναι μεγαλύτερες από $13\,\mathrm{dB}$, επομένως παρότι με την εξέλιξη της τεχνολογίας ίσως βελτιωθεί η ευαισθησία του δέκτη, το παρόν σύστημα έχει ήδη επαρκή απόδοση.

Εν κατακλείδι, στην παρούσα διατριβή παρουσιάσαμε τη μοντελοποίηση, το τεστινγ και τον χαρακτηρισμό δομικών στοιχείων για την ανάπτυξη ανθεκτικών στην ακτινοβολία SiPh πομπών και δεκτών για πειράματα φυσικής υψηλών ενεργειών. Αντιμετωπίσαμε τις σημαντικότερες προκλήσεις του συστήματος, δηλαδή τη θερμική ρύθμιση των διαμορφωτών δακτυλίου και τη διαχείριση της πόλωσης. Τα παραπάνω αποτελέσματα συντέλεσαν στην πρόοδο της προσπάθεια για τη συγκρότηση από τα διαθέσιμα εξαρτήματα ενός Σπομποδέκτη πυριτίου. Δεδομένου ότι η ανοχή στην ακτινοβολία των επιμέρους στοιχείων έχει ήδη επαληθευτεί, η πρόοδος στις επιδόσεις σε επίπεδο στοιχείων και στην ολοκλήρωση του συστήματος θα επιτρέψει την υιοθέτηση των παρουσιαζόμενων διατάξεων στην επόμενη γενιά οπτικών ζεύξεων στο CERN.

Chapter 1

Introduction

1.1 CERN

The European center for nuclear research (CERN) [1] is a research institute situated in the Franco-Swiss broader near Geneva. Its construction began in 1960 as an effort for a European and global collaboration for pushing research forward. CERN is a collaborative effort involving scientists and engineers from all over the world and its primary mission is to advance our understanding of the fundamental laws that govern the universe. The research taking place at CERN focuses on particle physics and specifically the study of the smallest particles that make up the universe and the fundamental forces that govern them.

CERN's core facility is the Large Hadron Collider (LHC), which is the world's largest and most powerful particle accelerator. Researchers use the LHC to accelerate particles, like protons and heavy ions, to incredibly high speeds and then collide them, enabling the study of subatomic particles at the smallest scales. These collisions recreate conditions similar to those in the early universe, allowing scientists to explore the building blocks of matter. These investigations have yielded significant discoveries, notably the confirmation of the Higgs boson, a particle critical to understanding the mechanism by which particles acquire mass.

CERN's research extends beyond particle physics, with applications in various scientific disciplines and practical domains. For instance, it contributes to medical advancements through the development of particle therapy for cancer treatment and fosters technological innovations in areas such as superconducting magnets, particle detectors, and high-performance computing. Moreover, CERN embodies international collaboration. Its scientists hail from diverse cultural and scientific backgrounds, uniting to tackle the most profound questions about the universe's nature. CERN also promotes open access to scientific data, fostering transparency and inclusivity in the global scientific community.

1.1.1 CERN accelerators and detectors

CERN is home to the Large Hadron Collider (LHC) [2], the world's largest accelerator. The LHC is a circular particle collider with 27 km circumference and it accelerates particles to energies up to 14 TeV. The LHC is one out of the currently eight operating accelerators at CERN. Besides the LHC, there are four other circular accelerators: the Proton Synchrotron Booster (PSB), the Proton Synchrotron (PS), the Super Proton Synchrotron (SPS) and the Low Energy Ion Ring (LEIR), that can accelerate protons and/or ions. The remaining three accelerate particles in a straight line (linear accelerators). They consist of Linac4 (L4) that accelerates negative hydrogen ions (H^-), Linac3 (L3) that accelerates lead ions and the CERN Linear Electron Accelerator for Research (CLEAR) that accelerates electrons. The network of all the CERN accelerators and the way they are coupled to each other is called the CERN Accelerator Complex and is illustrated in Figure 1.1.

At the LHC, and with the help of all the pre-accelerators, two different particle beams travel nearly to the speed of light in opposite directions and collide at four different points around the machine. These points are called interaction points and they house highly

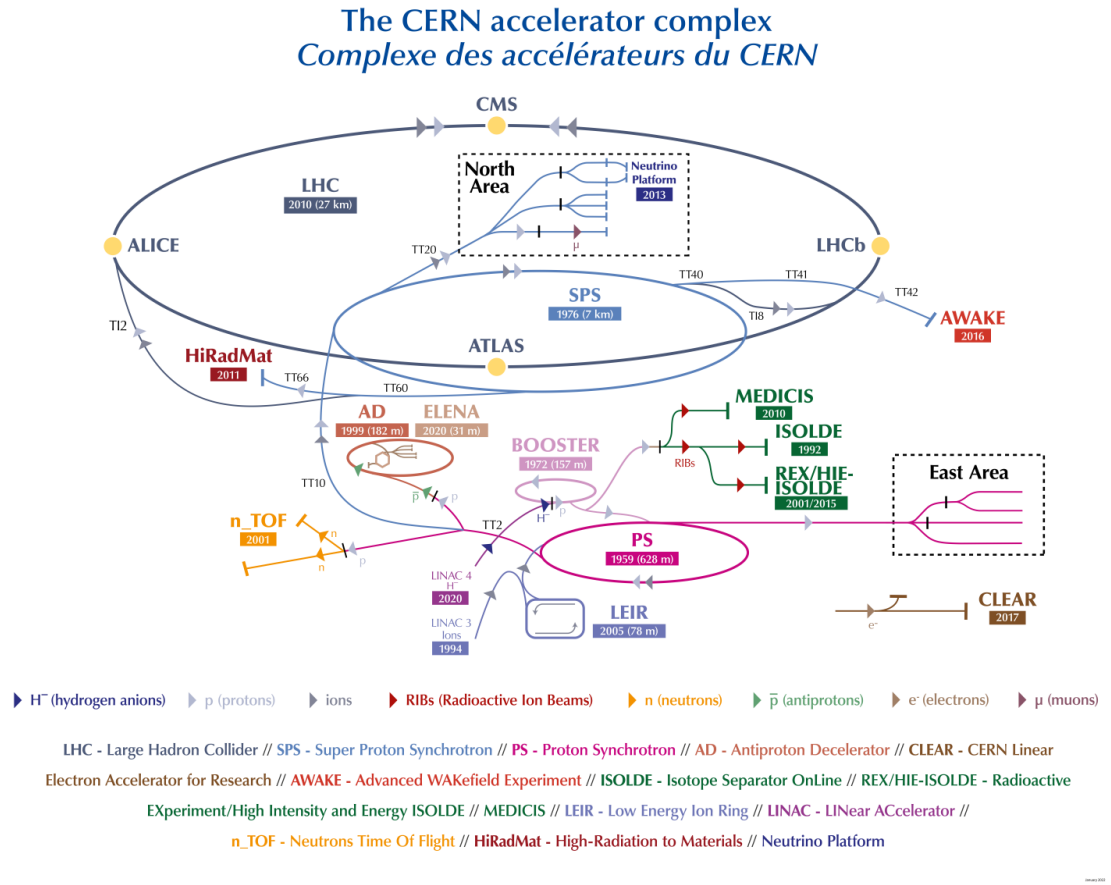

Figure 1.1. *A schematic of the accelerator complex at CERN.*

sophisticated particle detectors: ATLAS, CMS, ALICE and LHCb. ATLAS and CMS are general purpose detectors designed to investigate a wide range of physics phenomena. ALICE is specialized in studying heavy-ion collisions and LHCb focuses on studying the properties of particles containing bottom quarks (beauty quarks) to investigate potential differences between matter and antimatter that might help explain the universe's matter-antimatter imbalance. These detectors identify and track the particles that are produced by the beam collisions. Although each detector has a different purpose and architecture, according to the physics they were designed to study, they all share some common characteristics. They comprise magnets to enable particle momentum measurement, tracking stations to identify the trajectories of charged particles close to the interaction point, calorimeters to measure the energy of particles and muon stations to track and identify muons [3]. Moreover, they employ triggering systems that allow an on-line selection process to reduce the raw event rate from the proton-proton collisions and record only the interesting events.

The LHC baseline programme, as defined at the end of 2019 is shown schematically in Fig. 1.2. During Run 1 the LHC was operated with 50 ns bunch spacing (time interval between two consecutive bunch crossings at the LHC). After important consolidation measures in long shutdown 1 (LS1), the LHC was operated in Run 2 at 13 TeV centre-of-mass energy. The bunch spacing was reduced to 25 ns, the design value, and the luminosity

was progressively increased, attaining the nominal design luminosity of $10^{34}\,\mathrm{cm}^{-2}\,\mathrm{s}^{-1}$ on 26 June 2016. A peak luminosity of $2 \times 10^{34}\,\mathrm{cm}^{-2}\,\mathrm{s}^{-1}$ was achieved in 2018. This high-luminosity and the excellent availability of the machine and injectors have yielded a record annual integrated luminosity of $65\,\mathrm{fb}^{-1}$ in 2018. In the Run 3 period from 2022 to 2024 the LHC aims to further increase the integrated luminosity total: the present goal is to reach $300\,\mathrm{fb}^{-1}$ by the end of Run 3.

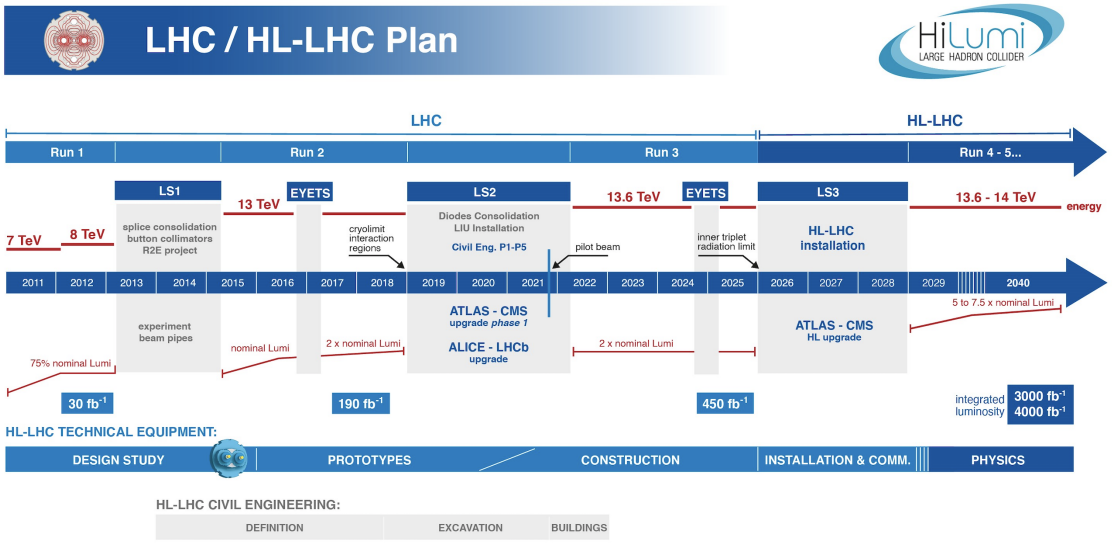

Figure 1.2. *LHC baseline plan for the next decade and beyond showing the collision energy (upper line) and luminosity (lower line). After LS3, the machine will be in the high-luminosity configuration [4].*

1.1.2 High-Luminosity LHC and future upgrades of CERN experiments

To fully exploit the physics potential of the LHC, CERN established the high-luminosity LHC project at the end of 2010 with the following targets: a peak luminosity of $5 \times 10^{34}\,\mathrm{cm}^{-2}\,\mathrm{s}^{-1}$ with levelling operation and an integrated luminosity of $250\,\mathrm{fb}^{-1}$ per year, with the goal of $3000\,\mathrm{fb}^{-1}$ in the 12 years or so after the upgrade [5]. This integrated luminosity is about ten times the predicted luminosity reach of the LHC in its initial configuration.

The goal of the High-luminosity upgrade of the LHC is to deliver an integrated luminosity of at least $250\,\mathrm{fb}^{-1}$ per year in each of the two high-luminosity general-purpose detectors, ATLAS and CMS. The ATLAS and CMS detectors will be upgraded to handle an average pile-up, the number of events per bunch crossing, of at least 140 (ultimately 200), corresponding to an instantaneous luminosity of approximately $5 \times 10^{34}\,\mathrm{cm}^{-2}\,\mathrm{s}^{-1}$ (ultimately $7.5 \times 10^{34}\,\mathrm{cm}^{-2}\,\mathrm{s}^{-1}$) for operation with 25 ns beams consisting of 2760 bunches at 7 TeV [5].

The luminosity and integrated luminosity achieved in the LHC detectors is a very important number. First of all, integrated luminosity directly influences the rate at which particle collisions occur within the collider. Higher luminosity means more collisions per

unit of time, resulting in a larger number of events recorded by the detectors. This is essential for studying rare or low-probability processes, as a higher collision rate increases the chances of observing these events. However, it requires more complex hardware and software that will be able to deal with the increased amount of data. At the same time, increased luminosity creates the need for components that will be more radiation hard and capable of operating reliably in the detectors for the required period. Therefore, operating the LHC at high luminosities presents technical challenges for both the accelerator and the detectors. Managing beam stability, mitigating radiation damage to detector components, and handling the enormous data rates generated by the detectors all become more demanding as luminosity increases. This signifies that every upgrade of the LHC that leads to increased luminosities, requires an accompanying upgrade of the detector systems, hardware and software, to cope with the ever increasing data rates and radiation levels. Eventually, the LHC systems will need to be changed and improved, because they either become vulnerable to breakdown and accelerated aging, or because they may become a bottleneck for operation at higher performance levels and in a higher radiation environment.

1.2 Radiation damage in CERN experiments

One of the most challenging aspects of building and operating the accelerators and detectors in high energy physics (HEP) experiments at CERN is the high radiation levels that the various electronic and photonic systems, placed near the collision points, have to withstand. Radiation damage in electronics and photonics is caused by the energy loss, via ionizing or non-ionizing processes, from incident particles. Radiation damage is attributed to one of three different mechanisms: damage due to ionizing energy loss, damage due to non-ionizing energy loss (NIEL) and single event effects (SEE).

Ionizing damage in attributed to high-energy charged particles (e.g., electrons, protons) that can ionize the atoms or molecules in detector materials. This creates electron-hole pairs, potentially altering the electrical or optical properties of the materials and introducing noise in electronic signals. We usually refer to this type of damage as Total Ionizing Dose (TID). Continuous exposure to ionizing radiation can accumulate a dose in photonic materials and devices, causing gradual degradation of optical properties over time. Damage due to NIEL is usually expressed as displacement damage (DD). High-energy neutrons and other particles can cause displacement of atoms within crystalline structures, leading to structural damage. This can affect the long-term performance of semiconductor detectors and electronic components. In SEE, high-energy particles can induce immediate and localized disruptions in photonic devices. SEEs in photonics can result in transient or permanent changes in device behavior. In photonic circuits, the most important types of radiation damage are caused by TID and NIEL.

The aforementioned radiation effects are categorized into two broad categories: cumulative and transient effects. Cumulative effects (like TID and DD) gradually build up during the time that a device is exposed to radiation and result in failure of the device once exposure to a certain level of radiation has been reached. The level of radiation at

which a device fails is expressed in units of Gray ($1\,\mathrm{Gy} = 1\,\mathrm{J\,kg^{-1}}$) or rad ($100\,\mathrm{rad} = 1\,\mathrm{Gy}$) for damage accumulated from ionizing energy loss, and in units of fluence (particles per cm^2) for damage accumulated from non-ionizing energy loss. Transient effects generally do not lead to device failure but can momentarily upset the operation of a device [3].

1.3 Opto-electronic links for HEP experiments

One of the most important challenges in the CERN experiments is the realization of links for transferring the data produced by the detectors to the back end, for processing and storage. Although the implementation details vary between the different detectors an sub-detectors, the data usually follow a similar path. The collision data are initially recorded in the front-end (FE) sensors, were a first selection takes place. Then they are read out by the FE read-out chips electronically. After this step, typically the opto-electrical conversion of the data takes place, before the data are transferred to the back-end through optical fibers.

Optical data transmission links are widely used for data transmission applications in all four of the LHC experiments because of the many advantages they provide over copper-based solutions. The attenuation, the loss in signal strength as a function of transmission distance, of high-speed signals is much lower in optical fibers than in copper cables; at a data rate of $10\,\mathrm{Gbit\,s^{-1}}$ the attenuation in a copper flex cable is approximately $0.2\,\mathrm{dB\,cm^{-1}}$ compared to the maximum attenuation of $0.3\,\mathrm{dB\,km^{-1}}$ in an SMF-28e optical fiber. Optical data transmission is therefore preferred in applications in which high-speed data transmission is required over long distances; for example in the CMS tracker which must transmit data over 50–100 m. Furthermore, optical data transmission systems are immune to Electromagnetic Interference (EMI). Finally, they help eliminate potential ground-loops between the back-end electronics and the detector front-ends since the two regions are not electrically connected to one another [3].

At CERN, a continuous effort takes place for the development of custom optical data transmission links that are compatible with the detector needs and have adequate performance to meet the radiation hardness and data rate requirements. In the final runs of the LHC program, the necessary optical links were developed within the Versatile Link project as a joint ATLAS-CMS effort aiming to develop a radiation hard bi-directional optical link for use in the LHC upgrade program. The link targeted data transmission between the on-detector and off-detector electronics at rates up to $5\,\mathrm{Gbit\,s^{-1}}$ with an emphasis on radiation resistance, low power dissipation and low mass components [6].

1.3.1 The current system

In the HL-LHC era, the upgraded accelerator system will yield an increase in the collision rate by a factor of up to ten [5], compared to the LHC system. The higher number of collisions will yield significantly increased data readout rates and radiation levels in the detector environment [7]. Consequently, the Versatile Link components will not be able to support the required data rates and withstand the radiation level. Therefore, an improved

generation of optical links had to be designed to meet the requirements of the initial runs of HL-LHC, namely the Versatile Link Plus (VL+) project.

The VL+ project has developed such an optical data transmission system capable of transferring up to 10.24 Gbit s^{-1} of data from the innermost detectors that must sustain the highest radiation levels during operation of the HL-LHC. These optical links are being deployed in all of the upgrades that the LHC experiments are preparing in order to exploit the physics potential of the increased luminosity that the HL-LHC will provide.

A typical detector system in the experiments at CERN comprises two main parts: the FE and the BE. The FE is the region inside the detectors, near the interaction point (radiation area) and it includes the sensors that record the collision data, the read out electronics that might also perform aggregation of the data, and the electro-optical converters that convert the recorded data to optical (with the help of the drivers) before they are transmitted to the BE through Single-Mode Fibers (SMFs). The FE also includes a receiver that receives the configuration data coming from the BE, and performs their opto-electrical conversion before they are directed to the FE electronics. The BE, situated away from the detectors in the radiation-free area, comprises the receivers that receive the collision data that are then reconstructed, stored and analyzed. It also comprises the BE transmitters that are responsible for transmitting to the FE the configuration, trigger and timing data. Of course, the exact architecture and components used depends on the TRx technology and the experiment where the system is deployed. For the case of the VL+ project, the FE and BE components and their arrangement is shown in Fig. 1.3b.

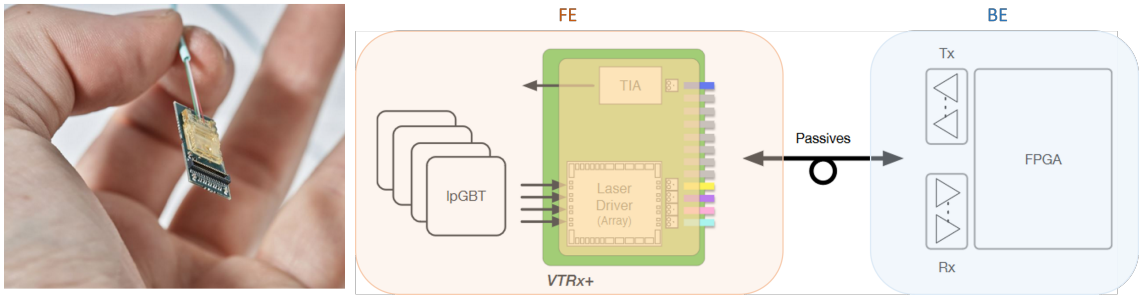

(a) **(b)**

Figure 1.3. *(a) Picture of the VTRx+ optical transceiver module (Credits: CERN) [8]. (b) Overview of the Versatile Link + system showing the components of the VTRx+ [9].*

The VL+ optical transceiver converts the electrical data produced by the detectors to optical signals that can be transmitted over 50-100 m of optical fibre to the shielded underground control rooms for further processing. The optical transceiver module (VTRx+), shown in Fig. 1.3a, is a miniaturised object measuring 10 mm x 20 mm and is below 2.5 mm in height. It is light enough to be placed throughout the initial HL-LHC upgrades of the pixel and tracker detectors of ATLAS and CMS. Radiation tolerance is also a key parameter for any component for future use inside the HL-LHC detectors and this has been designed into the components and assembly of the VTRx+ [8].

The front-end VTRx+ module comprises four optical transmitters (Tx) that convert electrical inputs, driven by a custom-designed laser driver ASIC, to modulated light. The

VTRx+ module also contains one optical receiver (Rx) to turn the optical input into an electrical signal for the control of the detector. An overview of the VL+ link is shown in Fig. 1.3b. The VTRx+ Tx is based on a radiation-hard laser diode driver (LDD) and commercial VCSELs, and the Rx is based on a transimpedance amplifier (TIA) application specific integrated circuit (ASIC) and a PIN photodiode (PD). A set of passive components (optical fibre and connectors) connects the VTRx+ to the off-detector electronics where Commercial Off-The-Shelf (COTS) optical transmitter and receivers will provide the interface to field programmable gate arrays (FPGAs). The completed module with its optical fibre pigtail is able to operate in the intense magnetic and radiation fields that will be encountered in the HL-LHC experiments. The strongest magnetic field present in the HL-LHC detectors is the 4 T field of the CMS Solenoid, which sets the tolerance limit for the VTRx+ module. The radiation levels used to qualify the VTRx+ module are 1 MGy of ionising dose, 10^{15} neutron cm^{-2} and 10^{15} hadron cm^{-2} [8]. The VL+ is designed to operate together with the low power gigabit transceiver (lpGBT) Serializer/Deserializer (SerDes) [10], although other SerDes types can be supported. The target operating data-rates for the VL+ are set by the lpGBT: 2.56 Gbit s^{-1} in the downstream towards the detector and 5.12 Gbit s^{-1} or 10.24 Gbit s^{-1} in the upstream away from the detector [9].

The radiation hardness and performance of the VTRx+ TRx is sufficient for the initial runs of the HL-LHC. However, during the final runs of HL-LHC, the components installed in the innermost regions of the detectors will have to withstand a TID of 12 MGy(Si) and a 1 MeV neutron equivalent fluence of $2.3 \times 10^{16}\,\mathrm{n_{eq}/cm^2}$ [11]. Consequently, the VTRx+ modules that will be placed the innermost regions of the detectors will not survive until the end of the HL-LHC. Although the replacement of these components with new ones of the same type would be possible, this solution does not offer any advantage from the physics side, since it does not improve the physics performance (resolution, accuracy, datarates). Therefore, the final runs of the HL-LHC have to be accompanied by a hardware upgrade of the detector optical readout to handle the ever-increasing data rates and radiation levels.

1.3.2 Future system needs and specifications

It becomes evident that a new generation of optical links needs to be developed, that will be compatible with the requirements of the final runs of the HL-LHC and future upgrades of the CERN experiments. Such links need first of all to be radiation hard. The front-end transceiver will have to withstand a TID of 12 MGy(Si) and a 1 MeV neutron equivalent fluence of $2.3 \times 10^{16}\,\mathrm{n_{eq}/cm^2}$. Moreover, the next generation of optical links will need to be capable of transmitting at the increased data rates of the experiment upgrades over relatively long distances with low losses in order to move data from the detector front-ends to the counting rooms. Although the exact data rates and architecture of the future links are not yet known, data rates up to 25 Gbit s^{-1} per channel are anticipated. Of course this will depend on the data aggregation in the electrical domain as well as on whether or not a WDM scheme will be adopted. A WDM scheme that will multiplex 4 x 25 Gbit s^{-1} channels is a choice that is being investigated. Eventually, targeting as data rate the 25 Gbit s^{-1}, the goal is to develop flexible links that will be able to support WDM

operation if that turns out to be the adopted solution.

Another key performance metric for the successful adoption of the next generation of TRx in HEP detectors will be sufficiently low electrical power consumption. Key elements to reducing the overall power consumption within the detector are the adoption of a technology that allows the remote placement of the laser sources that are required for the electro-optical conversion, as well as achieving sufficient high levels of integration between the FE electronic and the photonic circuits. The low power consumption must be accompanied by low mass components. This is a crucial requirement from the physics side because the tracking resolution is degraded by material interactions. Therefore, keeping the mass low ensures that multiple scattering in the tracking region is limited.

Another important aspect for choosing the technology platform for realizing the next generation of optical links is the cost. On one hand this signifies that the cost for developing the required components must be low and compatible with the CERN budget allocated for this purpose. This usually means utilizing well established and mature technologies that are commercially available, as for more exotic solutions the cost becomes prohibitive, even if the requirements can be easily met. On the other hand, ensuring the low cost means that the components that are developed for the FE due to the unique conditions within the detectors, must be compatible with COTS components that can be placed in the back-end (BE) side of the links (BE receivers, lasers, BE transmitters). This way it is not needed to develop custom components also for the BE, which would drastically increase the cost of the links.

1.3.3 Silicon photonics based optical links

Advantages of the Silicon photonics platform

Among the available technologies, Silicon Photonics (SiPh) technology has been identified as an excellent candidate for the development of the next generation of optical links at CERN. SiPh is a material platform from which photonic integrated circuits (PICs) can be made. It uses silicon on insulator (SOI) wafers as the semiconductor substrate material and most of the standard complementary metal-oxide semiconductor (CMOS) manufacturing processes can be applied [12].

The traditional argument in favor of SiPh is based on its compatibility with the mature silicon integrated circuit (IC) manufacturing, namely the CMOS fabrication processes. Silicon wafers have the lowest cost (per unit area) and the highest crystal quality of any semiconductor material. The industry is able to produce microprocessors with hundreds of millions of components, all integrated onto a thumb-size chip, and offer them at such a low price that they appear in consumer electronics. The compatibility of the SiPh platform with the CMOS fabrication processes allows to leverage the significant advancements in their maturity as developed for the electronics industry. Apart from the availability of the SiPh technology at low cost and for mass production, another motivation is the availability of inexpensive and high-quality SOI wafers, an ideal platform for creating planar waveguide circuits. The strong optical confinement offered by the high index contrast between silicon (n = 3.45) and silicon dioxide (SiO_2) (n = 1.45) makes it possible to scale photonic devices

to the hundreds of nanometer level. Such lateral and vertical dimensions are required for true compatibility with IC processing and allow the realisation of ultra compact and low components and devices [13].

However, the case for SiPh is even stronger. Silicon has excellent material properties that are important in photonic devices. These include high thermal conductivity (almost 10x higher than GaAs), high optical damage threshold (almost 10x higher than GaAs), and high third-order optical nonlinearities. Si showcases a low-loss wavelength window extending from 1.1 to nearly 7 µm [14], making it a ideal material for realizing optical circuits in the telecom and datacom wavelengths around the C-band and the O-band [13]. At the same time, the capabilities of the SiPh platform are further increased exploiting the epitaxial growth of germanium (Ge) on silicon or SOI substrates. Ge has found potential applications in the area of optics because its narrower bandgap lies within the telecom C and O band. Owing to its inherent compatibility with well-developed silicon CMOS processing and with III–V semiconductors, Ge has been considered as an attractive material for the active layer of integrated light emitting diodes, as well as near-infrared and mid-infrared integrated photodetectors [15].

Overall, the SiPh platform is a complete platform that enables the development of all the necessary passive and active components (waveguides, couplers, power splitters, polarization splitters and rotators, optical modulators, phase shifters, photodetectors etc.) that can be combined to realize complete optical data links. SiPh transmitters can achieve very high data rates. In literature, ring modulators with BW of more than 100 GHz have been reported [16], making the SiPh compatible with high speed applications. It is also possible to implement WDM schemes with SiPh transmitters, which can further increase the capacity of the SiPh links. Another advantage of the SiPh platform and its compatibility with CMOS fabrication processes is the possibility to achieve tight co-integration between the SiPh and electronic chips. This can be achieved with various methods of integration, like monolithic or hybrid integration, and in can further reduce the size and power consumption of the overall system.

Besides all the aforementioned advantages of the SiPh technology, that has led to its wide adoption in recent years in various applications including optical interconnects for telecom, datacom and high-performance computing systems, sensors, quantum computing, LIDARs etc, there is one advantage that is of particular interest for our application. This is the high radiation hardness of the SiPh passive and active components, that has been the subject of extensive research in the HEP community and at CERN. Various studies performed both at CERN and at other research facilities have been investigating the durability of SiPh components and devices against ionizing and non-ionizing radiation damage. The tests typically involve X-ray radiation to investigate the effects of TID, and neutron testing to investigate the effect of NIEL. SiPh Mach-Zehnder and ring modulators, Ge PD as well as Si waveguides have been found to be very radiation tolerant [17–22]. Given that the SiPh platform meets all the requirements of the next generation of optical links for HEP application, the radiation tolerance of the SiPh devices was the final prerequisite that triggered the selection of the SiPh technology for their development.

Vision of a SiPh based optical link

A typical detector system deployed in the CERN experiments was described in Sec. 1.3.1, highlighting the FE and BE parts and their roles. A similar architecture will also have to be adopted in the case of a SiPh based optical link. Such a system concept of an optical link based on a SiPh Tx and Rx is shown in Fig.1.4 [23]. The link, as most typical data links in HEP experiments, consists of the FE in the radiation area comprising the sensors, read-out electronics and SiPh TRx, and the BE in the radiation-free zone, including the lasers and commercial TRx. At the core of the link is the SiPh transceiver. The SiPh Tx is based on micro-ring modulators (RMs) and the Rx on Ge photodiodes (PDs). The SiPh Rx receives configuration, triggering and timing data from the BE Tx though SMFs that are then converted to electrical before being forwarded to the FE electronics. This is the downlink part. On the other hand, the SiPh Tx transfers the data produced by the sensors to the BE for processing and storage through long (>100 m) SMFs. This is the uplink. Such links are asymmetrical since much higher bandwidth (BW) is required for the uplink ($\gg$10 Gb/s) due to the large amount of data produced by the experiments, whereas for the downlink lower data rates (<5 Gb/s) are sufficient. One particularity of this system, contrary to most datacom applications and the previous optical link at CERN, is that the lasers that provide the Tx optical input are placed in the BE up to 100 m away from the RMs. This is necessary due to the high power consumption and low radiation tolerance of available laser technologies that would render their integration in the FE impossible. However, it adds an extra complication to the system and requires advanced techniques for polarization management [24].

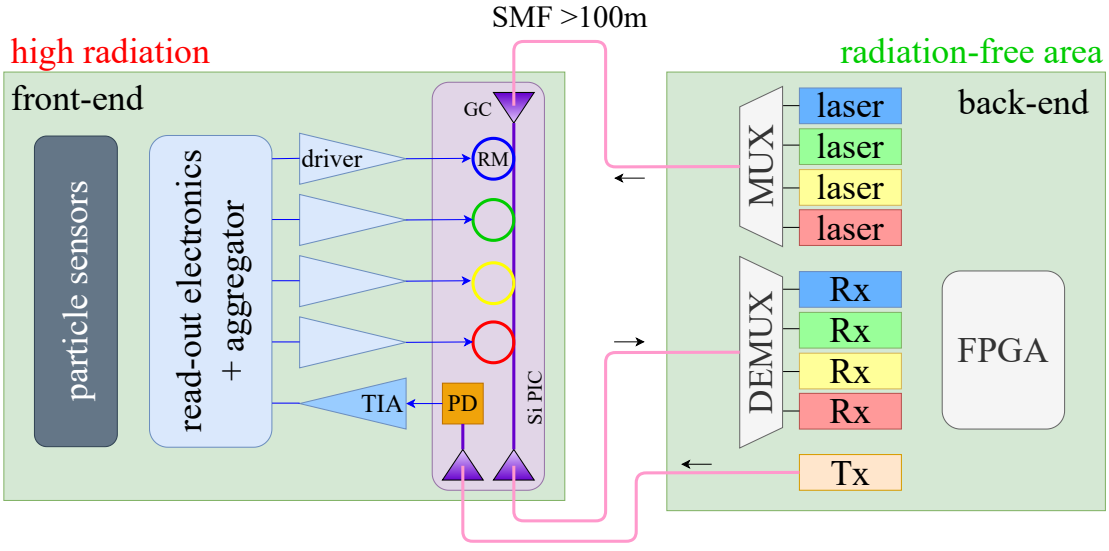

Figure 1.4. *System concept of a SiPh based data link for HEP.*

1.4 Research objectives

From the topics discussed in Chapter 1 it becomes evident that a new generation of optical links will be required in the future upgrades of the HEP experiments at CERN. Starting at the end of the HL-LHC era, the high radiation levels and increased data rates due to the increased luminosity of the accelerator will impose the need for a new generation of optical links, able to withstand the extreme condition in the detectors, and support the data rates. The currently available optical transceivers that are based on discrete InGaAs photodiodes and VCSELs will not be able to survive in the innermost regions of some of the detectors. Therefore, a new generation of optical links is necessary. SiPh has been identified as the perfect candidate for this upgrade, since it combines all the advantages that are required for such an application.

In recent years CERN has taken an interest in the SiPh technology for the aforementioned reason. An extensive effort has been taking place the past years within the EP-ESE Group at CERN that focuses on the modelling and development of SiPh transceivers for HEP application. This effort includes the simulation, design and fabrication of SiPh PICs for the development of the necessary building blocks that can be combined to realize radiation-hard SiPh transceivers. At the same time, part of this effort has been the testing and characterization of the designed structures as part of the feedback process that is required to make design, technology and architecture choices regarding the target system. An indispensable side of the development of radiation-hard SiPh based links is also the extensive study and validation of the radiation tolerance of the developed components and circuits. Without this study, the integration of SiPh based TRx is CERN experiments will not be possible.

Within the CERN collaboration, various SiPh test chips have been designed and characterized. Relevant to the work described in this thesis is the second chip that was designed at CERN in 2019 and was fabricated by imec's multi project wafer (MPW) in 2020, namely PICv2. This test chip, shown in Fig. 1.5, has dimensions of 5 mm x 5 mm and includes intellectual property (IP) blocks designed at CERN or made available by the foundry's libraries, combined to form structures for data transmission demonstrations. More specifically, the PIC includes various versions of RMs, Mach-Zehnder modulators (MZMs), Ge PDs, optical multiplexers, interferometers for polarization recovery studies, as well as a WDM circuit with four cascaded RMs connected in series.

This PIC serves first of all as a test vehicle for the characterization of the individual components, the implementation of radiation tests and the comparison of the different versions of the components in terms of performance and radiation hardness. At the same time, the building blocks that are available from the PIC can be combined and utilized for the assembly of a first version of transmitters and receivers, allowing higher level testing and characterization.

On a system level, the development and operation of SiPh based transceivers involves many challenges. On the transmitter side, a very important challenge is the wavelength stabilization of the RMs. This is necessary to achieve their stable operation at the desired wavelength of operation irrespective of variations in the environmental conditions (e.g.

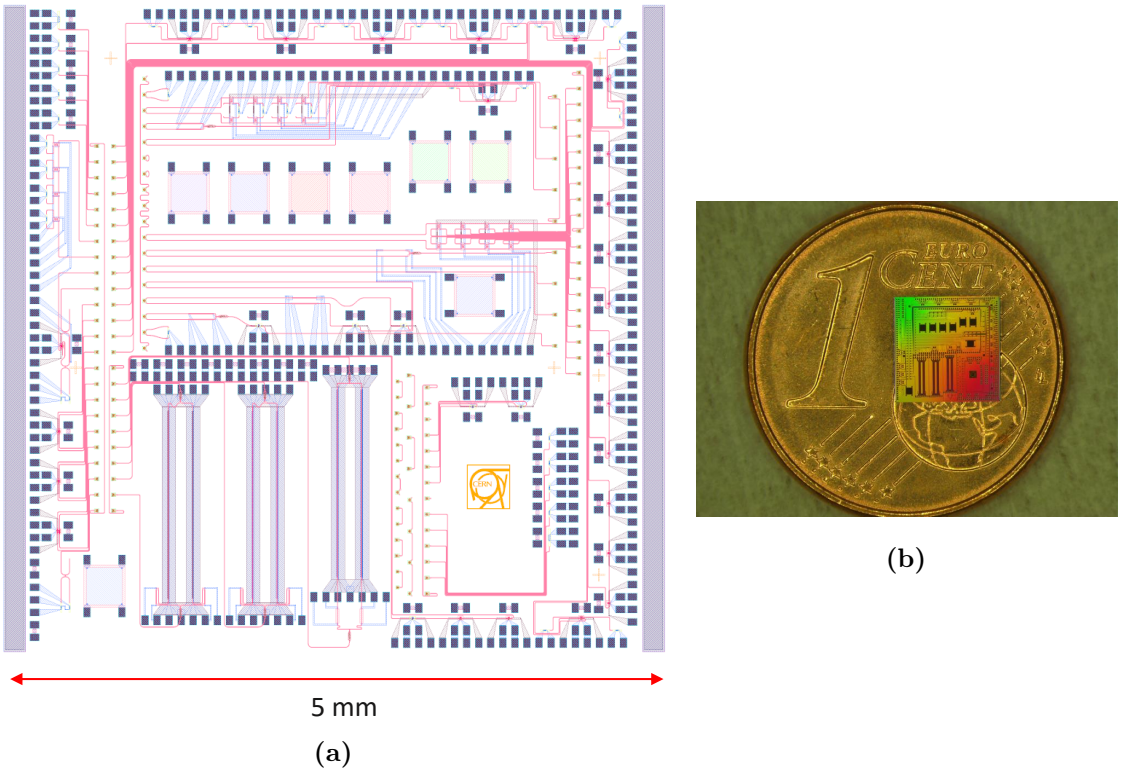

Figure 1.5. *(a) The mask layout of PICv2 designed at CERN. (b) Picture of the fabricated PIC on top of an one cent coin for size comparison.*

temperature, external laser wavelength variation). Another important challenge is the polarization management. This is required due to the unique architecture of such a link that imposes the placement of the optical sources in the back-end, away for the SiPh PICs, and their connection with SMFs that do not maintain the polarization. The same problem exists also on the receiver side, since the SiPh Rx will be connected to the BE Tx through long SMFs. The optical power supplies consist themselves an important challenge since no component with the required specifications is currently commercially available. Especially in the case of a WDM implementation, the architecture of the whole link, including the SiPh circuit, the power supplies and the polarization management and thermal tuning, becomes more complex and requires extra effort and problems to be addressed. Last but not least, the electronic components that need to interface with the SiPh PIC, namely the modulator driver that goes with the RM, and the TIA that goes with the Ge PDs, also require special development. These components will have to be custom designed for this system in order to meet the radiation hardness specifications.

The scope of this thesis, that also reflects the work that the writer carried out during the past three years, evolves around the development of a SiPh Tx and Rx based on the components provided by PICv2. It also concerns the addressing of the challenges that are involved in the development of such a SiPh TRx, from a system point of view. More specifically, the scope of the thesis can be summarized in the following objectives:

- Complete testing and characterization of the SiPh Tx comprising RMs from PICv2. This includes direct current (DC) and high speed measurements with low and high

input power, spectral measurements, as well as comparison of the performance between different RM designs. This requires the development of Tx test board as the test vehicle to perform the Tx characterization.

- Testing and characterization of the SiPh Rx, comprising the Ge PDs and radiation-tolerant TIA. This requires the development of the Rx test board as the test vehicle, and includes high speed and bit-error-rate (BER) measurements. The comparison between the different versions of PDs and TIAs is also targeted.

- Develop, test and implement a feedback control loop for the thermal tuning of the RMs. This is a necessary requirements from a systems aspect to achieve stable operation of the SiPh Tx.

- Test and characterize the available polarization diversity structures from PICv2. Given the results, design and implement a complete solution for on-chip polarization management for the SiPh link of this application.

- Test and characterization of the WDM circuit from PICv2. Develop solutions for the thermal tuning and polarization management that are compatible with multi-channel operation.

All the aforementioned objectives target the advancing towards a first demonstration of SiPh TRx for HEP experiments. Given the current progress during the beginning of this PhD, the thesis aims to move one step forward the effort to put together from the available components a SiPh Tx and Rx, and address the important system challenges.

1.5 Structure of the thesis

The thesis is structured in 7 chapters. Chapter 1 is the introduction. It introduces CERN and the LHC, the largest particle accelerator, and briefly describes the main detectors and experiments at CERN. Then, the upgrade plan of the LHC, namely the HL-LHC is explained, along with the anticipated impact on the experiments performance and requirements (data rates, radiation levels). The different mechanism of radiation damage in CERN experiments in then introduced. The rest of the introduction focuses on the optical data links in HEP experiments. The reason behind the choice of using data links is explained. Then the current generation of optical links, namely the VL+ project, its characteristics, principles of operation and performance and limitation is analyzed. Given the HL-LHC upgrade, the requirements of a new generation of optical links are established, followed by an introduction to the SiPh platform and its advantages that render it an excellent choice for this new generation of optical links. The vision of a SiPh based data link at CERN is then described. The chapter concludes with an overview of the research objectives of the thesis, as well as the structure of the thesis.

Chapter 2 reviews the material properties as well as the important optical and thermal effects in Silicon. It then includes a description of the passive and active SiPh components

and their principles of operation. These components are utilized to build the custom CERN SiPh Tx and Rx.

Chapter 3 focuses on the SiPh transmitter and its testing and characterization. First, the basic component of the SiPh Tx, namely the Si RM is described. The RM structure is explained and the RM circuit used by the SiPh is presented. This is followed by the characterization of the RM that includes measurements of its output spectra and extraction of the important figures of merit. Next, the different test boards that have been assembled for the testing of the Tx are presented. They include the DC test-board, the driver-less test board and the 25G test-board. The following section is the Tx characterization that includes the static measurements with low input power and high input power, the high-speed measurements, the micro-heater characterization (step response function, thermal and electrical characterization), the self-heating effect characterization and last the RM thermo-optic transfer function extraction. After that, the electrical modulation driving scheme is presented. The last section of this chapter is devoted to the 4-channel WDM transmitter circuit that comprises 4 RMs connected is series and constitutes a solution for a WDM Tx. Its static and high-speed characterization concludes the chapter.

Chapter 4 is a detailed presentation of the thermal tuning process of the SiPh RMs. It begins with an explanation of the motivation behind the need for thermal tuning, introduces the components and architecture of a generic feedback thermal control loop based on a sensor, a controller and an actuator. The different available techniques for the tuning of RMs are then reviewed. Among the available solutions, a feedback controller based on average power monitoring at the drop port is chosen for our application. The system requirements of this solution are analyzed and the physical implementation realized in the CERN lab is explained. This includes three versions, an initial one based on bench-top instruments, a more advanced one based on a custom board and a the vision for a final one that will be compatible with the final system requirements. Next, the design and tuning process of the PI controller is analyzed. This includes Matlab and Simulink simulations that are followed by the verification process of the designed controller. After having introduced the control loop principles and design process, the thermal tuning process of a RM is explained, that comprises the start-up procedure and the proportional-integral (PI) controller operation stage. The measurements and results of the single channel operation of the control loop are then presented, including measurements varying the input laser wavelength and the temperature. The final part of the chapter is the thermal tuning in WDM systems. This section includes the implementation of a thermal tuning loop for a WDM system, an overview of the extra challenges that such a system introduces, as well as solutions to address them. The chapter concludes with the measurement results of the thermal control loop testing for the WDM circuit.

Chapter 5 includes a study of the polarization management in SiPh integrated circuits and proposes complete solutions for on-chip polarization management. After explaining the reason why polarization management in necessary in Si PICs, it explains the polarization in SMFs and in Si PICs. Having established and explained the need for polarization recovery techniques, the available solutions are then reviewed .These include off-chip methods (use of polarization maintaining fibers or polarization controllers), as well as on-chip

methods (two dimensional grating couplers (2D-GCs) and polarization splitters-rotators (PSR)). The on-chip methods are more suitable for this application. For this reason, a polarization management solution based on 2D-GCs is proposed and the principle of operation is explained. The design and simulation of a complete circuit for polarization management based on 2D-GCs is then included, along with characterization and testing of existing structures based on 2D-GCs that are part of the complete circuit and allow for polarization mode dispersion compensation and partial control of the polarization. Their compatibility with existing RMs and WDM schemes is investigated. Next, solutions based on the use of polarization splitters and rotators are proposed. These include the detailed design and simulation of two custom components in the SiPh platform. The first is a C-band thermally tunable polarization rotator. The second component is a broadband O-band PSR based on mode conversion and phase matching.

Chapter 6 discusses the SiPh receiver, based on Ge photodiodes and a TIA. Its principle of operation is explained, followed by a description of the Rx test-boards that were developed at CERN. The chapter concludes with the characterization of the Rx that comprises the high-speed measurements and the BER measurements.

Last, Chapter 7 is the conclusions chapter. After summarizing the work that was done as part of this thesis, it lays out what are the next steps of the work related to the development of the next generation of optical links for HEP experiments based on SiPh. Solutions to address open problems described in thesis are proposed and finally research topics of interest to the subject and future work proposals are included.

Bibliography

[1] "CERN Official Website." Accessed 02/10/2023.

[2] O. S. Brüning, P. Collier, P. Lebrun, S. Myers, R. Ostojic, J. Poole, and P. Proudlock, *LHC Design Report Vol.1: The LHC Main Ring*. CERN Yellow Reports: Monographs, Geneva: CERN, 2004.

[3] S. Seif El Nasr, "Radiation-hard Optoelectronics for LHC detector upgrades.," 2016. Presented 16 Aug 2016.

[4] "The High-Luminosity LHC (HL-LHC)." Accessed: 02/10/2023.

[5] O. Aberle et al, *High-Luminosity Large Hadron Collider (HL-LHC): Technical design report*. CERN Yellow Reports: Monographs, Geneva: CERN, 2020.

[6] "Versatile Link Project Public Area." Accessed: 02/10/2023.

[7] CERN, "The HL-LHC Project," 2022. Accessed: October 2022.

[8] J. Troska, "Optical data transmission for lhc experiment phase-2 upgrades," 2019. Accessed: October 2022.

[9] J. Troska, A. Kraxner, A. Brandon-Bravo, S. Detraz, C. Scarcella, C. Sigaud, C. Soos, F. Vasey, and L. Olanterä, "The vtrx+, an optical link module for data transmission at hl-lhc," *PoS*, p. 048, 2017.

[10] P. Moreira, "The lpGBT: a radiation tolerant ASIC for data,timing, trigger and control applications in HL-LHC." Topical Workshop on Electronics for Particle Physics (TWEPP 2019), 2019.

[11] M. Backhaus, "The Upgrade of the CMS Inner Tracker for HL-LHC," tech. rep., CERN, Geneva, 2019.

[12] synopsys, "Silicon Photonics." Accessed: October 2023.

[13] B. Jalali and S. Fathpour, "Silicon photonics," *Journal of Lightwave Technology*, vol. 24, no. 12, pp. 4600–4615, 2006.

[14] B. Jalali, V. Raghunathan, R. Shori, S. Fathpour, D. Dimitropoulos, and O. Stafsudd, "Prospects for silicon mid-ir raman lasers," *IEEE Journal of Selected Topics in Quantum Electronics*, vol. 12, no. 6, pp. 1618–1627, 2006.

[15] H. Ye and J. Yu, "Germanium epitaxy on silicon," *Science and Technology of Advanced Materials*, vol. 15, p. 024601, mar 2014.

[16] H. Li, G. Balamurugan, M. Sakib, J. Sun, J. Driscoll, R. Kumar, H. Jayatilleka, H. Rong, J. Jaussi, and B. Casper, "A 112 gb/s pam4 silicon photonics transmitter with microring modulator and cmos driver," *J. Lightwave Technol.*, vol. 38, pp. 131–138, Jan 2020.

[17] L. Olanterä, C. Scarcella, M. Lalović, S. Détraz, A. Pandey, T. Prousalidi, U. Sandven, C. Sigaud, C. Soós, and J. Troska, "Effects of high fluence particle irradiation on germanium-on-silicon photodiodes," *IEEE Transactions on Nuclear Science*, vol. 71, no. 4, pp. 728–735, 2024.

[18] M. Lalović, C. Scarcella, A. Bulling, S. Detraz, L. Marcon, L. Olanterä, T. Prousalidi, U. Sandven, C. Sigaud, C. Soos, and J. Troska, "Ionizing Radiation Effects in Silicon Photonics Modulators," *IEEE Transactions on Nuclear Science*, vol. 69, pp. 1521–1526, July 2022.

[19] M. Lalović, S. Detraz, L. Marcon, L. Olanterä, T. Prousalidi, U. Sandven, C. Scarcella, C. Sigaud, C. Soós, and J. Troska, "Thermal annealing in silicon photonics ring modulators," *Journal of Instrumentation*, vol. 18, p. C03028, mar 2023.

[20] M. Zeiler, S. S. El Nasr-Storey, S. Detraz, A. Kraxner, L. Olantera, C. Scarcella, C. Sigaud, C. Soos, J. Troska, and F. Vasey, "Radiation Damage in Silicon Photonic Mach–Zehnder Modulators and Photodiodes," *IEEE Transactions on Nuclear Science*, vol. 64, no. 11, pp. 2794–2801, 2017.

[21] F. De Leonardis, B. Troia, C. E. Campanella, F. Prudenzano, and V. M. N. Passaro, "Modeling of Radiation Effects in Silicon Photonic Devices," *IEEE Transactions on Nuclear Science*, vol. 62, no. 5, pp. 2155–2168, 2015.

[22] A. Kraxner, S. Detraz, L. Olantera, C. Scarcella, C. Sigaud, C. Soos, C. Stile, J. Troska, and F. Vasey, "Radiation tolerance enhancement of silicon photonics for HEP applications," in *Topical Workshop on Electronics for Particle Physics (TWEPP2018)*, vol. 21, 2018.

[23] C. Scarcella, S. Detraz, M. Lalović, L. Marcon, L. Olanterä, T. Prousalidi, U. Sandven, C. Sigaud, C. Soós, and J. Troska, "System development of silicon photonics links for CERN experiments and accelerators," *Journal of Instrumentation*, vol. 18, p. C03002, mar 2023.

[24] T. Prousalidi, C. Scarcella, A. Ahmed, S. Detraz, M. Lalović, L. Olanterä, A. Pandey, C. Sigaud, C. Soós, J. Troska, and H. Avramopoulos, "System development of radiation tolerant silicon photonics transceivers for high energy physics applications," *IEEE Transactions on Nuclear Science*, pp. 1–1, 2023.

Chapter 2

Silicon Photonics

As it was explained in the previous chapter, SiPh is compatible with CMOS fabrication processes which translates to cost-effective production. Moreover, Silicon can be patterned with sub-micron precision, to realise small in size passive (e.g. waveguides and couplers) and active components. Doping the silicon allows for fabrication of modulators that can be very compact, due to the high refractive index contrast, and support the required high data rates. Germanium (Ge) epitaxy for the fabrication of photodetectors is also possible. Therefore, SiPh is a complete platform for the development of the transceivers for the next generation of data links at CERN. In this chapter, the basic material properties and effects of Silicon will be described, which is required to understand the operational principles of the different components that will be used next, both from the device and from the system point of view. Moreover, the relevant to this thesis passive and active components and their principles of operation will be summarized.

2.1 Silicon: material properties and effects

2.1.1 Material properties

The silicon material exhibits low absorption in the wavelength range of 1.1 µm to 8.5 µm, which covers the near-infrared (NIR) and mid-infrared (MIR) regions. This makes it an ideal candidate for the realization on low loss waveguides and passive components at the O-band and the C-band. The refractive index of Silicon at 1550 nm is 3.4752, and the refractive index of SiO_2 at 1550 nm is 1.444. In SOI based waveguides the use of Si as the core and of SiO_2 as cladding material creates very high index contrast allowing for the realization of very compact waveguides in the nano metre scale, with very sharp bends [1].

The indirect bandgap of silicon that is responsible for its low absorption in the aforementioned wavelength range, makes it an insufficient photo-conductive material, and the bandgap of 1.1 eV results in an absorption decrease beyond 800 nm with a typical photosensitive cutoff at 1100 nm. Therefore, silicon is not considered as an ideal photosensitive material, especially beyond the 1.1 µm [2]. This is why the use of other materials, like Germanium are required for the development of efficient photo-detectors in the SiPh platform, around the C-band and O-band. Ge is an indirect bandgap material having the gap energy of 0.66 eV. Ge reveals a large optical absorption for the wavelength below 1.55 µm, derived from the direct gap energy of 0.80 eV corresponding to 1.55 µm in wavelength. This has led to the application of Ge to photodetectors on Si in the NIR optical communication band (1.3 µm - 1.55 µm) [3].

At the same time, light emitter is one of the missing components in Si photonics due to the indirect bandgap nature of Si. One way to address this is using III-V materials integrated in the SiPh platform. III-V lasers bonded on Si waveguide have been demonstrated. However, for our application given the need for remote placement of the lasers, off-chip light sources are being used, which is another solution for light sources in SiPh [3].

2.1.2 Electro-optical effects in Si

Electro-optical effects in Si are very important for understanding the principles of operation as well as the limitations of active Si components. These effects are particularly important for understanding and realising optical modulation mechanisms in Si and consequently SiPh modulators. Optical modulation in photonic circuits is implemented by devices that cause direct changes in optical intensity via absorption, or cause changes in the refractive index of the material (and hence the phase of a propagating wave), which can be converted to an intensity change via an interferometer (e.g. MZI) or a resonant device. Such refractive index changes are typically produced via an applied electrical signal. The preferred means of implementing modulation is by the application of an electric field, because this implies little or no current flow (and hence low power) and a fast response time. The application of an electric field to a material can result in a change to the real and imaginary refractive indices. A change in real refractive index, Δn, is known as electrorefraction, and a change in the imaginary part of the refractive index, $\Delta\alpha$, is known as electroabsorption. The primary electric field effects that are useful in semiconductor materials are the Pockels effect (linear electro-optic effect), the Kerr effect, and the Franz-Keldysh effect. The real part of refractive index n of a metarial can be expressed as $n(E) = n_0 + a_1E + a_2E^2 + ...$, where E is the electric field, n_0 is the refractive index of the material without the presence of the electric field and a_1, a_2 are the linear electro-optic effect coefficient and second-order electro-optic effect coefficient respectively. The change in n proportional to E is called Pockels effect, while the change proportional to E^2 is called the Kerr effect. Both effects concern electrorefraction. All materials exhibit the Kerr effect, however the Pockels effect is exhibited by only certain crystalline solids [4]. The Franz-Keldysh effect is an electroabsorption effect. When an electric field is applied to Si, the energy band structure is modified. The applied electric field leads to a Stark shift in the energy levels of the valence and conduction bands. As a result of this shift, the effective band gap of silicon is altered, and it becomes easier for electrons to move from the valence band to the conduction band. The Franz-Keldysh effect results in a field-dependent change in the absorption characteristics of silicon. In other words, the material becomes more transparent to light with energies near the shifted band gap when an electric field is applied [5].

Soref and Bennett have examined electric field effects in Si to determine their relative efficiency, and have shown that the Kerr effect and the Franz-Keldysh effect are small in Si [6]. Furthermore, the Pockels effect is absent in crystalline Si. This leaves one candidate effect for electro-optical modulation in Si: the plasma dispersion effect [7].

The plasma dispersion effect is related to the density of free carriers in a semiconductor, which changes both the real and imaginary parts of the refractive index. This is described by the Drude-Lorenz equations that relate the concentration of electrons (N_e) and holes (N_h) to the absorption coefficient α and refractive index n. For a modulator, the most convenient way of expressing this is as the change in these parameters, $\Delta\alpha$ and Δn, with the change in electron and hole densities, (ΔN_e) and (ΔN_h), as follows:

$$\Delta\alpha = \frac{e^3\lambda_0^2}{4\pi^2c^3\epsilon_0 n}\left(\frac{\Delta N_e}{\mu_e(m_{ce}^*)^2} + \frac{\Delta N_h}{\mu_h(m_{ch}^*)^2}\right) \tag{2.1}$$

$$\Delta n = \frac{-e^2\lambda_0^2}{8\pi^2c^2\epsilon_0 n}\left(\frac{\Delta N_e}{m_{ce}^*} + \frac{\Delta N_h}{m_{ch}^*}\right) \tag{2.2}$$

Soref and Bennett evaluated Δn in experimentally produced absorption curves in the literature for a wide range of N_e and N_h . In particular, they focused on the communications wavelengths of 1.3 µm and 1.55 µm. Interestingly, their results were in good agreement with the classical Drude-Lorenz model only for electrons. For holes, they noted a $\Delta N_h^{0.8}$ dependence. They also quantified the changes that they identified in the literature for both refractive index and absorption. They produced the following extremely useful empirical expressions, which are now used almost universally to evaluate changes because of injection or depletion of carriers in Si. At $\lambda_0 = 1.55$ µm:

$$\Delta n = \Delta n_e + \Delta n_h = -[8.8 \cdot 10^{-22}\Delta n_e + 8.5 \cdot 10^{-18}(\Delta n_h)^{0.8}] \tag{2.3}$$

$$\Delta\alpha = \Delta\alpha_e + \Delta\alpha_h = 8.5 \cdot 10^{-18}\Delta\alpha_e + 6.0 \cdot 10^{-18}\Delta\alpha_h] \tag{2.4}$$

where: ΔN_e is the change in refractive index resulting from change in free electron carrier concentrations; ΔN_h is the change in refractive index resulting from change in free hole carrier concentrations; $\Delta\alpha_e$ is the change in absorption resulting from change in free electron carrier concentrations; and $\Delta\alpha_h$ is the change in absorption resulting from change in free hole carrier concentrations.

Another two non-linear electro-optic effects that are of interest in SiPh is the two-photon absorption (TPA) and free-carrier absorption (FCA). At telecommunication wavelength, TPA in silicon is an instantaneous nonlinear loss mechanism dominating at high optical intensities [8]. It is an optical process where the simultaneous absorption of two photons leads to electron excitation from the valence band to the conduction band. It occurs at higher light intensities and is characterized by a quadratic dependence on intensity. The TPA-induced free carriers cause FCA. FCA is the phenomenon in which incident light is absorbed due to the presence of free charge carriers, namely electrons and holes. As light with energy greater than the silicon bandgap is absorbed, it generates electron-hole pairs, or free carriers, which can further absorb additional photons, leading to a reduction in the transmitted light intensity. High FCA is Si can lead to increased optical losses in silicon photonic devices.

2.1.3 Thermo-optical effect in Si

The thermo-optic effect (TOE) is a physics phenomenon that determines the variation of the refractive index of a material with temperature. This effect has been extensively used in optoelectronics as well as in sensors technology for the realization of a large variety of devices, mostly based on interferometric principles, such as optical switches, tunable filters, tunable lasers and fiber-optic sensors. In order to characterize a material from the

thermo-optic point of view, the thermo-optic coefficient (TOC) is generally used. The TOC of silicon is a measure of how the refractive index of silicon changes with temperature. It quantifies the sensitivity of the silicon material to temperature variations in terms of its effect on the speed of light within the material. The TOC is typically expressed in units of refractive index change per degree Celsius (dn/dT, where n is the refractive index). Among the common thermo-optical materials silicon shows the highest coefficient. The TOC of silicon can vary slightly depending on the wavelength of light and the specific silicon material (e.g., crystalline silicon or amorphous silicon). At the fiber optic wavelength of 1550 nm, the TOC of Si is $dn/dT = 1.86 \times 10^{-4}\,^{\circ}\mathrm{C}^{-1}$. Silicon exhibits a positive thermo-optic coefficient, which means that as the temperature increases, the refractive index of silicon decreases. This change in refractive index affects the phase and velocity of light propagating through the silicon waveguides.

Thermo-optic effects can be harnessed to create tunable optical filters or ring modulators. By adjusting the temperature of the silicon waveguide, the center wavelength of the filter or modulator can be tuned. This is valuable in WDM systems and optical networking. Another useful application of the thermo-optic effect are the optical phase shifters: thermo-optic phase shifters can be used to modulate the phase of light in optical circuits. This is important in applications like interferometry, where precise phase control is needed for measurements [9].

2.2 Silicon Photonics components

Silicon photonics leverages the standard CMOS manufacturing process used in the microelectronics industry, thus enabling high integration density, high yield, and potentially low cost. The past two decades witnessed the rapid growth of silicon photonics research and development. Design and fabrication technologies have advanced significantly, which led to foundries offering MPW services [1], making the technology cheaper accessible by more users. The SiPh platform relies on the use of SOI wafers for the design and realization of photonic integrated circuits. A schematic of such a wafer is shown in Fig. 2.1. SOI wafers consist of a thin layer of silicon (the active layer) sandwiched between two insulating oxide layers, the top oxide and burried oxide layer. Another thick layer of Silicon works as the substrate. This structure provides many advantages for fabricating photonic devices. The use of SOI wafers allows for creation of high-quality, low-loss waveguides that can confine light within the active silicon layer. The insulating oxide layers prevent light from leaking out of the waveguide and into the substrate, which can cause signal loss and reduce device efficiency. The basic building blocks of photonic circuits are the waveguides. SOI wafers allow for the fabrication of high-quality waveguides that can be used to create a variety of photonic devices like wavelength filters, and switches. In addition, optical branches, modulators, and photodetectors can be fabricated on SOI wafers by using CMOS compatible processes. It is possible to make various individual Si photonics devices on a SOI wafer and most of these devices are already at a level suitable for practical applications [10].

One standard method for fabricating photonic devices on SOI wafers is to use a technique called silicon-on-insulator rib waveguide fabrication. This technique involves pat-

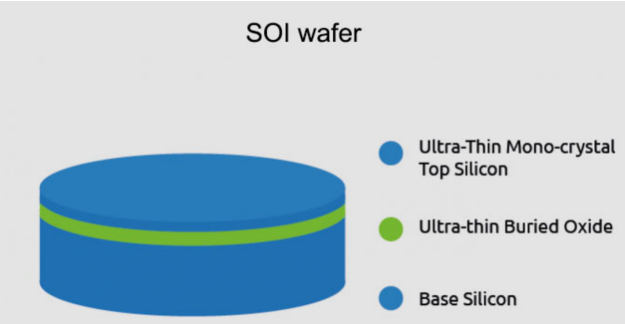

Figure 2.1. *Schematic of a SOI wafer. Source: [11].*

terning the oxide layer on the SOI wafer to define the waveguide structure, followed by etching the silicon layer to create the rib waveguide. The resulting waveguide creates a variety of photonic devices by further patterning and processing the active silicon layer. Another advantage of using SOI wafers is creating high-quality silicon-on-insulator PDs, by Ge epitaxy. Photodiodes convert light into electrical current and are essential components in many photonic systems. The use of SOI wafers allows for creation of PDs with low dark current and high responsivity, which can significantly improve device performance. Thanks to the semiconductor property of Si, it is also possible to create active components whose functionality is electrically controlled, such as a modulator. This is done by doping a PN junction in the optical guide, thus controlling the optical index of the guide. In this way, Mach-Zehnder modulators or ring modulators are designed. This allows the amplitude of the light output to be electrically controlled [12, 13].

In summary, photonic devices based on SOI wafers offer many advantages like high-quality, low-loss waveguides, photodiodes and modulators. The unique properties of SOI wafers allow for the creation of a wide range of photonic devices essential for many applications, including telecommunications, data centers and sensing. In this section we will summarise the basic active and passive devices fabricated in SOI wafers that are relevant to the TRx that this thesis focuses on.

2.2.1 Passive components

Waveguides

Si photonic devices are based on Si waveguides, which are composed of a submicrometer-scale Si core and SiO_2 cladding. The SOI structure is very suitable for making these waveguides. A Si layer is fabricated as the core and a SiO_2-BOX layer works as the cladding. Because the Si layer of the SOI wafer is made of single crystal, the light scattering due to defects in the Si core or on the Si surface is suppressed, which reduces propagation loss. Si waveguides of different types and shapes exist. The most typical types often used in Si chips are the rib waveguides, wire waveguides, slot waveguides and sub-wavelength grating (SWG) waveguides. A schematic of these type of waveguides in shown in Fig. 2.2. The wire waveguides consist of a strip of silicon with height of 220 nm in the SOI platform we are using, and width of 450 nm in the C-band (or 380 nm in the O-band). This silicon strip is the waveguide core where the light is confined, and it surrounded by SiO_2. Wire

waveguides are the typical waveguide structures and various ultracompact passive optical and dynamic functional devices have already been developed using Si wire waveguides, like power splitters and combiners, tapers, polarization splitters and rotators, couplers and MMIs. Si rib waveguides consist of three parts: a silica substrate, a thin silicon layer on top of the substrate and a rectangular silicon rib part. Light is wave-guided mainly in the rib part, and a bit in the thin silicon layer. This type of waveguides are preferred for the realisation of active components like modulators, by doping the silicon regions. SWG and slot waveguides are more exotic components typically used in more complex devices like polarization rotators, grating structures or silicon sensors. Moreover, bent or ring shaped waveguides can be fabricated in the SiPh platform, for the realization both of passive and active components, like ring resonators, ring filters or ring modulators. Depending on the device type, ring shaped waveguides can be based on either rib or ridge waveguide. In the SiPh platform, due to the strong confinement of the light in the waveguides, radius as small as 5 µm can be achieved, leading to very compact devices and tight integration.

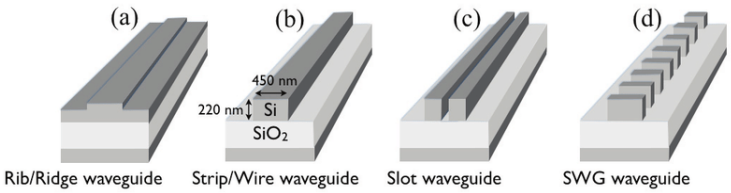

Figure 2.2. *Basic types of waveguides in the SiPh platform. Source: [14].*

Silicon wire and ridge waveguides are considered planar waveguides. As a result, to understand the waveguiding principles of the Si waveguides we can analyze the waveguiding in planar waveguides. The light propagation can be generally described by Maxwell's equations. However, these are very complex equation to solve, and there are much simpler approaches that can be employed to describe the planar waveguide. One of these approaches is the ray optical model.

We consider a light ray (E_i) propagating in a medium with refractive index n_1, and impinging on the interface between two media, at an angle ϑ_1, as shown in Figure 2.3(1). At the interface the light is partially transmitted (E_t) and partially reflected (E_r). The relationship between the refractive indices n_1 and n_2, and the angles of incidence (ϑ_1) and refraction (ϑ_2), is given by Snells law: $n_1 sin\theta_2 = n_2 sin\theta_2$.

In Figure 2.3(1), the refractive index of medium 1 (n_1) is clearly higher than the refractive index of medium 2 (n_2), as the angle ϑ_2 is greater than ϑ_1. Consequently as ϑ_1 is increased, ϑ_2 will approach 90°. For some angle ϑ_1, the corresponding angle ϑ_2 will reach 90°, and hence Snell's law simplifies to: $n_1 sin\theta_1 = n_2$. Hence we can define this critical angle ϑ_c as: $sin\theta_c = \frac{n_2}{n_1}$

For angles of incidence greater than this critical angle, no light is transmitted and total internal reflection (TIR) occurs. If we now consider a second interface below the first, at which the wave also experiences total internal reflection, we can understand the concept of a waveguide, as the light is confined to the region of refractive index n_1, and propagates to the right (Fig. 2.3(2)). The light confinements both in planar waveguides and also optical

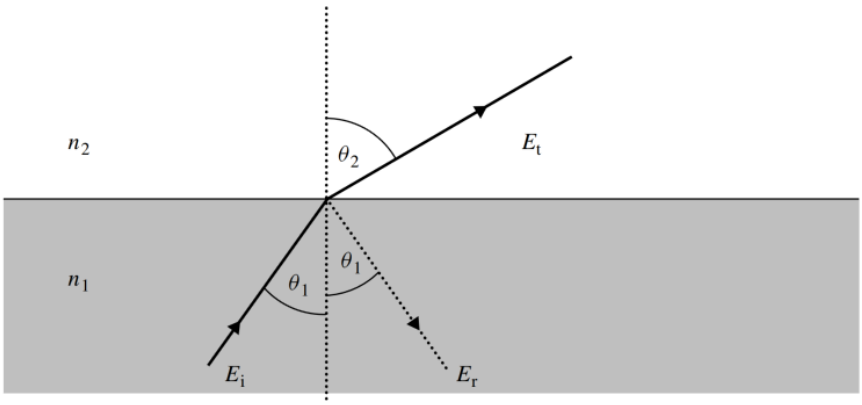

1 Light rays refracted and reflected at the interface of two media

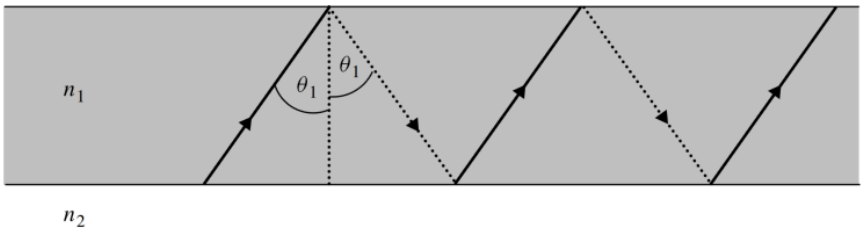

2 Total internal reflection at two interfaces, demonstrating the concept of a waveguide

Figure 2.3. *Schematic describing the light propagation between two media, according to the ray optical model. Source: [14].*

fibers is based on the phenomenon of TIR [15].

Although this simplistic approach suggests that the waveguide will support propagation at any angle greater than the critical angle, this is not true. The light cannot propagate at any angle θ but only at one of the allowed discrete angles. Each of these allowed angles corresponds to one solution of the Maxwell's equation and it is referred to as a mode of propagation. The modes are identified using a notation utilising the polarisation and the mode number. In planar waveguides the supported modes are usually either quasi-transverse-electric (quasi-TE) or quasi-transverse-magnetic (quasi-TM) modes. Quasi-TE modes are the modes in which there is almost no electric field component in the direction of propagation, while quasi-TM modes are the modes in which there is almost no magnetic field component in the direction of propagation. They differ from the TE and TM modes, where there is no electric or magnetic field component in the direction of propagation respectively. For example, the first TE mode, or fundamental mode, will be described as TE_0. Higher-order modes are correspondingly described using the appropriate number. There is also a further limit on this number, indicating that there is a limit to the number of modes that can propagate in a given waveguide structure. The limiting conditions correspond to the propagation angle, ϑ_1, becoming less than the critical angle at either the upper or lower waveguide interface.

In SiPh, single mode operation is usually preferred. Therefore the geometrical parameters of the SiPh waveguides (the core dimensions) are designed so that only the fundamental

mode both for TE and TM polarization is supported. When the effective index of a mode (n_{eff}) is greater than the refractive index of the envelope and lower than the refractive index of the core, the mode is guided into the waveguide. At the same time, the higher the effective index, the stronger is the confinement of the mode in the waveguide. In the waveguide system consisting of a silicon core and silica cladding, the refractive index contrast between the core and cladding is as large as 40%, which allows a TIR with a very large incident angle of 60°. In SiPh wire waveguides, therefore, the core dimension that fulfills a single-mode condition should also be smaller than or comparable to a half-wavelength of a guided wave in silicon. Since the refractive index of silicon is about 3.5 for photon energies below the band-gap energy, the core dimension of a silicon photonic wire waveguide should be less than or comparable to 400 nm for 1310 - 1550 nm telecommunications-band infrared light. Generally, the core shape is made flat along the substrate to reduce the etching depth in practical fabrications.

Fig. 2.4 illustrates the fundamental TE mode waveguided in a Si waveguide with height of 220 nm and width of 450 nm at a wavelength of 1.55 µm. Each mode is transmitted through the waveguide with a phase velocity $v_p = \frac{\omega}{\beta}$, where ω is the angular frequency and β is the propagation constant of the mode. The phase velocity is related to the effective refractive index of the mode with the formula $n_{eff} = \frac{c}{v_p}$, where c denotes the speed of light in the vacuum. The n_{eff} defines how much optical power is concentrated in the core of the waveguide. Most types of waveguides support two independent polarizations, either with the main magnetic (quasi-TM) or with the main electric (quasi-TE). Fig. 2.5 shows the value of the n_{eff} of the supported waveguide modes varying the waveguide width. The value of n_{eff} depends on the cross-section of the waveguide, and the materials of the core and the cladding. Higher order modes travel with different propagation constants compared to the fundamental mode and are less confined in the waveguide core. As a consequence of the different propagation constants between the waveguided modes, modal dispersion happens which reduces the product of the distance and bandwidth of the waveguide. Due to the low confinement of the mode's energy in the waveguide core in the case of higher order modes, the density of integration that can be achieved is reduced. At the same time these modes become more leaky especially around the waveguide turns, resulting in an increase in propagation losses. Also, in the case when higher order modes are not supported, and thus single mode operation is achieved, it is desirable to design the waveguide is a way such that the values of the effective indices of the fundamental TE and TM modes are very different. This helps to limit the coupling of optical power from one mode to the other. It is worth noting that for waveguides with width less than 550 nm, only the fundamental mode for each polarisation state is supported. Moreover, the propagation losses of these waveguides for the 220 nm SOI platform are less that 2 dB cm^{-1} for propagation in the C-band (nominal width 450 nm) and less than 3 dB cm^{-1} for O-band propagation (nominal width 380 nm).

A detailed analysis of the guided modes can be performed by various numerical methods such as the finite difference eigenmode method (FDE) [18], or the Finite Difference Time Domain method (FDTD) [19]. Fig. 2.4 that shows the calculated effective indices n_{eff} of the guided modes for 1550 nm infrared light in various core geometries was produced

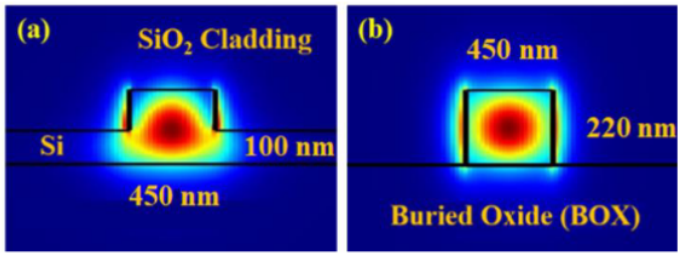

Figure 2.4. *Schematic and transverse electric (TE) mode profiles for a (a) single mode rib waveguide, and (b) single mode strip waveguide, at* $\lambda = 1550\,\text{nm}$. *The Si thickness is* 220 nm *in both cases, with the slab thickness equal to* 100 nm *for the rib waveguide. The waveguide width is* 450 nm. *Source: [16].*

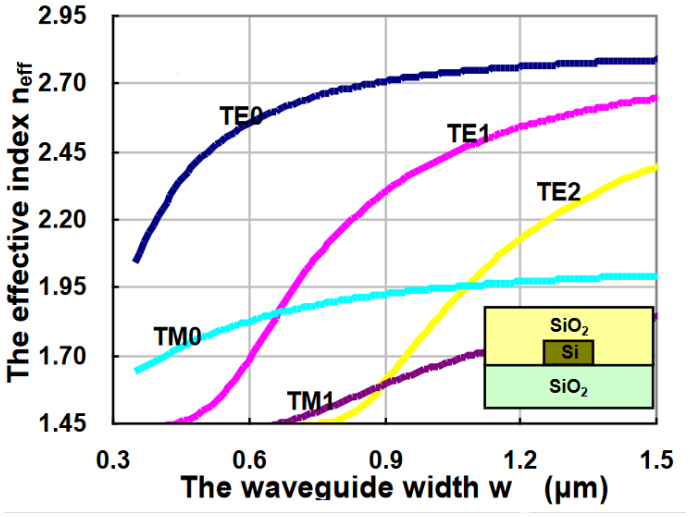

Figure 2.5. *The calculated effective indices for the modes of SOI nanowires with* SiO_2 *upper cladding. The thickness of the Si core layer is* 220 nm. *Source: [17].*

using the Lumerical FDE solver. These data verify that for waveguides of 220 nm silicon thickness, single-mode conditions are fulfilled when the core width is less than 460 nm for TE-like guided modes in which the dominant electric field is parallel to the substrate. For a TM-like mode in which the dominant electric field is perpendicular to the substrate, the single-mode condition is fulfilled in a core larger than that for the TE-like mode. The effective indices of TE and TM fundamental modes show a large difference. In other words, the 220 nm SOI platform produces a large polarization dependence.

Couplers

One key challenge encountered by silicon photonic chip is to couple light to and from optical fibers efficiently. The standard fiber for datacom is single-mode fiber (SMF), which has a mode field diameter (MFD) of near 10 µm at 1550 nm. Efficient coupling from SMF to waveguide with size of hundreds of nanometers is a challenge due to the large modal size mismatch. This problem is usually addressed using two solutions, in-plane (butt) edge coupling and off-plane (vertical) grating coupling [20].

Grating couplers One of the most popular solutions to implement fiber-to-waveguide optical couplers is represented by vertically coupled diffractive grating structures. The wide adoption of these devices in the field of silicon photonics is due to several factors. First of all, they are compact in size and provide access to any point on the PIC, thus facilitating wafer-level testing. At the same time they do not require intensive post-fabrication processing, such as cleaving and facet-polishing while also providing relatively relaxed fiber-positioning tolerances, usually higher than that of typical edge couplers. A diffractive grating coupler (GC) is realized by varying the waveguide refractive index profile according to a periodic pattern defined along one or more dimensions. This allows for phase-matching between the (near vertical) optical mode incident on the grating structure and the Si waveguides in the horizontal plane of the PIC (see Fig. 2.6). In other words, a vertical GC changes the off-plane wave-vector direction of light to the in-plane waveguide direction, and then couples the light into waveguide using a spot-size converter. If the refractive index distribution is engineered only along the direction of light propagation, then a 1D-GC is obtained. If the refractive index is also varied along the width of the waveguide, then a 2D-GC is realized. SOI-based integrated waveguides usually exhibit a high birefringence, thus making it challenging to achieve efficient coupling into a standard 1D-GC for both the orthogonal (and degenerate) light polarization states propagating in an SMF. As a consequence, 1D-GCs are usually optimized for a single state of polarization, whereas more complex structures are required to implement polarization-insensitive couplers. Although GCs have the above-mentioned advantages, they also have some drawbacks coming with their operation principles. First, they usually have lower CE compared with edge couplers, while numerous research works have focused on improving CE of GC. Secondly, gratings are intrinsically sensitive to both wavelength and polarization. Overall, the choice of the coupling schemes depends on the requirements and tolerances of each application [20, 21].

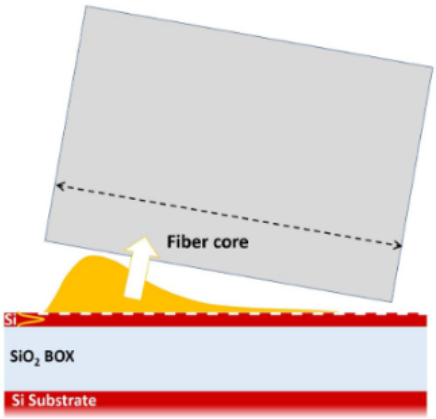

Figure 2.6. *Schematic representation of a 1D-GC used for light coupling between a chip and an SMF. Source: [21].*

A GC is basically a varying arrangement of different materials or structures on a certain surface, usually periodic. On SOI-based photonic chips, it is realized through etching on SOI or selectively depositing amorphous silicon on SOI. Either etching or deposition creates

a refractive index variation. If the index variation has a period larger than the wavelength of light inside the grating material, the diffraction effect prevails. Otherwise, the light propagation in the grating will exhibit similar features as in a uniform medium. GCs work in the diffraction regime.

The diffraction behavior for a GC, as illustrated in Fig. 2.7a, can be described using Bragg condition (phase matching condition), which shows the relationship between the wave vector k_0 of an incident light beam above chip and the propagation constant β of the corresponding coupled light beam into the waveguide. The Bragg condition is expressed as follows in Eq. 2.5:

$$k_0 sin\theta + mG = \beta_m \tag{2.5}$$

where G is the grating vector and m is the grating diffraction order. The same principles of operations also apply for the 2D-GCs.

Although 1D-GCs are very useful and widely adopted components, the have some important disadvantages. One of the main ones, relative to our application, is that 1D-GCs generally exhibit strong polarization sensitivity and offer optimum CE for only one polarization state. 2D-GCs offer an alternative solution for fiber-to-PIC coupling, where the fiber mode has an unknown or unstable polarization state. In its simplest form, a 2D-GC can be viewed as the superimposition of two orthogonally orientated 1D-GCs, each of which couples light from the fiber mode into a TE-polarized mode on the Si PIC, as shown in Fig. 2.7b. Any random polarization at the SMF will be projected onto the 2D-GC as the linear superposition of the two orthogonal fiber modes E_x and E_y, each of which is TE-polarized with respect to one of the 1D-GCs. As the polarization state varies, the fraction of power in the E_x and E_y modes and equivalently the fraction of power coupled by an individual 1D-GC changes, but the overall power coupled to both 1D-GCs is almost constant. As a result, the 2D-GC will couple the E_x and E_y polarization modes of the SMF onto two separate output waveguides. During this process both E_x and E_y SMF modes are split and converted to TE modes of the silicon waveguide on the chip [22, 23].

Ideally, the total coupling efficiency of a 2D-GC would be entirely independent of the polarization state of the input fiber mode polarization. In practice, this is not the case and a variation called polarization dependent loss (PDL) appears in practical implementations of simple uniform 2D-GC. This means that the two orthogonal polarization states of the SMF will be coupled onto the PIC with slightly different efficiencies, resulting in a total coupling efficiency that depends on the input polarization state.

Edge couplers In edge coupling, the fiber is placed at the chip facet and aligned with the on-chip waveguide horizontally. Edge couplers usually consist of an inverse tapered waveguide, which means the width of waveguide is gradually decreasing along the propagation of light to the edge. As it gradually decreases, light confinement is reduced and the mode size becomes larger (its effective cross-section increases, while its effective index decreases) to be comparable with fiber mode. It is reversed for fiber-to-chip propagation case, where Gaussian fiber mode distribution will be confined in the tapered waveguide as its size gradually increase. A schematic of an edge coupling scheme between a fiber and a

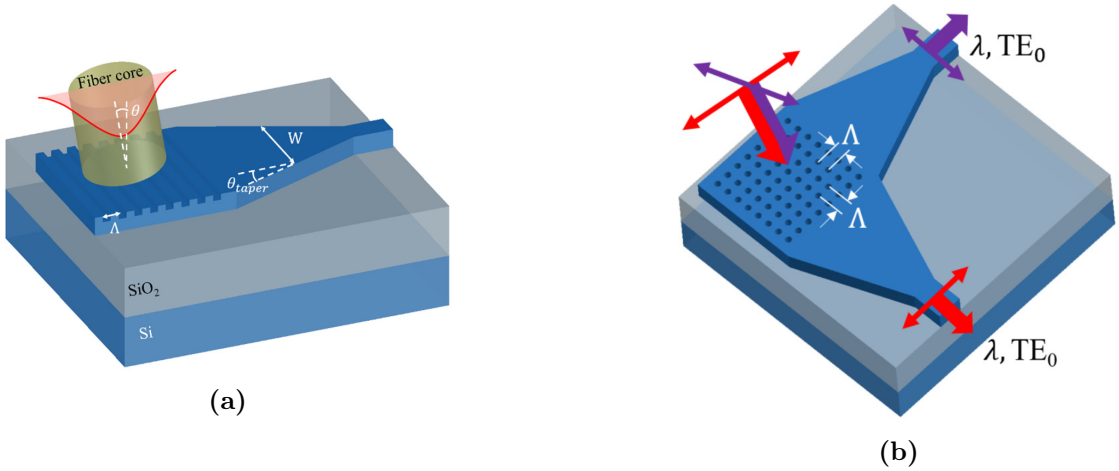

Figure 2.7. *(a) Schematic representation of a SiPh 1D-GC. (b) Schematic representation of a 2D-GC. Source: [20]*

photonic chip is shown in Fig. 2.8. Edge couplers can achieve high coupling efficiency (CE), large bandwidth and low PDL. The coupling losses determined by effects such as reflection at the chip facet, fiber-to-tip mode mismatch, and mode-conversion loss along the tapered SOI waveguide. Typically, tapers longer than 100 µm are required for adiabatic conversion of the optical mode in the waveguide, which is contrary to the drive to minimize the dimensions of photonic components, in order to achieve dense on-chip integration. Moreover, a properly cleaved and polished facet with strict smoothness requirement is needed to reduce the loss, which adds extra fabrication cost considering mass manufacturing. The high performance also comes with reduced flexibility, since they have relatively large footprint and must be placed at the edge of chip. In addition, edge coupling solutions have low fiber-chip alignment tolerance and prohibit wafer-level testing, which will further increase the cost per chip and require higher accuracy for testing and packaging [21].

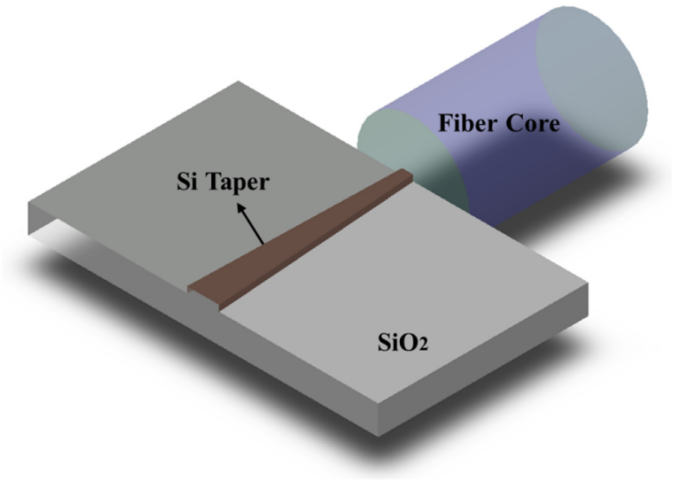

Figure 2.8. *Schematic of an edge coupling scheme between a fiber and a photonic chip. Source: [24].*

Power couplers

Silicon photonics power couplers are pivotal components within PICs due to their crucial roles in signal distribution, WDM, and the efficient integration of optical components on a single silicon chip. These couplers are instrumental in routing and distributing optical signals, enabling the splitting of an incoming optical signal into multiple paths or the combining of signals from different sources. At the same time, they enable the simultaneous transmission of multiple wavelengths in WDM systems and contributing to the miniaturization and cost-effectiveness of photonic circuits. Their significance extends to interferometric devices like Mach-Zehnder interferometers and ring resonators, facilitating optical modulation and wavelength-selective coupling. Well-designed power couplers not only enhance efficiency by minimizing insertion losses but also enable the creation of optical switches and routers for flexible network configurations. Their versatility in design, offering options like directional couplers, Y-branches, and multimode interference (MMI) couplers, allows for tailored solutions in terms of size, coupling ratio, and functionality. Overall, silicon photonics power couplers play an indispensable role in advancing integrated and high-performance optical communication systems. Power couplers that are compact in size, efficient and wavelength-independent (broadband), are especially important for data communication applications, such as wavelength-division-multiplexing and signal switching. In this section we will analyze the principle of operation of the main types of power couplers.

Directional couplers The directional coupler (DC) is a fundamental and widely employed building block in SiPh, serving as a power splitter/combiner to construct complex devices, such as Mach–Zehnder interferometers (MZIs), wavelength division multiplexers, optical switches, polarization splitters, and electro-optics modulators. In optical communication and sensing, the DC is commonly used to construct waveguide taps to extract a portion of the light signal traveling along a primary waveguide. These taps serve monitoring purposes, allowing for the precise measurement of the light signal's characteristics at a specific location [25]. DCs have been widely adopted as power couplers is such applications due to their simple configurations and the ease with which they can be fabricated in the SOI platform [26].

The schematic diagram of a conventional DC is presented in Fig. 2.9(a). The DC is composed of two symmetric arms that have a uniform width of W. Each arm comprises a straight waveguide of length L_C and two S-bends, functioning as the input and output ports, respectively. Power exchange occurs between the two straight waveguides, and thus, the term coupling length is applicable to describe the length of the straight waveguide. A cross-sectional view of the coupling region is shown in Fig. 2.9(b). Careful design of the rib waveguide height H, slab thickness h, gap size G, and W is required to achieve the desired coupling strength.

Although DCs are very useful components, coupled mode theory demonstrates that the coupling efficiency of conventional DCs with parallel waveguides sections is highly dependent on the propagation constants. This leads to a varying amplitude of the coupling power

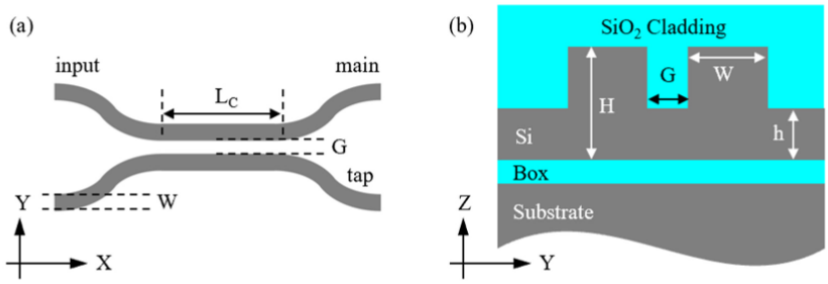

Figure 2.9. *(a) Top view of a conventional DC. (b) Cross-section of the coupling region of a conventional DC. Source: [25].*

with the operating wavelength, resulting in strong wavelength dependence, which is unfavorable for signal power tapping and monitoring applications. In the past two decades, researchers have made significant efforts in developing broadband DCs. Adiabatic directional couplers have demonstrated promising broadband operation, using tapered waveguides for achieving adiabatic transitions; however, they have the disadvantage of large footprints. Another approach involves the use of SWG structures to enhance the coupling strength and reduce device size while maintaining broadband operation. However, achieving this requires high fabrication accuracy to control the dimensions of waveguides. Additionally, broadband MZI-based couplers which integrate MZI structures into DCs still have challenges in terms of their larger footprints compared to conventional DCs on the same SiPh platform. Consequently, the development of DCs with broadband characteristics, low loss, and high fabrication tolerance continues to be a topic that requires further exploration [25].

Y-splitters The Y-branch is one of the most basic integrated optical devices. A conventional Y-branch structure is composed of an input waveguide and two branching output waveguides, as shown in Fig. 2.10. The two branching waveguides can either have the shape of a cosine arc or they can be straight waveguides with a certain branching angle. However, a Y-branch with cosine-arc branching waveguides has a more compact size as compared with the one with straight branching waveguides. The splitting ratio of a Y-branch can be engineered. Uniform power splitting can be achieved by using the longitudinal symmetric design of the y-branch. Any number of output power splitting ratio can be achieved through the asymmetric design of the branch.

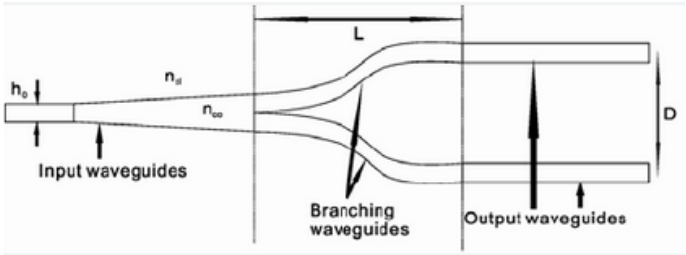

Figure 2.10. *Schematic diagram of a Y-branch power splitter. Source: [27].*

Y-branch splitters have the advantage that they are polarization and wavelength in-

dependent, i.e. one device can be used to split optical signals in the whole operating wavelength window. This is one of the main reasons why Y-branch splitters are broadly deployed. However, the main disadvantage of these components is that processing of the branching point, where the two waveguides start to separate, is very difficult to fabricate. This generally leads to an asymmetric splitting ratio causing non-uniformity of the split power over all the output waveguides, while causing important losses. The conventional Y-branch was found to suffer severe radiation loss when the branching angle is larger than 2°. To reduce the loss, the branching angle must be small and the length of splitter device must be extended, leading to devices with large foorprints. To date, several efforts have been made to overcome the loss problem, especially when the branching angle is large [28]. Special structures like SWG waveguide, photonic crystal waveguide, surface plasmon polaritons (SPPs) and 3D polymer structures can be combined with the traditional y-branch, to realize devices with very high efficienies, even close to 100% [27, 29].

MMI couplers MMI couplers are another type of couplers often used in PICs. Based on the self-imaging principle, MMI couplers offer the advantages of the compact size, low cross-talk, broadband operation and low power imbalance. Compared with other kinds of splitters, such as Y-branches and directional couplers, MMI couplers are superior in terms of relaxed fabrication requirements and scalability and have been widely used. However, they usually have large footprints. Several work has been done to develop high-performance MMI couplers based on the silicon nanowire waveguide [30, 31].

The operation principle of the MMI coupler is based on the self-imaging theory: self-imaging is a property of multimode waveguides by which an input field profile is reproduced in single or multiple images at periodic intervals along the propagation direction of the guide. For example, for a 1 by 2 MMI coupler, twofold images are needed. The central structure of an MMI device is a waveguide designed to support a large number of modes (typically more than 3). In order to launch light into and recover light from that multimode waveguide, a number of access (usually single-moded) waveguides are placed at its beginning and at its end. Such devices are generally referred to as N x M MMI couplers, where N and M are the number of input and output waveguides respectively [32]. An example of a 1 by 2 MMI is shown in Fig. 2.11

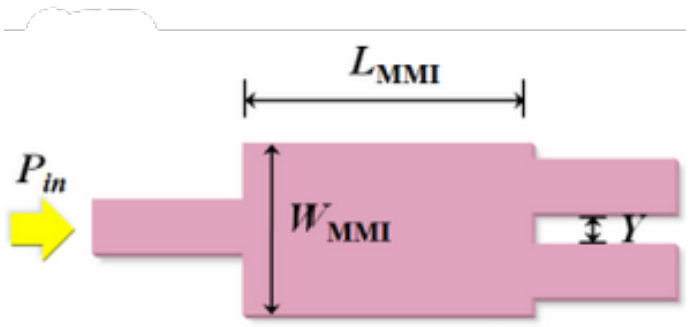

Figure 2.11. *Schematic diagram of a 1 by 2 MMI coupler. Source: [33].*

A typical MMI consists of the of a multimode waveguide section, where light can exist

in multiple modes simultaneously, and the input and output waveguides, that are usually designed to be single mode. The dimensions of the multimode waveguide, especially its length and width, along with the position of the input and output ports with regard to the MMI section, are critical in determining the interference pattern and, consequently, the power distribution among output ports. The number of input and output ports, as well as the output power splitting ratio can be engineered. Properly designed MMIs can achieve even power distribution among output ports, making them suitable for applications such as power splitters.

Polarization handling components

Polarization management is crucial in silicon photonics due to the anisotropic nature of silicon and its sensitivity to the polarization state of light. Silicon devices exhibit different refractive indices for TE and TM modes, due to the high birefringence of the Si waveguides, which introduces polarization-dependent effects. Strategies for polarization management, such as polarization-insensitive designs and polarization diversity circuits, are employed to mitigate these effects and ensure consistent and optimal device operation. This is particularly important in our application, were single mode TE operation is required, while interfacing the Si PICs with SMFs that do not maintain the polarization. Therefore, polarization diversity schemes need to be adopted to ensure constant power coupling in the Si PICs. The main SiPh components used for polarization management are the polarization splitters and rotators.

Polarization beam splitters A SiPh polarization beam splitter (PBS) is an optical device designed to separate the two orthogonal polarization states of light travelling in a waveguide, typically the TE and TM modes. Leveraging the inherent anisotropic properties of silicon, these devices exploit the birefringence of silicon waveguides to induce differential phase shifts or other polarization-dependent effects. This differential behavior leads to the efficient separation of TE and TM polarizations, directing them into distinct waveguide paths or output ports. Silicon photonics PBSs play a crucial role in managing polarization states within integrated photonic circuits, ensuring reliable operation of various optical components. They find applications in telecommunications, quantum optics, and optical sensing, contributing to the development of compact and efficient photonic devices in silicon-based technologies. Since a PBS is a basic functional element for all these applications when polarization control is desirable, many kinds of waveguide-type PBSs have been reported in different material platforms. Typically they employ various structures like MMIs, gratings, evanescent coupling structures, directional couplers, MZIs or photonic crystal (PhC) structures [34].

Fig. 2.12 illustrates two examples of PBS in the SiPh platform based on evanescent coupling structures. This approach is popular for PBS design because of its simplicity and easy design. Fig. 2.12a shows an asymmetrical PBS consisting of a SOI-nanowire and a nanoslot waveguide. The S-bend section of the nanoslot waveguide plays a role as a mode converter between the input/output SOI-nanowire and the nanoslot waveguide.

In the coupling region, these two waveguides are designed to satisfy the phase-matching condition for TM polarization so that it is completely coupled to the cross-port when choosing the length of the coupling region appropriately. On the other hand, the phase-matching condition is not satisfied for TE-polarized light and consequently it goes through the SOI-nanowire almost without coupling. Consequently, the TE and TM-polarized light are separated within a very short length [17]. Fig. 2.12b shows the schematic of a PBS which consists of a bent coupling section with two bending waveguides and an S-bend section with a sharp bend. The S-bend section is not only for decoupling the two bent waveguides, but also functions as a TE-passed polarization filter by choosing a small radius for which the TM polarization has a much higher loss than the TE polarization. The bent coupling section is designed to make the phase-matching condition satisfied for one polarization (e.g., TM) by choosing different core widths (w_1 and w_2) for the two bent waveguides and consequently a complete cross coupling occurs when choosing the length of the coupling region. For the other polarization (e.g. TE), there is almost no coupling since the phase-matching condition is not satisfied due to the strong waveguide birefringence [35].

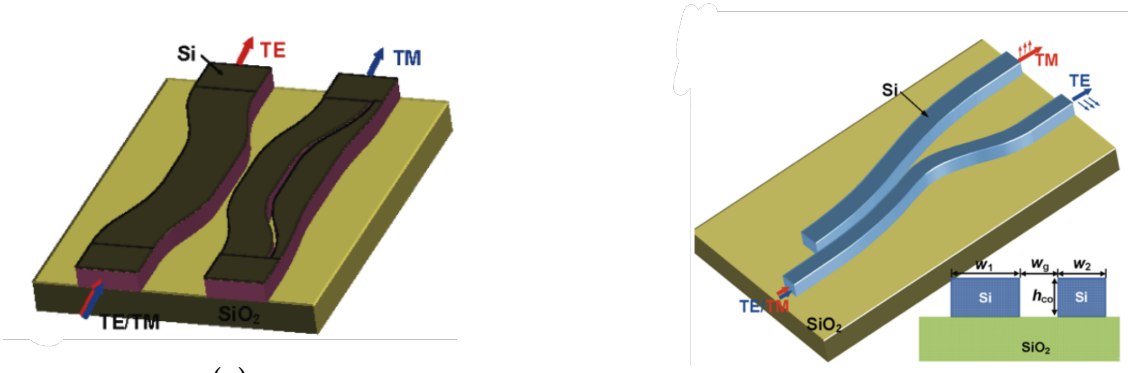

Figure 2.12. *(a) Schematic of a PBS based on an asymmetrical coupler consisting of a SOI-nanowire and a nanoslot waveguide. (b) The configuration of PBS based on a bent DC. Source: [34]*

Polarization rotators Apart from the PBSs, another key component to enable on-chip polarization diversity is the polarization rotator (PR). PRs are devices that can rotate the polarization axis of a light beam (direction in which the electric field vector is polarized) by a desired angle as shown in Fig. 2.13a. In contrast to PBSs, the realization of waveguide-type PRs is even more challenging because planar waveguides typically have a good ability to maintain polarization and therefore the rotation of the optical axis is a difficult task. Nevertheless, great efforts have been made to design PRs by introducing an asymmetry or anisotropy in the waveguide structure. This can be achieved with the use of slanted, slotted, triangular or asymmetric waveguides, waveguides with cut corners, double waveguide systems or multiple etch depths [36]. The combination of a PBS and a PR constitutes a complete solution for on-chip polarization management and is often adopted in applications that require polarization control, like coherent optical receivers,

data-centre transceivers and quantum photonics.

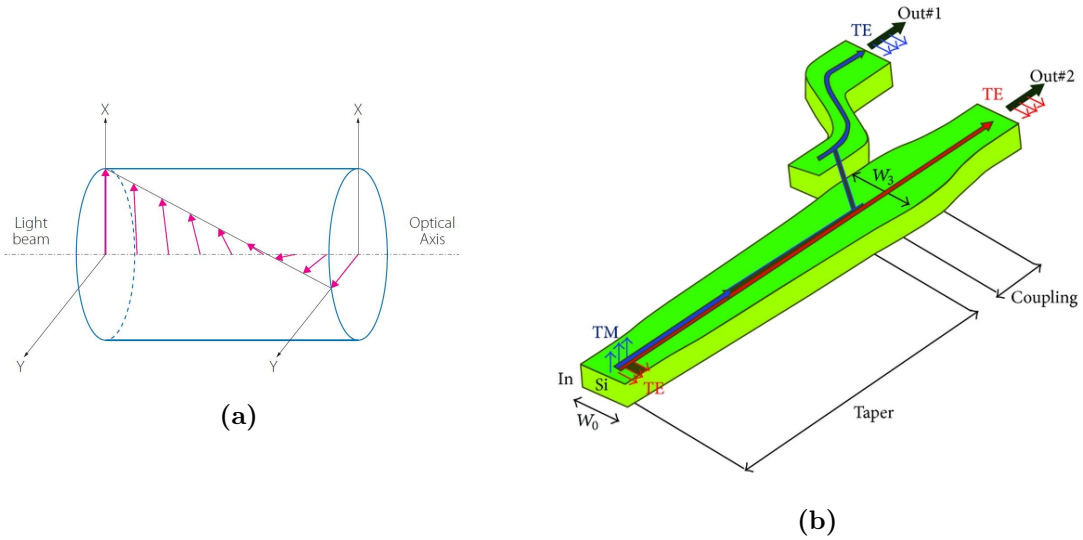

Figure 2.13. *(a) Schematic of a polarization rotator that rotates the optical axis of a light beam. Source [37] (b) Schematic of a Si polarization splitter-rotator. Source [38].*

Polarization splitter-rotators Alternatively, instead of the combination of a PBS and PR a single component can be employed for polarization control, namely a polarization splitter and rotator (PSR). PSRs combine polarization splitting and rotation simultaneously to realize ultra-compact on-chip polarization diversity circuits (see Fig. 2.13b). For a waveguide-type PSR, an asymmetrical cross-section shape is required to break the waveguide symmetry [1]. Many different types of PSR can be realized employing components like strip, rib or slot waveguide based asymmetric direction couplers (ADCs), sub-wavelength grating based ADCs, double etched ADCs, taper-etched ADCs, double-etched bent ADCs, tapers, bi-layer tapers, slanted waveguides, MMIs, Y-junctions or multiple materials (e.g. Si, SiN, air) [39–52]. The designs employing ADCs are usually compact in size but not very tolerant to fabrication imperfections and may require complex fabrication techniques like multiple etch-depths that are not compatible with deep ultra violet (DUV) lithography. On the other hand, the rest of the available components have different advantages and drawbacks. Structures based on tapers are tolerant but have high losses, while the ones based on MMIs, Y-junctions and slanted waveguides are efficient but have big footprints. In any case there is a trade-off between efficiency, size, fabrication complexity and tolerance to fabrication imperfections. Usually, a combination of methods is adopted to achieve better performance.

In general, PSRs as well as PBSs and PRs can be based on different principles of operation: mode coupling, mode conversion, mode evolution, or a combination of them. Mode coupling refers to the interaction or coupling between different modes of light within a waveguide or between waveguides. It occurs when there is a coupling mechanism that allows energy transfer or exchange between the modes. In a planar waveguide, multiple modes can exist, each representing a different spatial distribution of the electric field.

When these modes interact, they can exchange energy and influence each other's propagation characteristics. Mode coupling can occur due to structural variations or imperfections in the waveguide, such as bends, discontinuities, or perturbations. The coupling between modes can lead to phenomena such as mode conversion, where the energy of one mode is transferred to another, or mode dispersion, where the propagation characteristics of a mode change along the waveguide. Mode coupling is typically unwanted in many applications, as it can cause signal degradation or loss of information. However, it can also be intentionally engineered to achieve specific functionalities, such as mode polarization rotation in our application. Mode conversion, on the other hand, refers to the process in which the energy of a particular mode is transferred or transformed into another mode within the waveguide. It occurs when there is a coupling mechanism that allows energy transfer or exchange between different modes. Mode conversion can happen due to variations or perturbations in the waveguide structure or surrounding environment. It often occurs at interfaces or regions where the waveguide properties change abruptly. Mode conversion can result in the transfer of energy from one mode to another or the generation of new modes. It can lead to changes in the mode's spatial distribution, polarization, or propagation characteristics. While mode coupling and mode conversion can both involve energy transfer between different modes, they differ in the nature of the interaction. Mode coupling refers to the general interaction between modes, which can involve energy transfer, while mode conversion specifically refers to the transformation or transfer of energy from one mode to another. Mode coupling can occur without mode conversion if the energy exchange is between modes of similar properties, whereas mode conversion necessarily involves a change in mode properties. Mode evolution refers to the inherent changes that occur to a single mode as it propagates along the waveguide without any interaction with other modes. It describes how the properties of the mode itself, such as its spatial distribution, intensity profile, phase distribution, and polarization state, naturally change along the waveguide. Mode evolution can be influenced by factors such as the waveguide geometry, refractive index profile, or external perturbations. Examples of mode evolution include mode compression or expansion in tapered waveguides or mode dispersion due to changes in the propagation constant in waveguides with a varying refractive index. Each method has advantages and disadvantages and typically a component is based on a combination of them.

Filters

Among the passive SiPh components that have been developed, one of the most important elements is high-performance photonic filters, which are used for the spectrum manipulation in various optical systems. They play a key role especially in WDM circuits were multiplexing or demultiplexing of multiple wavelengths is required. Silicon-based on-chip WDM filters can be based on different structures, such as MZIs, micro-ring resonators (MRRs), waveguide Bragg gratings, arrayed-waveguide gratings (AWGs), and echelle diffraction gratings (EDGs) [53]. For most applications, silicon photonic filters are desired to have flat spectral response and be athermal so that they can work with little

influence from the temperature variation.

MZI based filters As a two-beam interferometer, an MZI has wavelength-dependent transmissions and can be used for wavelength filtering. An MZI comprises a power splitter, a power combiner and two arm-waveguides with a given length difference. A single-stage MZI based filter has a sine-like spectral response, making it non-ideal form most application that require flat responses. Nevertheless, flat-top spectral responses can be realized by using multiple cascaded MZIs. A filter based on cascaded MZIs is shown in Fig. 2.14. As it was previously analyzed, the large TOC of silicon makes MZI-based silicon photonic filters very sensitive to temperature variations, affecting their spectral response. Furthermore, the fact that the transmission is sensitive to the random wavelength shift of the dense WDM (DWDM) filters or the laser source is a big challenge for DWDM systems with narrow channel spacing. As a result, a complicated and expensive control for wavelength trimming or tuning is usually needed for silicon photonic devices used in the DWDM systems in practice, which could give rise to power consumption and cost. On the other hand, the coarse WDM (CWDM) technology with a large channel-spacing (e.g. 20 nm) has been a promising option, which greatly relaxes the critical requirement for the wavelength alignment of the laser source and the WDM filter, as well as the environment temperature control. Recently, MZIs-based silicon photonic filters have been developed for realizing the (de)multiplexers used in CWDM systems, that address the aforementioned challenges.

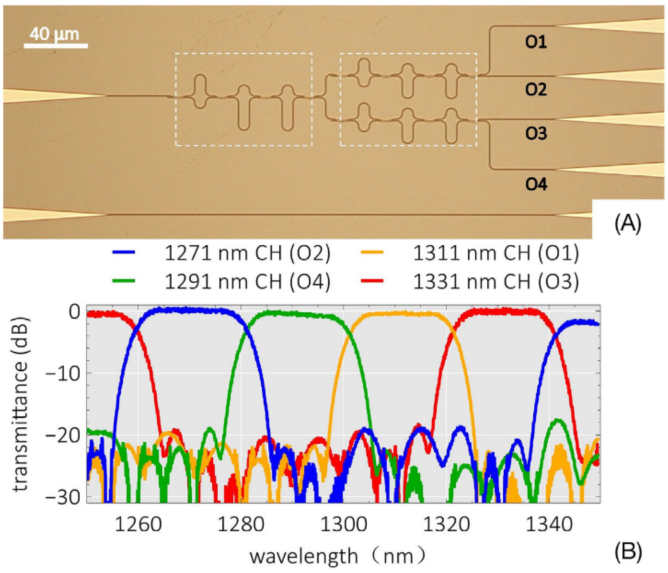

Figure 2.14. *(a) Microscope picture a four-channel CWDM filter based on multiple cascaded MZIs with bent directional couplers (DCs). (B) Measured spectral responses of the filter. Source: [54].*

Ring resonator based filters Ring resonators (RRs) have attracted lots of attention in the past decades due to their compact footprint and functional versatility. RRs can be applied as wavelength filters by utilizing their wavelength selectivity. An RR-based photonic filter is composed of an RR coupled to the input/output waveguide and the

add/drop waveguide. The spectral response of an RR is Lorentzian-like, which limits its applications for filtering. Fortunately, the response can be synthesized be using multiple rings (high-order RRs), or cascaded high order RRs. In order to obtain compact footprints, high integration density, and large free spectral range (FSR), it is desired to achieve RRs with a sharp bending radius. RRs reported tyically in literature usually have radii of 5-10 µm as a trade-off between the Q-factor and the FSR. Correspondingly the FSR is usually around 10 nm. Lots of works have been done to reduce the RR radius for increasing the FSR. Two examples of RR based filters with a flat-top response using different structures high-order RRs and cascading second-order RRs are shown in Fig. 2.15. However, such devices require thermal tuning for stable operation.

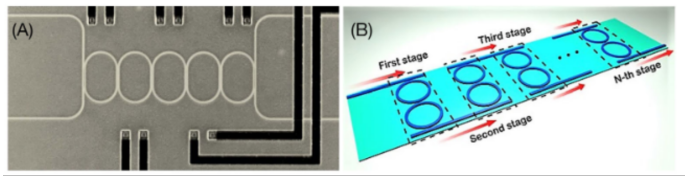

Figure 2.15. *Schematic configurations of the RR based filters with a flat-top response by using different structures, (A) high-order RRs (source: [55]) and (B) cascading second-order RRs (source: [56]).*

Bragg grating based filters A Bragg grating is a structure with a periodical modulation of the effective refractive index along the direction of propagation. This modulation can be realized by varying the refractive index of the material or the physical dimensions of the waveguide. Silicon photonic Bragg gratings can be implemented by physically corrugating the silicon core. Bragg-grating photonic filters have been attractive due to the flat-top spectral responses, the flexible wavelength selectivity, and ultra-large FSRs. For traditional Bragg-grating filters, there are usually only two ports available (i.e. input/reflection and through). Therefore, circulators are usually needed for separating the reflected light from the input port, which makes the system very complicated. In order to solve this problem, a promising approach is developing add-drop photonic filters with four ports (i.e. input, through, drop and add) by introducing some other waveguide structures. An example of a silicon-based four-channel CWDM (de)multiplexer with 18 nm channel spacing is shown in Fig. 2.16. It is composed of four cascaded optical filters with flat-top spectral responses. Although these type of filters offer many advantages they require thermal tuning for stable operation.

AWG based filters As the most well-known wavelength-division-(de)multiplexer, AWGs have been commercialized for many years. Usually, an AWG is composed of two free propagation regions (FPRs) connected with arrayed waveguides which have constant length difference. With SOI nanophotonic waveguides, which have an ultra-high index-contrast, the footprints of the AWGs have been significantly decreased from several cm^2 to about 0.1 mm^2 or less. However, it is still desired to further minimize the AWG footprint to achieve high integration density and reduce the phase errors due to the non-uniformity

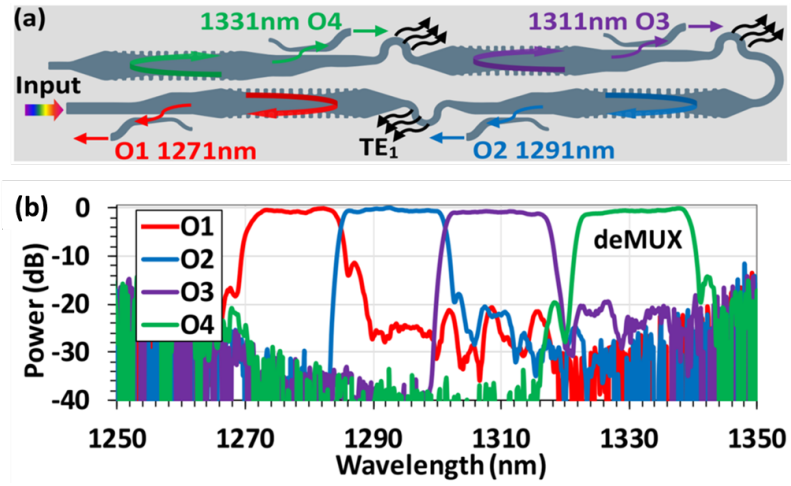

Figure 2.16. *(a) Schematic configuration of the silicon-based four-channel CWDM (de)multiplexer working in the O-band proposed by [53], with* 18 nm *channel spacing. It is composed of four cascaded optical filters with flat-top spectral responses, which are realized by combining an multimode waveguide grating and a two channel mode (de)multiplexer. (b) The measured spectral response of the fabricated CWDM filter as a demultiplexer.*

in a large area. For this sake, some solutions have been reported, including bi-directional AWGs and reflective AWGs.

Thermo-optic phase shifters

Phase shifters in SiPh are usually implemented as heaters and exploit the thermo-optic effect [57]. Resistive heaters for thermo-optic control of silicon waveguides have already been demonstrated in many variations: resistors in doped silicon, Ni-silicide, and Tungsten (W) wiring. These different types of resistive heaters are supported by the same silicon photonics technology platform. The heaters have different line resistivities, making it possible to build heaters with very different dimensions that can still be directly driven from a low-voltage CMOS circuit. Heater efficiency is mainly determined by the phase that can be induced in the waveguide for a certain amount of dissipated electrical power. This is expressed in power (in mW) needed for a π phase shift. As a resistor converts all electrical power into heat, the efficiency of a thermo-optic tuner will be largely determined by the thermal environment: how much heat is transferred to the waveguide, and how much leaks to the surrounding. To minimize unwanted leakage of heat, it is possible to add thermal insulation trenches, including an undercut of the silicon substrate [58].

In a CMOS-like silicon photonics process different materials can be used for heaters. This is schematically depicted in Fig. 2.17. A resistor can be made in in doped silicon, positioned next to the waveguide, or alternatively in a silicide line. For lower line resistivities, metals can be used. Because the heater lines should have a higher resistivity than the copper metallization, W lines are used above the waveguide, which makes them suitable in situations where no space is available next to the waveguide. An alternative is using the waveguide itself as a resistor, by lightly doping it, but this will induce additional loss in the waveguide.

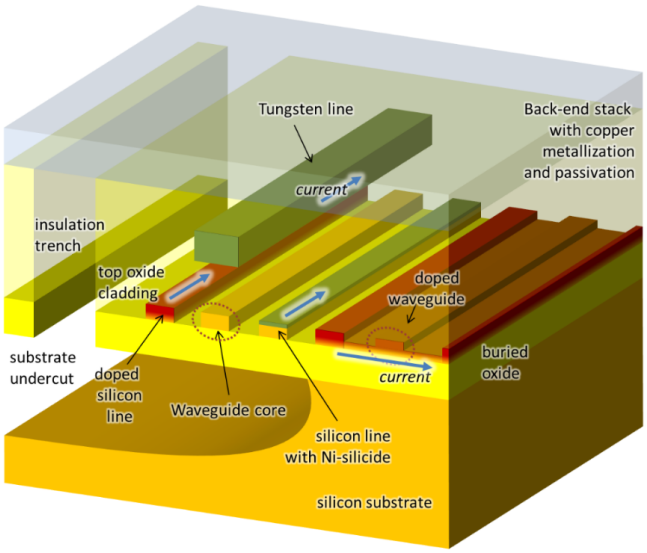

Figure 2.17. *Different heater architectures in the SiPh platform. Source: [58].*

The performance of the different heater types is reported in Fig. 2.18. The efficiencies of the different heaters are comparable and around 21 mW/π. However it can be observed that the Tungsten heaters have much lower line resistivity, meaning that to reach the same heating power they require much lower operation voltages compared to doped silicon heaters. This is very important for our application where the maximum voltage supplies that can be achieved in the FE is low, therefore W heaters are preferred in this regard. The W heaters are also preferred for the thermal tuning of the ring modulators, where there is no space for placing doped silicon heaters at the sides of the ring shaped waveguide. It is however possible to integrate the W heaters on top of the ring waveguide.

HEATER PERFORMANCE COMPARISON

Heater type	Efficiency [mW/π]	Line Resistivity [$\Omega/\mu m$]	Heating τ $1/e$ [μs]	Cooling τ $1/e$ [μs]
Without Insulation				
Doped silicon	20.4	293	21.3	66.0
Silicide	22.5	27.3	19.1	75.8
Tungsten	23.4	1.1	38.2	45.11
Doped waveguide	21.9	N/A*	43.4	39.8
With Insulation				
Doped silicon	1.42	317	151	217
Silicide	1.49	28.0	188	218
Tungsten	1.42	1.3	198	227
Doped waveguide	1.30	N/A*	236	156

* in-waveguide heaters have a line conductivity

Figure 2.18. *Comparison of the performance of the different heater types. Source: [58].*

2.2.2 Active components

Active silicon photonic devices play critical roles in future silicon photonic integrated circuits including light emitting devices, optical modulators and detectors. Generally speaking, in order to integrate active functions into a passive device system, it is nec-

essary to dope the silicon waveguide with either donor or acceptor ions. In this process, free carriers are introduced in the silicon material. By changing the concentration of these free carriers, modulation of the optical signal can be achieved exploiting the plasma dispersion effect. In a similar manner, epitaxy and doping of Ge on the Si allows for the formation of pin germanium photodetectors. [59].

Modulators

As was already described in Section 2.1.2, optical modulation in photonic circuits is implemented by devices that cause direct changes in optical intensity via absorption, or cause changes in the refractive index of the material (and hence the phase of a propagating wave), which can be converted to an intensity change via an interferometer or a resonant device. Such refractive index changes are typically produced via an applied electrical signal, thanks to the plasma dispersion effect [60, 61]. Here, we will introduce the main types of electro-optical modulators employed in SiPh.

Main performance parameters of optical modulator include switching speed, modulation efficiency and insertion loss in which absorption loss takes a large part. As the high additional loss of general PN junction modulator mainly comes from the free carriers' absorption in the doped regions.

Mach-Zehnder Modulators Mach-Zehnder Modulators (MZMs) are a common type of optical modulator. MZMs are based on the original concept of a MZI, which relies on separating light into two optical paths at some form of input coupler. The light travelling in one or both of these pathways can then have its phase modulated before the paths recombine and interference occurs. Depending on the interference condition, that can vary between fully constructive and fully destructive interference, the amplitude of the output light is defined. This way the phase modulation on the MZM arms is translated to amplitude modulation at the MZM output. Fully constructive interference corresponds to the one level of the transmission, while fully destructive interference corresponds to the zero level. In the case of most semiconductors, the pathway arms of the MZM are equipped with phase modulators relying on a driving voltage to achieve the required phase shift [62].

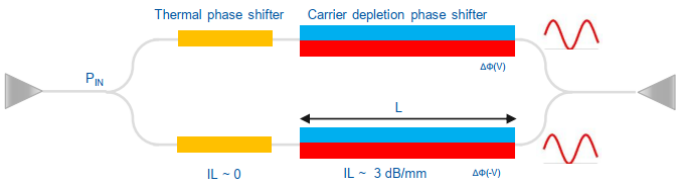

Figure 2.19. *Schematic diagram of a Mach-Zehnder modulator.*

MZMs can be noted for their high-contrast optical transmission without deterioration due to spectral broadening and frequency chirping. In silicon photonics the monolothic integration of MZMs with other photonic components such as photodiodes is achievable with fabrication technologies to create integrated devices with small footprints. In silicon MZMs the method of modulation relies on high speed refractive index modulation via free

carrier plasma dispersion effect, or the carrier-refraction effect. Silicon optical modulators based on the plasma dispersion effects typically use a PIN or PN diode structure across the optical waveguide to alter the density of free carriers available to interact with light within the guide. Alternatively, demonstrations have been made which use the accumulation of free carriers around a thin dielectric layer in the waveguide. PN junction based MZM modulators benefit from simple fabrication and high-speed performance but lack the modulation efficiency of the carrier injection and accumulation techniques.

A schematic diagram of the MZM designed within the CERN project CERN is shown in Fig. 2.19. This device includes carrier depletion phase shifters based on PN junctions formed around the MZM arm waveguide, for the high speed driving of the RMs. At the same time, the device is equipped with thermal phase shifters. This is required to compensate for any unbalance between the two arms that can be induced by manufacturing tolerances, while also controlling the operational point of the MZM. The design shown in Fig. 2.19 is a balanced MZM, but it is also possible to have unbalanced MZMs, where a difference in the optical path between the two arms is induced by design. In our PIC, the included MZM designs have modulation efficiency of $1.6\,\mathrm{V\,cm^{-1}}$. However, these modulators require relatively high modulation voltages of at least 6 V in reverse bias, which is not compatible with the available voltage levels in the FE of the final systems. At the same time, the are much larger devices compared to the RMs that will be presented next, therefore in this thesis we have chosen to work with RMs.

Ring Modulators Ring resonators have played a very prevalent role in the field of silicon modulators. In general, a ring resonator consists of a closed loop optical waveguide, which creates a resonant condition for wavelengths which are a whole number of the optical path length. Typically, there are many wavelengths which satisfy this condition which leads to a ring having multiple resonances. The spacing between these resonances is dependent on the length of the ring resonator and is referred to as the FSR, which is commonly expressed in GHz or nm.

A ring resonator is only useful when light can be coupled in and out of the resonant cavity. The most common method of coupling is co-directional evanescent coupling between the ring and an adjacent waveguide, as shown in Fig. 2.20(a). A resonator is a passive device but a ring can also be used as an active device such as a modulator. By doping the Si, a PN junction can be formed around the ring. This is illustrated in Fig. 2.20(b) that shows a cross-section of the ring waveguide with the different doping regions that form the PN junction. This converts the ring resonator to an active device, a ring modulator, that can modulate the optical input data with a high-speed modulation voltage V_{mod} (the electrical data). In a ring modulator (RM) the resonator is made to align the operating wavelength with the resonance peak. In this way, modulating the optical path length of the ring shifts the resonance peak. This phenomenon is illustrated in Figure Fig. 2.20(c). High speed modulation has been demonstrated many times over with ring resonators via shifting the carrier density of the material, changing the refractive index, and therefore the resonance wavelength through the application of an external voltage to the device's PN junction.

In operation, the primary benefits of the RM are its small footprint, low power consumption, and narrow wavelength selectivity. The challenges of silicon RMs stems from silicon's third order non linearity, which generates nonlinear effects, resulting in carrier and thermal induced optical bistabilities and self pulsation from these phenomena acting in competition to each other [62].

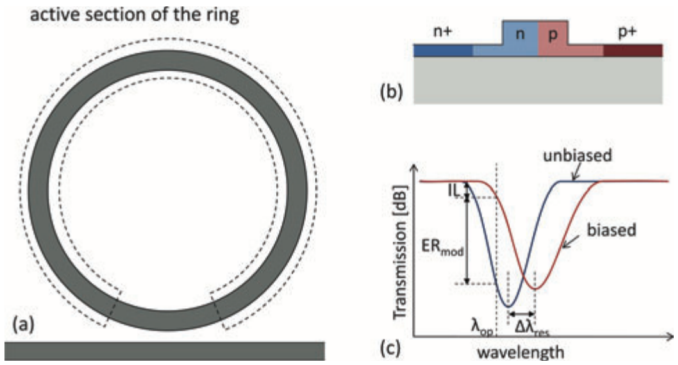

Figure 2.20. *Ring modulator schematic with (a) Top down view showing the ring and the coupling waveguide (b) the diode embedded in the cross section (c) The effect biasing has on the transmission of the ring. Source: [63].*

When using ring resonators, the most commonly explored configuration is a single all-pass filter close to critical coupling. In this configuration, there is a strong dip in the transmission spectrum of the bus wave-guide, which means that a large modulation depth extinction ratio (ER) can be achieved with a relatively small shift of the ring's resonance frequency. The modulation is more efficient as the slope of the resonance is steeper, i. e. when the ring has a higher Q and finesse. Also, it is best to operate the modulator in the linear regime, where the slope of the resonance is close to a straight line. However, this implicates a penalty in modulation depth, and also introduces a certain insertion loss (IL). At higher Q, light is trapped in the ring for a longer time, and this will eventually limit the modulation speed of the ring. For fast modulators, rings with a Q of 5000–25000 are typically used.

The modulation of the effective index in the ring can be done with different mechanisms. The temperature can be used to this effect, but due to the relatively large time constants (some µs) this is not a suit-able technique for fast signals. The most commonly used technique relies on manipulating the carrier density in the ring, by exploiting the plasma dispersion effect. According to the plasma dispersion effect, the concentration of the free carriers in Si affects the real and imaginary parts of the refractive index of the material [6,61]. A change of the refractive index of the RM waveguide will in turn induce a change of the RM resonant wavelength (λ_{res}), and a consequent variation of the output optical power at the RM through port, given that the RM is always operated at a fixed wavelength. In total, when a voltage is applied to the PN junction of the RM, its refractive index will change leading to an amplitude modulation of its optical output signal. This is illustrated in Fig. 2.21. Given that the operational wavelength of the external laser source is fixed (denoted with λ_{laser} in Fig. 2.21), when the V_{mod} alternates between two different values (0 V and −5 V in this example), the λ_{res} and transmission of the RM changes and the

power at the through port of the RM will also alternate between two different levels, denoted with P_1 and P_0. These correspond to the one and zero levels of the transmission. Hence, amplitude modulation of the continuous wave (CW) optical input is achieved.

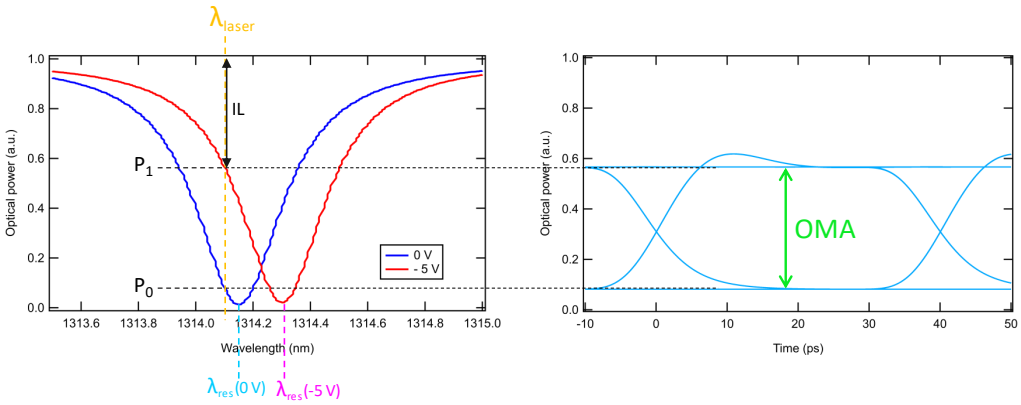

Figure 2.21. *Left: the transmission of an RM for two different modulation volatges (V_{mod}) values of* 0 V *and* −5 V*. For operation at λ_{laser} this corresponds to two different power levels at the RM through port, denoted with P_1 and P_0. These correspond to the one and zero levels of the transmission. A schematic of the corresponding eye diagram is shown as the right side of the figure.*

The most efficient mechanism in terms of magnitude, to achieve modulation through the plasma dispersion effect, is carrier injection in a PIN diode: The intrinsic zone is located in the waveguide core. By forward biasing the diode, majority carriers are forced into the core, strongly affecting the refractive index. However, this mechanism is limited in operation speed by the recombination time of the carriers in the core (some ns). Better, one can start with a PN diode in the core, which can be reverse-biased to increase or decrease the depletion zone in the junction. Because the effect moves around much less carriers, the effect is weaker, but it is also potentially much faster, as it is not limited by recombination times, but rather by the capacitance of the junction and the carrier saturation velocity. Manipulating the carrier density in the ring will not only result in a modulation of the effective index, but also of the absorption. This, in turn, will have an effect on the Q of the ring. When injecting more carriers, the Q will decrease, and thus also the slope of the resonance. In addition, changing the Q will also move the ring away from critical coupling, potentially reducing the achievable modulation depth.

An advantage of ring resonators for modulation is that they are quite compact and can be actuated directly as a lumped element, even at high speeds (10–25 GHz). Also, the relatively small area limits the necessary power to modulate. Therefore, ring modulators currently hold the best track record in terms of modulation energy per bit. However, it is essential that the edge of the transmission dip is spectrally aligned with the operating wavelength of the source. This will require good process control, but ultimately a tuning mechanism to compensate for external influences, such as thermal variations. The modulator could be tuned by applying a bias to the modulation voltage, but as the modulation effects are typically quite small, in most cases the tuning range will be too small. Adding thermal tuning will help, but it can only be used in one direction (heating not cooling). This

means that, to compensate for thermal fluctuations in the chip, the operating temperature must be set near the upper boundary of the operation specs. This means continuous heating is required, which translates in an additional power consumption, negating partially the low energy consumption of the ring modulator. In addition to the spectral alignment requirements, the phase response of the modulated ring resonator can induce chirp in the signal if the signal bandwidth occupies a significant fraction of the ring linewidth [63].

Photodetectors

Photodetectors are devices that convert an optical signal into an electronic form. The working process is the following: the photodetector absorbs the incident photons, generating free electron-hole pairs which are then swept to the electrodes by an electric field. The output is an electrical current, or photocurrent. In order to generate electron-hole pairs, the energy of incident photons must be equal to or greater than that of the bandgap. One of the most important parameters that characterizes the performance of a photodetector is the responsivity, bandwidth, dark current and operation voltage. Responsivity is wavelength dependent and can be calculated by the ratio of the generated photocurrent to the total incident optical power. Dark current refers to the electric current that flows through the device in the absence of incident light. It is essentially the current generated by thermally generated carriers within the detector even when no optical signal is present. Dark current can be a critical parameter in determining the performance of a photodetector, especially in low-light conditions, and it should be as low as possible. Ideally, a photodetector can respond to a fast-modulated optical signal with a low operation voltage. Based on their physical structures, silicon photodetectors are classified into three categories: Schottky metal-semiconductor-metal (MSM), PIN, and avalanche photodiodes. A MSM photodetector consists of two back-to-back Schottky diodes with two metallic electrodes on a semiconductor material. When light irradiates on the semiconductor between the metallic electrodes, it generates electron–hole pairs, which are then swept by the electric field and thus forming a photocurrent. The Schottky barriers at the metal-semiconductor interfaces of the electrodes limit the dark current. A PIN photodiode comprises an intrinsic silicon region, sandwiched between an n- and a p-doped region. When the photodiode is illuminated with photon energy greater than or equal to the bandgap of the semiconductor material, the photons are absorbed, and electron-hole pairs are generated. By applying an external reverse bias, a depleted region is formed. This results in the entire voltage drop on the depleted region and thus a high electric field, facilitating the collection of the photo-generated electron-hole pairs. Due to this high electric field, the photo-generated carriers travel at their saturation velocity. This PIN structure is particularly important in designing photodetectors for silicon photonics as it can easily meet the high-speed demand in the range of tens of GHz. Compared to the PIN photodiodes, avalanche photodiodes (APDs) have a PN junction with an internal depletion region where electron multiplication occurs with a relatively high external reverse voltage. The electron multiplication process results in an amplified output signal, making the APDs well suited for detecting low light levels at high speed. Due to the material transparency at the communication

wavelength range, optical detection on the silicon platform requires the incorporation of other active materials. Group III–V materials and germanium have been commonly used to assist silicon platform for detection at wavelengths ranging from 1300 to 1500 nm [64].

Germanium Photodiodes Although III–V detectors are efficient for detection at the communication wavelength range, low-loss integration to the silicon platform still remains a challenge due to the intrinsic lattice mismatch between the materials. An enormous amount of research has been directed towards the implementation of monolithic integration of photodetectors on silicon. Ge, a Group IV element, has similar properties to silicon, but with a small energy bandgap (0.7 eV versus Si's 1.1 eV). Ge and SiGe alloys exhibit strong photon absorption in the entire communication wavelength range, up to 1.7 µm. Another benefit of using Ge is that it is highly compatible with Si CMOS processes, thus allowing monolithic integration of Ge/SiGe photodetectors on Si PICs, at low cost [64]. In silicon photonics, the vertical Ge photodetector is the most straightforward design as shown in Fig. 2.22(a), which is widely used and shows promising device performance. Another widely studied Ge PIN photodetector design is based on a lateral PIN configuration with both anode and cathode metal contacts on Si, as shown in Fig. 2.22(a)(b). Although metal contacts can be made on Ge to form anther type of lateral PIN configuration as shown in Fig. 2.22(a)(c), it will introduce a large responsivity loss and increases the process flow complexity as well [65].

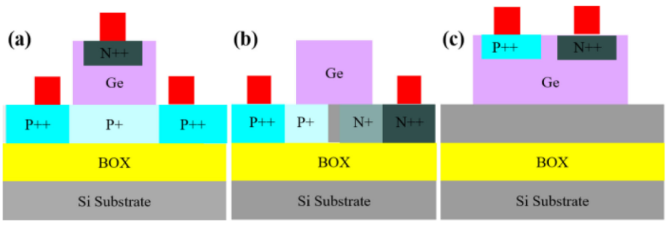

Figure 2.22. *(a) Vertical Ge PIN photodetector. (b) Lateral Ge PIN photodetector. (c) Variant of lateral PIN photodetector. Source: [65]*

For the vertical Ge photodetector, responsivities as high as 1.12 A W^{-1} at −1 V have been reported in literature, with bandwidth of 25 GHz at −1 V. Concerning the lateral Ge photodetector, responsivities of about 0.8 A W^{-1} at −1 V have been reported, while the bandwidth can easily reach 31 GHz at −1 V, which then quickly ramps up to over 40 GHz at −5 V. This indicates a notable increase in the response speed with a higher reverse bias. The dark current is well controlled for both vertical and lateral Ge photodetectors. Particularly, dark current lower than 10 nA at −3 V has been reported for lateral Ge photodetector [65].

Bibliography

[1] Y. Su, Y. Zhang, C. Qiu, X. Guo, and L. Sun, "Silicon photonic platform for passive waveguide devices: Materials, fabrication, and applications," *Advanced Materials Technologies*, vol. 5, no. 8, p. 1901153, 2020.

[2] W. Yang, J. Chen, Y. Zhang, Y. Zhang, J.-H. He, and X. Fang, "Silicon-compatible photodetectors: trends to monolithically integrate photosensors with chip technology," *Advanced Functional Materials*, vol. 29, no. 18, p. 1808182, 2019.

[3] Y. Ishikawa, J. Osaka, and K. Wada, "Germanium photodetectors in silicon photonics," in *2009 IEEE LEOS Annual Meeting Conference Proceedings*, pp. 367–368, 2009.

[4] M. J. Deen and P. K. Basu, *Silicon photonics: fundamentals and devices*. John Wiley and Sons, 2012.

[5] B. Bennett and R. Soref, "Electrorefraction and electroabsorption in inp, gaas, gasb, inas, and insb," *IEEE Journal of Quantum Electronics*, vol. 23, no. 12, pp. 2159–2166, 1987.

[6] R. Soref and B. Bennett, "Electrooptical effects in silicon," *IEEE journal of quantum electronics*, vol. 23, no. 1, pp. 123–129, 1987.

[7] G. T. Reed and C. Jason Png, "Silicon optical modulators," *Materials Today*, vol. 8, no. 1, pp. 40–50, 2005.

[8] X. Sang, E.-K. Tien, and O. Boyraz, "Applications of two photon absorption in silicon," *Journal of optoelectronics and advanced materials*, vol. 11, no. 1, p. 15, 2009.

[9] G. Cocorullo, F. G. Della Corte, I. Rendina, and P. M. Sarro, "Thermo-optic effect exploitation in silicon microstructures," *Sensors and Actuators A: Physical*, vol. 71, no. 1, pp. 19–26, 1998.

[10] S. Itabashi, K. Yamada, H. Fukuda, T. Tsuchizawa, T. Watanabe, H. Shinojima, H. Nishi, R. Takahashi, Y. Ishikawa, and K. Wada, "Silicon photonics devices based on soi structures," *ECS Transactions*, vol. 35, p. 227, apr 2011.

[11] "SOI wafer." Accessed: 16/10/2023.

[12] A. Rigny, "Silicon-on-Insulator Substrates: The Basis of Silicon Photonics," March 2018. Accessed: 20/10/2023.

[13] SOITEC SOI, "Soi wafers to fabricate photonic devices." Accessed: 20/10/2023.

[14] N. Eti and H. Kurt, "Model analysis of ridge and rib types of silicon waveguides with void compositions," *IEEE Journal of Quantum Electronics*, vol. 52, no. 10, pp. 1–7, 2016.

[15] Y. Su, Y. Zhang, C. Qiu, X. Guo, and L. Sun, "Silicon photonic platform for passive waveguide devices: Materials, fabrication, and applications," *Advanced Materials Technologies*, vol. 5, no. 8, p. 1901153, 2020.

[16] C. G. Littlejohns, D. J. Rowe, H. Du, K. Li, W. Zhang, W. Cao, T. Dominguez Bucio, X. Yan, M. Banakar, D. Tran, S. Liu, F. Meng, B. Chen, Y. Qi, X. Chen, M. Nedeljkovic, L. Mastronardi, R. Maharjan, S. Bohora, A. Dhakal, I. Crowe, A. Khurana, K. C. Balram, L. Zagaglia, F. Floris, P. O'Brien, E. Di Gaetano, H. M. Chong,

F. Y. Gardes, D. J. Thomson, G. Z. Mashanovich, M. Sorel, and G. T. Reed, "Cornerstone's silicon photonics rapid prototyping platforms: Current status and future outlook," *Applied Sciences*, vol. 10, no. 22, 2020.

[17] D. Dai, Z. Wang, and J. E. Bowers, "Ultrashort broadband polarization beam splitter based on an asymmetrical directional coupler," *Opt. Lett.*, vol. 36, pp. 2590–2592, Jul 2011.

[18] Ansys, "Lumerical fde solver." Accessed: 20/11/2023.

[19] Ansys, "Lumerical fdtd solver." Accessed: 20/11/2023.

[20] L. Cheng, S. Mao, Z. Li, Y. Han, and H. Y. Fu, "Grating couplers on silicon photonics: Design principles, emerging trends and practical issues," *Micromachines*, vol. 11, no. 7, 2020.

[21] R. Marchetti, C. Lacava, L. Carroll, K. Gradkowski, and P. Minzioni, "Coupling strategies for silicon photonics integrated chips," *Photon. Res.*, vol. 7, pp. 201–239, Feb 2019.

[22] T. Watanabe, Y. Fedoryshyn, and J. Leuthold, "2-d grating couplers for vertical fiber coupling in two polarizations," *IEEE Photonics Journal*, vol. 11, no. 4, pp. 1–9, 2019.

[23] R. Marchetti, C. Lacava, L. Carroll, K. Gradkowski, and P. Minzioni, "Coupling strategies for silicon photonics integrated chips," *Photonics Research*, vol. 7, no. 2, pp. 201–239, 2019.

[24] X. Mu, S. Wu, L. Cheng, and H. Fu, "Edge couplers in silicon photonic integrated circuits: A review," *Applied Sciences*, vol. 10, no. 4, 2020.

[25] D. Lv, L. Wu, C. Liu, A. Li, R. Wang, and A. Wu, "Broadband and low-loss silicon photonic directional coupler for signal power tapping on the 3 mu;m soi waveguide platform," *Photonics*, vol. 10, no. 7, 2023.

[26] Z. Lu, H. Yun, Y. Wang, Z. Chen, F. Zhang, N. A. F. Jaeger, and L. Chrostowski, "Broadband silicon photonic directional coupler using asymmetric-waveguide based phase control," *Opt. Express*, vol. 23, pp. 3795–3808, Feb 2015.

[27] Y. Xu, Z. Tian, X. Meng, and Z. Chai, "Methods and applications of on-chip beam splitting: A review," *Frontiers in Physics*, vol. 10, 2022.

[28] P. Wang, G. Brambilla, Y. Semenova, Q. Wu, and G. Farrell, "Design of an extra-low-loss broadband y-branch waveguide splitter based on a tapered mmi structure," *Progress in Electromagnetics Research Symposium*, 01 2011.

[29] C. Burtscher, D. Seyringer, A. Kuzma, and M. Lucki, "Modeling and optimization of 1× 32 y-branch splitter for optical transmission systems," *Optical and Quantum Electronics*, vol. 49, pp. 1–12, 2017.

[30] Z. Sheng, Z. Wang, C. Qiu, L. Li, A. Pang, A. Wu, X. Wang, S. Zou, and F. Gan, "A compact and low-loss mmi coupler fabricated with cmos technology," *IEEE Photonics Journal*, vol. 4, no. 6, pp. 2272–2277, 2012.

[31] A. Z. Chowdhury, "Performance study of silica-on-silicon based multimode interference (mmi) optical coupler," *Photonic Sensors*, vol. 4, pp. 34–42, 2014.

[32] L. Soldano and E. Pennings, "Optical multi-mode interference devices based on self-imaging: principles and applications," *Journal of Lightwave Technology*, vol. 13, no. 4, pp. 615–627, 1995.

[33] J. Lee, Y. Yamahara, Y. Atsumi, T. Shindo, T. Amemiya, N. Nishiyama, and S. Arai, "Compact inp-based 1×2 mmi splitter on si substrate with bcb wafer bonding for membrane photonic circuits," *2012 International Conference on Indium Phosphide and Related Materials*, pp. 8–11, 2012.

[34] D. Dai, L. Liu, S. Gao, D.-X. Xu, and S. He, "Polarization management for silicon photonic integrated circuits," *Laser and Photonics Reviews*, vol. 7, no. 3, pp. 303–328, 2013.

[35] D. Dai and J. E. Bowers, "Novel ultra-short and ultra-broadband polarization beam splitter based on a bent directional coupler," *Opt. Express*, vol. 19, pp. 18614–18620, Sep 2011.

[36] G. Poulopoulos, D. Kalavrouziotis, J. Missinne, E. Bosman, G. Van Steenberge, D. Apostolopoulos, and H. Avramopoulos, "Integrated polymer polarization rotator based on tilted laser ablation," in *Integrated Optics: Devices, Materials, and Technologies XXI*, vol. 10106, pp. 62–72, SPIE, 2017.

[37] I. Laserand, "Polarization rotator." https://laserand.com/optics/polarization-optics/other-products/polarization-rotator/ [Accessed: (02/06/2023)].

[38] B. Troia, F. De Leonardis, M. Lanzafame, T. Muciaccia, G. Grasso, G. Giannoccaro, C. E. Campanella, and V. Passaro, "Design and optimization of polarization splitting and rotating devices in silicon-on-insulator technology.," *Advances in Optoelectronics*, 2014.

[39] Y. Ma, Y. Liu, H. Guan, A. Gazman, Q. Li, R. Ding, Y. Li, K. Bergman, T. Baehr-Jones, and M. Hochberg, "Symmetrical polarization splitter/rotator design and application in a polarization insensitive wdm receiver," *Optics express*, vol. 23, no. 12, pp. 16052–16062, 2015.

[40] Y. Yin, Z. Li, and D. Dai, "Ultra-broadband polarization splitter-rotator based on the mode evolution in a dual-core adiabatic taper," *Journal of Lightwave Technology*, vol. 35, no. 11, pp. 2227–2233, 2017.

[41] W. Chang, S. Xu, M. Cheng, D. Liu, and M. Zhang, "Inverse design of a single-step-etched ultracompact silicon polarization rotator," *Optics Express*, vol. 28, no. 19, pp. 28343–28351, 2020.

[42] J. Wang, B. Niu, Z. Sheng, A. Wu, X. Wang, S. Zou, M. Qi, and F. Gan, "Design of a sio 2 top-cladding and compact polarization splitter-rotator based on a rib directional coupler," *Optics express*, vol. 22, no. 4, pp. 4137–4143, 2014.

[43] Z. Hui, T. Zhang, M. Zhang, D. Pan, D. Han, and A.-H. Soliman, "Inverse asymmetrical ridge taper polarization splitter–rotatorcovering optical fiber communication band from o to u," *Optics Communications*, vol. 495, p. 127107, 2021.

[44] H. Guan, A. Novack, M. Streshinsky, R. Shi, Y. Liu, Q. Fang, A. E.-J. Lim, G.-Q. Lo, T. Baehr-Jones, and M. Hochberg, "High-efficiency low-crosstalk 1310-nm polarization splitter and rotator," *IEEE Photonics Technology Letters*, vol. 26, no. 9, pp. 925–928, 2014.

[45] K. Tan, Y. Huang, G.-Q. Lo, C. Yu, and C. Lee, "Experimental realization of an o-band compact polarization splitter and rotator," *Optics express*, vol. 25, no. 4, pp. 3234–3241, 2017.

[46] G. B. De Farias, Y. R. Buscamante, H. A. De Andrade, and U. Moura, "Demonstration of a low-loss and broadband polarization splitter-rotator with a polysilicon waveguide in soi platform," in *2019 SBFoton International Optics and Photonics Conference (SBFoton IOPC)*, pp. 1–5, IEEE, 2019.

[47] K. Yu, L. Wang, W. Wu, Y. Luo, and Y. Yu, "Demonstration of an on-chip broadband polarization splitter and rotator using counter-tapered coupler," *Optics Communications*, vol. 431, pp. 58–62, 2019.

[48] Y. Xiong, D.-X. Xu, J. H. Schmid, P. Cheben, S. Janz, and N. Y. Winnie, "Fabrication tolerant and broadband polarization splitter and rotator based on a taper-etched directional coupler," *Optics express*, vol. 22, no. 14, pp. 17458–17465, 2014.

[49] C. Sun, Y. Yu, G. Chen, and X. Zhang, "A low crosstalk and broadband polarization rotator and splitter based on adiabatic couplers," *IEEE Photonics Technology Letters*, vol. 28, no. 20, pp. 2253–2256, 2016.

[50] K. Tan, Y. Huang, G.-Q. Lo, C. Lee, and C. Yu, "Compact highly-efficient polarization splitter and rotator based on 90° bends," *Optics Express*, vol. 24, no. 13, pp. 14506–14512, 2016.

[51] D. Dai and J. E. Bowers, "Novel concept for ultracompact polarization splitter-rotator based on silicon nanowires," *Optics express*, vol. 19, no. 11, pp. 10940–10949, 2011.

[52] H. Guan, Q. Fang, G.-Q. Lo, and K. Bergman, "High-efficiency biwavelength polarization splitter-rotator on the soi platform," *IEEE Photonics Technology Letters*, vol. 27, no. 5, pp. 518–521, 2014.

[53] D. Liu, H. Xu, Y. Tan, Y. Shi, and D. Dai, "Silicon photonic filters," *Microwave and Optical Technology Letters*, vol. 63, no. 9, pp. 2252–2268, 2021.

[54] H. Xu and Y. Shi, "Flat-top cwdm (de)multiplexer based on mzi with bent directional couplers," *IEEE Photonics Technology Letters*, vol. 30, pp. 169–172, 2018.

[55] J. Ong, R. Kumar, and S. Mookherjea, "Ultra-high-contrast and tunable-bandwidth filter using cascaded high-order silicon microring filters," *Photonics Technology Letters, IEEE*, vol. 25, pp. 1543–1546, 08 2013.

[56] L. Zhang, H. Zhao, H. Wang, S. Shao, W. Tian, J. Ding, X. Fu, and L. Yang, "Cascading second-order microring resonators for a box-like filter response," *Journal of Lightwave Technology*, vol. PP, pp. 1–1, 11 2017.

[57] A. Masood, M. Pantouvaki, G. Lepage, P. Verheyen, J. Van Campenhout, P. Absil, D. Van Thourhout, and W. Bogaerts, "Comparison of heater architectures for thermal control of silicon photonic circuits," in *10th International Conference on Group IV Photonics*, pp. 83–84, IEEE, 2013.

[58] A. Masood, M. Pantouvaki, G. Lepage, P. Verheyen, J. Van Campenhout, P. Absil, D. Van Thourhout, and W. Bogaerts, "Comparison of heater architectures for thermal control of silicon photonic circuits," in *10th International Conference on Group IV Photonics*, pp. 83–84, 2013.

[59] X. Tu, T.-Y. Liow, J. Song, M. Yu, and G. Q. Lo, "Fabrication of low loss and high speed silicon optical modulator using doping compensation method," *Opt. Express*, vol. 19, pp. 18029–18035, Sep 2011.

[60] A. Dhiman, "Silicon photonics: a review," *IOSR Journal of Applied Physics*, vol. 3, no. 5, pp. 67–79, 2013.

[61] G. T. Reed, G. Mashanovich, F. Y. Gardes, and D. Thomson, "Silicon optical modulators," *Nature photonics*, vol. 4, no. 8, pp. 518–526, 2010.

[62] J. Mulcahy, F. H. Peters, and X. Dai, "Modulators in silicon photonicsmdash;heterogenous integration amp; and beyond," *Photonics*, vol. 9, no. 1, 2022.

[63] W. Bogaerts, P. De Heyn, T. Van Vaerenbergh, K. De Vos, S. Kumar Selvaraja, T. Claes, P. Dumon, P. Bienstman, D. Van Thourhout, and R. Baets, "Silicon microring resonators," *Laser & Photonics Reviews*, vol. 6, no. 1, pp. 47–73, 2012.

[64] W. N. Ye and Y. Xiong, "Review of silicon photonics: history and recent advances," *Journal of Modern Optics*, vol. 60, no. 16, pp. 1299–1320, 2013.

[65] S. Y. Siew, B. Li, F. Gao, H. Y. Zheng, W. Zhang, P. Guo, S. W. Xie, A. Song, B. Dong, L. W. Luo, C. Li, X. Luo, and G.-Q. Lo, "Review of silicon photonics technology and platform development," *J. Lightwave Technol.*, vol. 39, pp. 4374–4389, Jul 2021.

Chapter 3

Silicon Photonics Transmitter

3.1 Si Ring Modulators

The SiPh transmitter consists of a reverse-biased Si carrier-depletion RM [1] with BW of 50 GHz and radius of 5 µm. A schematic of the device is shown in Fig. 3.1 and a picture in Fig. 3.2a. The RM consists of a ring resonator (ring-shaped waveguide) coupled to a straight waveguide. The one end of this waveguide is used as the optical input port. The other, called through port, is used for the high-speed data transmission. Our custom RM design includes an additional optical drop port that taps a small percentage of the power that circulates in the ring. A Ge PD connected at the drop port output allows for monitoring the drop port average power (P_{avg}), as illustrated in Fig. 3.1. This configuration is useful for implementing a thermal tuning control loop based on average power monitoring at the drop port, as it will be described in Sec. 4. An integrated Tungsten micro-heater (µ-heater) placed on top of the RM waveguide (as shown in the ring waveguide cross-section of Fig. 3.2b) allows for active temperature and resonance wavelength (λ_{res}) control through the thermo-optic effect in Si. This can be achieved by adjusting the µ-heater bias voltage (V_{heater}) with a voltage source. The high-speed modulation of the Si RM can be achieved by applying a high-speed modulation voltage V_{mod} (the electrical data) through the high-speed terminals of the RM.

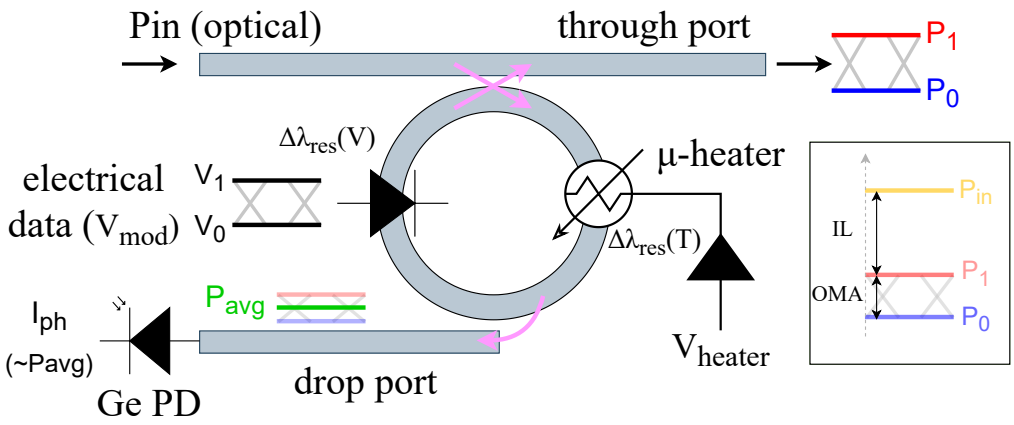

Figure 3.1. *A schematic of the Si RM. The ring waveguide is coupled to two straight waveguides that include the through and drop ports. A Ge PD is connected to the drop port. A Tungsten micro-heater is integrated on top of the RM.*

The coupling between the on-chip RM circuit and the SMFs in achieved with standard 1D grating couplers. The mask layout of the complete RM circuit in the drop-port configuration is shown in Fig. 3.3.

3.1.1 RM characterization

Some initial measurements were performed to extract the passive characteristics of the ring that was designed at CERN and is employed in the Tx circuit. These characteristics are the static response or transmission spectrum of the ring, the FSR, the full width at half maximum (FWHM) and the quality factor (Q-factor). These are design dependent and therefore have the same value across the different test-boards. Moreover, they characterize

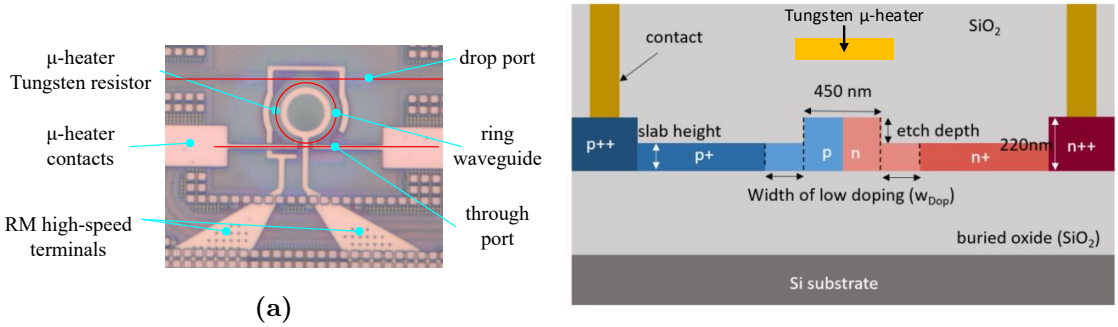

Figure 3.2. *(a) A picture of the RM from PICv2. The ring structure is connected at the top and bottom with straight waveguides to form the drop and through ports respectively. A tungsten μ-heater placed on top of the ring waveguide can be used for active temperature control. (b) A cross-section of the custom RM design showing the rib waveguide, the etch depth, core and slab widths .*

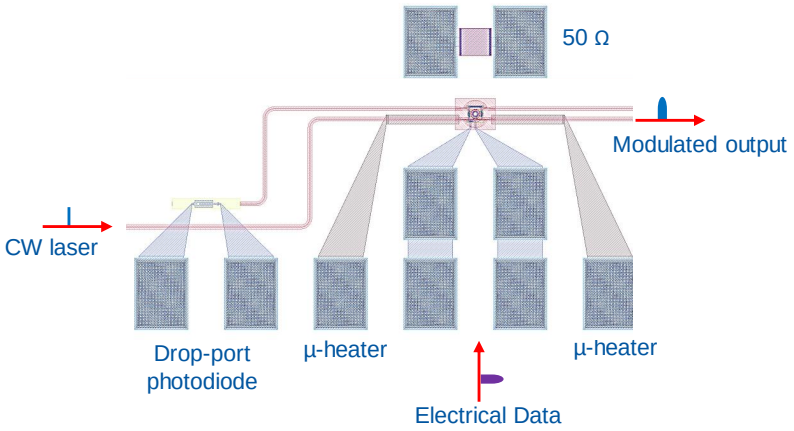

Figure 3.3. *The RM circuit from PICv2 in the drop-port configuration.*

the passive ring waveguide structure and not the PN junction. The characteristics that concern the active behaviour of the RM and the PN junction will be presented later on, in section 3.3.

The response of the RM cannot be measured directly, without including the contribution of the grating couplers IL and response, since the GCs are parts of the circuit and are necessary for the coupling of the light between the SMFs and the RM. For this reason, to measure the RM response, two different structures are required, one that includes only the input and output GCs connected with a shunt waveguide as shown in Fig. 3.4a, and the structure that also includes the RM we want to characterize between the input and output GCs, as shown in Fig. 3.4b. From the first circuit we can measure the GC and waveguide response and IL, that is shown in Fig. 3.4c in red. From the second structure we measure the response of the complete Tx circuit that includes the two GCs, the waveguide and the RM. This is shown in Fig. 3.4c in blue color. By subtracting the second line from the first one we decouple the response of the RM from that of the GCs, and we get the response of the RM alone. This is shown in Fig. 3.4d. There we see the expected resonant notches of the RM, and its flat response outside of the resonant regions. From this plot we can also

extract the FSR, that is the distance between two neighboring resonant notches. This is around 20 nm for our design. The FSR is given from Eq. 3.1 [2]

$$FSR = \frac{\lambda^2}{n_g * L} \tag{3.1}$$

where λ is the operational wavelength that is almost constant in this application, n_g is the group index that depends on the geometrical parameters of the waveguide, and L is the optical path length or ring circumference, given by $L = 2\pi r$, where r is the ring radius. Given the operational wavelength and the group index, to achieve FSR of 20 nm, the ring radius r was chosen to be 5 µm. The measured FSR agrees with the simulated and expected value given the design parameters. The FSR is an important parameter since it defines the necessary RM thermal tuning range. In the worst case, to achieve optimal operation at the chosen wavelength, a resonance peak needs to be moved across a whole FSR. The movement of a resonance peak when heating the RM is also illustrated in Fig. 3.4d. The choice of FSR is also important in the case of WDM schemes since it is related to the possible channel spacing.

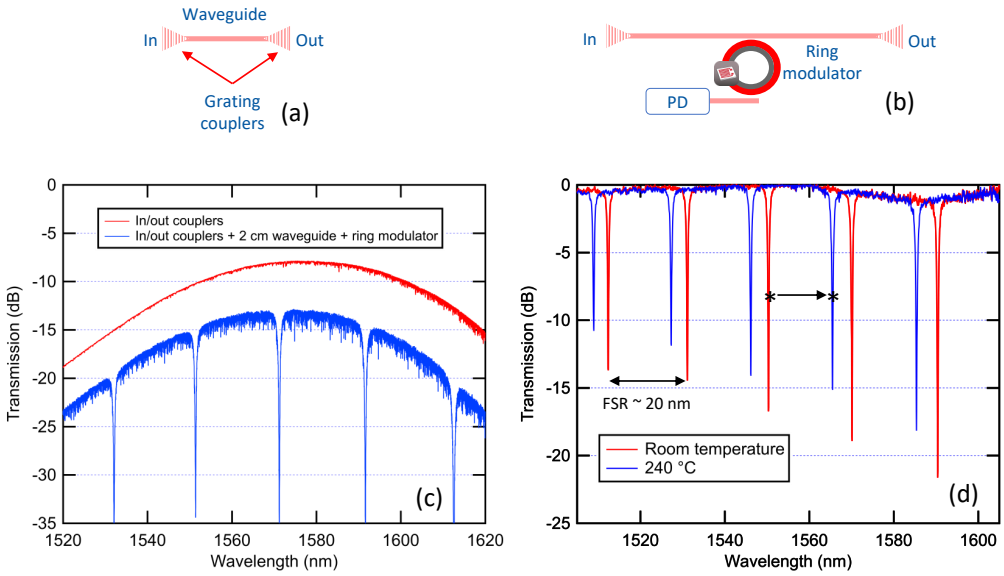

Figure 3.4. *(a) The testing structure that includes the input and output 1D-GCs connected by a shunt waveguide, that can be used to measure the response of the GCs. (b) The test structure that includes the input and output GCs, and the RM structure connected in between. This structure can be used along with (a) to extract the RM response. (c) The measured transmission of structure (a) in red and of structure (b) in blue. (d) The normalized transmission of the RM, computed by subtracting the red and blue curves of (c), for two different temperatures.*

Another important metric of the ring resonator is the FWHM, the width of a resonance notch at the point where the power has dropped by half (−3 dB). This is an important parameter that provides valuable information about the quality, losses, coupling efficiency and performance of the ring resonator. We have measured FWHM for one of the peaks of our RM. The result is shown in Fig. 3.5, and FWHM was measured to be 0.7748 nm for

the resonance peak (λ_{res}) at 1552.135 nm.

FWHM and λ_{res} allow for the computation of another very important parameter of the ring, its Q-factor. The Q-factor is given by Eq. 3.2.

$$Q_{factor} = \frac{\lambda_{res}}{FWHM} \tag{3.2}$$

The physical meaning of the Q-factor relates to the number of round-trips made by the energy in the resonator before being lost to internal loss and the bus waveguides [3]. A high Q-factor indicates lower losses. In other words, the Q-factor is a measure of how "sharp" or "narrow" the resonance peak is. A high-Q resonator has a narrow FWHM, indicating that it can store energy for longer periods of time and has reduced energy loss. On the other hand, a low-Q resonator has a wider FWHM, indicating higher energy losses and a broader resonance. For ring modulators, a higher Q-factor also signifies a higher modulation efficiency, which is another advantage and can allow operation of the RMs with lower driving voltages. However, for high Q-factors the light is trapped in the ring for a longer time, eventually limiting the modulation speed of the ring and its BW. At the same time, a high Q-factor RM has a more narrow region were it can be optimally operated, given the increased slope around the resonance peak, while it also becomes more sensitive to temperature fluctuations, thus requiring faster and more accurate thermal tuning. This increases the complexity of the required thermal tuning control loop. Overall, a compromise between modulation efficiency and speed is necessary. For our application, given the requirements we have chosen to work with RMs with Q-factor of around 2000. This number can also be verified from the plot in Fig. 3.5. Given the FWHM and λ_{res}, the extracted Q-factor is indeed 2000.

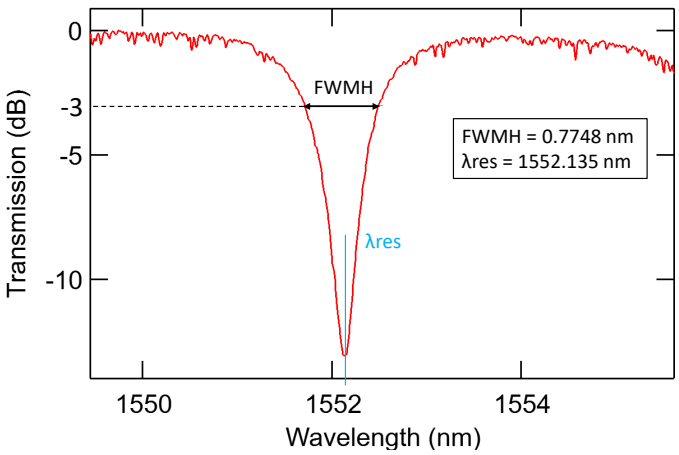

Figure 3.5. *The normalized transmission spectrum of the RM varying the input laser wavelength, zoomed in around the resonance peak at* 1552.135 nm. *From this plot we can measure the FWHM, the notch width for transmission* −3 dB, *which is equal to* 0.7748 nm.

3.2 Transmitter test-board

For the purpose of testing and characterizing the RM, different test boards have been designed and assembled. The various versions have different design characteristics and specifications to address the needs of the tests performed. In this section we describe the three most important board designs that were used for the SiPh Tx characterization.

3.2.1 DC test-board

The DC test boards were designed for low speed testing, including various irradiation tests, that do not require the high-speed driving of the RMs. The have the necessary optical connections to the RMs under tests. This is achieved by attaching fiber arrays on the chip, as shown in Fig. 3.6 that show a picture of the board with the fiber array attached on top of it. The advantage of this board is that a big number of electrical connections can be implemented simultaneously. Since the electrical signals are low speed, the electrical traces on the board can be long and placed relatively closed to each other, while the output electrical PIN connectors are also small in size. This allows to connect, access and operate many RMs at the same time. Although no high-speed driving in possible, we can still bias the RMs, the µ-heaters and the PDs. This functionality in enough to perform the DC characterization of the RMs, so typically these are the boards that we use for this purpose.

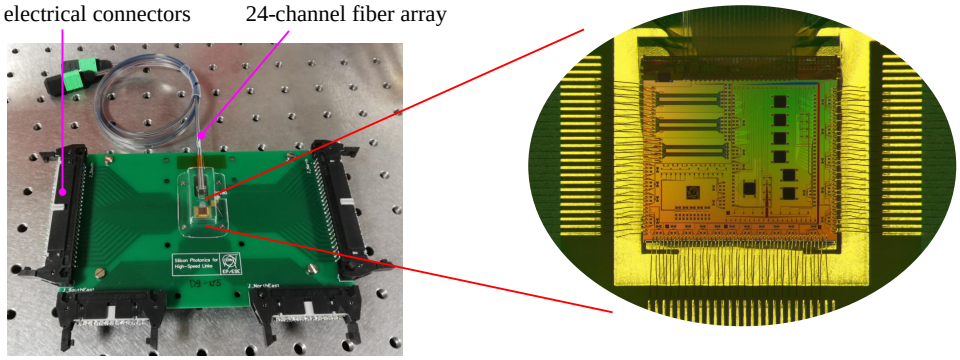

Figure 3.6. *Left: a picture of the DC test-board that was designed at CERN for the DC testing of the RMs with low speed signals. Right: A zoomed in picture of the SiPh PIC from the center of the board, were the wire-bonds are visible.*

3.2.2 Driver-less test board

The driver-less test boards are the first generation of high speed test boards that were designed for the high-speed characterization of the Tx. The are more compact in size compared to the DC boards and include much fewer electrical connections. This happens to ensure that the traces on the board are short and placed with enough space between themselves to avoid interference. Usually, the driver-less test boards include electrical SMA connection to one RM, meaning the high-speed driving signal, the µ-heater and the PDs at the drop port of the RM. They also have an attached fiber array on top of the PIC GCs for optical connection. A picture of such a board in shown in Fig. 3.7. There, the

electrical SMA connectors and the attached fiber are marked. The disadvantage of these boards is that they can support data rates up to $10\,\mathrm{Gbit\,s^{-1}}$. For higher data rates the quality of the electrical signal is deteriorated and the resulting eye diagrams are not very open. This is because the traces and the wire-bonds are still long for the needs of even higher data rates, and the SMA connectors are close to their limit. However, operation up to $10\,\mathrm{Gbit\,s^{-1}}$ was sufficient for the initial high-speed characterization of the RMs, and also for the development of the thermal tuning control loop.

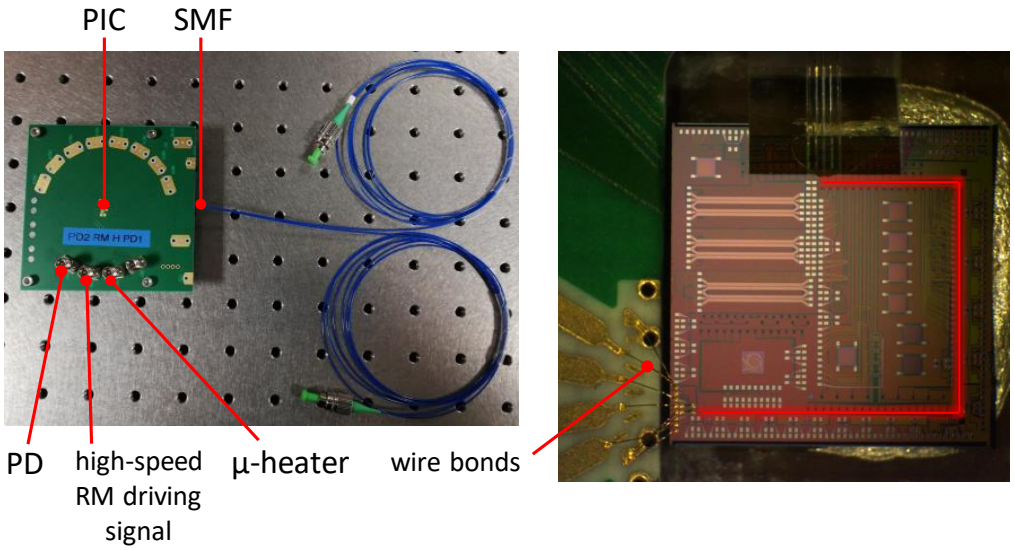

Figure 3.7. *Left: a picture of the Tx driver-less test-board that was designed at CERN for the high speed testing of the RMs up to* $10\,\mathrm{Gbit\,s^{-1}}$. *Right: A zoomed-in picture of the PIC attached on the boards. The waveguide from the input GC to the RM13 that is connected in this board, is highlighted in red.*

3.2.3 25G test-board

To test the Tx in even higher data rate, and manage to reach the limit of the lab equipment that for the moment allows us to test the RMs with driving signals up to $25\,\mathrm{Gbit\,s^{-1}}$, another improved high-speed board was designed. The priority of this board was to ensure as short traces and wire bonds as possible, so that it can support the increased data rates. The size of the board was further reduced to less than one forth of the driver-less test boards and the wire boands of the high speed signals were kept short, at $400\,\mu\mathrm{m}$. A picture of the 25G test board is shown in Fig. 3.8. On the right side of the picture, the short wire bonds are shown. For this board, 2.92 mm connectors were employed for the high-speed signal, and PIN connectors for the low speed signals of the µ-heater and PD. As usual, a fiber array is attached on the PIC, providing the optical inut and output connections. This is also illustrated in Fig. 3.8.

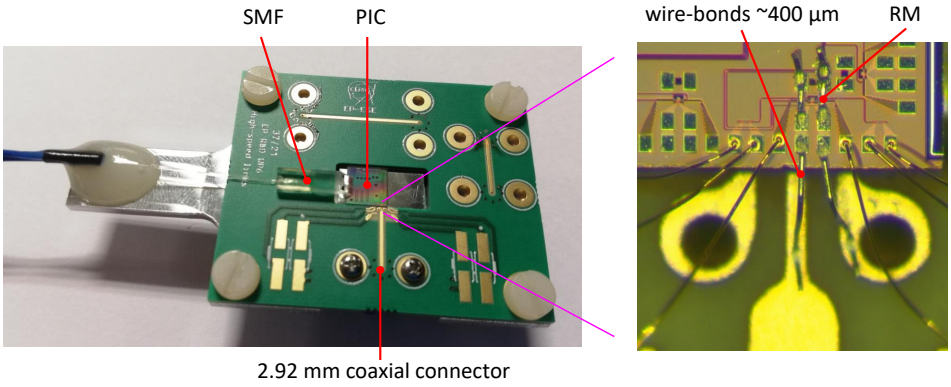

Figure 3.8. *Left: a picture of the Tx test-board that was designed at CERN for the high speed testing of the RMs up to* $25\,\mathrm{Gbit\,s^{-1}}$*. Right: a zoomed in picture of one of the RMs where the high-speed and low-speed wire-bonds are visible. The high-speed wire-bonds are kept short at* $400\,\mu\mathrm{m}$

3.3 Tx Characterisation

The characterization of the Tx includes the static and the high speed measurements. The static measurements are performed only with DC signals and no high speed driving. They are a powerful tool to measure most of the characteristics and figures of merit (FOM) of the RM and the Tx, simply and without the need for high-speed driving. As a second step, the high-speed testing allow the measurements of the high-speed eye diagrams and the validation of the high-speed operation of the Tx. They are more complicated to perform, since high speed equipment both for driving the RMs and recording the eye diagrams is required. In the next sections we present first the DC and then the high-speed characterization of the Tx.

3.3.1 Static measurements

The static measurements involve the characterization of Tx that is performed only with DC signals. They include the recording of the transmission spectrum of the RM for different bias voltages (V_{bias}). From these data most FOMs of the RM can be extracted. This type of measurements are a powerful tool because the DC characterization allows to extract almost all important FOMs of the high-speed operation of the RM, in a simple way.

The FOM that we are interested in measuring and are typically used to characterize a RM are the optical modulation amplitude (OMA), the extinction ratio (ER), the intention loss (IL) and transmission penalty (TP) [4, 5]. These FOMs are given by Eq. 3.3.

$$\begin{aligned} OMA(mW) &= P_1 - P_0 \\ ER &= P_1/P_0 \\ IL &= \frac{P_1}{P_{in}} \\ TP(dB) &= -10 \cdot \log(\frac{OMA}{2 \cdot P_{in}}) \end{aligned} \tag{3.3}$$

where P_1 and P_0 (in mW) are the one and zero levels of the transmission respectively, as shown in Fig. 2.21 and P_{in} (in mW) is the input optical power at the input port of the RM. These characteristics are also illustrated in the inset of Fig. 3.1. The OMA (in mW) shows the opening of the eye diagram. The IL expresses the losses of the RM that are related to the resonance condition. IL can also be expressed in dB after doing the appropriate conversion: $IL(dB) = 10\log(\frac{P_1}{P_{in}}) = P_1(dBm) - P_{in}(dBm)$. ER shows the ratio of the one and zero levels. It indicates the quality of the optical signal. A higher ER is desirable for reliable optical communications. ER can also be expressed in dB. In that case it is given by $ER(dB) = 10\log(\frac{P_1}{P_0})$. Last, TP is a metric that characterizes the performance of the RM independently of the input power, allowing also to compare different devices that were tested under different conditions. TP is always defined with respect to a driving voltage swing, since its value depends on the voltage swing of the RM driving signal. Unless it is otherwise stated, from now on when we refer to a TP value, this value is for voltage swing of 1 V. Although the values of the OMA and IL only have meaning given the P_{in}, the TP has been normalized to the input power making its absolute value important and useful independently of P_{in}. In brief, TP expresses the percentage of the input power that is converted to useful OMA. The higher the TP the smaller is this percentage and we get a lower OMA for a given P_{in}. Overall, we want our RMs to have high OMA and ER, and small IL and TP.

All these parameters are design dependent, and part of the design process of an RM is to optimize their values, according to the application. In our PIC we have RMs with minimum TP with voltage swing of 1 V that ranges from 15 dB to 10 dB. However, a trade-off exists between the TP and BW of the RMs. Decreasing the TP also means that the BW reduces, so the design must take into account both characteristics. Another important thing to note is that higher TP requires higher driving voltage since the power budget of the link, including the input optical power is constant. This will eventually be a problem for our system, since a driving voltage limit of 1 V is imposed by the FE due to the system requirements. This signifies that eventually we need to improve the design of our RMs to achieve high enough modulation efficiencies with adequate TPs with voltage swing of 1 V.

With low input power

As a first step, the DC characterization of the RM is performed with low input power ($<$0.5 mW) to avoid any self-heating effects that cause an artificial red-shift of the curves, distorting their shape. The measured transmission spectrum of the RM varying the external laser wavelength (λ_{laser}) for different modulation voltages V_{mod} from 0 V to -5 V, is shown in Fig. 3.9a. The extracted modulation efficiency is 40 pm V^{-1}. From this plot we extract the FOM (OMA, TP, ER, IL), as shown in Fig. 3.9b. The OMA is normalized ($OMA_{norm} = OMA/P_{in}$). It is evident that at a specific wavelength ($\lambda_{optimal}$) near the resonance, OMA maximizes and TP with voltage swing of 5 V minimizes. This is the optimal operating point of the RM where the eye diagram opening is the biggest and is denoted in Fig. 3.9b with a vertical dashed line. The corresponding values of the FOM are also marked in the plot. Operation of the RM at this optimal point is achieved when

$\lambda_{laser} = \lambda_{optimal}$. As will be analyzed in the next chapter 4, due to environmental variations (e.g. temperature variations) that affect the λ_{res} of the RMs, continuous active control of the devices is necessary to ensure stable operation at this optimal operating point.

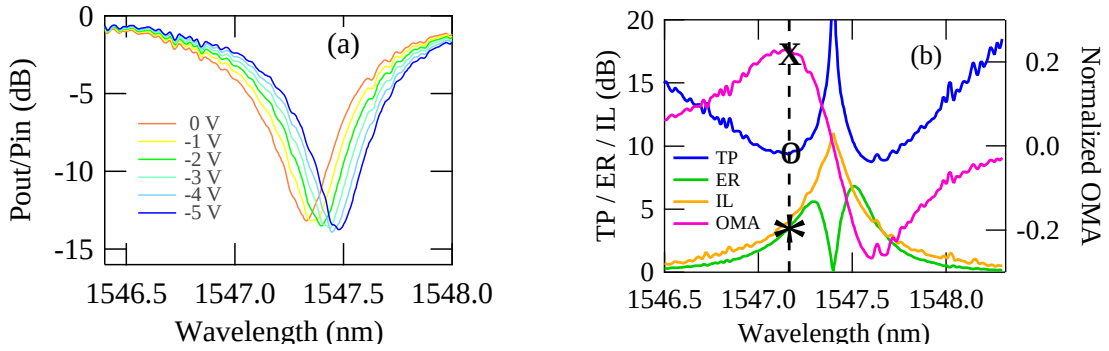

Figure 3.9. *(a) Through port transmission spectrum of the RM for different V_{mod} and the corresponding normalized OMA for V_{mod} between 0 and −5 V. (b) TP, ER, and IL of the RM as calculated from the transmission spectra from (b), for voltage swing of −5 V. In all plots the optimal operating point is denoted with the vertical dashed line and the corresponding values of the FOM are also marked.*

The measured photocurrent (I_{ph}) at the drop port PD when varying λ_{laser} is shown in Fig. 3.10. It peaks at the resonance wavelength (λ_{res}). The I_{ph} at $\lambda_{optimal}$ is marked in red in Fig. 3.10.

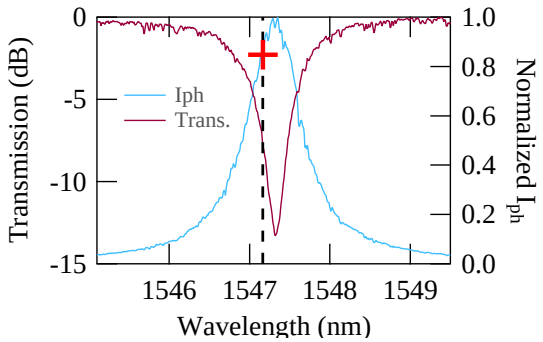

Figure 3.10. *The measured through-port transmission spectrum of the RM and the corresponding normalized drop port I_{ph} ($I_{ph}/I_{ph\text{-}max}$) varying λ_{laser} for low P_{in}.*

With high input power

The previous measurements were performed with low P_{in} (<0.5 mW), therefore the spectra are symmetric and no self-heating effect is observed [6]. However, in data communication applications P_{in} must be higher to meet the power budget requirements of the link. In this case the self-heating effect modifies the response of the RM. Fig. 3.11a shows the measured transmission spectrum and drop-port I_{ph} varying the external laser wavelength for high P_{in} (few mW). Fig. 3.11b shows also the measured characteristic plots of the OMA and ER for the same high P_{in}. The curves appear red-shifted and no longer symmetric due to the self heating effect. However, as before, there is a particular $\lambda_{optimal}$ for which the OMA reaches a maximum. A characteristic value of the I_{ph} called setpoint

corresponds to this optimal point, denoted with a red cross in Fig. 3.11b. For a given RM design this setpoint equals a fixed percentage of the max I_{ph} ($I_{ph} = k \cdot I_{ph-max}$). k is design-dependent and its computation allows for easy calculation of the setpoint. For the RMs from our PIC k was measured in the range $0.65 - 0.8$. It shows a small variation within this range between RMs. To account for variations we choose to work with the median value of $k = 0.7$. The computation of k and consequently of the setpoint (optimal I_{ph}) is necessary since it enables the easy location of the optimal operating point of the RM during operation. This in turn allows for the active control and thermal stabilization of the RM to ensure the stable operation.

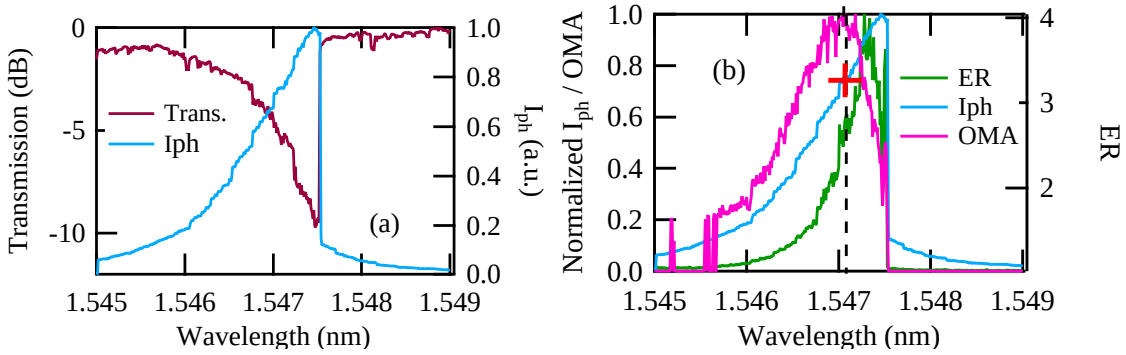

Figure 3.11. *(a) Through port transmission spectrum of the RM and the corresponding normalized drop port I_{ph} ($I_{ph}/I_{ph\text{-}max}$) varying λ_{laser} for high P_{in}. (b) The measured normalized I_{ph} and OMA, as well the ER varying λ_{laser} for high P_{in}. OMA and I_{ph} are normalized to their maximum values. The optimal operating point is denoted with the vertical dashed line and the corresponding value of the I_{ph} is also marked with a red cross.*

3.3.2 High-speed measurements

To validate the high-speed operation of the Tx, high-speed eye diagram measurements were performed. To enable the operation at 25 Gbit s^{-1}, the 25G test-board was used for this test. A schematic diagram of the setup is shown in Fig. 3.12a. The setup included also a high-speed pattern generation (SHF 12126 A) (Fig. 3.12b) that can reach datarates up to 32 Gbit s^{-1} NRZ, and a high-speed sampling scope with BW of 27 GHz. Since the RM under test has high BW of 50 GHz and also high TP with voltage swing of 1 V, it is not compatible with low swing driving signals. Therefore, electrical amplification of the driving signal is required. This is ensured by connecting a wide-band amplifier with BW of 35 GHz and a Biat-T with BW of 45 GHz in series, at the output of the pattern generator. Both components are shown in Fig. 3.12c. This way the electrical driving signal is amplified at 5 V of voltage swing, between 0 V and 5 V. The electrical eye diagram at the output of the bias-T at 25 Gbit s^{-1} is shown in Fig. 3.13a. The corresponding optical eye diagram at the output of the RM is shown in Fig. 3.13b. The eye diagram is open and clean, without jitter and noise. This is a proof of concept of the high-speed operation of the SiPh RMs.

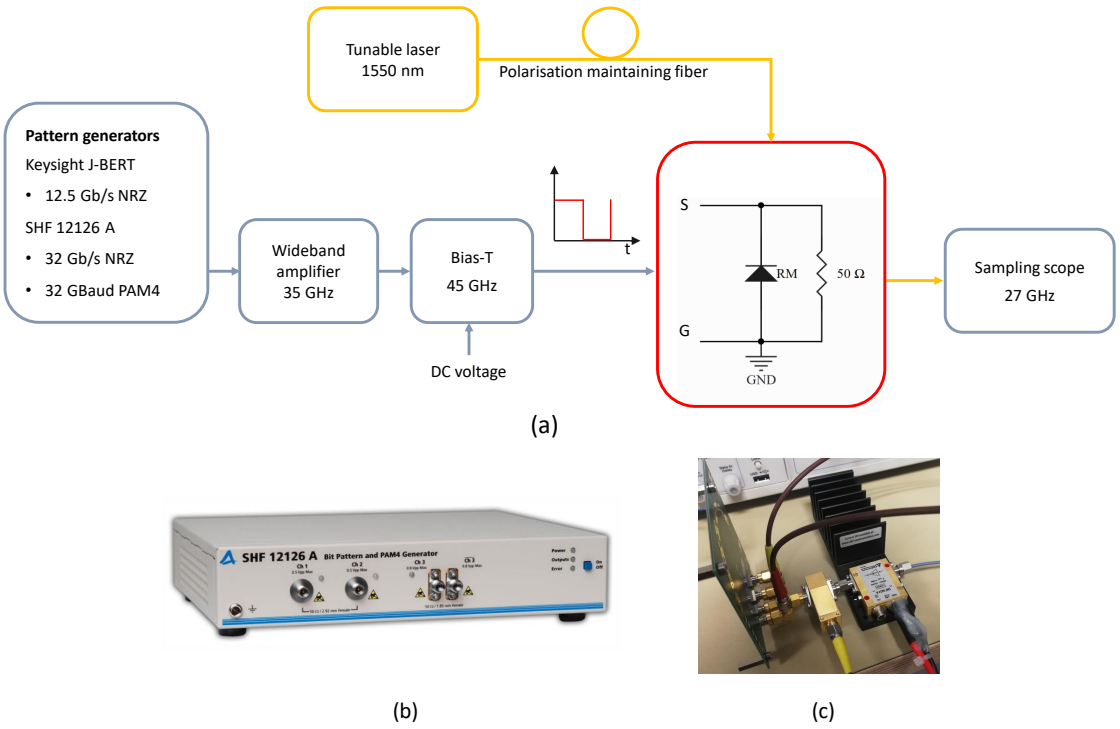

Figure 3.12. *(a) Schematic diagram of the high-speed characterization setup for measuring the RM eye diagrams at* $25\,\mathrm{Gbit\,s^{-1}}$*. It includes a pattern generator, an electrical amplifier and Bias-T, the Tx test board and the sampling scope. The optical input is provided by a tunable laser connected to the Tx board through a PM fiber.*

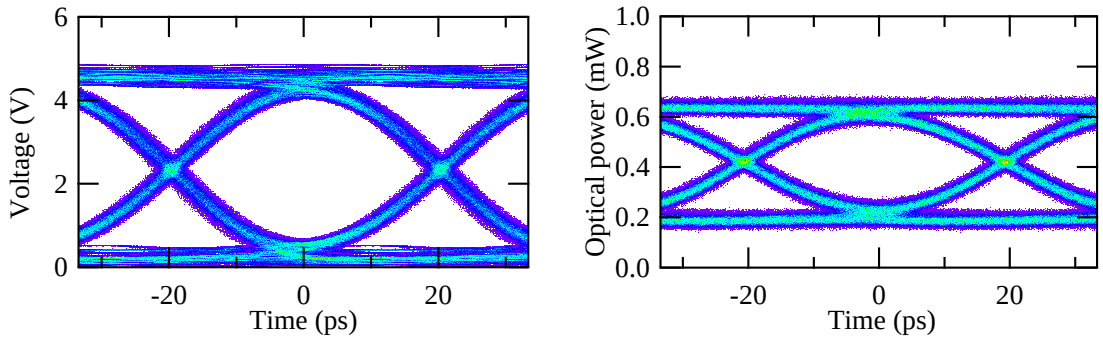

Figure 3.13. *(a) The electrical eye diagram at the input of the RM at* $25\,\mathrm{Gbit\,s^{-1}}$*. (b) The corresponding optical eye diagram at the output of the RM at* $25\,\mathrm{Gbit\,s^{-1}}$*, for* V_{mod} *between* $0\,\mathrm{V}$ *and* $-5\,\mathrm{V}$*.*

3.3.3 Micro-heater characterization

Step response function

As shown in Fig. 3.1 and Fig. 3.2a, the RM includes a Tungsten µ-heater placed on top of the RM waveguide that can be used to actively tune the temperature and therefore the resonant wavelength of the device. The response of the µ-heater was characterized. To measure its step response function, the setup shown in Fig. 3.14 was used. The setup

includes the Tx circuit with the RM and the integrated µ-heater, a laser to provide the optical input to the RM, at the optical output a photodiode, a linear electrical amplifier and a scope, to record the output of the RM, and voltage source to drive the µ-heater. When applying a step function at the µ-heater (changing the voltage from zero to one in a very short time, as shown in the inset of Fig. 3.14), the measured output is the step response of the µ-heater.

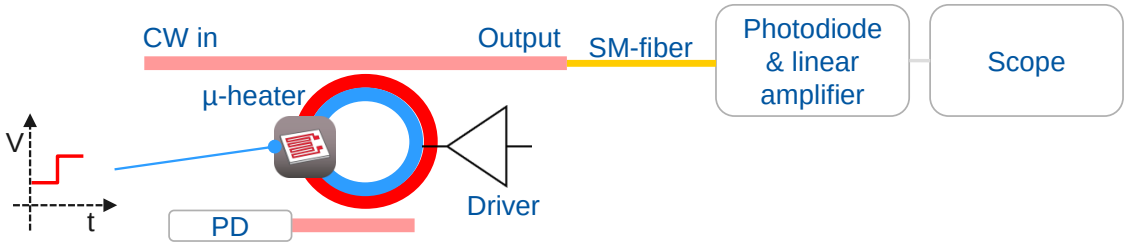

Figure 3.14. *The setup for measuring the step response function of the µ-heater*

The results of this measurement are shown in Fig. 3.15. Given that the initial condition of the RM is illustrated with the green line in the left plot of Fig. 3.15 left, when applying a step response at the µ-heater (heating), the resonance will move to the right (depicted by the blue resonance notch), following the red arrow. Given that the input laser is fixed at around 1565 nm. marked by the dashed red vertical line, this change in the resonance of the RM will lead to the sudden decrease of the output power. This is because in the initial condition the RM is out of resonance and all the power is directed at the through-port output, while after applying the step function, the resonance is aligned with the laser (resonance condition), leading in a decrease of the power at the through port. The resulting output power vs. time plot is shown in Fig. 3.15 right with red color. The same measurement was repeated when decreasing the µ-heater voltage from one to zero, with a reverse step function. This corresponds to cooling, and was done to verify if the time constants for cooling and heating are the same. The principle of operation in the same. The resonance is moved from the blue position back to the green, following the blue arrow of Fig. 3.15 left. The output this time will increase, going from the resonant condition to the out of resonance condition. The result is shown in Fig. 3.15 right with the blue curve. In both cases, the measured time constant is very similar, and it is around 10 µs when heating and 20 µs when cooling. Using as µ-heater time constant the slowest of the two ($\tau = 20\,\mu s$), we can also calculate the µ-heater BW as following $\omega = 2\pi f = \frac{1}{\tau} \rightarrow f = \frac{1}{2\pi\tau} \rightarrow f = 8\,\text{kHz}$.

This measurement is important for the design of the thermal control loop, as will be explained in chapter 4, as it defines how fast the µ-heater can correct a drift in the operating point of the RMs.

Thermal characterization

The thermal characterization of the µ-heater was performed. It included the measurement of the resonance wavelength shift varying the temperature as well as the the resonance wavelength shift varying the µ-heater electrical power. The results are shown in Fig. 3.16. It is evident from the plot that the λ_{res} shift is linear with temperature, and with µ-heater

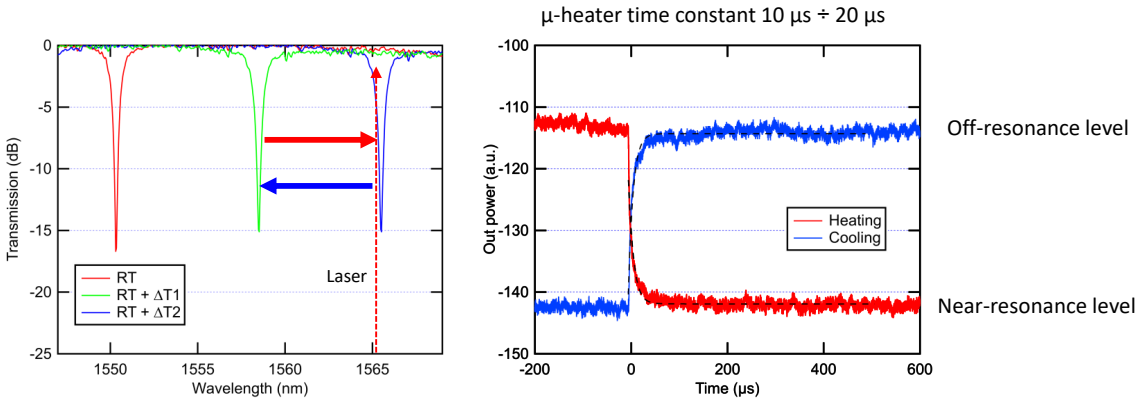

Figure 3.15. *Left: the process of measuring the μ-heater step response. Right: the measured μ-heater step response when heating up and cooling down. The extracted μ-heater time constant is* 10 µs *when heating and* 20 µs *when cooling.*

power. The extracted slopes are the following:

$$\frac{d\lambda_{res}}{dT} = 70\,\frac{\text{pm}}{^{\circ}\text{C}}$$

$$\frac{d\lambda_{res}}{dP_{heater}} = 272\,\frac{\text{pm}}{\text{mW}}$$

. We can also extract the temperature shift per mW of electrical power that equals:

$$\frac{dT}{dP_{heater}} = 4\,\frac{^{\circ}\text{C}}{\text{mW}}$$

.

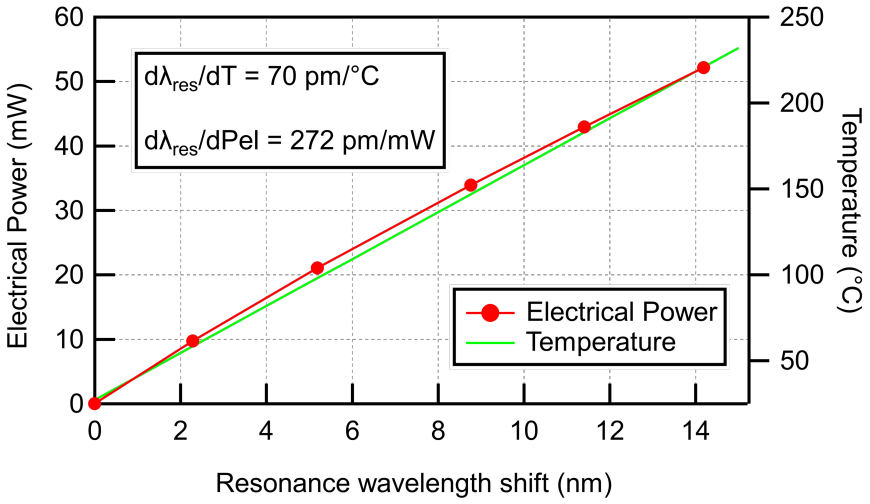

Figure 3.16. *The measured resonance wavelength shift of the SiPh RMs from PICv2 varying the temperature (in green) and varying the electrical power of the integrated micro-heater (in red).*

Electrical characterization

The IV of the µ-heater, as well as the heater power vs. voltage curves have been measured. The results are shown in Fig. 3.17 with pink and red color respectively. At low temperatures, the resistance of the µ-heater is around 25 Ω while at high temperatures (high V_{heater}) the resistance increases at around 50 Ω. For voltages above 0.6 V the power changes almost linearly. The slope of the curve is calculated to be $\frac{dP_{heater}}{dV} = 43\,\frac{mW}{V}$. With the current technology and device, the maximum electrical power of the µ-heater is 60 mW which corresponds to around 2 V of V_{heater}. For higher values the µ-heater will burn. Therefore, we typically operate the µ-heater with voltages up to 1.6 V in normal operation, and maximum at 2 V.

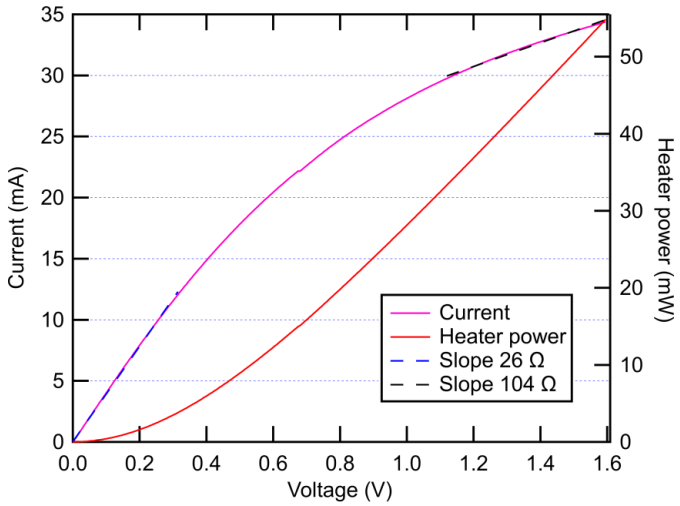

Figure 3.17. *The measured IV curve of the integrated Tungsten µ-heater from PICv2 (in pink) and the corresponding plot of the heater power varying the heater biasing voltage (in red).*

3.3.4 Self-heating effect

Depletion-type Si RMs suffer from self-heating caused by FCA of the input light circulating in modulator ring waveguides. The ring waveguide effective index increases due to temperature rise caused by self-heating and the ring λ_{res} red-shifts. The amount of the shift depends on the input optical power. Since Si RMs characteristics greatly depend on the λ_{res}, self-heating can strongly influence the modulation performance and, consequently, its influence must be well understood in order to reliable operate the RMs [6,7]. As part of the RM characterization, we have measured the self-heating step response function. The setup used for this measurements is shown in Fig. 3.18 and it comprises the Tx circuit with the RM, a laser for the optical input, a driver for biasing the RM and a photodiode, amplifier and scope to measure the RM output.

The measurement process is similar to the one followed to measure the µ-heater response. We apply a step function to the RM high-speed contacts and then we measure the output of the RM with the scope. The results are shown in Fig. 3.19. The initial transmission of the RM before applying the step function is shown in green. The RM is near

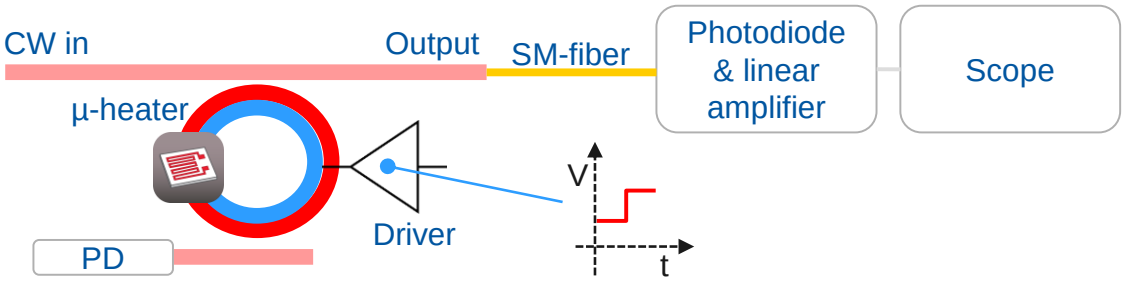

Figure 3.18. *The setup for measuring the step response function of the self heating effect.*

the resonance, meaning a lot of power circulates in the ring and the resonance is affected by the self-heating effect. After applying the step function, since we increase the reverse bias of the junction the resonance red-shifts. The new transmission plot is shown in red in Fig. 3.19. However, this change of the resonance, given that the λ_{laser} is constant (also marked in the figure), means that the power at the output increases and consequently the power circulating in the ring decreases (we move away from the resonant condition). This reduction in the power circulating in the ring translates in self-cooling, which in turn moves the resonance a bit to the left (light blue curve in the figure). This effect is illustrated also in Fig. 3.19 right with the blue line (output power vs. time) . The sudden increase of the output power and the consequent decrease due to self-cooling is evident. The increase happens very fast due to the high speed of the electro-optic effect, but the gradual decrease due to self cooling is slower since it is a thermal effect. We can measure the self-heating time constant from the plot, the is found to be around 1.2 µs.

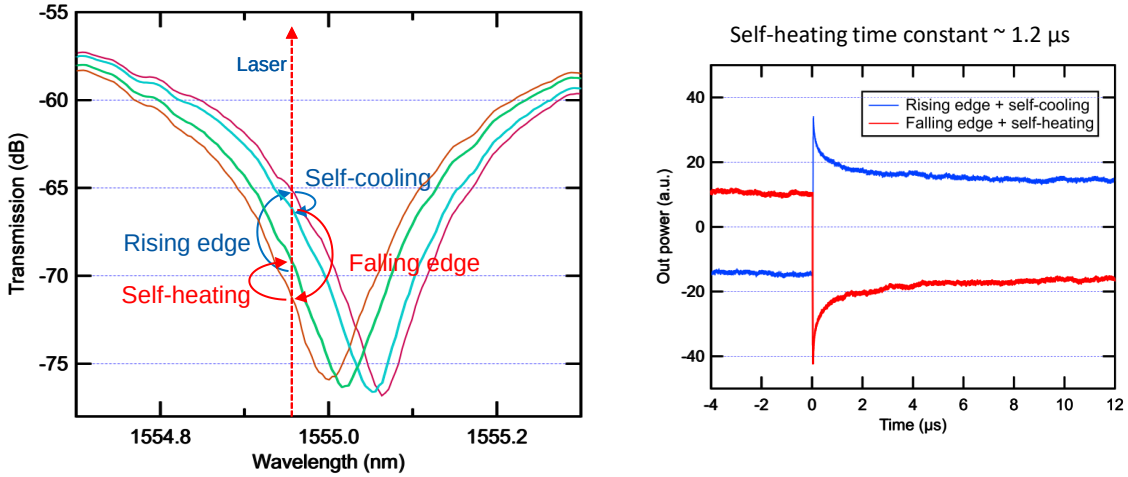

Figure 3.19. *Left: the process of the self-heating effect. Right: the measured step response of the self-heating effect. The extracted self-heating time constant is* 1.2 µs *when heating and* 20 µs *when cooling.*

The same measurement is then repeated with the falling edge of the step function. Being at the state marked by the light blue line in Fig. 3.19 left, we bring the biasing voltage back to 0 V very quickly. This moves the resonance to the left (orange line in the plot. This transition is marked as falling edge. Since the resonant peak moves to the left and the RM approaches closer to the resonant condition, the power that circulates in the

ring increases. This causes self heating that in turn will shift the resonance a bit to the right. The final state in illustrated with the light green light and is marked as self-heating in the plot. The corresponding response of the RM (output power vs time) is illustrated in Fig. 3.19 right with red color. We can measure again the self-heating time constant at around 1.2 µs.

It is evident from these measurements that the self-heating effect has a high time constant, being a thermal effect. It is much slower compared to the plasma dispersion effect that is exploited for the high-speed modulation. However, it is ten times faster than the µ-heater. This makes sense because it is an effect localised inside the waveguide, while the µ-heater is placed 1 µm away with insulating SiO_2 in between. Therefore is takes more time for the heat to propagate from the µ-heater to the RM waveguide.

Overall, the λ_{res} shift induced by self-heating from FCA further affects the data modulation of a depletion RM. It may cause unstable "1" and "0" signal levels, as well as inconsistent and reduced ER. It is, however, a relatively low-speed effect due to its thermal nature. Measurements and experiments from bibliography confirm that it only affects low frequency data contents, <1 MHz, in high-speed data transmission. For the modulation time scale of interest for our application (>10 GHz) the self-heating does not directly affect the modulation frequency response. Being a slow thermal effect, the time scale for self-heating is much larger than the modulation time scale. Another issue that might arise in a system is data dependent self-heating: for DC-unbalanced patterns that consist of many 1s or 0s in series with duration that becomes comparable with the self-heating response time, the ring may have enough time to be impacted by this data dependent heating. However, is our system we work with DC balanced signals so such data patterns are not used. In the end, the self heating creates a constant offset in the λ_{res}, since the RM will "see" only the average optical power of the transmitted ones and zeros that should be constant it time (when averaged in periods of time comparable to the self heating time constant). Therefore, the operation of our RMs is not affected by self heating [8].

3.3.5 RM thermo-optic transfer function

Another important characteristic of the Tx is its thermo-optic transfer function (TF). Its measurement is necessary also for the realization of the thermal control loop, as it will be explained in chapter 4. The plant whose TF we need to measure includes the ring modulator, the µ-heater, the drop-port photodiode and the instrument that is used to measure the drop-port photocurrent (e.g. sourcemeter). The plant is shown in Fig. 3.20 top. The input of the system is the electrical power of the µ-heater, and the system output is the drop-port photocurrent. Such a plant can be described by a first order single pole transfer function, as shown in Eq. 3.4. To compute the TF we need two parameters: the time constant of the micro heater step response, denoted with τ in Eq. 3.4, and the system gain H. In our case H is given by $\frac{I_{PD}}{P_{el}}$ which is the slope of the linear region of the I_{PD} vs. P_{el} curve. The curve is shown in Fig. 3.20 and the fit of the linear region is illustrated with the black dashed line. The slope of this line is the system gain. This was calculated to be $H = -0.028$. The time constant has already been measured as presented in Sec.

3.3.3 and is $\tau = 20\,\mu s$. Given the values of these parameters, the TF of the system is given by Eq. 3.5

$$H(s) = \frac{I_{PD}(s)}{P_{el}(s)} = \frac{H}{1 + s \cdot \tau}(\frac{mA}{mW}) \tag{3.4}$$

$$H(s) = \frac{-0.028}{1 + s20 \cdot 10^{-6}}(\frac{mA}{mW}) \tag{3.5}$$

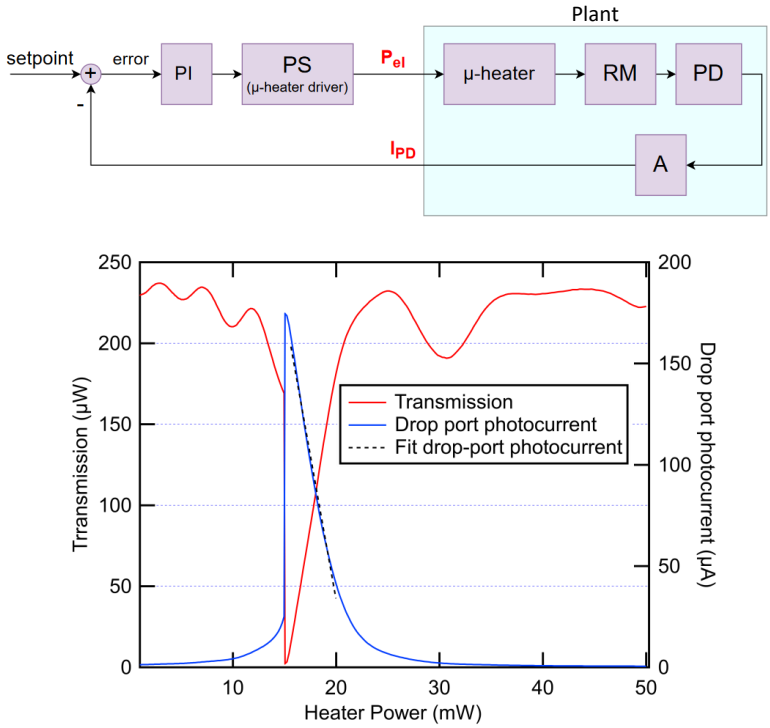

Figure 3.20. *Top: block diagram of the closed loop feedback system, including the plant. The plant comprises the RM, μ-heater, PD and amperometer. Bottom: The drop port I_{ph} vs. P_{heater} plot. The linear fit of the plot's linear region is illustrated with the black dashed line.*

3.4 Electrical Driver and Modulation Scheme

Although the RM electrical driver design and functionality is outside of the scope of the thesis, it would be worth to mention a few details here that can help to justify some design and system choices.

First of all, it is useful to note that any design and system choice needs to adhere to the system requirements that impose the use of simple, compact and low power electronics at the FE, and compatibility with the tight power budget of the link. On the BE side, the transceivers that we are planning to use should be commercially available. Moreover, the data-rates we need to achieve are estimated at $25\,\mathrm{Gbit\,s^{-1}}$ per channel for the moment.

Given these requirements, the modulation scheme that has been chosen and we are investigating so far is the Intensity Modulation / Direct Detection (IM/DD) scheme. This

is a simple and cost-effective scheme used in fiber optic communications. It involves modulating the optical power of the carrier signal to represent the transmitted data. The intensity-modulated optical signal is generated by modulating the RM and shift its resonance through the plasma dispersion effect. At the receiver end, direct detection (DD) is used to recover the modulated signal. The modulated optical signal is detected by a photodetector which in our case will be a commercial SFP module that will convert the optical power variations into corresponding electrical voltage variations. Other schemes such as coherent detection that requires much more complicated and power hungry FE drivers, the use of a local oscillator as well as complicated electronics for the digital signal processing (DSP) at the BE are not suitable for such application.

Out of the available IM/DD schemes we are focusing on the non-return to zero (NRZ) modulation technique. Since this technique has only two voltage levels, a simple digital driver in the form of a limiting amplifier can be used in the FE for driving the RM. This ensures the low complexity and low power consumption of the FE driver which is crucial in our system. It also showcases a good signal to noise ratio (SNR) and low BER, being compatible with the power budget of the link. Its disadvantage is however that the datarates that can be achieved with current technology available to us are limited to $25\,\mathrm{Gbit\,s^{-1}}$ per fiber.

To increase the link datarates we have investigated two different options. The first involves the use of the pulse-amplitude modulation 4 (PAM4) scheme. Moving to a PAM4 scheme doubles the bit rate for a given baud rate over NRZ, bringing higher efficiency for high-speed optical transmission. At the same time, PAM4 allows twice as much information to be transmitted per symbol cycle as NRZ. Therefore, at the same bitrate, PAM4 only has half the baud (or symbol) rate of the NRZ signal, so the signal loss caused by the transmission channel in PAM4 signaling is greatly reduced [9]. However, the eye height for PAM4 is 1/3 of that for NRZ, causing the PAM4 to decrease SNR by almost 10 dB, as shown in Fig. 3.21. This adds an important link budget penalty. For our system that has a tight power budget this poses an important challenge since the signal quality will be impacted and there might not be enough margin to compensate for it. Also, the 33% smaller eye opening makes PAM4 more sensitive to noise, resulting in a higher BER. Eventually, if such a solution is adopted, forward-error correction (FEC) will be required to achieve the desired BER, which complicates the BE electronics. At the same time the power consumption of the PAM4 transmitter and driver will be increased. Given the previous, the PAM4 approach is still under investigation to define if it would be an interesting alternative for our system, or whether the link power budget penalty and necessary FEC render it a not so appealing solution.

Another approach for increasing the link capacity without employing more complicated modulation schemes is WDM. This solution is very appealing since it does not require more complex electronics in the FE compared to the single channel solution, while allowing to reduce the fiber count and achieve datarates of up to $100\,\mathrm{Gbit\,s^{-1}}$ per fiber if we adopt a 4 x $25\,\mathrm{Gbit\,s^{-1}}$ scheme with four wavelengths multiplexed in the bus waveguide. For this reason, this solution has been extensively investigated at CERN. In the next section, Sec. 3.5 we analyze the 4-channel WDM Tx that we have designed and characterized at CERN.

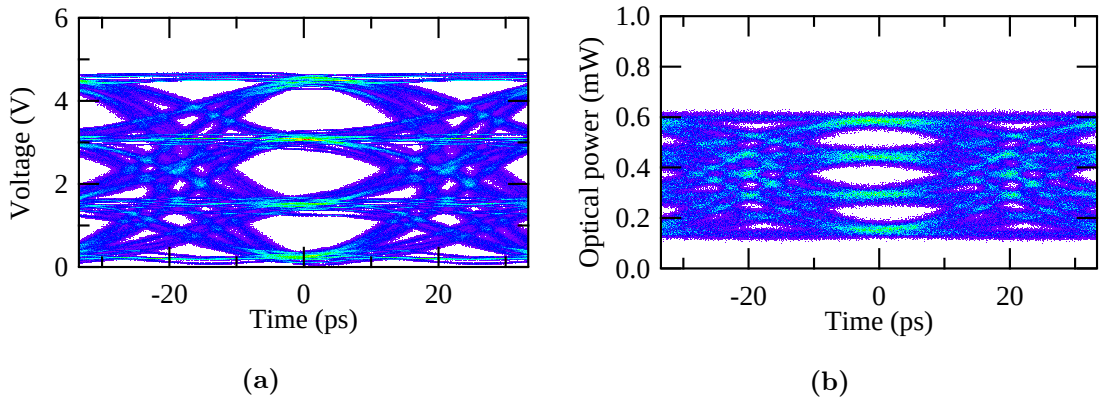

(a) (b)

Figure 3.21. *(a) The electrical eye diagram at the input of the RM at* 25 GBd*, for PAM4 modulation. (b) The corresponding optical eye diagram at the output of the RM at* 25 GBd*, for* V_{mod} *between* 0 V *and* −5 V*.*

3.5 4-channel WDM transmitter

The PIC designed at CERN includes a 4-channel WDM Tx circuit that was designed with the purpose of investigating the compatibility of WDM schemes with our application. The implementation of a WDM Tx would offer great advantages in terms of datarates that can be achieved and material budget. Multiplexing four or more wavelengths in a common channel would increase the capacity of each link without adding new fibers or SiPh Tx circuits. This is very important since the material budget of the FE TRx needs to be as low as possible to be compatible with the strict spacing and powering margins of the detectors.

PICv2 was designed for C-band operation, therefore this 4-channel circuit was also designed to work in the C-band. It comprises four RMs that are coupled to a common bus waveguide. The channel spacing is set by design to 5 nm, around the center wavelength of 1550 nm therefore this is a DWDM Tx, also compatible with the RM FSR of 20 nm.

3.5.1 The 4-channel circuit

The 4-channel WDM circuit comprises four cascaded RMs coupled to a common bus waveguide. Fig. 3.22a shows a schematic representation of the circuit that was designed to be compatible with the DWDM wavelength grid. The rings have different radii (r = 5 µm with Δr = 24 nm) that induce by design uniformly spaced resonance notches with 5 nm spacing. Fig. 3.22b shows a micrograph of the fabricated circuit. The RMs included in this circuit are in the drop-port configuration, meaning that they include a drop port with a Ge PD connected at its output. Moreover, each RM has its own high-speed terminals and µ-heater. This allows to control, thermally tune and operate each RM independently but also simultaneously.

The principle of operation of the circuit is based on typical WDM. The optical input, provided by an external laser, includes four different wavelengths that are multiplexed in the common bus waveguide. The different wavelengths are marked with blue, green, orange and red colour in the figures. Each RM is designed to operate at one of the four

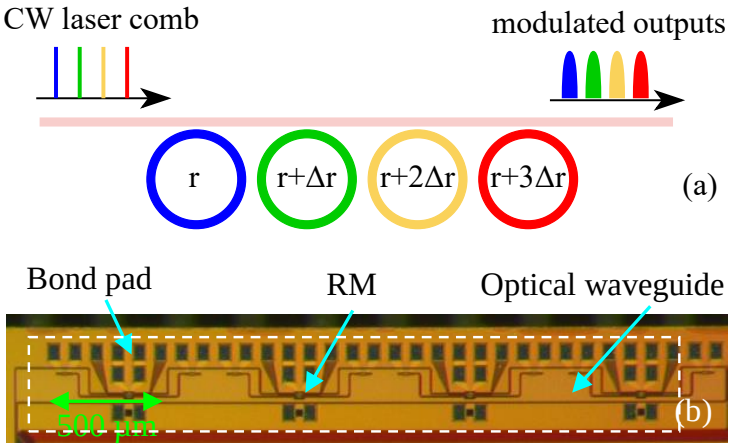

Figure 3.22. *(a) Schematic diagram of the 4-channel Tx circuit. The rings have different radii to set by design an offset in the λ_{res}. (b) Picture of the 4-channel Tx circuit from the CERN PIC.*

wavelengths (different for each RM). Therefore each RM, driven by an individual electrical driver, will modulate one wavelength, without interacting with the rest, that will propagate unchanged through the bus waveguide. In the presence of fluctuations in the temperature or fabrication variations, thermal tuning of the RMs is necessary to ensure this. For our application, it is important that every RM of the WDM circuit will be operated at its design and target wavelength. This is required because every RM corresponds to a specific FE and BE channel, and the origin of the data (FE channel) is crucial for the data reconstruction that will happen in the BE. This is another reason why thermal tuning is necessary in such a circuit to ensure that each RM will be operated at its target wavelength.

The external laser DWDM grid that is compatible with our circuit includes the four wavelengths with the appropriate channel spacing of 5 nm. Since for the moment there was no single component available providing the required spectra, this was reconstructed in the lab using two tunable and two DFB lasers that were multiplexed in a common fiber with the help of an optical filter. Since all channels need to operate with the same power budget, optical attenuators and amplifiers were used in the circuit to bring the power of each wavelength in the same level, given that the different lasers have different output powers. The measured normalized optical power of the constructed input optical signal that imitates a 4-channel DWDM grid is shown in Fig. **??**a.

It is worth noting that the coupling of the optical power between the PIC and the fibers, both at the input and the output, is done with typical 1D-GCs for this circuit. Given that both the GCs and the circuit itself operate with TE polarization, the polarization of all four optical signals had to be adjusted and aligned so that all wavelengths arrive at the fiber-PIC interface with the equivalent of TE polarization. The control of the polarization was performed with the use of manual polarization controllers and ensured the maximum optical power coupling to the PIC.

On the output side, the four wavelengths need to be demultiplexed for the purpose of testing each channel individually. In the lab this can be done with the use of an optical

filter as demultiplexer. In the final system, in the BE this operation will be performed by the commercial SFP modules that will operate as BE Rx of the data transmitted by the SiPh Tx module. This is one of the reasons why it is important for the components we design to be compatible with the commercially available components that will be employed in this link.

3.5.2 Static characterization

The static characterization of the 4-channel circuit includes the measurement of the transmission spectrum at the output of the circuit, varying the input wavelength. This measurement is performed with a scanning tunable laser source. The normalized measured transmission spectrum of the circuit at room temperature is shown in Fig. 3.23b. The λ_{res} notches of the RMs are marked with numbers whose color represents their target operational wavelength. As was defined by design, it is confirmed that the resonance notches have a spacing of 5 nm and the RMs FSR is still 20 nm. The RMs are not aligned with their target λ_{laser}, as already remarked. This alignment is achieved with the thermal tuning control loop, as shown in Fig. 3.23c. For testing purposes, the correspondence between RM and λ_{laser} is sometimes freely chosen for convenience. However, in the final system each RM needs to operate at a specific λ, for interoperability between the FE and BE channels.

3.5.3 High speed characterization

The high-speed characterization of the 4-channel circuit included the measurement of the high-speed eye diagrams for all four RMs at 25 Gbit s^{-1}. The setup that was employed for this purpose is shown in Fig. 3.24a. It comprised the constructed 4-channel laser source based on the four multiplexed external lasers, the circuit and at the output an optical amplifier and the high-speed scope. The electrical driving signal is provided by the pattern generator. Given the availability of the equipment in the lab, we measured one eye diagram at a time, connecting the scope to a different channel output with the help of a demultiplexer. The results for all RMs are shown in Fig. 3.24b. The measurements show good uniformity among the four channels [10].

3.6 Conclusions

In this chapter, we introduced the concept of a SiPh based transmitter that employed RMs for the high-speed modulation of light. The different test-boards that were assembled for the characterization of the RM and Tx are then presented. The RM was fully characterized with measurements of its output spectra and figures of merit. This work allowed to perform an extensive characterization of the Tx, that included both DC measurements with low and high input power, as well as high-speed measurements, and characterization of the self-heating effect and µ-heater. This validates the high-speed operation of the Tx and its performance characteristics that are well in agreement with the values extracted

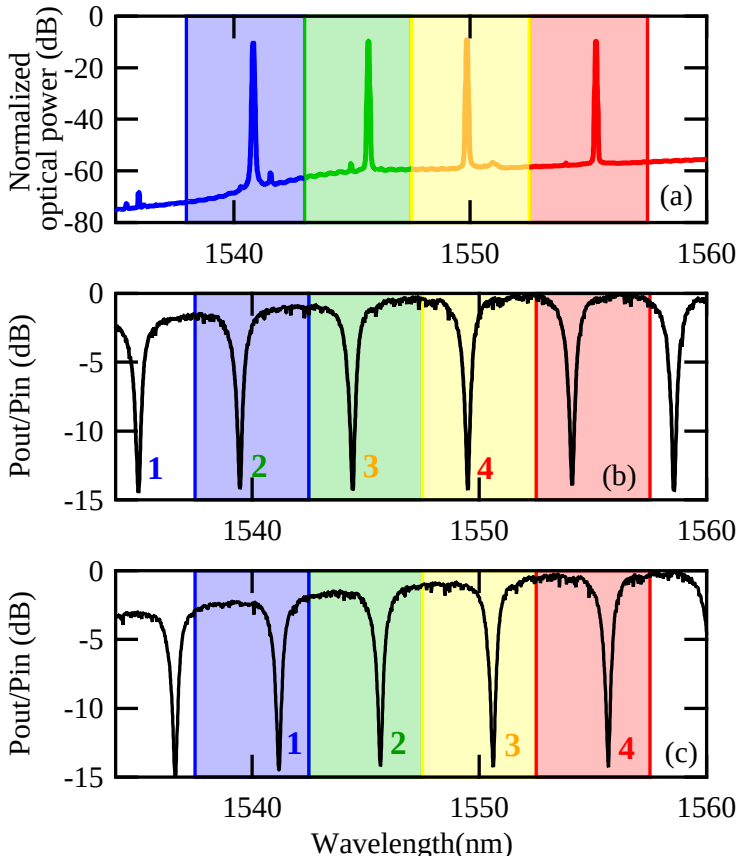

Figure 3.23. *(a) The 4-channel external laser source spectrum, normalized to the maximum power. (b) Pout/Pin of the 4-channel Tx at room temperature and (c) after the tuning process.*

from simulations. The development of the SiPh Tx also includes the design and characterization of a 4-channel circuit based on 4 cascaded RMs that can be utilized in WDM schemes. As a first step, the DC and high-speed characterization of this 4-channel circuit was performed and validated its spectral characteristic and high speed operation. Overall, these measurements constitute a complete characterization of the SiPh Tx and its components. This was necessary first of all for understanding the SiPh platform limitations and performance and understand what optimizations and improvements are required from a design and fabrication process aspect, to meet the application requirements. This way the next PICs that were designed so far and will be designed in the future can take advantage of this valuable experience to improve the components. At the same time, the complete characterization of the Tx allowed to successfully operate the Tx test vehicles that enable further testing, characterization and development in higher levels. This opens the way to investigate system challenges that need to be addressed for such a SiPh TRx to operate, like the thermal tuning and the polarization management.

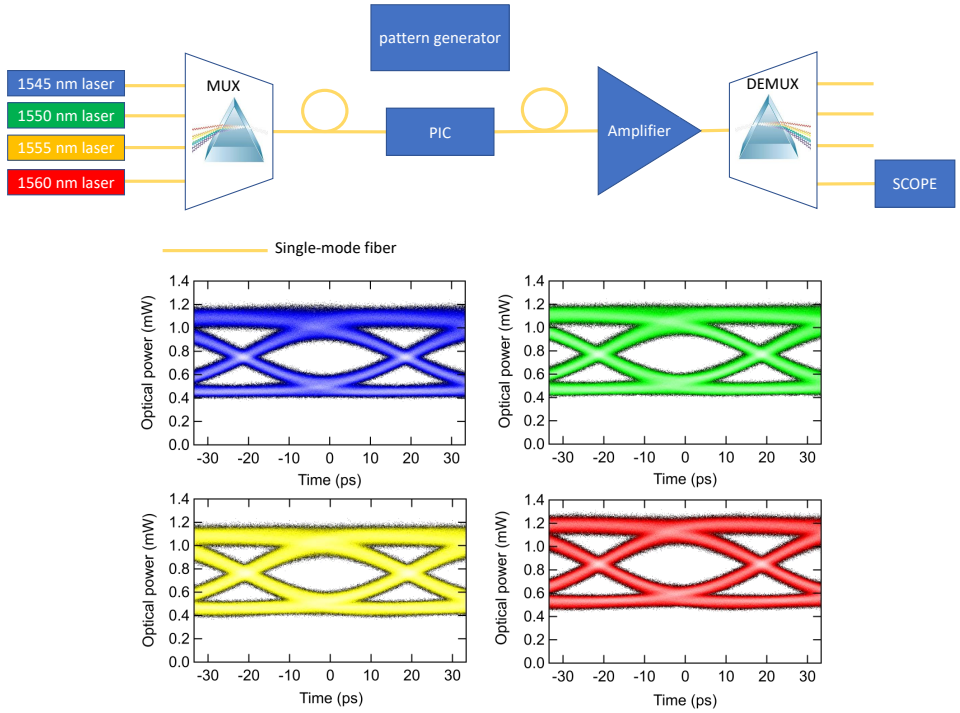

Figure 3.24. *(a) The test setup for measuring the high-speed eye diagrams of the 4-channel circuit (b) The measured eye diagrams of the four RMS of the 4-channel circuit, at* 25 Gbit s^{-1}.

Bibliography

[1] G. Li, X. Zheng, H. D. Thacker, J. Yao, Y. Luo, I. Shubin, K. Raj, J. E. Cunningham, and A. V. Krishnamoorthy, "40 gb/s thermally tunable cmos ring modulator," *The 9th International Conference on Group IV Photonics (GFP)*, pp. 1–3, 2012.

[2] B. Ouyang, Y. Xing, W. Bogaerts, and J. Caro, "Silicon ring resonators with a free spectral range robust to fabrication variations," *Opt. Express*, vol. 27, pp. 38698–38707, Dec 2019.

[3] W. Bogaerts, P. De Heyn, T. Van Vaerenbergh, K. De Vos, S. Kumar Selvaraja, T. Claes, P. Dumon, P. Bienstman, D. Van Thourhout, and R. Baets, "Silicon microring resonators," *Laser & Photonics Reviews*, vol. 6, no. 1, pp. 47–73, 2012.

[4] H. Yu, M. Pantouvaki, P. Verheyen, G. Lepage, P. Absil, W. Bogaerts, and J. Van Campenhout, "Silicon dual-ring modulator driven by differential signal," *Optics letters*, vol. 39, no. 22, pp. 6379–6382, 2014.

[5] S. Agarwal, M. Ingels, M. Pantouvaki, M. Steyaert, P. Absil, and J. Van Campenhout, "Wavelength locking of a Si ring modulator using an integrated drop-port OMA monitoring circuit," *IEEE Journal of Solid-State Circuits*, vol. 51, no. 10, pp. 2328–2344, 2016.

[6] M. J. Shin, Y. Ban, B.-M. Yu, J. Rhim, L. Zimmermann, and W.-Y. Choi, "Parametric Characterization of Self-Heating in Depletion-Type Si Micro-Ring Modulators," *IEEE Journal of Selected Topics in Quantum Electronics*, vol. 22, no. 6, pp. 116–122, 2016.

[7] M. Novarese, S. R. Garcia, S. Cucco, D. Adams, J. Bovington, and M. Gioannini, "Study of nonlinear effects and self-heating in a silicon microring resonator including a shockley-read-hall model for carrier recombination," *Opt. Express*, vol. 30, pp. 14341–14357, Apr 2022.

[8] X. Zheng, Y. Luo, G. Li, I. Shubin, H. Thacker, J. Yao, K. Raj, J. E. Cunningham, and A. V. Krishnamoorthy, "Enhanced optical bistability from self-heating due to free carrier absorption in substrate removed silicon ring modulators," *Optics express*, vol. 20, no. 10, pp. 11478–11486, 2012.

[9] "Nrz vs. pam4 modulation techniques." https://community.fs.com/blog/nrz-vs-pam4-modulation-techniques.html [Accessed: (13/07/2023)].

[10] C. Scarcella, S. Detraz, M. Lalović, L. Marcon, L. Olanterä, T. Prousalidi, U. Sandven, C. Sigaud, C. Soós, and J. Troska, "System development of silicon photonics links for cern experiments and accelerators," *Journal of Instrumentation*, vol. 18, no. 03, p. C03002, 2023.

Chapter 4

Thermal Tuning

4.1 Motivation

RMs are resonant devices whose λ_{res} depends on their optical path length. The optical path length is in turn determined by the geometrical parameters of the RM (ring radius, waveguide dimensions) as well as by the effective refractive index of the Si waveguide. As mentioned in Sec. 2.1.3 Silicon exhibits a strong TOE meaning that the refractive index of Si waveguides depends on the temperature. It is therefore evident that the λ_{res} of an RM will exhibit a strong temperature dependence [1]. For the RMs available from our PIC we have experimentally measured the λ_{res} shift with temperature and as shown in Fig. 4.1 (right axis) have verified that it is linear and is given by Eq. 4.1

$$\frac{\Delta\lambda_{res}}{\Delta T} = 70\,\frac{\text{pm}}{^{\circ}\text{C}} \tag{4.1}$$

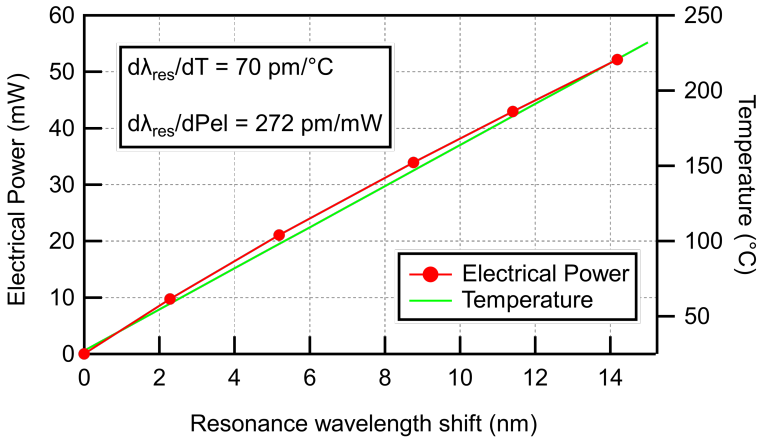

Figure 4.1. *The measured resonance wavelength shift of the SiPh RMs from PICv2 varying the temperature (in green) and varying the electrical power of the integrated micro-heater (in red).*

This showcases that even a small change of 1 °C in the temperature of the RM will significantly affect its λ_{res}. Given that the region around the optimal operating point of the RM where the OMA remains adequate and close to its maximum value is narrow (there is a tolerance of around 200 pm), any small change in the ambient temperature results in misalignment between the λ_{res} and λ_{laser} and consequently degradation of the optical modulated signal.

At the same time, process variations induced by the manufacturing process affect the geometrical parameters of the device [2]. The final dimensions of RMs across the wafer varies from the specified ones and their λ_{res} shows a subsequent variation from its target value. However, every RM is designed and needs to be operated at a specific wavelength. This in turn requires a specific λ_{res}. Therefore, the inherent variation of the RM geometrical parameters due to the process variations can also detune the λ_{res} from the target λ_{laser}. Last but not least, the optical sources, depending on their quality and operational conditions might present variations: the λ_{laser} can also deviate from its nominal value due to thermal drifts and fabrication variations.

In all the above cases the result is the same: the λ_{res} is detuned from the λ_{laser} and the RM is no longer operated at the optimal point where the OMA is maximum. This might cause degradation of the optical signal or complete loss of modulation. A tuning mechanism is therefore necessary to compensate for the aforementioned effects, adjust the λ_{res} of the RM so that it is aligned with the λ_{laser} and ensure stable operation at the optimal point irrespective of external variations. Some types of variations like the change of the device temperature are continuous so the correction mechanism needs to operate continuously as well. It should include a feedback process that allows to monitor in real time the operating condition of the RM and if it deviates from the targeted one, apply a correction to the system. Such a feedback control system can be realised with a sensor-controller-actuator architecture.

Multiple methods exist for realizing this type of feedback control systems. The choice of the type of sensor, controller and actuator depends on the application and the system requirements. The different options will be analyzed in Sec. 4.2. In all cases, the common goal of the tuning technique is to perform the wavelength locking between the λ_{res} and λ_{laser} and stabilize the RM resonance so that the stable operation of the RM at its optimal point is achieved. The techniques that are more relevant to our application will be analyzed in section, Sec. 4.3.

4.2 Architecture and components of feedback tuning techniques

Different approaches exist for the realisation of a feedback mechanism for active tuning or the λ_{res} of RMs, each including the use of various architectures and building blocks for negative feedback control systems. The choice of the type of sensor, controller and actuator is not unique and depends on the specific application and systems requirements. The same is true for complete system architecture and principle of operation. In this section we will analyse the different types and principles of operation for the sensor, controller and actuator.

The sensor of the feedback control loop aims to acquire and monitor the feedback signal of the closed loop system. For this application, the sensor can monitor one of many parameters of the RMs such us the BER, the temperature, the OMA, the average power in the resonator or optical power in some other part of the circuit, the bit statistics, an error signal or the transmitted signal. The sensor type is chosen based on the feedback signal nature. For monitoring optical power, average power, bit statistics, transmission signals or OMA, usually low or high speed photodetectors or receivers are required respectively, like photodiodes. In such cases, the feedback signal can be acquired from either the trough-port of the RM, or the drop-port if one is available. For monitoring the temperature on can use a temperature sensor.

The controller is responsible for carrying out the control functionality: record the feedback signal produced by the sensor, compare it with a reference value that has been previously defined, and produce the error value that is then used to accordingly operate

the actuator. Various controller types are available with most common solutions being PID and bang-bang controllers [3]. A schematic representation of a PID controller is shown in Fig. 4.2. The feedback value is subtracted from the setpoint (reference value) to calculate the error. Given this error and the proportional (P), integral (I), derivative (D) gains of the controller, the P, I and D terms are computed. The PID output is the sum of these terms and it corresponds to the actuator input [4]. Concerning the PID controller hardware implementation, this is another open question that depends on the application requirements. Depending on the required BW, the controller can be implemented on an FPGA, microcontroller, ASIC, or even in software running on a PC. This will also define if it will be an analog or digital controller.

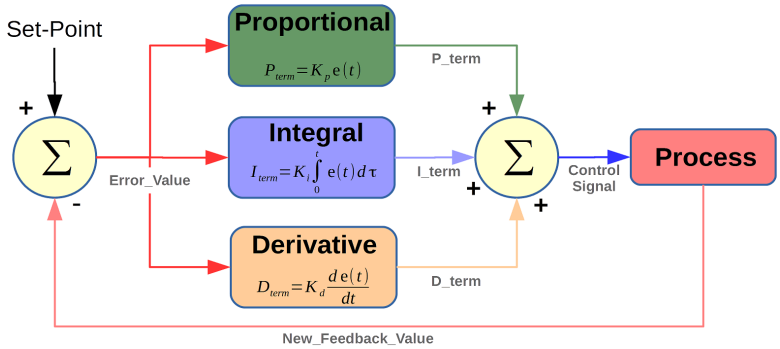

Figure 4.2. *Schematic representation of the operation of a PID controller. Source: [5]*

Finally, the actuator is responsible for adjusting the operating point of the RM and aligning the λ_{res} to the λ_{laser}. Multiple approaches are available for controlling the RM. Typically they involve thermal tuning exploiting the thermo-optic effect. This is achieved with the use of integrated µ-heaters as actuators that can actively control the device temperature and change its λ_{res}. This solution is more often adopted thanks to its simplicity and easy implementation and operation. Other solutions include bias-based tuning exploiting the electro-optic effect [6, 7]. This is achieved through electrical drivers. However this approach interacts with the modulated data, disturbs the RM operation and might affect the quality of the transmitted signal. In general, the various options are based on different principles of operation and require different hardware implementations.

4.3 Review of available techniques for the tuning of RMs

In this section we analyze the different techniques that are proposed in literature and are usually employed for the tuning of RMs.

4.3.1 Athermalization

There have been attempts to reduce temperature susceptibility of micro-ring resonators using negative thermo-optic materials as an overlay on micro-ring. These attempts require extra fabrication steps and do not fit standard CMOS process flows. Also, any process variation causes imperfect athermalization and fluctuations in resonance frequency [8].

4.3.2 Bit-error rate monitoring

The bit-error-rate monitoring based technique allows wavelength locking and resonance wavelength tuning of RMs by monitoring the BER of the optical modulated signal [9]. The block diagram of such a control system is shown in Fig. 4.3. The RM includes a drop port and a local Rx connected at its output is used for monitoring the optical signal that is equivalent to the through port optical modulated signal. Then an error detector compares the local Rx output with the electrical modulating signal provided by the driver, to calculate the BER. This is the error signal of the controller. According to the error value the operating point of the RM is adjusted and aligned with the λ_{laser} with the help of a micro-heater, so that error-less transmission is achieved at the remote link Rx. The controller circuit uses simple logic. Due to the nature the feedback loop that uses the BER as feedback signal, this system can inherently compensate for all types of variations, either in the RM temperature, λ_{laser} or fabrication process related. Also, this feedback control loop is insensitive to variations of the input power level and other link parameters that might vary with time, like the heater aging. No dithering or calibration of the system is required, and not reference value that might vary with time is necessary. This technique is suitable for RM stabilization, but cannot be used for filters. However, the biggest drawback of this method is that it requires high speed logic for recovering the BER which not only will result in high power consumption, but will also require the integration of high speed electronics in the front-end system. It is also a not scalable solution for the case of a WDM scheme. Therefore, is it not suitable for our application.

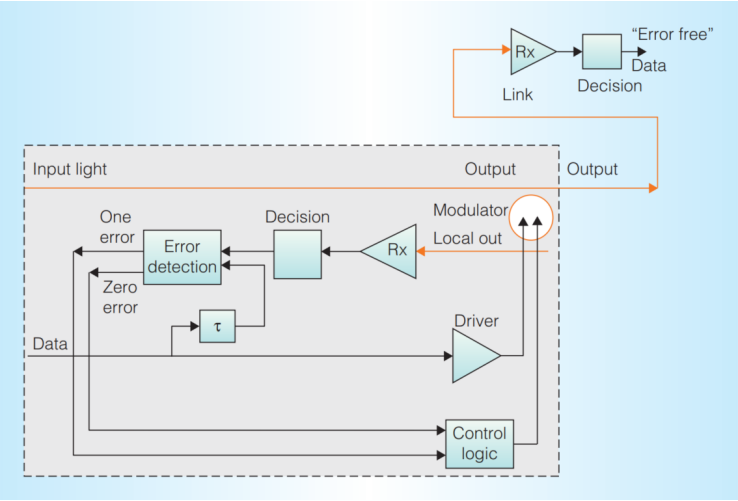

Figure 4.3. *Block diagram of the BER-monitoring based control technique. The error detection is achieved with the use of a local Rx that compares the RM drop-port signal with electrical modulating signal to measure the BER. The BER is the error signal that is used to then adjust the operational point of the RM and achieve errorless transmission at the remote link Rx. Source: [9].*

4.3.3 Temperature sensing

Another approach for the thermal tuning of RMs is based on temperature sensing. Typically this type of RM tuning techniques involve the use of an integrated temperature sensor that allows for the direct monitoring of the RM temperature, along with an integrated micro-heater for adjusting the RM temperature [8, 10]. The feedback signal of this controller is the temperature. Temperature error signal is defined as the difference between the measured temperature and the target temperature. Such a control system therefore requires a reference value to compare the feedback signal with. Although this technique can compensate for temperature fluctuations, it cannot compensate for the variation of λ_{laser}. At the same time, the design of the integrated temperature sensor and micro-heater is a complicated process that requires trade-offs between the heater efficiency and temperature sensing accuracy. This is because both components require to be in close proximity to the RM waveguide so they cannot be optimized at the same time. The presence of a heater near the sensor limits the reliability of the measured temperature since the heat dissipation caused by the micro-heater will inevitably disturb the sensor. Temperature sensing with the high accuracy required for the tuning of high-Q RMs has not yet been demonstrated. Overall it is evident that this technique presents important drawbacks and is therefore not suitable for our application.

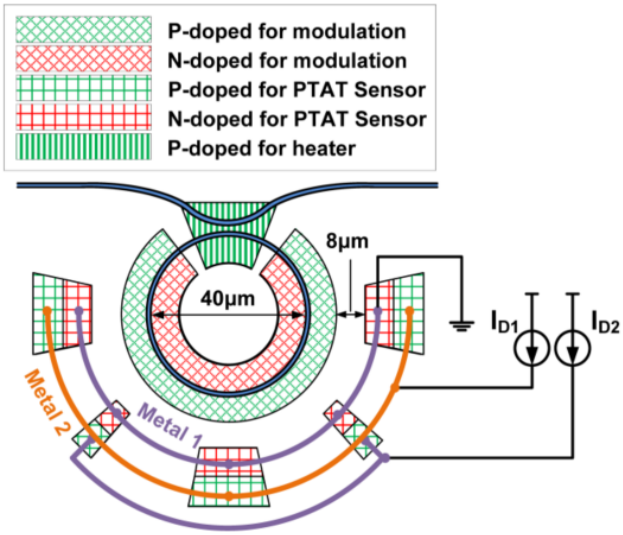

Figure 4.4. *The structure proposed in [8] for the thermal tuning of a RM, based on an integrated temperature sensor for temperature monitoring, and an integrated micro-heater for active temperature control of the RM.*

4.3.4 Dither locking

The wavelength locking and thermal stabilization of RMs can be implemented using dithering signals [11]. The main principle of this method is the use of dithering signals to break the RM symmetry. This is required because typically, as it has already been described, the optimal operation of the RM is achieved when λ_{res} is almost aligned with the λ_{laser}, with a small offset of some pm. This operational condition is characterized

by a specific optical power of the transmitted signal. However, it is difficult to lock the RM to the λ_{laser} just by measuring the transmitted optical power, because the direction of λ_{res} shift is ambiguous in relation to the transmission of optical power. This happens because of the symmetric response of the RM around its resonance. Depending on which side of the resonance the λ_{laser} is at, a red-shift in the λ_{res} can cause either the increase or decrease of the transmitted optical power and vice-versa. This means that if the change of the transmitted power is our error signal, then its sign does not uniquely determine what correction needs to be applied to the RM (red-shift or blue-shift of λ_{res}). The purpose of the dithering signals approach is to generate an anti-symmetric error signal. The dithering mechanism that is applied thermally is illustrated in Fig. 4.5a. A small modulation is applied to the RM temperature which in turns produces a small modulation of the optical signal. This optical modulation, depending on which side of the RM resonance the λ_{laser} is found, will either be in phase or out of phase with the driving signal. The mixing of the signals, namely the driving dithering signal and the the modulated optical signal allows for acquiring this information, as shown in Eq. 4.2.

$$cos(f_D t) \otimes cos(f_D t + \phi) = \frac{1}{2}[cos(2f_D t + \phi) + cos(\phi)] \tag{4.2}$$

where f_D is the frequency of the dithering signal, and ϕ is the relative phase (0 or π) of the modulated optical signal.

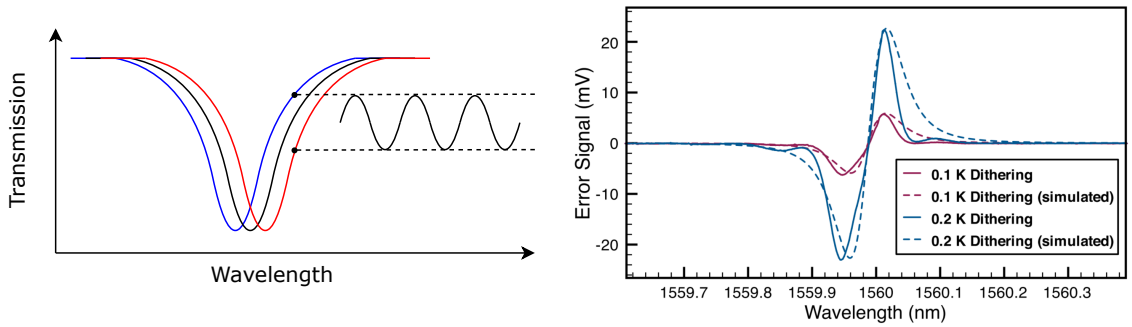

(a) **(b)**

Figure 4.5. *(a) Illustration of the small dithering signal that is thermally applied to the RM, and the resulting modulation of the optical signal. (b) An example of produced error signals from a RM (simulations in dashed) as it is subjected to thermal dithering signals of varying magnitude. Source [11].*

After filtering the higher harmonic we are left with the sign of the $cos(\phi)$ term that represents the dc component. This sign indicates the position of the λ_{res} with respect to λ_{laser}. This value is the desired anti-symmetric error signal, as illustrated in Fig. 4.5b.

This technique offers many advantages. First of all, it allows for the realization of scalable, low-cost and energy efficient systems that are not affected by fluctuations in the input optical power. Moreover, there are no inherent features of the dithering technique that render it non-compatible with the use of WDM schemes. The dithering signals are locally applied to each RM and adjacent rings, even when cascaded, are not affected. Additionally, the use of multiple distinct dithering frequencies for the different RMs allows

to exploit the orthogonality principle, shown in Eq. 4.3.

$$\int cos(f_n t)cos(f_m t)dt = 0, f_n \neq f_m \tag{4.3}$$

Given this principle there is no crosstalk in error signals of different RMs even when the RM spectral responses overlap. Hence, this technique can be implemented in WDM systems. Such a thermal tuning system is also simple to realize since it does not require additional photonic structures. Also, this technique does not require a reference and can uniquely determine tuning direction.

However, the use of the thermal dithering signal reduces the ER of the RM, which is an important parameter that should be maximized in our application for ensuring high modulation efficiency and optimal operation. Moreover, this dithering signal will inevitably impact the integrity of the optical data signals, causing broadening of the one level and reduction of the OMA of the transmitted signal. This in critical for application that require very precise locking, and will degrade the RM performance. At the same time, the electronics required for recovering the error signal are complex [11] (e.g. lock-in amplifier). However, the most important downside is that dithering techniques that rely on the modulation of the RM temperature which in turns produces a modulation of the optical signal, are affected by the self-heating effect. The self-heating effect induces changes in the temperature and optical signal of the RM. These changes will interact with the thermal tuning technique that relies on precise control of the RM's optical signal to achieve wavelength tuning. Self-heating introduces a dynamic and often nonlinear component to this relationship. It can introduce instability and hysteresis in the thermal response of the silicon modulator. Changes in the modulator's temperature may not instantaneously follow changes in the applied dithering signals, leading to hysteresis effects and potential difficulties in achieving accurate and repeatable tuning. Calibrating the dither locking system becomes more complicated in the presence of self-heating. The relationship between the applied dither signal, the resulting temperature changes, and the modulator's response may require careful calibration to ensure accurate and reliable performance. More specifically, the relationship between the applied dither signal and the resulting changes in the modulator's resonant wavelength may become nonlinear due to self-heating. This nonlinearity can complicate the control algorithms used in the dither locking feedback loop, potentially requiring more sophisticated compensation strategies. More studies are required to verify if dither locking based tuning techniques are compatible with applications with high input power, where the self-heating effect is important. For these reasons, although this method is interesting, especially in the case of a WDM scheme, further investigation would be required to verify if the consequent disturbance in the RM performance and interaction with self-heating are acceptable.

4.3.5 Balanced homodyne locking

Balanced homodyne detection is another method that can be used for the precise interrogation of the phase and amplitude status of a resonant cavity without causing any

disturbance either to the signal itself or to the resonant cavity. It is therefore a technique that can be used for the wavelength tuning of RMs [12, 13].

Balanced homodyne locking (BHL) is based on the balanced detection of an unbalanced MZI that has the RM coupled to one of its arms. An optical phase shifter is placed in the other arm, allowing to adjust the locking point of the RM. A schematic diagram of such a BHL-based control loop implementation for the resonance wavelength tuning of a RM is shown in Fig. 4.6. The principle of operation is the following. First, the optical input (denoted with a_0) that would typically be directed to the RM is split in two paths at the MZI input using a directional coupler. A small percentage of the power is directed towards the arm where a phase shifter is inserted. The power at its output is denoted with a_1. The rest of the optical power is directed towards the other arm where the RM is placed. The amplitude at the RM output is denoted with a_2. a_1 is affected by the the phase introduced by the top-arm phase shifter. The RM will affect both the phase and the amplitude a_2 of the signal that goes through the bottom arm. The two paths are then recombined using a 50% directional coupler. The amplitudes at the two output ports of this coupler are denoted with a_3 and a_4. The balanced detector at the MZI output subtracts the two signals a_3 and a_4 to generate the error signal Y. This is the error signal used then in the feedback loop to tune the RM.

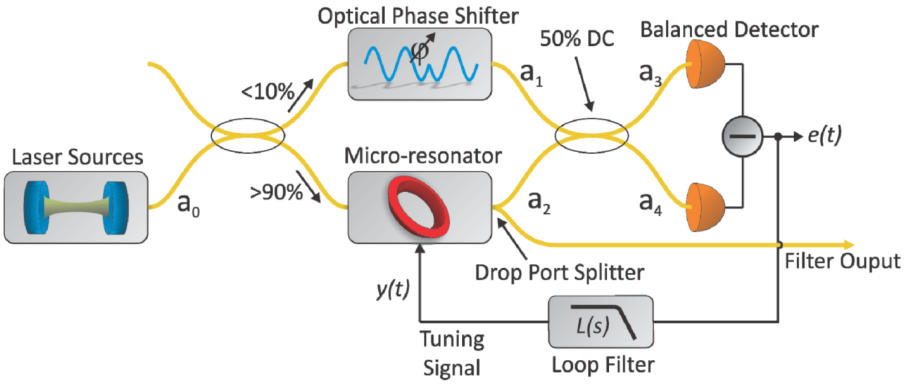

Figure 4.6. *Schematic diagram of a thermal tuning control loop based on the balanced homodyne locking method. It is based on a MZI. This is formed by splitting the input light into two separate paths with splitting ratios of 90% and 10% that go to the RM and a phase shifter respectively. Then the power is recombined to a balanced photodetector with the help of a 50% directional coupler. The signal recorded by the photodetector is the error signal e(t) and it is used to drive the loop filter to tune the RM. The locking point can be adjusted by varying the phase shift of the top MZI arm. Source [13].*

This system is compatible with WDM implementations. This is because when other wavelengths are present in the system they will beat with the filtered signal, a_2, at frequencies above the band pass of the photodetector or the loop filter. A zero background error signal will be maintained because the spurious signals will be canceled out by the balanced detector.

Fig. 4.7 shows two example plots of the BHL error signal for different phase shifts φ, of 0 and $\pi/4$ rad. In these plots it is easy to note the shift in locking point. Fig. 4.7a shows the error signal with zero phase shift. The plot has an odd shape centered around

the resonance. This φ value is employed in the case of filters based on ring resonators, where locking exactly at the point of resonance is targeted. By locking the loop to the zero crossing of the error signal, intensity noise fluctuations do not impart a shift in locking point. By varying the phase with the phase shifter, the zero crossing lock point can be shifted to the side of the resonance, as illustrated in Fig. 4.7b. In this way, a RM can also be locked with the BHL technique at its optimal operating point that is found a bit off the resonance. This is achieved for a φ of π/4 rad.

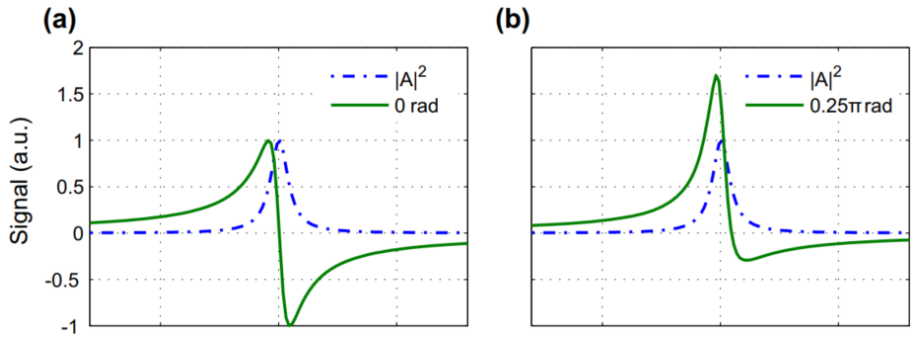

Figure 4.7. *An example of the response of a RM (in dashed blue lines) and the corresponding calculated BHL error signals (in green lines) for different relative phase shifts (φ) in the MZI. (a) The case when* $\phi = 0$ rad *that corresponds to the ideal locking point for a ring resonator (b) The case when* $\phi = \pi/4$ rad *that corresponds to approximately the ideal locking point for a RM. Source [13].*

The BHL method is a very convenient method for the tuning or RMs. As it was already described it is a compact method that is insensitive to fluctuations of the input power amplitude and is also fully compatible with WDM implementations. It does not require an arbitrary reference to lock which simplifies the tuning process. Moreover, it does not disturb the RM and does not cause any degradation of the modulated optical signal. However, this method requires a complicated photonic circuit that includes the MZI structure, phase shifter and balanced photodiode. The extra phase shifter implies higher electrical power consumption of the Tx. The thermal cross-talk between the RM heater for adjusting its temperature and the thermal phase shifter can cause degradation of the tuning process. Last but not least, BHL is affected by the self heating effect of the RM that will also change its transfer function for high input power. For these reasons, although it is a very interesting method, it was not chosen for realising a RM control loop for our application.

4.3.6 Bit-statistical tuner

A thermal tuner can also be based on the extraction of bit statistics acquired from the optical modulated data stream. The bit statistics processing allows to perform decoupled optical one-level and zero-level tracking. This can be achieved with a low-speed analog front-end. In other words, such a tuner can extract the one and zero optical power levels without the need of high-speed receivers, which have high power consumption and limited sensitivity. After extracting the one and zero levels a controller can take over to lock these levels to a predefined optimal reference value. The advantage of this method compared

to average power monitoring is that it also works for arbitrarily non-dc-balanced data. In the case of a controller based on average power monitoring, because of the on-off keying nature of the transmitted data, the controller cannot distinguish between a change in power due to a drift in the λ_{res} of the RM from changes in power due to a change in the ratios of zeros-to-ones. However, the circuit required in a bit-statistical tuner is more complex from the one required from simple average power monitoring [14]. In our application we work with dc-balanced data therefore there was no advantage in choosing to implement a bit-statistical controller compared to an average power monitoring one.

4.3.7 OMA monitoring

OMA monitoring is another technique that can be employed for the wavelength locking and thermal tuning of a SiPh RM. Direct OMA monitoring can be performed by either tapping a small percentage of the optical power at the through-port of the RM, or at the drop port if one is available. Typically the OMA monitoring is performed by a high-speed Rx, like a high-speed PD that allows to compute the OMA from the one and zero levels of the transmission, as $OMA = P_1 - P_0$. The principle of operation is the following: a sensitive OMA monitoring circuit is used which effectively drives a feedback loop to control an integrated, local heater implemented around the ring. The heater, in turn, tunes λ_{opt} to align with λ_{las} and thus stabilizes the optical transmission at the maximum OMA, as shown in Fig. 4.8 [15].

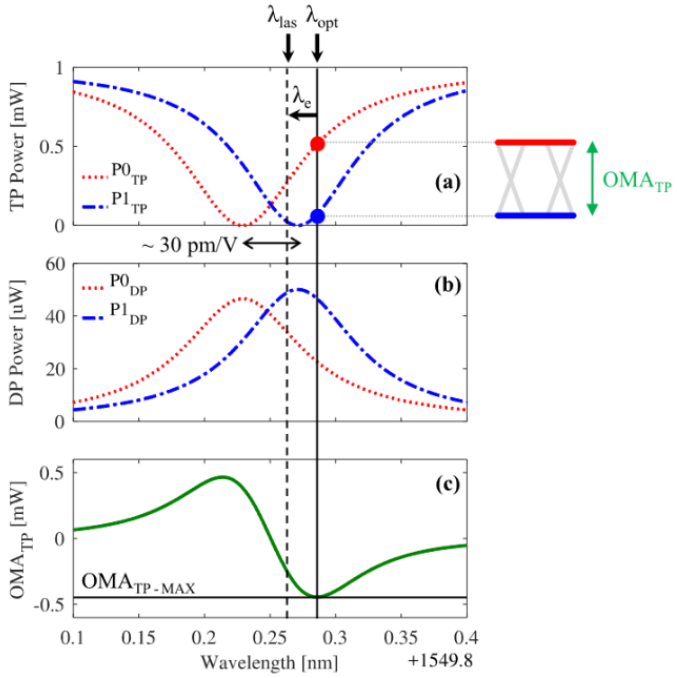

Figure 4.8. *Simulated transmission characteristics of an RM showing the need of wavelength locking. The optimal operating point coincides with the point where the OMA becomes maximum. Source [15].*

Given that one of the most straightforward figures of merit of the RM's operating point is the OMA, and typically the optimal operation of an RM is considered as the operation

at the point where the OMA maximizes, this technique is the most direct way to thermally stabilize a RM. The direct OMA monitoring enables automatic compensation for process variations, it is robust to the variations in the input laser power and wavelength and also has the potential of being low-power. At the same time, it also works in the case of non-DC-balanced modulation data. However, its main disadvantage is the requirement for high-speed Rx for the OMA monitoring that causes increased power consumption in the FE and a large area on chip. These requirements are not compatible with our application.

4.3.8 Monitoring of the average power

Instead of the direct monitoring of the RM OMA, another technique that can be used for thermal tuning is based on the average power monitoring. The measurement of the average power can be performed at the through port by tapping a small percentage of the transmitted signal. However, since this might disturb the signal, one can also measure the average power at the drop port, if the RM includes one.

The average power monitoring is equivalent to the OMA monitoring. This can explained with the help of Fig. 4.9 that shows the simulated transmission characteristics of a RM at the through port and drop port. The optimal operating point of the RM is defined as the point where the through port OMA (OMA_{TP}) becomes maximum. As can be seen in Fig. 4.9(b) and (d), the maximum OMA_{TP} coincides with the maximum OMA at the drop port (OMA_{DP}). This means that instead of working at the through port and risking of disturbing the transmitted signal, one can equivalently work with the drop port signal for the thermal tuning. At the same time, as it is obvious in Fig. 4.9(d) and (e), the average power at the drop port ($P_{avg\text{-}DP}$) changes linearly around the maximum OMA_{DP} point and there is a characteristic value of the $P_{avg\text{-}DP}$ that corresponds to the maximum OMA_{DP} point (and equivalently to the maximum OMA_{TP}). This means that instead of using a high-speed Rx for the direct monitoring of the OMA, one can equivalently monitor the $P_{avg\text{-}DP}$ to get an indirect indication about the OMA. By locking on this characteristic value of the average drop port power the same goal of operation at the maximum OMA point can be achieved, in a much simpler way. The $P_{avg\text{-}DP}$ can be monitored with a low speed photodiode that can be easily integrated in a FE PIC without requiring large on chip area or increasing the power consumption. Moreover, the average power of the drop-port transmission not only is linear around the optimal operating point, but it also shows relatively large variations even when the ring is effectively wavelength locked at the maximum OMA, meaning that the slope of the $P_{avg\text{-}DP}$ is large around the optimal point. This allows to tune the RM at its optimal point with very big accuracy. Overall, the principle of operation of the drop port average power monitoring technique is the following: a PD connected at the drop port output can be used as the sensor, to record the average drop port power that is the feedback signal of the closed loop feedback controller. This feedback signal is then compared with the reference value (characteristic value of $P_{avg\text{-}DP}$ that corresponds to max OMA point) to produce the error. Given the error, a correction is then applied to the system through an integrated micro-heater, to compensate for any fluctuations, align the λ_{res} with the λ_{laser} and ensure operation at the optimal point. The

reference point can be easily computed at the beginning of the process, since for a given RM the characteristic value equals a fixed percentage of the maximum value of the $P_{avg\text{-}DP}$ that can be easily measured with the PD.

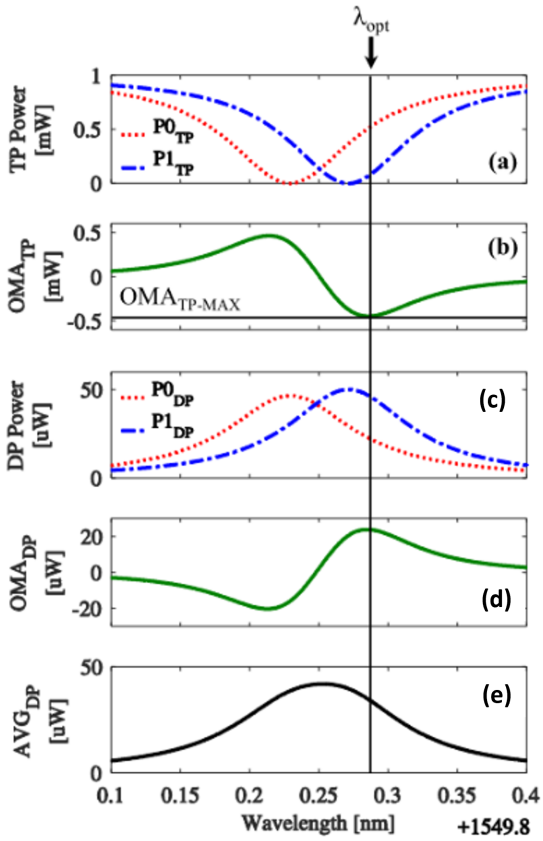

Figure 4.9. *Simulated transmission characteristics of a ring modulator, showing the transmission and OMA at the through port and drop port, as well as the drop port average power. Source [15].*

This technique is especially useful for our application, and compatible with the FE requirements that would render the direct OMA monitoring impossible. It requires simple photonic (PD) and electronic (integrated micro-heater) components in the Si PIC, and the necessary logic that reads the PD signal, computes the error and the correction to be applied in the system and biases the heater can be easily implemented in a simple ASIC block, that can be integrated in the FE without adding a big overhead in the power consumption. Nevertheless, the technique has its own disadvantages. First of all, it does not work with non-DC-balanced data. In such a case the average power depends on the percentage of ones and zeros in the data stream that does not remain constant, therefore the characteristic $P_{avg\text{-}DP}$ will not be constant. Fortunately in our system, we work with DC-balanced data, therefore this downside does not affect us. On the other hand, this method requires an arbitrary reference (the characteristic value of $P_{avg\text{-}DP}$ that corresponds to max OMA point) that needs to be computed. However, if the link intensity drifts this value will change. This downside can be addressed by periodically recalibrating the reference value, which is feasible in our system.

All in all, this technique has been identified as the most suitable thermal tuning method

so far for our application. It is very simple to implement, and it is believed that the aforementioned disadvantages can be successfully addressed. One important concern is the compatibility of this method with WDM implementations that generates extra complexity in the system, but possible solution are proposed in this chapter in this regard. Therefore, in the rest of the thesis the wavelength tuning of the RMs is based on this technique. Also, any considerations about future design and implementation choices are also based on the use of this thermal tuning technique.

4.4 Feedback controller for thermal tuning based on average power monitoring at the drop port

For our application, after evaluating the available options for the realization of a feedback control loop for the thermal tuning of RMs, and taking into consideration their advantages and drawbacks, we have chosen to adopt a feedback controller based on average power monitoring at the drop port. This method combines many advantages that are necessary for our system. It requires low speed and simple electronics that are potentially low power. The DC readout of the feedback signal can be performed by a slow and low power ADC while the biasing of the µ-heater can be performed by a DAC. The available µ-heaters have low power consumption. This technique requires an arbitrary reference that must be recalibrated at the power up of the transmitter unit. The recalibration functionality can be integrated in the FE electronics and will not introduce extra complexity. This method requires a PID controller that can be easily implemented on an FPGA, or integrated as an ASIC block with the rest of FE electronics, requiring low power and having simple functionality. Moreover, it is a scalable method and fully compatible with WDM schemes. Overall, it is compatible with our system and it was identified as the best choice among the available alternatives. Given the general feedback control loop architecture, in the following subsections the detailed system requirements will be presented, as well as the physical implementation and proposed design for the final version that will be used in the transceiver prototypes for HEP.

4.4.1 System requirements

The thermo-optic effect that affects the RM λ_{res} imposes the need for thermal tuning. It is a slow effect with bandwidth lower than 10 kHz. On the other hand, the possible drift of the λ_{laser} are also slow variations with low bandwidth. Consequently, the BW required for the thermal tuning control loop that needs to compensate for these aforementioned variations is estimated at 100 kHz. This BW is expected to be sufficient, giving enough margin for the compensation of effects at frequencies lower than 10 kHz. Higher bandwidths would not offer any important advantage in the tuning accuracy, but would increase the power consumption and complexity of required electronics components.

The sensor of the feedback control loop in this application is the Ge PD connected at the drop-port output of the RM. The output of the PD is the drop-port photocurrent (I_{ph}). In the current RM designs from PICv2 that have a small gap between the ring and

drop-port, this I_{ph} is in the range of 1 mA. The Ge PD has $BW = 50$ GHz. However, for monitoring the drop-port average I_{ph} that corresponds to the drop-port average power, much lower BW is sufficient. The readout of the I_{ph} can therefore be performed with a much lower frequency. This frequency depends on the physical implementation of the control system and might be limited by the available read-out electronics. For the final system implementation we intend to use an ADC for the readout. However, since a ADC can read a voltage but not a current, we need to interpose a current to voltage converter between the PD and ADC. One solution would be to use a shunt resistor connected in series with the PD. A resistance of 1 kΩ would be sufficient to convert the I_{ph} in a voltage value with dynamic of 1 V. This voltage range of 0 V-1 V is chosen because it is compatible with most ADCs and with the power supply voltages available in FE electronics for particle detecors. Alternatively, in a CMOS ASIC control block a transimpedance amplifier can be implemented. This is simpler to implement and will allow to amplify the I_{ph} converting it into a voltage matching the ADC dynamic range. It is worth mentioning that in the designs following PICv2 we have increased the gap between the ring and drop-port. In these designs we expect a I_{ph} in the range of 1 µA. Although this value is much smaller, overall it is better for the RM performance since is taps almost 1000 times less power from the RM, being almost transparent for the transmitted eye diagram. With the smaller gap, the TP of the RM with voltage swing of 1 V is increased, resulting in a small reduction of the RM OMA. With such small I_{ph} it is no longer possible to use a shunt resistor or operational amplifier for the PD read-out. It is necessary to use a TIA as low-speed amplifier that simultaneously amplifies the I_{ph} and converts it to a voltage. However, this solution was included in our ASIC roadmap.

As already mentioned, the target BW for the I_{ph} read-out can be low. In the case of the final system implementation, a first estimation would be to use a ADC with sampling rate of 1 $\frac{\text{MS}}{\text{s}}$. This is probably a conservative estimation, since it is much higher that the thermal effect's BW. More studies on the speed of the signals than we need to compensate for are required. This sampling rate can also be achieved in FPGA based implementations. For initial implementations exploiting benchtop instruments lower closed loop BW is possible, in the range of some Hz that is a valid solution for static characterization in the lab.

As explained before, the read-out value of the actuator will be a voltage between 0 V and 1 V that corresponds to the average I_{ph}. There is one optimal I_{ph} value (setpoint) that corresponds to the maximum OMA point. The OMA maximizes at a specific point, but it has a plateau around this optimal point where it remains almost maximum, with deviation of less than 10%. This plateau region is highlighted in Fig. 4.10 and Fig. 4.11 with markers A and B, and is about 200 pm wide. This indicates that there is a 200 pm tolerance when it comes to the thermal tuning of the RMs, as near optimal performance in terms of OMA can be achieved is this 200 pm wide region. If we only consider the OMA at the operating point this would also greatly relax the I_{ph} setpoint. The I_{ph} values that correspond to the maximum OMA region are typically between $0.6 * I_{ph,max}$ and $0.8 * I_{ph,max}$ as shown in Fig. 4.10 with the markers E and F. However, another important parameter is the ER. The ER shows a steep slope around the optimal OMA region, as shown in Fig.4.10 and Fig. 4.11 with the green lines. If we were to lock the RMs at any point of this region this

would result in big fluctuations of the ER (and equivalent DC optical power) from 2 up to 4. However, it is better if also the ER remains relatively stable, or if at least it fluctuates in a smaller region. This is why eventually we would like to lock the RM with much bigger accuracy than 200 pm. Such a smaller region is marked in Fig. 4.11 with the markers E,F and G,H and it is around 25 pm wide. To have some margin we choose 10 pm as tuning accuracy of the RM operating point. This will results in both stable OMA and stable ER. To achieve this accuracy, it means that we need to be able to measure the feedback signal with 10 pm accuracy. A 10 pm wavelength accuracy corresponds to around a 1% of the measures ADC voltage (0.01 V) as it can be extracted from the previous plots. This means that we need at least 100 levels for the read-out ADC. We choose a standard 8-bit ADC that allows for the read-out of 256 different I_{ph} levels with step of 4 mV.

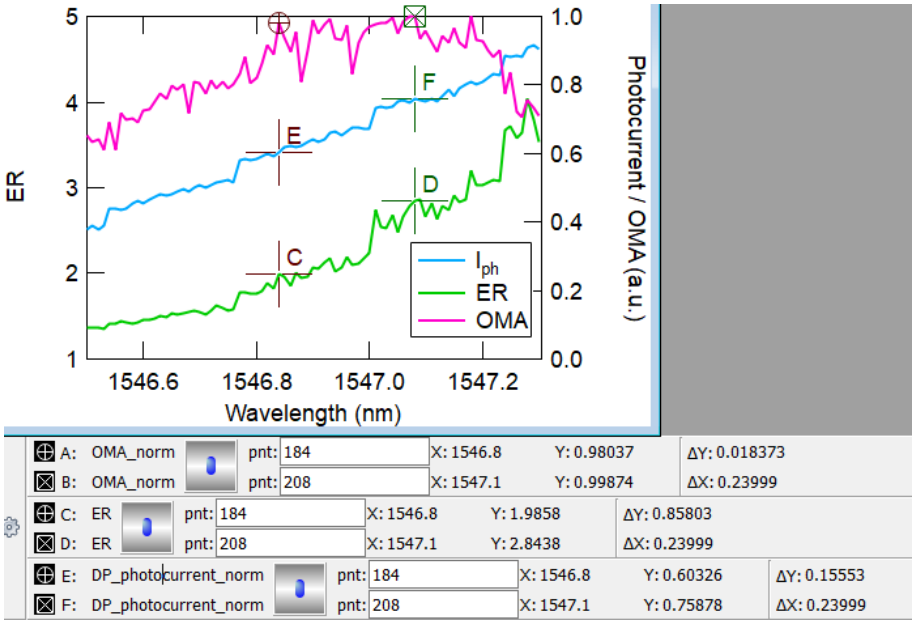

Figure 4.10. *The measured RM normalized OMA, normalized I_{ph} and ER. The plot is zoomed in around the optimal operating point where the OMA is maximum.*

The actuator of the thermal tuning control loop is the integrated Tungsten µ-heater that is placed on top of the ring shaped waveguide. The characterization of the heater was presented in the previous chapter. Its bandwidth is around 10 kHz. With the current design the µ-heater can be operated with power up to 60 mW and voltage of up to 2 V. For the C-band device this is not enough to scan a full FSR of the RMs. The full FSR can be scanned only for some O-band devices that PICv2 includes, for the same power and voltage limits. The required voltage to reach power of 60 mW can be reduced in future devices by optimizing the µ-heater design. The power requirements, however, to be able to scan a full FSR, can only potentially be reduced if the fab improves the efficiency of the heaters by changing the manufacturing process. The µ-heater requires a voltage driver. For the final system implementation we intend to use a DAC for biasing the µ-heater. The DAC BW is targeted to be 1 MS s^{-1} to give enough margin. This is again a conservative estimation and further studies are required to identify the final number that is expected to be smaller. This BW can also be achieved in FPGA based implementations.

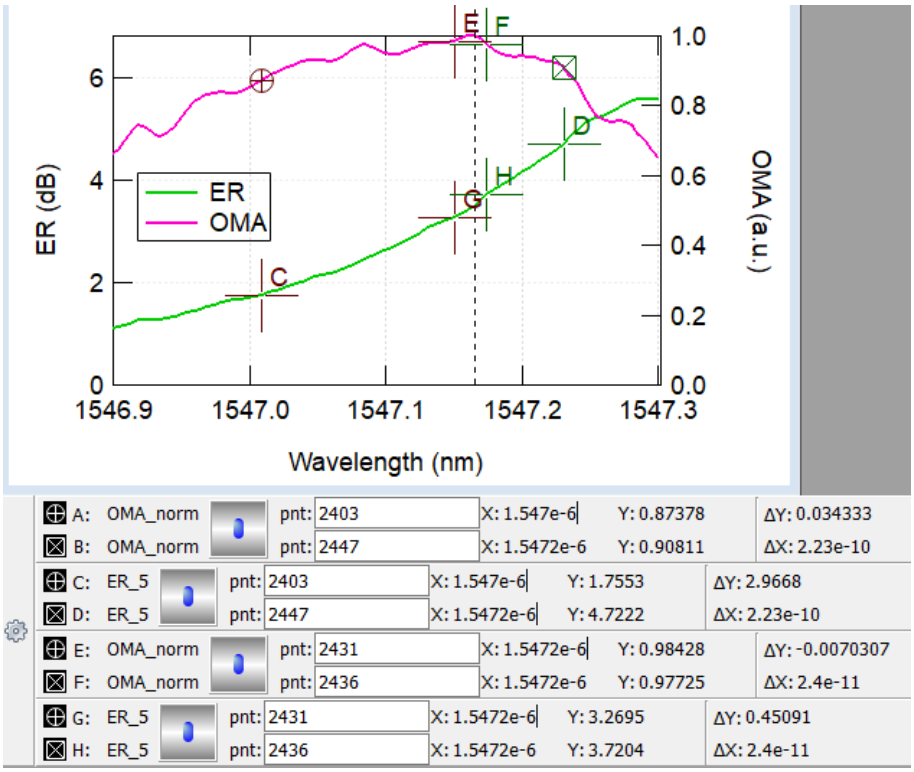

Figure 4.11. *The normalized RM OMA and ER as calculated from spectral measurements for voltage swing of* 5 V. *The plot is zoomed in around the optimal operating point where OMA is maximum.*

Concerning the resolution of the DAC, it was already mentioned that although the λ_{res} tuning has a tolerance of around 200 pm is terms of the OMA values, it is preferred to work in a region 10 pm wide round the optimal point instead. This can ensure both stable OMA and stable ER performance. 10 pm of λ_{res} shift requires 0.037 mW according to Eq. 4.4 that shows the measured tuning efficiency of the µ-heaters from our PIC.

$$\frac{d\lambda_{res}}{dP_{el}} = 272\,\frac{\text{pm}}{\text{mW}} \tag{4.4}$$

This efficiency was extracted from the red curve of Fig. 4.1 that shows the resonance wavelength shift varying the electrical power of the µ-heater. The 10 pm λ_{res} shift corresponds also to around 0.14 °C as concluded from Eq. 4.1. From Fig. 3.17 we can calculate the µ-heater power vs. voltage slope. From this slope we can them compute what is the minimum voltage step required to achieve the desired electrical power step of 0.037 mW. Since the plot is not linear, we are interested in its maximum slope. This corresponds to the worse operating point where a given change in electrical power requires the smallest voltage step. This condition is observed for he high voltage and power values. The extracted slope is given from Eq. 4.5.

$$\frac{\Delta P}{\Delta V} = 41.67\,\frac{\text{mW}}{\text{V}}. \tag{4.5}$$

This means that a 0.037 mW µ-heater power step requires roughly a 0.001 V step. To achieve this resolution of 1 mV with total voltage swing of 2 V, 2000 voltage levels are

required. This required in turn a DAC of at least 11 bits. However, no 11-bit DACs exist, therefore we have to go with a 12-bit or 16-bit DAC, depending on the components availability. For this application, a linear DAC would be required. Although this is the simplest solution, it is at the same time challenging to implement as an ASIC block, and being not very power efficient due to the linear output stage. Alternatively, a Δ-Σ DAC can be employed with the equivalent number of bits that has lower complexity and higher efficiency. Overall, in the final system implementation we target to use a 1 $\frac{\text{MS}}{\text{s}}$ 12-bit DAC to drive the µ-heater.

The closed loop BW of the feedback control loop is targeted to be also 100 kHz which can be certainly achieved when the sampling frequency is 1 MHz. This is possible both in the ASIC-based and FPGA-based implementations. Further investigations will allow us to better understand the required frequencies and probably trim down these numbers. For the initial implementation that will be based on bench-top instruments we are limited by the sampling time which was measured around 0.45 s. Concerning the response time and transient behaviour of the controller, it was decided that a good set of values for this implementation would be to choose a $BW = 0.1$ Hz and phase margin = 60°. These values will be used for tuning the PID controller.

4.4.2 Physical implementation

First version: based on bench-top instruments

For the purpose of testing the feasibility and performance of the drop-port average power monitoring control loop, and verify its compatibility with the PICv2 RMs, a first version of the closed feedback control loop was assembled. This first implementation was based on bench-top instruments for the readout of the drop-port I_{ph} as well as the biasing of the µ-heater. This setup did not aim a high-speed controller with the final system requirements, but an implementation of a control loop to study and compensate slow environmental temperature drifts. The detailed control loop implementation is shown in Fig. 4.12.

For biasing the µ-heater, a bench-top power supply is employed. The read-out of the drop-port I_{ph} involves an external resistor of 20 kΩ connected in series at the drop-port PD output. The PD and resistor are biased at 1 V using a bench-top power supply. This way the PD I_{ph} is converted into a voltage signal between 0.2 V and 1 V, corresponding to resonance and off-resonance condition respectively. A bench-top multi-meter connected in parallel with the PD is used to measure the voltage drop across the resistor. This is the feedback signal.

The PI controller is implemented as a software C-like function that runs on Igor software on a dedicated PC. The same Igor program is also used for the remote control of the complete setup. The PD multimeter is connected to this PC, allowing to acquire the feedback signal that is processed by the PI controller. The controller output (V_{heater}) is then applied to the power supply that drives the µ-heater (this is also connected to the PC).

The high-speed electrical signal for driving the RM is provided by a pattern generator

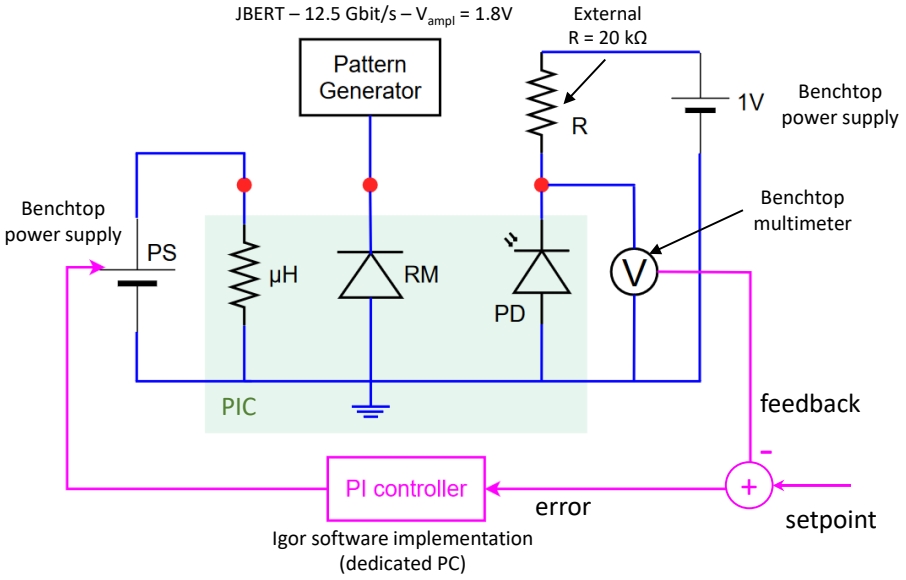

Figure 4.12. *The implementation of the thermal tuning test setup based on bench-top instruments for the photocurrent readout and µ-heater biasing. This setup was put together for the testing and verification of the PID controller.*

at 12.5 $\frac{\text{Gbit}}{\text{s}}$, with amplitude of 1.8 V. The CW optical input is provided by a tunable laser. The modulated optical output is recorded by a 12.5 $\frac{\text{Gbit}}{\text{s}}$ high-speed scope, allowing to monitor the eye diagram parameters, like OMA and ER. The transfer function was measured and is given by Eq. 4.6 and 4.7. This is the transfer function used for tuning the PI controller gains. The sampling time of this control loop was experimentally measured to be around 0.45 s. The delays are mainly due to the time required for the remote communication between the PC and bench-top instruments.

$$H(s) = \frac{V_{PD}(s)}{P_{el}(s)} = \frac{H}{1 + s \cdot \tau}(\frac{mA}{mW}) \tag{4.6}$$

$$H(s) = \frac{-0.028}{1 + s20 \cdot 10^{-6}}(\frac{mA}{mW}) \tag{4.7}$$

Second version: based on custom board

In a second step, to optimize the size and scalability of the thermal control test setup as well as its operational frequency, the bench-top instruments for the photocurrent readout and µ-heater biasing were replaced by a custom board, shown in Fig. 4.13. The detailed implementation is shown in Fig. 4.14. The custom board was designed at CERN for the purposes of this project. It includes two different types of channels: voltage source channels that can provide an output voltage between 0 V and 2 V. This type of channel can be used for driving the µ-heater. The other type of channels consists of ADCs that can be employed for the read-out of the photocurrent. The PD output can be directly connected at the ADC channel input without the need to interpose any amplifier in-between. An appropriately chosen shunt resistor placed on the board ensures that the I_{ph} is converted to a voltage value with range of 1 V. The use of the custom board that replaced the bench-

top instruments allowed to achieve lower sampling time of around 0.02 s. This increased the frequency of the control loop from 2 Hz to 50 Hz enabling faster error correction. Another important advantage of this approach is that it constitutes a much more compact solution compared to the bench-top instruments. One custom board includes 4 channels, two of each type, and therefore one board can be used to operate 2 RMs simultaneously. The custom board has dimensions of 10 cm by 10 cm. At the same time, the use of the custom boards enables the operation of the WDM circuit that includes 4 RMs. This requires the use of only 2 custom boards, offering a very compact solution.

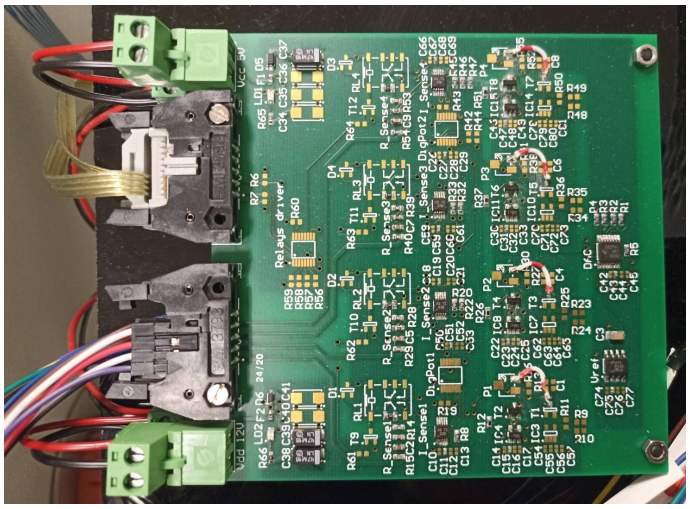

Figure 4.13. *Photo of the custom board designed at CERN that includes two voltage source channels and two ADC channels*

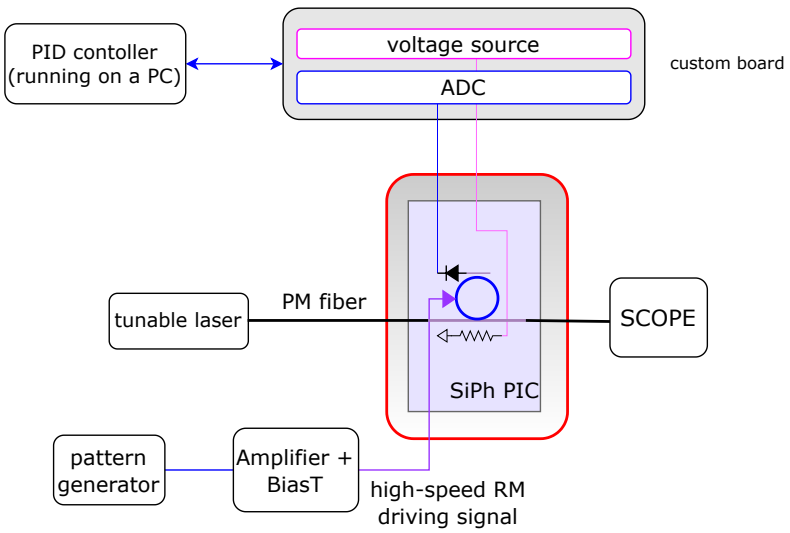

Figure 4.14. *The second implementation of the thermal tuning test setup. The photocurrent readout and μ-heater biasing is done using a custom board.*

Final system implementation

For the final system, a different implementation of the thermal tuning control loop will be required to adhere to the system requirements described in Sec. 4.4.1. This version will need to have much higher BW of 100 kHz, low power consumption and low material budget to be compatible with the FE restrictions. As a first step towards the final version, the PI controller functionality can by implemented in an FPGA and the photocurrent read-out and µ-heater biasing can be performed by an ADC and DAC respectively. Eventually, all the necessary components (PI controller, DAC, ADC) will have to be implemented as ASIC blocks and integrated with the rest of the FE electronics. The development of such ASIC blocks has already started within the CERN collaboration with the electronics team. In the next years, initial testing and verification of this approach is expected.

4.4.3 PI controller design and tuning

A PI controller can only work reliably and efficiently in a system, being able to automatically and responsively correct the system's operational point, if it has been appropriately designed and tuned. The tuning includes the choice of the P, I and D gains to set the response time and transient behaviour of the controller. The response time will define how fast the system will reach the steady state, while the transient behaviour defines how robust or aggressive the controller is (trade-off between reference tracking and disturbance rejection). If the gains are not appropriately chosen, the system might end up having increased rise and fall times, very high overshoot, steady state error or even show instability. Defining the system requirements and needs allows for choosing the correct gains that will lead to the desired controller behaviour, managing this way to bring the system error to zero and ensure minimal process oscillation around the setpoint after a disturbance has occurred.

There are different ways to tune the PID. The first approach involves designing the PID using the physical system, by tweaking the gains manually. However, this requires that a PID implementation already exists and the region where the optimal gains will be found is somewhat known. However, this was not the case for our system and the design and tuning process started before an actual implementation existed, so this approach was not suitable for us. Alternatively, one can use model-based tuning methods where a model of the system plant and controller is created using a simulator tool. In this approach, usually the transfer function of the plant as well as the sampling time of the sensor and the frequency of the actuator need to be known. Once the model has been created, manual tuning is possible, employing methods like pole placement, loop shaping or other heuristic methods. Is the software supports it, there are also automatic tuning methods that can be very helpful and provide accurate results.

For our application, we have chosen to use the Matlab Simulink software. Simulink is a block diagram environment used to design systems with models and allowing to simulate before moving to hardware. Is is therefore simple to add the system blocks (plant and controller) in the simulator tool and simulate their response. Simulink is a very versatile environment that also allows to perform different operations like transformations from

continuous to discrete time systems, work in the z-domain, or even with hybrid systems. It allows for manual PID tuning with pole placement or loop shaping, but also offers very robust automatic tuner tools. All those functionalities where exploited during the design and tuning process.

Matlab-Simulink simulations

Fully continuous model As a first approach we created a fully continuous model of the physical system, comprising the continuous plant with its transfer function as described in 4.7 as well as a continuous PID controller. The block diagram of the simulated model is shown in Fig. 4.15a. The model includes also a random number generator that randomly changes the setpoint. This is equivalent to an external disturbance of the system output (feedback signal) that can be caused due to environmental variations, but is much more complicated to model. In all the simulations we show we consider a variation of the setpoint instead of the equivalent variation of the system output for simplicity.

In the case of a continuous time (CT) controller, Simulink provides a very robust PID Tuner application for auto-tuning that is transfer function based. This auto-tuning mechanism linearizes the plant. Then, once we provide the desired response time and transient behaviour (in the time domain) or equivalently the bandwidth (BW) ($\mathrm{rad\,s^{-1}}$) and phase margin (PM) (°) (in the frequency domain), the P, I gains are automatically calculated. For this application a good set of values is $BW = 0.628\,\mathrm{rad\,s^{-1}}$ and $PM = 60°$, that correspond to response time 3.185 s and transient behaviour of 0.6. The PID tuner app is shown in Fig. 4.15b, illustrating the reference tracking plot that shows how fast the reference will be tracked, and what will be the transient behaviour. The rise and settling time of the controller are marked. The response time setting is highlighted in the green box and the transient behaviour in the purple box. The calculated PI parameters are marked with the red box. Their calculated values were approximately $P = 3.4265 \cdot 10^{-6}$ and $I = 0.1713$. The corresponding PI controller tranfer function is given by Eq. 4.8. Using these values in the continuous PID block of the model, we then simulated the response of the system when varying the reference value. The results are shown in Fig. 4.15c. The reference value (setpoint) in plotted in blue, the error in red, the feedback signal in green and the PID output in yellow. It is evident that the error is quickly brought to zero and the feedback signal tracks the setpoint with response time of around 3 s. The P,I parameters were also manually calculated. The results of the two methods are in agreement. This was a first attempt to calculate the PI parameters and also simulate the closed loop system response.

$$G_{cont}(s) = P + I\frac{1}{s} = \frac{3.427 \cdot 10^{-6}s + 0.1713}{s} \tag{4.8}$$

Model with discretized controller and continuous plant Although the method presented so far constitutes a convenient and easy way for calculating the PI parameters, it provides with results that cannot be used in practice. This is because the plant (system to control) is a continuous time system. However the controller, whether it is implemented on software and employs bench-top instruments or custom boards, or it is implemented

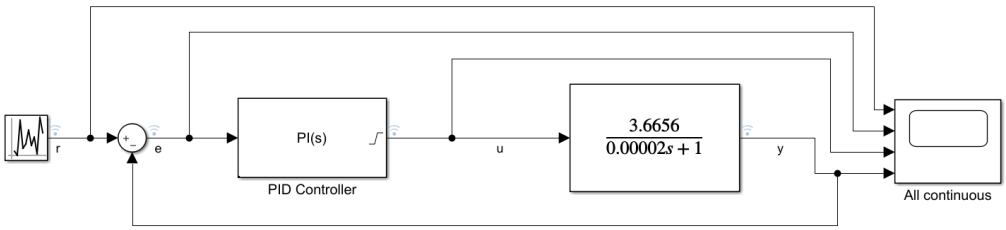

(a)

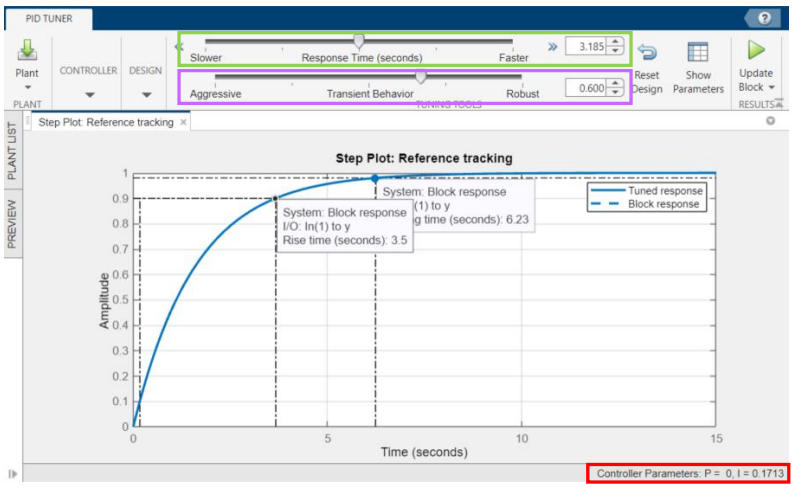

(b)

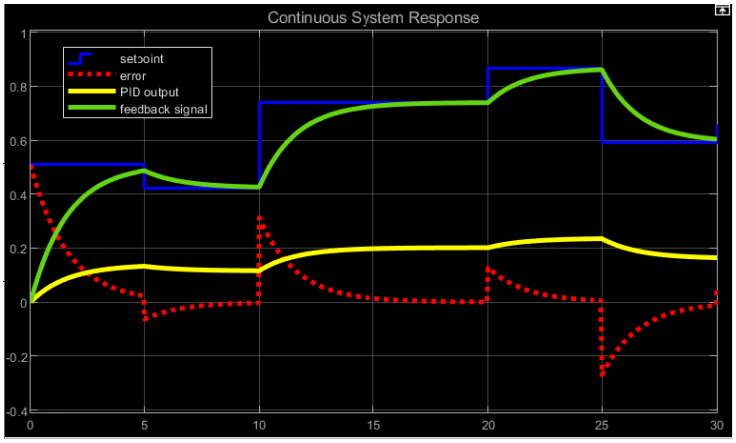

(c)

Figure 4.15. *(a) Fully continuous model of the physical system in MATLAB Simulink simulator. (b) The PID tuner app that automatically calculates the P, I gains after we set the response time and transient behaviour. (c) The simulated response of the system.*

on an FPGA, is a discrete controller. This is because the sensor will have some sampling frequency, the PI controller requires a bit of time for calculations and the actuator also operates with a given frequency and is only able to apply the correction in a discrete way, in steps. Also, depending on the implementation, some time is required for the interfacing of the controller with the sensor and actuator. Therefore, the fully continuous system does not take into account the discrete nature of the physical controller and the delay between consecutive iterations. For this reason, the P, I gains that are calculated will not work in practice and there is no way to test them with an actual continuous controller.

To address this problem, as a first approach we discretized the controller. The block diagram of the simulated model is shown in Fig. 4.16a. Matlab offers a variety of methods to perform this discretization. We chose to use the Tustin method and discretized the controller, for sampling time of 0.45 s which is the measured sampling time of the physical controller. The resulting controller transfer function in this case in given by Eq. 4.9 and the gains are $P = 0.03855$ and $I = 0.171311$. The simulated response of the system when varying the reference value is shown in Fig. 4.16b.

$$G_z(z) = P + I * T_s * \frac{1}{z-1} = \frac{0.03855z + 0.03854}{z-1} \tag{4.9}$$

However, this approach is still not correct and might results is an unstable controller. This is because we started from a continuous controller that has no zero-order-hold (zoh) logic and we discretized it with a method that does not take into account the zoh. However, the final hybrid system should have zoh logic. This means that in practice, the controller output will not comprise an impulse train or a series of discrete values each sample time, between which the output is zero. More accurately the controller output will have a step-like shape, where each output value is maintained until the next sample time when is replaced by the next one. This is the zoh logic that we are missing. In this regard, a more accurate method was necessary to get a stable controller.

Hybrid model with pade approximation In principle it is much more convenient to work with the CT model. This is because the methods and auto-tuning solutions we have available mostly work with CT controllers, making it much simpler and more robust to tune a CT controller and then discretize it. For this reason, to address the aforementioned problem of the lack of zoh in the CT model, and continue to work in the CT domain, we introduce another block in the fully continuous system that imitates the zoh logic. This block is a pade approximant that approximates time delays for continuous-time linear time invariant (LTI) models [16]. Its inclusion allows us to work in the CT domain, tune our CT controller and then discretize it, taking into account this time the necessary zoh logic. We will then end up with a correct hybrid model. The CT model with the extra pade approximant block is shown in Fig. 4.17a. The transfer function of the pade approximation that models the time delay in our CT LTI model that is equal to 0.45 s, is given by Eq. 4.10.

$$pade(0.45, 1) = \frac{-s + 4.444}{s + 4.444} \tag{4.10}$$

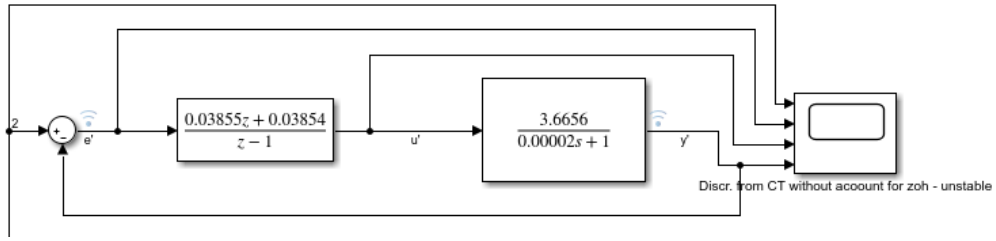

(a)

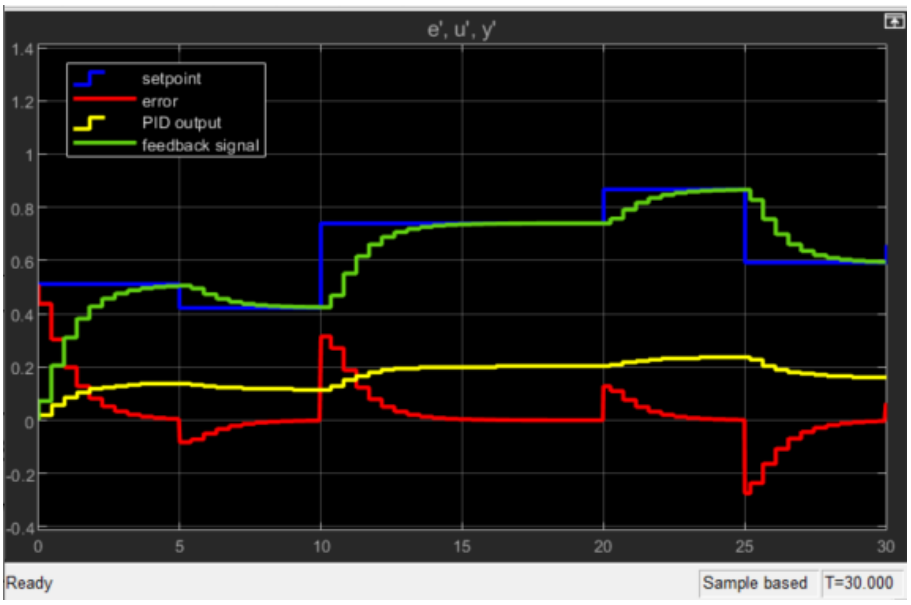

(b)

Figure 4.16. *(a) Model with continuous system and discretized controller, without accounting for zoh, in MATLAB Simulink simulator. (b) The simulated response of the system.*

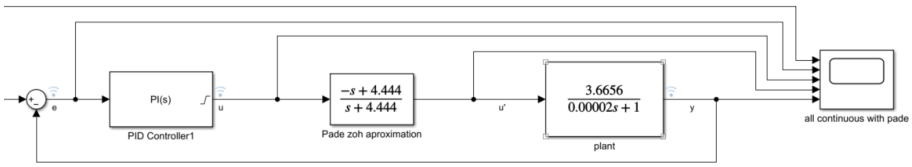

(a)

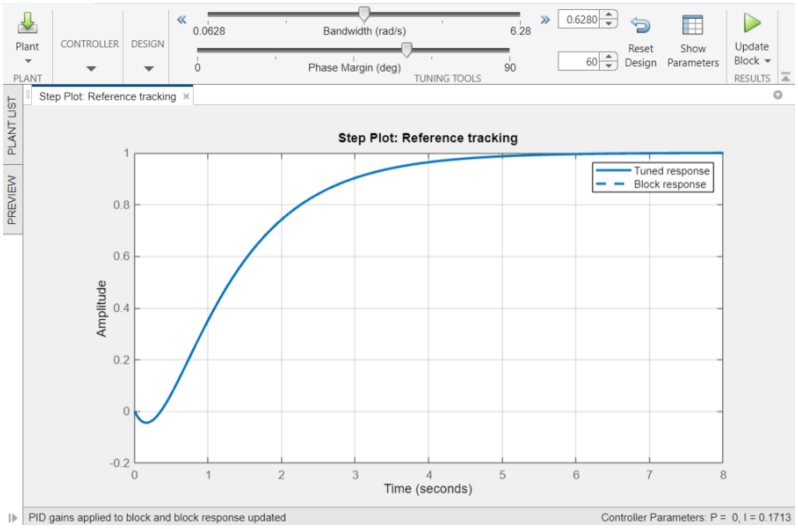

(b)

Figure 4.17. *(a) Fully continuous model of the physical system with pade approximation to account for the zoh logic, in MATLAB Simulink simulator. (b) The PID tuner app that automatically calculates the P, I gains after we set the response time and transient behaviour.*

Once this block has been added, it is possible to tune the CT PID controller with the same automatic PID tuner app as before, to achieve the desired phase margin and bandwidth. The tuning process is shown in Fig. 4.17b along with the calculated P and I gains. At this point it is possible to convert the CT controller to a discrete time controller and get a hybrid system that will be stable and for which the zoh in properly accounted for. Using again the Tustin method for the discretization, the transfer function of the resulting discretized controller is given by Eq. 4.11.

$$G_{pade}(z) = P + I * T_s * \frac{1}{z-1} \frac{0.03855z + 0.03855}{z-1} \tag{4.11}$$

From this transfer function we can extract the P and I gains of the discrete controller, which are $P = 0.03855$ and $I = 0.171333$. The hybrid model with the CT plant and discrete controller with zoh logic is shown in Fig. 4.18a. The simulated response of this hybrid model is shown in Fig. 4.18b. It is evident that the controller manages to ensure the reference signal tracking and brings the error to zero. The transient behaviour is smooth without overshooting and the response time is around 3 s as specified. This showcases that the controller is appropriately designed and tuned and its operation and behaviour has been verified with simulations. The P and I parameters calculated for the discretized controller, that can be extracted from its transfer function of Eq. 4.11 are the final PID

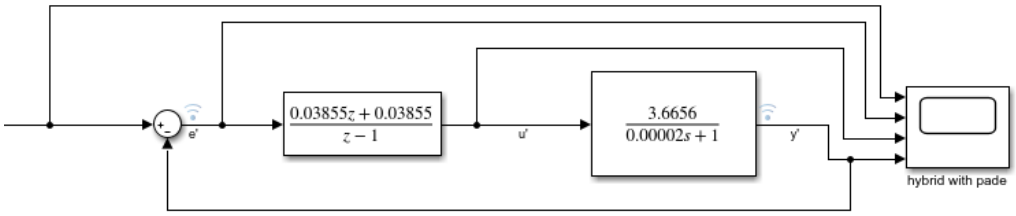

(a)

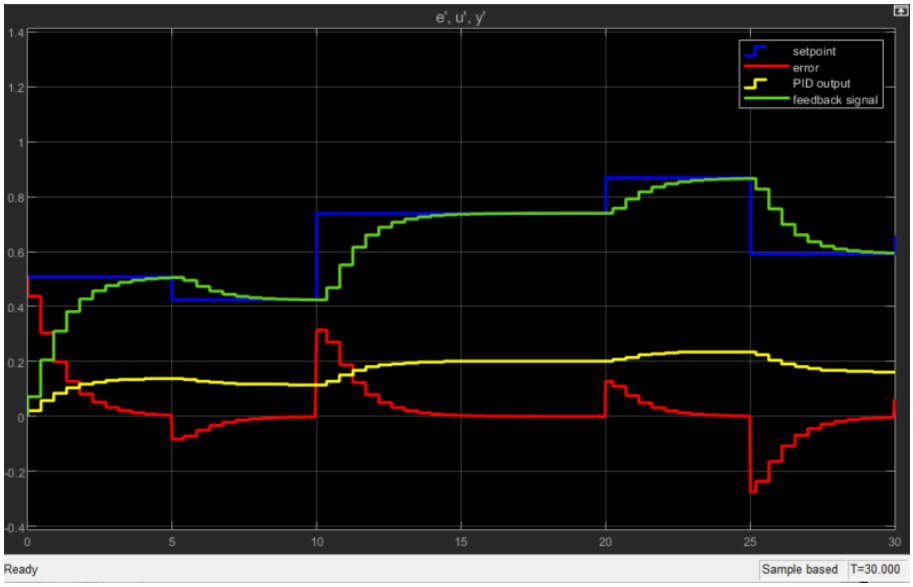

(b)

Figure 4.18. *(a) Hybrid model of the physical system with pade approximation to account for the zoh logic, in MATLAB Simulink simulator. (b) The simulated response of the model.*

gains that can be used in the physical system.

Verification

After the PID controller has been designed, tuned and verified with simulations, the next step would be to experimentally validate the physical PID controller implementation. This allows to verify if the extracted P and I gains were correctly computed, to fine tune the controller and ensure it works with the physical system.

The test setup that was put together for the testing and verification of the PID controller is shown in Fig. 4.12. The setup included first of all a high-speed test board with PICv2 and all the necessary optical and electrical connections to operate one RM. The optical input was provided by an external tunable laser, while the optical output was monitored by a high-speed scope, to record the eye diagrams and eye diagram parameters. The modulation voltage was provided by a pattern generator, the JBERT, at 12.5 Gbit s^{-1} with 1.8 V output voltage amplitude. The feedback control loop comprised bench-top instruments. Since the direct monitoring of the drop-port Ge photocurrent without the use of an amplifier is complicated due to its small value (some µA) a shunt resistor was connected in series to the drop-port output. The resistance of this resistor was around 20 kΩ. The Ge PD and external resistor were biased at 1 V with the help of a bench-top power supply.

In this configuration it was possible to monitor the voltage drop across the Ge PD (V_{PD}) with a bench-top multi-meter. This was used as the feedback signal for our controller, and it is analogous to the drop-port photocurrent. When $V_{PD} = 1\,V$ there is no current flowing through the PD, meaning the RM is out of resonance. When the RM is near resonance and there is optical power at the drop port, then the I_{ph} starts increasing and the corresponding V_{PD} will start decreasing. For the specific configuration V_{PD} can be between 1 V and 0.2 V, with an optimal value (setpoint) of around 0.385 V that corresponds to an optimal I_{ph} value. Finally, a bench-top power supply was used for biasing the µ-heater.

The PI controller is implemented as a C function running on a lab PC. The controller functionality as well as the complete setup is controlled though the Igor software, where the PI controller is implemented. The Igor program interfaces with the bench-top multimeter for acquiring the feedback signal (V_{PD}). This is subtracted from the setpoint to calculate the error, that is then fed to the PI controller function. The output of the PI controller is the new voltage bias that needs to be applied to the µ-heater, to bring the error to zero and ensure that the feedback signal tracks the setpoint. The PI gains were set in the software implementation to $P = 0.03855$ and $I = 0.171333$. as calculated with the simulations. The setup and PI controller were then tested in closed loop operation. A change in the λ_{laser} was introduced as the external variation. Scanning the temperature is more complicated, so we chose to work with varying the λ_{laser} for this initial verification step. The PI controller was then continuously adjusting the RM λ_{res} so that the RM would track the external variation and optimal operation was ensured. The results of the test are shown in Fig. 4.19. Fig. 4.19a shows the PI error that is brought to zero every time a variation happens. Fig. 4.19b shows the reference signal (V_{PD}) that successfully tracks the setpoint, as well as the µ-heater biasing voltage (V_{heater}) that is adjusted by the controller to tune the RM, according to the external variations. Finally, Fig. 4.19c show the P and I terms of the PI controller that are used to calculate the PI output. Their values change following the change of the λ_{laser}. There measurements validate the effective operation of the PI controller and serve as a proof of concept of a bench-top instrument based feedback control loop with a PI controller implemented as a software function that can be used to ensure the stable operation of our RMs independently of external fluctuations.

Although the controller behaviour was already satisfactory, fine tuning of the P, I gains allowed to perfect it and enhance a bit the transient behaviour, reducing the small overshooting that is noted in Fig. 4.19a, b and c. Using the physical setup for testing the gains were reduced a bit and the final values of $P = 0.01$ and $I = 0.1$ lead to even better performance of the PI controller, as shown in Fig. 4.19d, e and f. The small discrepancy between the calculated values and eventual optimal values of the P, I gains is probably introduced by the inevitable error in measuring the system transfer function and sample time. These values might also vary between different chips. Also some variation is expected with time since changes in the connections in the actual setup and small variation of the measurements instruments are expected. However, in the end, the combination of the very powerful simulation tools that allowed as to estimate PI gains, and the experimental verification and fine tuning, allowed for the implementation of a very robust feedback control system for tuning the RMs. This was a necessary step for the further characterization and

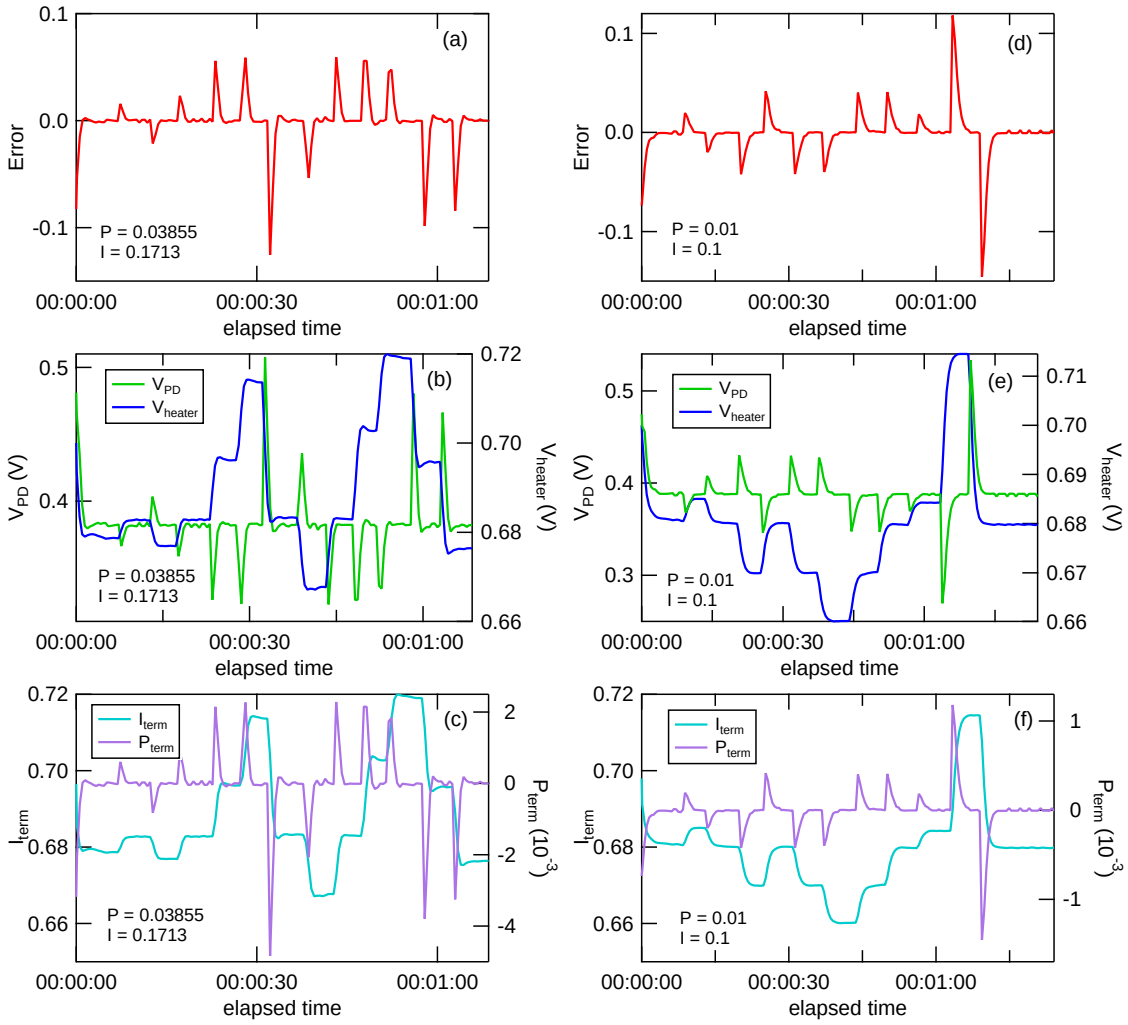

Figure 4.19. *Experimental verification results of the PI controller operation for two different sets of PI parameters. (a) The controller error, (b) V_{heater} and V_{PD}. (c) P and I terms of the controller for P, I gains values of $P = 0.03855$ and $I = 0.1713$. d(a) The controller error, (e) V_{heater} and V_{PD} as well as (d) P and I terms of the controller for P, I gains values of $P = 0.01$ and $I = 0.1$.*

system development of the SiPh transmitter.

PI gains for different hardware implementation

The previous simulations results were calculated for the case of the benchtop instruments based control loop, where the PI controller is implemented in software and runs on a PC. However, as it was already mentioned, eventually the PI controller will need to operate in the much higher bandwidth of 100 kHz to compensate fast for temperature and λ_{laser} variations. The sampling frequency required for such a controller is much higher that what can been achieved with the presented implementation. Such sampling times can be achieved in an FPGA based implementation, where the PI controller runs in the FPGA and the read-out of the sensor and biasing of the actuator can be done with ADCs and DACs respectively. Of course such an implementation will require different PI gains. Using the same transfer function as before, but the new sampling time, we simulated a set of

PI parameters that would be required in a system with the same hardware implementation but much faster sampling time. The calculation was performed in the same method as before, with the Matlab Simulink simulator. The calculated values are $P = 0.441$ and $I = 15240$. Although these values will not be of use if the system transfer function changes, it helps to understand in what way the P, I gains required are changing when the system is improved, and it helps to get a feeling on what values to use for each different implementation. Eventually, every time the physical system is changed, from one version to another, the PI gains must be adjusted, but the initial estimation helps to have a feeling on what the new values will be, so that the adjustment can be performed manually.

4.5 Thermal tuning process

The thermal tuning process is the process performed by the feedback control loop to align the resonant wavelength of a RM with its corresponding laser wavelength, and ensure stable operation at the optimal point where OMA maximizes, irrespective of any external variations in the temperature or laser wavelength. The thermal tuning process consists of two discrete steps. The first step is called startup procedure and it is performed during the power-up of the transmitter. During this step that constitutes a first coarse tuning, an initial, near-optimal operating point of the RM and μ-heater is identified and the system is initialized at this state so that the λ_{res} is coarsely aligned with the λ_{laser}. This first step is also denoted as wavelength locking and is a critical functionality for any given RM-based platform as the lasers and RMs will be initially offset in wavelength due to fabrication tolerances or changes in the environment temperature. When this step is done, λ_{res} and λ_{laser} are aligned and the RM is operated in near optimal regime, at the linear region around the resonance. Once in this linear region, the PI controller is employed for fine tuning of the operating state. This operation is done continuously and ensures operation at the optimal operating point that was defined in the previous step. This functionality is also crucial for the RM operation, because once the link has been initialized, it is necessary to guard it against thermal or other fluctuations. To maintain the RM operating point, the heat generated by the integrated μ-heater is adjusted in response to decreases or increases in the ambient temperature or variations of the λ_{laser}. It is evident that this method allows for the compensation of all possible variations, namely temperature and λ_{laser} variations, as well as process variations.

4.5.1 Start-up procedure

The start-up procedure aims to perform an initial wavelength locking of the λ_{res} to the λ_{laser}. This involves calculating the optimal operating point and bringing the RM to near optimal operation by appropriately initializing the μ-heater. To achieve this, the I_{ph}=f(V_{heater}) curve is measured, shown in Fig. 4.20b. This curve is measured by scanning the μ-heater biasing voltage (V_{heater}) and consequently moving the λ_{res} point of the RM, as shown in Fig. 4.20a.

The detailed process for measuring the I_{ph}=f(V_{heater}) curve is described in Fig. 4.21.

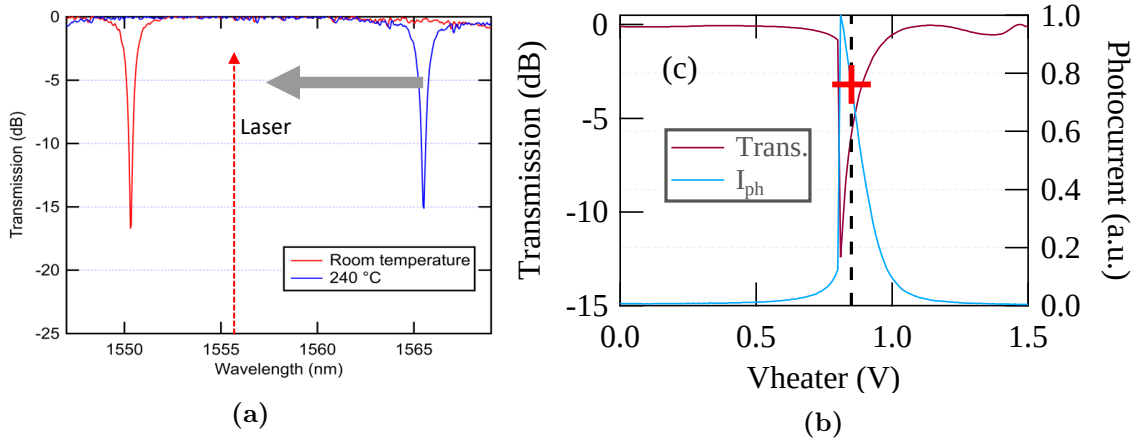

Figure 4.20. *(a) The RM transmission spectrum at room temperature and at 240 °C, showing the thermal tuning principle of operation that involves moving the RM resonance to align the resonance peak with the laser wavelength. (b) I_{ph}=f(V_{heater}) and transmission vs. V_{heater} for a single RM.*

It includes scanning the V_{heater} from 1.5 V down to 0 V while measuring the I_{ph}. Scanning the V_{heater} moves the λ_{res}. When λ_{res} is away from λ_{laser} the RM is off resonance and the drop port I_{ph} is 0. As λ_{res} approaches λ_{laser} the drop port I_{ph} increases and peaks when $\lambda_{res} = \lambda_{laser}$ (resonance condition).

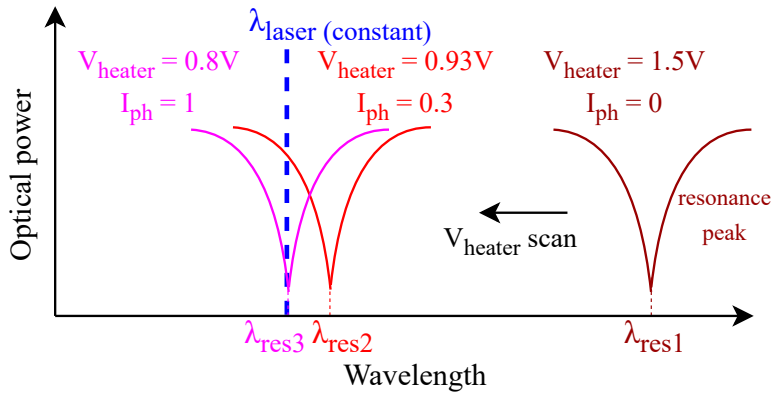

Figure 4.21. *Measurement method of the I_{ph}=f(V_{heater}) curve. V_{heater} is scanned from 1.5 V down to 0 V and I_{ph} is recorded.*

From this plot it is very simple to identify the optimal operating point (setpoint). As it was already described, there is a particular $\lambda_{optimal}$ for which the OMA reaches a maximum. A characteristic value of the I_{ph} called setpoint corresponds to this optimal point, denoted with a red cross in Fig. 4.20b. For a given RM design this setpoint equals a fixed percentage of the maximum I_{ph} ($I_{ph} = k \cdot I_{ph_max}$). k is design-dependent and its computation allows for easy calculation of the setpoint. For the RMs from our PIC k was measured in the range 0.65 – 0.8 that corresponds to the OMA plateau region. It shows a small variation within this range between RMs. To account for variations we choose to work with the median value of k = 0.7. Given the k value, the optimal I_{ph} (setpoint) that corresponds to the desired operating point is easily computed from the plot: after locating

the max I_{ph} from the scan and given the k parameter we can compute the setpoint. Then, as a second step, the PI controller takes over to lock the I_{ph} to the setpoint value. This way stable operation of the RM at its optimal point is ensured.

4.5.2 PI controller

The PI controller operation is the second step of the thermal tuning process. After the start-up procedure that is performed once at the powerup of the transmitter, the PI controller takes over. The setpoint and initial µ-heater biasing voltage have been identified during the start-up procedure. The PI controller uses this calculated setpoint as its reference value. Given its P, I parameters that have been defined during the tuning process, the PI controller runs continuously: it compares the feedback value with the setpoint, computes the error and then calculates the V_{heater} that is required to compensate for external variations and lock the feedback value (I_{ph}) to the setpoint.

Since the PI controller can only work with a LTI feedback system, there are some constraints in the operation of the loop. The feedback loop can only work in the region where the system has a LTI behaviour. This only happens around the resonance point, in the linear region of Fig. 4.20b. Outside of the region, the calculated transfer functions of the system are no longer valid and the PI controller cannot operate. This is another reason why the start-up procedure is a necessary first step before the PI controller. The system needs to be initialized and brought to the linear region before the PI controller can operate. This also signifies that for very abrupt and large variations for which the PI controller cannot compensate fast enough to ensure operation within this allowed linear region, the system will become unstable and the PI controller will crush, no longer being able to adjust the operating point. Variations that might cause instability and move the working point out of the linear region would require a temperature increase or decrease that is equivalent to more than 0.15 V or 0.05 V of µ-heater bias voltage change respectively, with frequency higher than the expected 10 kHz. This equivalent V_{heater} change corresponds to a temperature increase of 24 °C or temperature decrease of 8 °C, according to Eq. 4.1, 4.5. However, such variations are not expected in the actual system. Nevertheless, even in the case that for any reason the system looses stability, it is always possible to reinitialize it by repeating the start-up procedure and bring it once more it the LTI region. Therefore, the stable operation of the system is ensured in all cases, either by the PI controller for acceptable variations or by repeating the start-up procedure if necessary, and restarting the PI controller.

It is worth mentioning at this point that the thermal tuning control loop can only heat up the RM and not cool it down. This adds extra complexity to the thermal tuning process and would typically only allow to adjust the RM operation in a single direction, that of heating up (that corresponds to a decrease in the ambient temperature or an equivalent variation). To bypass this problem the solution is to operate the RM µ-heaters with an initial offset. This means that during the start-up process the initial µ-heater voltage that is chosen to initialize the loop should be a value in the middle of the available range. For example, if the available V_{heater} range is 2 V, the system should be designed in such a way

that in normal conditions around 1 V is required for operations at the setpoint. This gives enough margin to adjust the operation in both directions. If the temperature decreases it is possible to increase the V_{heater} and heat up the RM. If the ambient temperature increases there is also margin to decrease the V_{heater} and imitate a cooling down effect. If on the other hand the RM is operated with V_{heater} close to 0 V under nominal conditions, then only increasing the V_{heater} is possible, and the operating point can only be adjusted in one direction.

In practice, in the final system implementation every RM needs to be operated at a specific wavelength, so there might not be enough flexibility to ensure the RM is typically operated with V_{heater} in the middle of the available range. This can be partially ensured by design. The RM geometrical parameters can be chosen so that its resonance at room temperature (or the target operating temperature) has a small offset with respect to the target operating laser wavelength, so that in normal conditions a V_{heater} in the middle of the available range is required. If the λ_{res} is by design aligned with the λ_{laser} then we find ourselves in the problematic condition that it is only possible to correct the operation in one direction, since decreasing the power is not possible, if the power dissipated in the µ-heater is already zero. Regardless, it is always possible that even if this has been taken into account during the design process, the final λ_{res} will show some variation due to the process variations. This expected inter- and intra-wafer variation in the RM dimensions might result in unfavorable operational conditions for some of the RMs. In the most unfavorable case the RM will require a V_{heater} close to the available range limits to operate in the target λ_{laser}. Even is that case though, given that the available range is enough to cover a full FSR, operation it the chosen or next (or previous) resonance peak should be possible, even with small margin.

4.6 Single channel measurements and results

After the design, simulation, implementation and verification process of the thermal control loop was completed, the loop was experimentally tested in single channel, closed loop operation. The test setup used for this test is based on the second version control loop employing the custom board and was shown in Fig. 4.14. The PI controller runs on a dedicated PC as an Igor function. The custom board is used for biasing the µ-heater and monitoring the photocurrent. The high-speed modulation signal of the RM is provided by a pattern generator at $10\,\mathrm{Gbit\,s^{-1}}$ and is amplified with the help of an amplifier and BiasT to have a voltage swing of 5 V. The optical input is provided by the tunable laser and the modulated optical output is recorded by a scope. The PIC is placed within a climatic chamber (denoted with the red box in Fig. 4.14) that allows to control the RM temperature. The climatic chamber as well as the scope are controlled by a separate PC that allows to record the eye diagram parameters and temperature of the RM. Employing this setup, the control loop was tested in closed loop operation. To test it against all types of fluctuations we varied in turn both the temperature and the λ_{laser}. The results are presented in the next two sections.

4.6.1 Measurements varying the wavelength

The first test that was performed involved the scanning of the input laser wavelength. Such variations are expected in the final system as it has already been described, due to thermal drifts on the lasers. For testing purposes, the λ_{laser} variation is achieved with the help of the tunable laser. The λ_{laser} was varied in a 6 nm range from 1550 nm up to 1556 nm. While λ_{laser} was scanned the PI controller was running in closed loop operation to compensate for the variation and adjust the RM operating point. Also, the eye diagram parameters were continuously monitored. Fig. 4.22 shows the measured eye diagram OMA and ER varying the wavelength. As it can be observed, the OMA and ER are stable with fluctuations smaller than 10% of the average value across 6 nm. This showcases the robustness and effective operation of the thermal control loop that can effectively compensate for variations in the input λ_{laser}, ensuring operation of the RM will optimal OMA and ER.

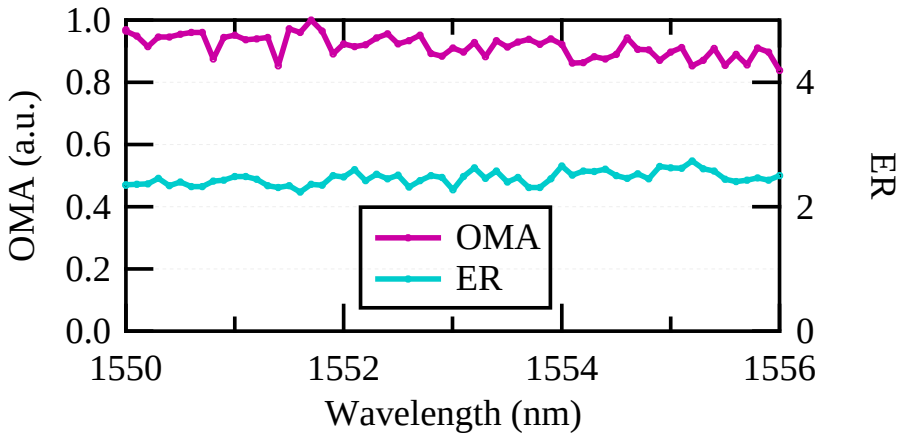

Figure 4.22. *Measured OMA and ER of the RM varying the λ_{laser} while the thermal tuning control loop is running in closed loop operation.*

4.6.2 Measurements varying the temperature

As a second step, the behaviour of the control loop was tested also when varying the temperature in the RM. In this case the λ_{laser} was kept constant. The temperature of the RM was scanned using the climatic chamber inside which the SiPh PIC was placed. This type of measurement is more complicated than simply scanning the λ_{laser}. This is because the test board and its electrical and optical connections are sensitive to big changes of the ambient temperature. The test board includes different components (PCB, PIC, wire bonds, fiber, glues etc) made from various materials that have different thermal expansion coefficients. This results in small movements between the components that break the alignments and affect the performance of the devices. The most sensitive component was the fiber array that is attached on the PIC using multiple glues. As it was observed during the measurements small movements between the board, PIC and fiber affect the alignment between the grating couplers and fiber channels and the coupling efficiency is reduced. This fact limited the temperature range of the test. However, after multiple tries

and with careful adjustment of the assembly process of the test boards we were able to successfully perform this measurement. The measured eye diagram OMA and ER varying the temperature in a range of 55 °C from 20 °C down to −30 °C are shown in Fig. 4.23. The OMA and ER are relatively stable and present fluctuations of less than 20% over the temperature range of 55 °C. This is a measurement artefact introduced by the dependence of the optical coupling on temperature. More studies are required to optimize the test-board assembly process and achieve stable and temperature independent coupling between the SMFs and grating couplers. Nevertheless, if we take into account this effect it becomes evident that the thermal tuning control loop is also effective in compensating for ambient temperature variations and ensuring the stable operation of the RM.

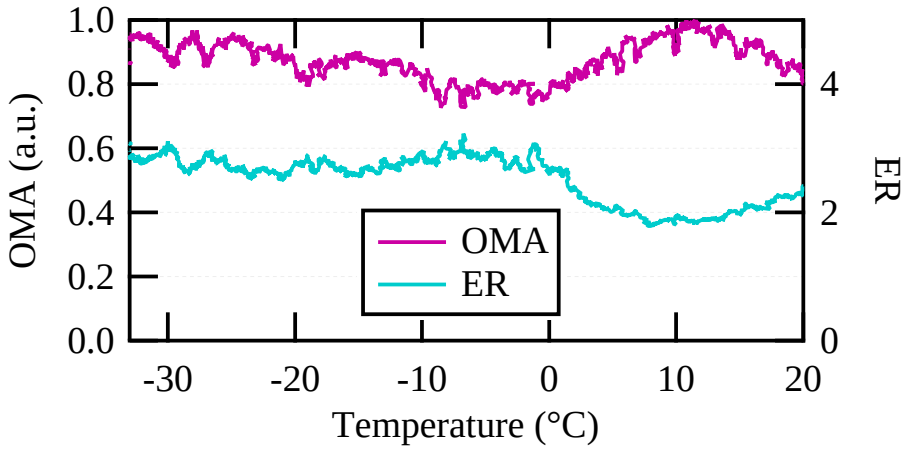

Figure 4.23. *Measured OMA and ER of the RM varying the temperature while the thermal tuning control loop is running in closed loop operation.*

4.7 Thermal tuning in WDM systems

So far we have described the thermal tuning mechanism we have adopted in our system for the case of single channel operation, where only one RM is operated and needs to be thermally controlled. However, it is possible that a WDM scheme is instead chosen for this application. A WDM solution would offer many advantages like the reduction of material at the FE and increase in the BW of each link. As happens with the single channel system, the WDM system also requires thermal tuning. This can be observed in Fig. 4.24. The spectrum of the 4-channel external laser source coupled into the common bus waveguide is shown in Fig. 4.24a and the normalized measured transmission spectrum of the WDM circuit at room temperature is shown in Fig. 4.24b. The λ_{res} of the RMs are marked with numbers whose color represents their target operational wavelength. The RMs are not aligned with their target λ_{res}. The alignment is achieved with the thermal tuning control loop, as shown in Fig. Fig. 4.24c. Of course, such a WDM system would require additional hardware and adjustment of the thermal control loop for the multi-channel operation. The scaling of the single channel system, its challenges as well as its experimental characterization will be presented here.

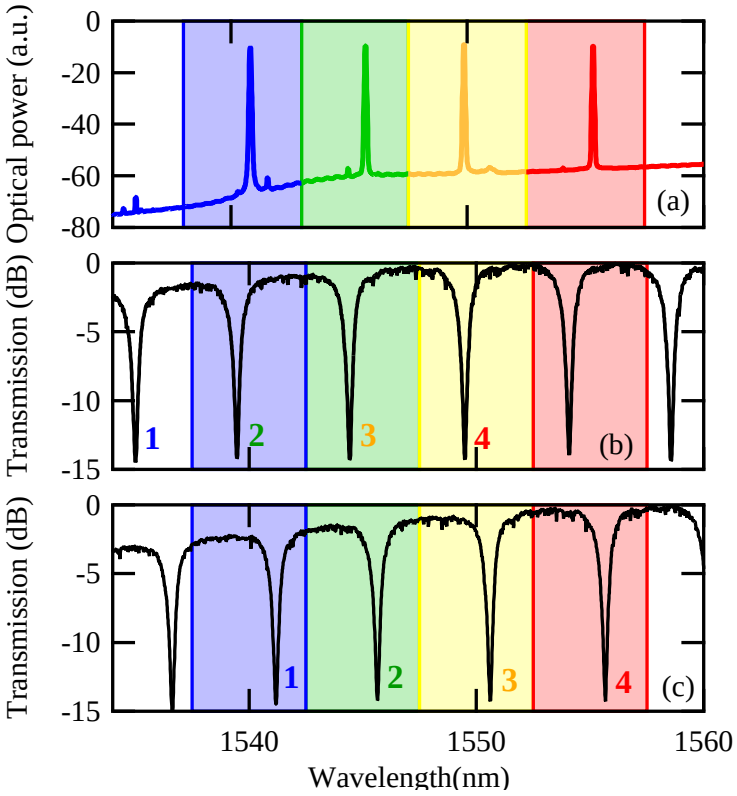

Figure 4.24. *(a) The 4-channel external laser source normalized spectrum. (b) The normalized through port transmission spectrum of the 4-channel Tx at room temperature and (c) after the tuning process.*

4.7.1 WDM system implementation

To support the multi-channel operation, the single channel thermal tuning system and setup were upgraded. This required both hardware and software adjustments. A schematic of the upgraded setup is shown in detail in Fig. 4.25. First of all, the WMD system requires a 4-channel laser input that can no longer be provided by a single tunable laser. Since for the moment no 4-channel laser comb was available in the lab, the necessary input was provided by multiplexing four single-channel lasers in a common fiber. For this purpose we used the two tunable lasers along with two DFB lasers that we have available in the lab. At the output of each laser we connected a manual polarization controller for aligning the polarization of all four lasers, and then we multiplexed them in a common SMF with the help of an optical filter that works as a multiplexer (MUX). The MUX output was then amplified for compatibility with the power budget of the setup. Another polarization controller at the amplifier output allows to adjust the polarization at the PIC input and achieve optimal coupling. The polarization controller output is then connected through a PM fiber to the 4-channel test board optical input. The normalized spectrum at the output of the amplifier was verified with the help of an optical spectrum analyzer (OSA) and is shown in Fig. 4.24a. It has a 5 nm channel spacing as required for compatibility with the 4-ch circuit transmission spectrum that is shown in Fig. 4.24b.

Given the available equipment in the lab, only two RMs could be driven simultaneously. The high-speed RM driving signal at 10 Gbit s^{-1} is generated by the pattern generator and

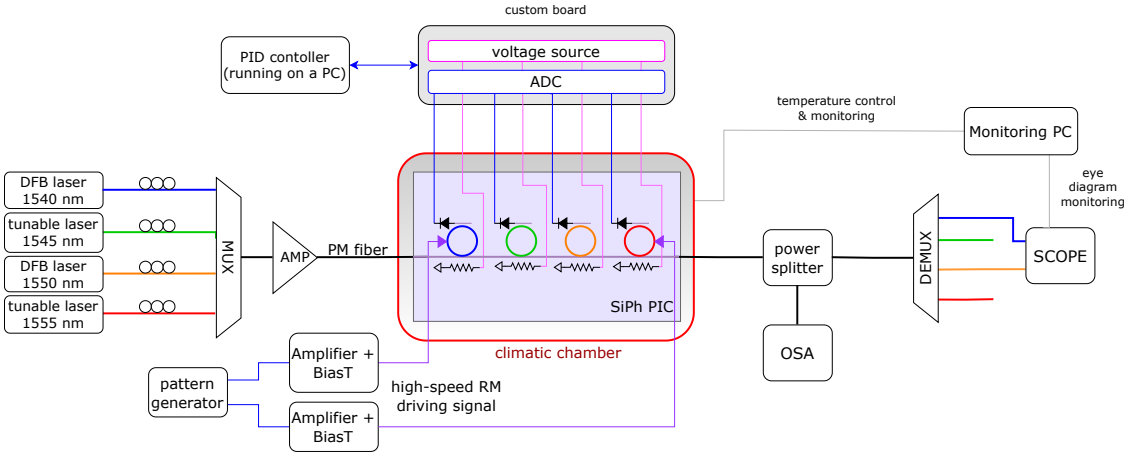

Figure 4.25. *Schematic of the 4-channel WDM test setup.*

then amplified with the help of an amplifier ans BiasT. This amplification is necessary to achieve a voltage swing of 5 V, required due to the high TP of the available RMs with voltage swing of 1 V and increased IL of the setup. This is partially caused by the high losses at the GC-fiber interface that are introduced by the fiber attachment process.

The modulated optical output is split in two paths. A small percentage of the power is directed to an OSA for monitoring the status of the setup. This greatly facilitates the startup procedure and is a powerful tool for troubleshooting the performed measurements. The rest of the power is directed to a second filter that acts as a demultiplexer (DEMUX) and separates the four wavelengths that were multiplexed in the system. A high-speed scope is then employed to record the eye diagrams and eye diagram parameters of the two channels that are modulated with the high-speed signal. The test board is placed inside a climatic chamber that allows to control and monitor the temperature of the devices and perform temperature scans for testing the thermal tuning loop operation. The eye diagram parameters monitored by the scope as well as the temperature of the climatic chamber are recorded by a monitoring PC with the help of an Igor program. This allows to record the necessary data that are required to evaluate the operation of the control loop in the case when the WDM scheme is adopted.

Concerning the thermal tuning control loop implementation, it was possible to realise a 4-channel control loop that runs simultaneously and independently for all four RMs. On one hand this was possible thanks to the use of the custom boards for the biasing of the µ-heaters and readout of the drop-port I_{ph}. For this purpose only two boards were required, each one offering two ADC and two voltage source channels as it was already described already in Sec. 4.4.2. These 8 channels (4 of each type) are sufficient to thermally control the 4 RMs. It is worth reminding here that a 4-channel control loop could not be realised with bench-top instruments due to their large footprint and non-availability of that many power supplies and multi-meters. The control loop details are shown in Fig. 4.25. On the other hand, the software implementation of the PI controller was also adjusted to support multi-channel operation. The PI controller was adapted to run sequentially in a loop for

all channels, one channel at a time. The PI gains chosen are common, but every RM has its own setpoint and computed V_{heater} at every PI cycle.

The thermal tuning process was also adapted to the 4-channel operation. The start-up process is run sequentially for all channels to calculate the setpoint of each RM and initialize them. Then the PI controller function starts running to control all RMs simultaneously and sequentially but independently. For the multi-channel system we chose to use two different PCs for running the PI controller and the eye-diagram and temperature monitoring. This was done to increase the BW of the control loop. Communication with the scope for retrieving the eye diagram parameters takes much more time compared to the communication with the custom board to perform a read of the I_{ph} and a write for the V_{heater}. Decoupling those two operations allows to run much faster the PI controller without the limitation of the eye diagram parameters read time required by the scope. At the same time, these parameters can be independently recorded every given number of cycles of the PI controller. The data recorded and produced by the two distinct Igor programs can always be correlated afterwards thanks to the timestamps that are also recorded. The speeding up of the PI controller that is achieved is especially beneficial in the case of the WDM system because the PI needs to run simultaneously for all four channels and repeat each cycle four times, which reduces by a factor of four the system BW.

4.7.2 Challenges

Although the WDM approach offers many advantage as it has already been described, it would add extra complexity in the thermal tuning system and additional challenges that need to be addressed.

Initial wavelength locking mechanism

The first one concerns the thermal tuning process. In the case of a WDM Tx, multiple RMs are connected in series in a common bus waveguide, where all operational wavelengths are multiplexed. Each ring modulates a different channel of the link and is therefore designed to operate at a specific and distinct wavelength. To ensure the reliable operation of the multi-channel transceiver, each RM needs to be independently tuned to its operational wavelength, as it happens with the single-channel Tx. This not only requires extra hardware for the simultaneous control of multiple channels, but also makes the thermal tuning process more complicated due to the presence of multiple wavelengths in the common bus waveguide. Additional logic is necessary to perform the startup procedure and ensure that every RM is always locked to the appropriate wavelength, irrespective of the initial conditions and variations. We will describe here how the single-channel thermal tuning control loop can be adjusted for a WDM scheme. We will work with the 4-channel WDM circuit that is available in out PICv2. However, the same methodology can be applied for WDM systems with any number of channels (as long as the number of channels is compatible with the limitations imposed by the RM FSR).

As it was described in detail in Section 4.5, in the case of single-channel operation, the thermal tuning process based on average power monitoring of the drop-port photo-

current is simple and consists of two steps: the startup procedure and the PID controller operation. The start-up procedure involves scanning the voltage applied to the RM heater and monitoring the DP I_{ph}. A single peak will appear at the I_{ph}=f(V_{heater}) plot for some values of V_{heater} (Fig. 4.26a). This peak corresponds to the resonance point of the RM. Its position depends on the RM characteristics and environmental conditions, however it uniquely identifies the V_{heater} required for operation at the optimal point, and the linear region near the resonance where the PID controller can operate.

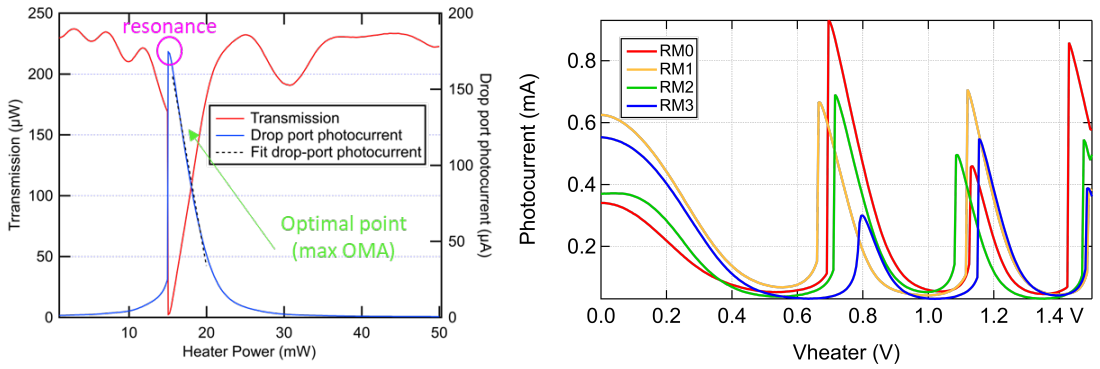

Figure 4.26. *I_{ph}=f(V_{heater}) (a) for a single RM circuit and (b) for the 4-channel WDM circuit that includes 4 cascaded RMs.*

This is not the case for a multi-channel system. If a WDM scheme is employed, many wavelengths are multiplexed in the common waveguide where all the RMs are coupled. If we repeat the V_{heater} scan for an RM of the WDM Tx, in the same way described in Fig. 4.21, instead of observing only one peak of the I_{ph}, we will observe multiple peaks, in principle one for every wavelength present in the system. This happens because as we scan the V_{heater} the resonance wavelength of the RM will shift and it will coincide with all or multiple of the input laser wavelengths. This is evident in Fig. 4.26b where the I_{ph}=f(V_{heater}) plots for the four RMs of the 4-ch WDM circuit from PICv2 are shown, when a 4-channel external laser comb is used. From the data retrieved from this scan (I_{ph} for the different V_{heater} applied) that are the only data the feedback control mechanism possesses to perform the initial wavelength locking, it is impossible to distinguish which peak corresponds to which input laser. At the same time, when the initial conditions (temperature, exact value of input λ_{laser}) change, the I_{ph} peak position that corresponds to each λ_{laser} will change. Therefore, even if it was possible to identify once the correspondence between I_{ph} peak and input λ_{laser}, this would change with time.

This fact constitutes an important obstacle for the realisation of a WDM SiPh based Tx for HEP applications. In HEP experiments the data from the FE sensors are organised in read-out channels. Every RM will be driven by a FE driver containing data of a specific read-out channel. In the optical links and BE, the channel separation in case of a WDM scheme is based on the use of multiple wavelengths per fiber that are demultiplexed and matched to the corresponding electrical channels in the BE. Given the current architecture of the system, an one-on-one correspondence between the FE and BE channels is mandatory since the origin of the data is crucial for the data reconstruction. This is ensured when

every RM always modulates a specific input λ_{laser}, the one it was designed to operate at. Consequently, a mechanism is necessary to identify for each RM the peak of the I_{ph}=f(V_{heater}) scan that corresponds to its unique operational wavelength.

There are different mechanisms that can be employed to ensure that every RM is operated at its distinct and dedicated wavelength. In the following section we will analyse these mechanisms.

Use of drop-port filters The most straight-forward way to identify for each RM the peak of the I_{ph}=f(V_{heater}) that corresponds to its unique operational wavelength is using on-chip filters at the drop-port of the RM. The filters can be placed at the drop-port output before the Ge PD. By appropriately tuning the BW and center wavelength of the filter, this method allows to reject the signals generated by the interaction of the RM with the lasers assigned to the neighbouring channels during the startup procedure. This way the PD of each RM will only record the correct peak ensuring that the feedback control loop locks the RM to the appropriate wavelength.

The market research we have done has revealed a tendency to migrate towards the O-band for the telecom and datacom systems. Between the emerging standards, the one that matches our system specifications (4-channel WDM inter data center links with bitrates of 25 Gbit s^{-1} per channel) and we estimate will dominate the market is the 100G CWDM4 MSA Ethernet standard. Therefore, we try to align with this standard with the systems and components we design. This is also true for the next generation of 4-ch WDM circuits we have designed, and the components, like the drop-port filters, that need to be compatible with it.

In this regard, to match the 20 nm channel spacing of the CWDM4 MSA standard, the drop-port filters will need to have FSR greater than 80 nm and BW of 20 nm. Smaller BW will make the filters very narrow and not compatible with channel BW and the expected small fluctuation of the λ_{laser} and RM λ_{res}, while bigger BW will result in interference with neighboring channels. Also, the filters need to have flat-top spectral response, for uniform operation in their designated BW. Of course, low cross-talk between the channels is preferable, and compatibility with MPW fabrication processes. Ideally, the chosen filter should constitute a solution for an absolute wavelength reference on-chip. If this is not possible and some tuning is still required, this should be achieved with low power and without feedback control otherwise some logic for identifying the correct peak will be required, coming again back to the problem we are trying to solve.

Various silicon based on-chip photonic filters have been proposed in bibliography, based on MZIs, MRRs, waveguide Bragg gratings, AWGs and echelle gratings, as it was analyzed in 2.2.1 [17].

MRR based on-chip filters although can be very compact but are not suitable for this application. It is difficult to achieve MRR with FSR of 80 nm, since radius smaller than 1 µm is required. Also, complicated structures of higher-order cascaded MRRs are necessary to achieve box-like response with BW of 20 nm. Last but not least, RRM are very sensitive to temperature variations, therefore an active thermal tuning mechanism would be requires for their operation, rendering this solution unsuitable for our application.

Similarly, AWG-based filters have very large footprints and very small FSR and BW, so they are not preferred in this type of application.

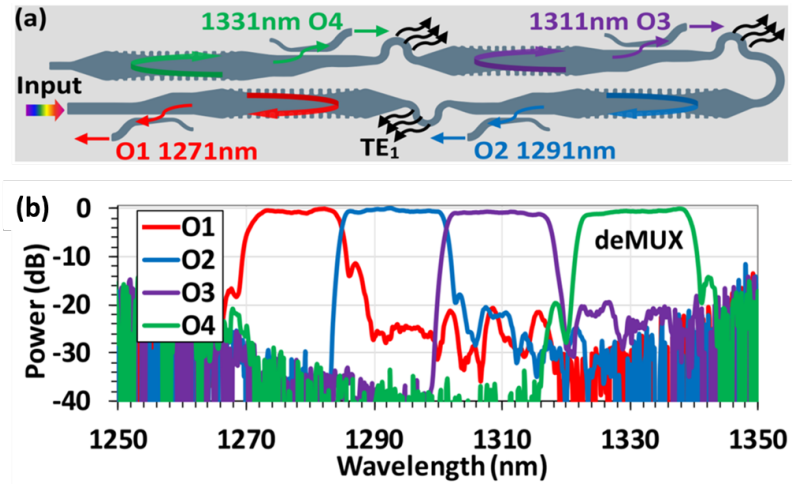

Figure 4.27. *(a) Schematic configuration of the silicon-based four-channel CWDM (de)multiplexer working in the O-band proposed by [18], with* 18 nm *channel spacing. It is composed of four cascaded optical filters with flat-top spectral responses, which are realized by combining an MWG and a two channel mode (de)multiplexer. (b) The measured spectral response of the fabricated CWDM filter as a DEMUX.*

Another way of realising integrated filters is using waveguide Bragg grating structures. Bragg gratings can be combined with MMI structures or directional couplers to form four-ports filters. These filters have flat-top responses, very large FSRs and can be designed to operate at various wavelengths. Liu et al. [18] have proposed and realised such a Si-based four channel CWDM (de)multiplexer for the O-band. The device comprises four cascaded optical filters that are realised by combining multimode waveguide gratings (MWGs) and two-channel mode (de)multiplexers. The device and its measured spectral response are shown in Fig. 4.27 (a) and (b) respectively. It showcases box-like spectral response with 20 nm channel spacing and 80 nm BW. This (de)multiplexer is compatible with the 100G CWDM4 MSA standard that we are planning to adopt and some variation of the it could be used is our system to realise drop-port filters (note that we do not need a 4-channel filter, but four single-channel ones, but with the aforementioned BW, FSR and center wavelengths). Moreover, this structure has reduced thermal sensitivity of 46 pm $^{\circ}C^{-1}$ thanks to an SU-8 upper-cladding and could potentially be operated without the need for thermal tuning in a wide temperature range. This specific device requires complex fabrication processes and is not compatible with MPW processes, however it serves as a proof of a Bragg-grating based filter for our application. Since in general Bragg grating structures and couplers are compatible with common MPW processes, a device employing the same principle of operation could be designed at CERN. This would allow to practically test its behaviour and also verify its thermal sensitivity when only simple materials like SiO_2 or air are available for the upper cladding since it is known that the reflection and transmission of Bragg gratings are very sensitive to temperature variations. For the final system that will be deployed in at least ten years from now possibly more complex processes will be

available allowing for further improvement of the performance of such devices. In any case, they remain an interesting solution to possibly investigate.

Experimental verification of the proposed drop-port filter solution To experimentally verify the proposed drop-port filter solution for rejecting the signals generated by the interaction of the RM with the lasers assigned to the neighbouring channels during the startup procedure, we assembled a test setup of a RM with an external filter, since at the current generation of PICs the filter functionality is not yet integrated on chip. The setup is shown in Fig. 4.28. It includes a RM whose drop port is connected to a grating coupler instead of a PD. An external pass-band filter tuned to the nominal wavelength of this RM is then connected to the drop port output. The initial wavelength locking scan (startup process) was then repeated. This time, instead of recording multiple peaks for the RM, in principle one for every wavelength present in the bus waveguide, as shown in Fig. 4.26b, only a single peak is recorded, corresponding to the nominal RM λ_{laser}. This is illustrated in Fig. 4.29.

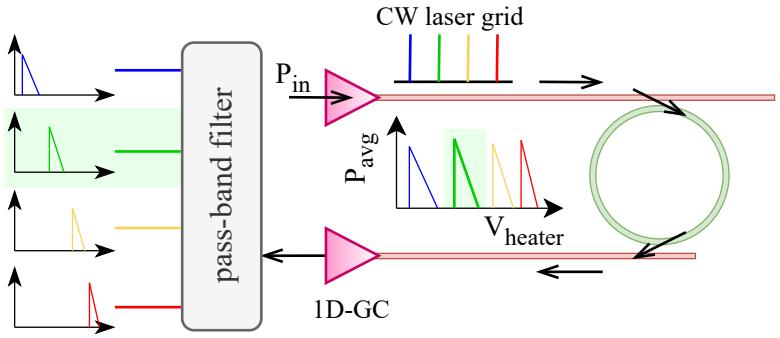

Figure 4.28. *Schematic of the setup including a RM with a grating coupler at the drop port and a pass-band filter connected at its output, allowing to record a single peak that corresponds to the nominal RM λ_{laser}, denoted with green.*

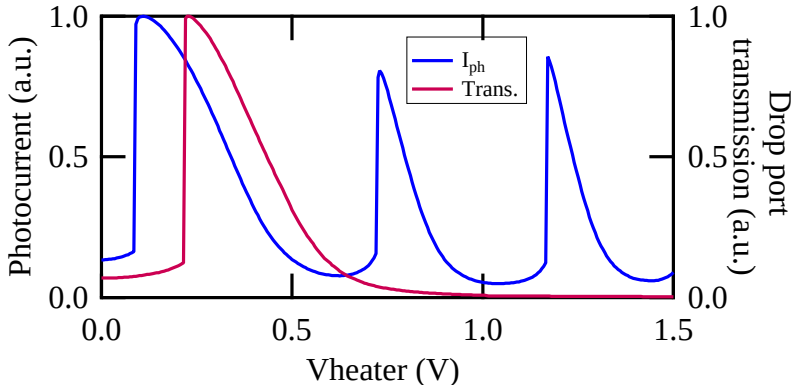

Figure 4.29. *In blue the normalized drop port I_{ph} varying V_{heater} for one RM of the WDM circuit. In red is the equivalent plot (normalized drop port transmission) of the RM when adding a pass-band filter at the drop port output (as shown in Fig. 4.28). In both cases, the 4-channel laser source is used.*

This solution simplifies the 4-channel WDM implementation, rendering its operation

equivalent to the single channel one. This serves as proof-of-concept of a drop port filter based solution for locking each RM to its design wavelength. Future PIC designs can integrate this functionality on-chip, by adding optical filters like the ones presented in paragraph 4.7.2 between the RM drop port and the PD.

Adoption of a different thermal-tuning technique So far we have considered that the thermal tuning control loop employed in the WDM system is based on a feedback controller that monitors the average power at the drop port. Therefore, to simultaneously perform the thermal tuning in multiple channels and perform the initial wavelength locking process at a specific wavelength for every RM, extra logic is required, to distinguish between the multiple wavelengths present in the system. Nevertheless, by using a different thermal tuning technique that is not based on the average power monitoring at the drop port we do not have to deal with this problem, since the distinction between the channels can happen in a different way.

Such a technique is the bit-error rate monitoring, described in Sec. 4.3.2. If this thermal tuning method was used instead, then we could employ four receivers, each one working at one of the four wavelengths used in the system, and for every RM compare the RM driver data with the Rx data that corresponds to the wavelength that this RM is supposed to operate at. This way, for every channel the BER is zero only if this RM is locked at the correct wavelength. However, as it was already mentioned, this method removes one challenge but adds many more, since it requires high speed logic for recovering the BER in the FE, and also tampering with the FE driving signals. This not only will result in high power consumption, but will also require the integration of high speed electronics in the front-end system. Although this approach is not feasible for our application, it might be useful in other applications than do not have strict power and spacing margins for the transceivers.

Another technique that would simplify that startup procedure is balanced homodyne locking, as described in Sec. 4.3.5. This technique is compatible with WDM systems. If the phase response of each control loop is optimized for a different laser, then this method could work for a WDM system, allowing to operate each RM at its designated laser. However, extra adjustments might be required to compensate for variations that are induced by manufacturing tolerances. Overall, this could be a feasible solution, although extra care would be required due to the complicated photonic circuits (phase shifters and photodiodes) that this method employs.

Last but not least, dither locking would be another interesting technique in this regard, as analyzed in Sec. 4.3.4. Although the obstacle that this method necessitates complex electronics to recover the error signal and disturbs the RM in a way that can degrade its performance remains, it is fully compatible with WDM implementations. This can be ensured by using different dithering frequencies and different filters for each RM.

Overall, all these alternative techniques would require further investigation to verify their compatibility with our application. The adoption of one of them would also necessitate important modifications in our system that might render it even more complex that it is now. However, they are mentioned here to provide an alternative in case the current

system choices turn out to be not feasible, and alternatives route need to be identified.

Adoption of different system architecture One of the main factors that renders the thermal tuning process more complicated, and imposes the need for extra logic to realise the startup procedure for a WDM system is the chosen system architecture. More specifically, given the current architecture of the system, an one-on-one correspondence between the FE and BE channels is mandatory since the origin of the data is crucial for the data reconstruction. This is ensured when every RM always modulates a specific input λ_{laser}, the one it was designed to operate at.

Instead of adding extra logic in the control loop, that allows to distinguish between the available wavelengths, as it was already described, or implementing more complex thermal tuning processes, another possible solution to address this challenge would be to adopt a different system architecture overall. If the one-on-one correspondence between the FE and BE channels is not required, the thermal tuning process would be greatly simplified. In such a case, instead of tuning each channel (RM) to a specific assigned wavelength, RMs can be simply tuned to the nearest available wavelength at the time of the startup process, or even at some random wavelength, unique for every RM. This can be done simply, without the need for extra hardware and logic to distinguish between the wavelengths present in the system. Such approaches have already been reported and tested in literature [19, 20]. However, even though they could potentially greatly simplify the startup process complexity, they come with important drawbacks. First of all, the first solution only works if the spacing between the multiple RM resonances is homogeneous, meaning that the process and temperature shifts need to be common to all RMs, so that every RM will eventually lock to a different input λ. Nevertheless, this is not always the case. Depending on the final system implementation, temperature variations might differ between the RMs, depending on the position of every RM in the FE chips and their contiguity with electronic chips or other components that might affect their temperature. At the same time, fabrication process tolerances might affect different RMs in different ways and cause non-uniform resonance spacings by design. As for the second approach, one would need to ensure that every RM is locked to a different wavelength every time. In both cases, even if we could ensure that the RM resonances are homogeneous and that every ring is tuned to a different wavelength, the approaches still involves important challenges. When locking every RM to the nearest available wavelength (in terms of spectral position) or to a arbitrary wavelength, depending on the unique and ever-changing initial condition every time the startup process is performed, the correspondence between RM and wavelength will be arbitrary and variable. This means that the origin of the data (FE channel) is no longer contained as information in the wavelength. Instead, the electrical BE will need to distinguish between channels and perform all necessary bit-ordering operations. This might require adding extra information in the data that are sent to the BE, that will allow to identify their FE channel of origin. This adds extra complexity both in the FE and in the BE. Overall, although in theory this could be an alternative solution for such a system, in practice it might not be feasible for this application, since it requires fundamental changes in the complete system architecture that would need to be incorporated by various teams

that collaborate for the realisation of the CERN experiments systems. This renders such system architecture changes vary complex to implement, and solution that are localized in a single system are usually preferred.

Solutions related to the of-chip laser functionality Another approach to address the problem caused by the presence of multiple wavelengths in a WDM system and the consequent presence of many peaks for each RM in the initial I_{ph}=f(V_{heater}) scan concerns the operation of the BE laser sources. Typically the laser sources (either four different lasers or a single 4-channel laser source) that are multiplexed in the common bus waveguide are turned on simultaneously during the initialization of the control loop to provide a constant power input. However, if it were possible to turn on one input laser channel at a time, this would allow to execute the startup procedure independently for each RM, in series. Every time a specific RM is initialized, the corresponding laser channel can be turned on while the rest are kept off, allowing to record only a single peak during the I_{ph}=f(V_{heater}) scan, and more specifically the peak that this RM should operate at. This process can be then repeated for all four RMs in turn, before starting the PI control loop, at which point all four laser channels will be turned on.

For this approach to work reliably it will be necessary to move away from the designated region of operation of the RM that is being tuned, the resonance notches of the rest of the RMs. This is necessary because otherwise the I_{ph} measured for the RM that is being tuned, will be lower than its maximum value due to the interference with the other channels if they resonate it the region of operation of this RM. This will in turn lead to a wrong calculation of the optimal I_{ph} (since this is calculated as $I_{ph-opt} = k \cdot I_{ph-max}$ and the $I_{ph\text{-}max}$ measured will be wrong). The resonant notches of the rest of the RMs can be moved away be appropriately biasing the RMs either with a fixed voltage that ensures that they will not be found in the critical region, or by biasing all RMs with the same voltage as the single RM is being scanned, which ensures that the resonant notches of all 4 channels will retain a fixed distance and will not interfere.

Although this solution would consist an interesting approach, it would require laser sources that probably will not be commercially available. The plan for the final system implementation is to adopt a commercially available 4-channel laser COMB with the four desired laser outputs, that has been identified as the optimal solution. In such a component turning on and off individual channels will not be possible. The adoption of a custom component as 4-channel laser source is prohibitive since it would drastically increase the cost of the link development. Therefore, it probably is not feasible. Moreover, it would require communication between the BE lasers and FE chips that will perform the startup procedure, to turn on and off the relevant channels. This not only increases the complexity of the FE electronics and BE lasers, but would also increase the required connections and material budget. Overall, this approach has been rejected for the moment due to its incompatibility with our system requirements.

Solutions adopted for testing For testing purposes, the correspondence between RM and λ_{laser} can be freely chosen for convenience. This allows to test the thermal control

loop in multichannel operation and verify other aspects of the systems without having to address at this stage the initial wavelength locking challenge. However, in the final system each RM needs to operate at a specific λ, for interoperability between the FE and BE channels.

Assembly of the WDM test board

Another important challenge of the WDM approach is the assembly of a WDM test board that can be tested against temperature variations. As it was described for the single channel case, the test boards we had assembled turned out to be sensitive to temperature. The power coupling was showing a large temperature dependence, that could not be attributed only to the temperature dependence of the GC efficiency. After some repeated temperature scans it was permanently degrading. This problem was amplified in the case of the WDM test board. This happened because of the board architecture and components. The initial test board shown in Fig. 4.30a consisted of pieces of different PCBs plus the Si PIC. The different parts were glued together. The fibber array was attached to the PIC, but parts of it were also touching the other boards and plastic base, as it can be seen in Fig. 4.30b. Given the different thermal expansion coefficients of the different parts, it was assumed that the temperature variations caused a relative movement between them eventually leading to the breaking of the fiber alignment. Another possible explanation was that the glue used for the fiber attachment, although in theory should have almost zero expansion in a wide temperature range, was eventually the cause of the problem.

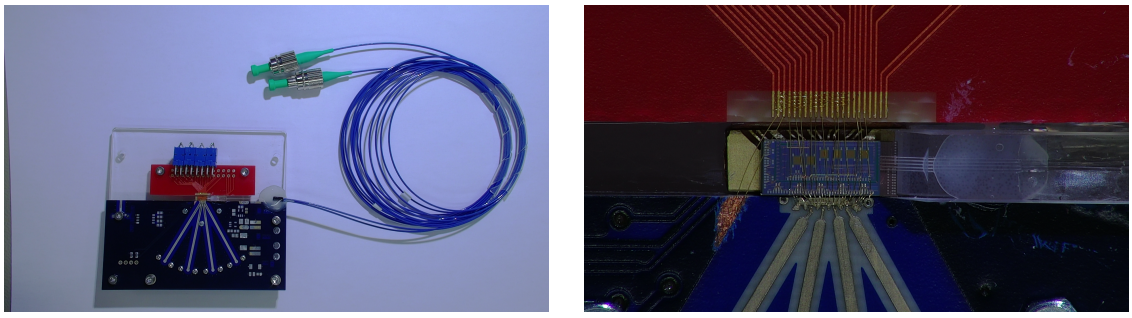

(a) **(b)**

Figure 4.30. *(a) A picture of the initial WDM test board. (b) A zoomed in picture of the initial WDM test board showing the Si PIC, the two PCB parts with the electrical traces that are wire bonded to the PIC electrical contacts, as well as the fiber array that is attached on top of the PIC.*

The transmission at the 4-channel circuit output of the initial board for different temperatures is shown in Fig. 4.31 showcasing the temperature dependent coupling. Since the thermal tuning technique that we have adopted is sensitive to the input power, this was a problem that had to be addressed. This turned out to be a not trivial task and multiple solutions were tried out. The first one was to reattach the fiber, in case it was misaligned during the initial assembly process. Then since the problem persisted we tried with a new fiber array and eventually a new glue that had a wider temperature range. As a next step, a new board was assembled employing different techniques for the fiber attachment

and different components. A single PCB with all the necessary traces was used instead of multiple ones as happened with the first test board, in case the issue was caused by the use of multiple PCBs. Then the fiber was attached on top of the PIC. However, even in that case the problem persisted. Given this wide investigation, another possible explanation is that the temperature change might cause the bending of the PCB that houses the PIC which could be the eventual cause of the breaking of the alignment between the PIC and fiber arrays. This investigation is still ongoing and more studies are required to identify a new board design and assembly process to achieve stable and temperature independent coupling. Thankfully, in the initial test board the temperature dependence of the coupling appeared after a few temperature cycles, which allowed to collect a good set of measurements and verify the operation of the thermal control loop for multi channel operation. These measurements are presented in the next section.

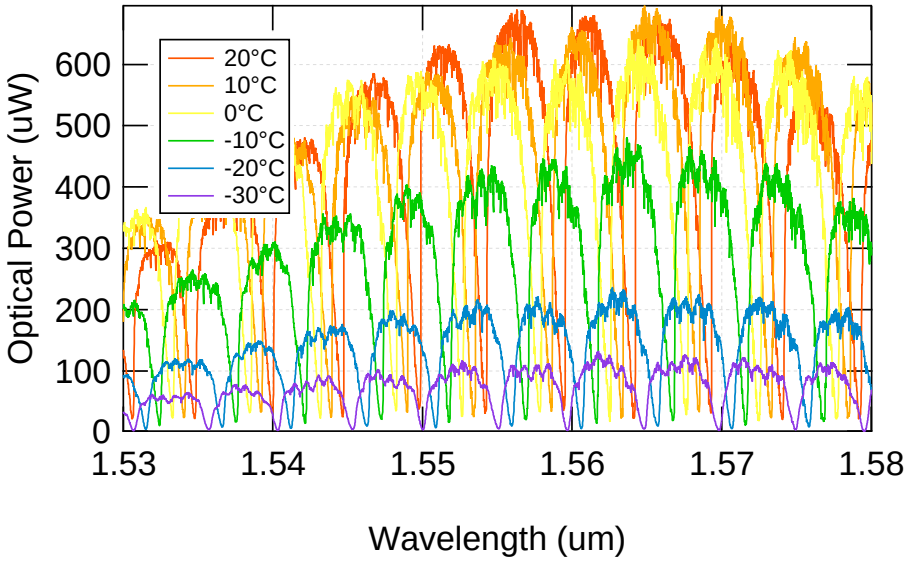

Figure 4.31. *The transmission spectrum of the 4-channel WDM circuit varying the input laser wavelength for different ambient temperatures.*

4.7.3 Measurements varying the temperature

Using the setup described in Fig. 4.25 ans Sec. 4.7.1, a test was performed to verify the operation of the thermal tuning control loop for multi-channel operation. To this end, a temperature sweep was performed with the climatic chamber, while the PI controller was simultaneously running in closed loop operation for all four RMs. High-speed modulation was performed for two of the RMs. The measured eye diagram parameters (OMA and ER) for these two RMs are presented in Fig. 4.32. For both RMs the OMA remains stable in a wide temperature range of 30 °C, from 25 °C down to −5 °C. The variations are below 20% of the nominal value. The ER of both rings is also very stable. This proves that the thermal tuning control system can be successfully scaled for the 4-channel system and ensure its stable and optimal operation. No effects degrading the performance of the RMs and caused by the thermal cross-talk between neighbouring channels were observed. These results also

serve as a validation of the thermal tuning process followed for the multi-channel system. Further improvement of the assembly process of the test boards will eventually allow to test the circuit in an even wider temperature range.

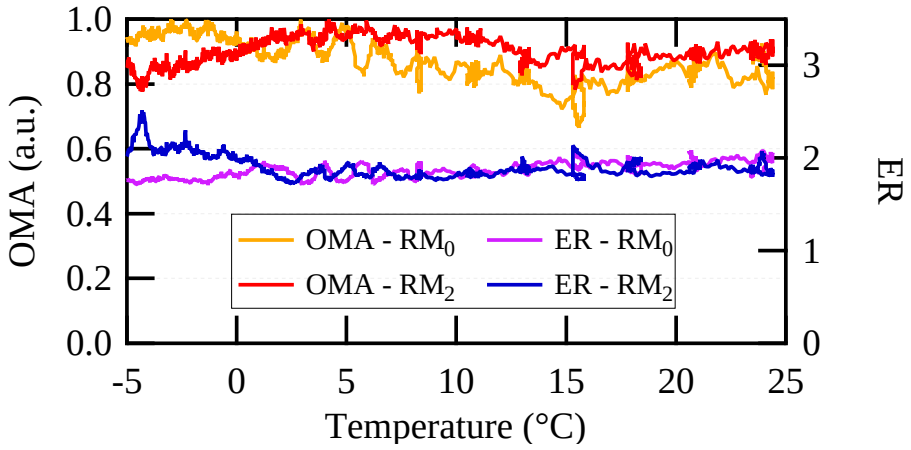

Figure 4.32

4.8 Conclusions

The thermal tuning constitutes one of the main system challenges that need to be addressed. It is required in all circuits that rely on RMs, since these devices are very sensitive to temperature and process variations, that result is continuous variation of their resonant wavelength. This can be solved by using an active thermal tuning mechanism that will counteract these external fluctuations and ensure the stable operation of the RMs at their optimal operating point. During this PhD, an extensive effort took place to realise a thermal tuning mechanism based on average power monitoring at the drop port. This effort included the design, tuning and implementation of a PI controller as part of the feedback control loop. After the PI controller was experimentally validated, two different versions were implemented, each one compatible with a different phase of the Tx development. The implemented control loop was successfully tested in single channel operation, managing to compensate both for temperature and external laser wavelength fluctuations. This is a milestone in the development of the SiPh Tx, since without the thermal tuning the stable operation of the Tx is not possible. The availability of a thermal tuning test setup also also to perfect the tuning process, consisting of the power-up procedure and the PI operation, and adjust it for our system. As a second step, the thermal tuning control loop was adjusted for multi-channel operation. This was a very complex task and involves many complications, like the assembly and the scaling of the system, the required test-boards and the performance of the tests. However, we successfully demonstrated the operation of the thermal control loop in multi-channel operation, correcting for temperature variations. These results serve as a proof of concept of the compatibility of this solution with our system. However its adoption in a final WDM system implementation involve extra challenges that stem from the presence of multiple wavelengths in the system. The

thesis aims to address the challenge, by proposing various solutions that include either use of drop-port filters or adoption of different system choices. Overall, the work that was done related to the thermal tuning control loop not only resulted in the implementation of a first thermal tuning system that allowed further testing and characterisation of the Tx both in single and multi channel operation, but at the same time it provides the methodology and research that will allow the implemented control loop to be adjusted for a different system or be improved for compatibility with the final system requirements.

Bibliography

[1] P. Dumon, G. Priem, L. R. Nunes, W. Bogaerts, D. Van Thourhout, P. Bienstman, T. K. Liang, M. Tsuchiya, P. Jaenen, S. Beckx, *et al.*, "Linear and nonlinear nanophotonic devices based on silicon-on-insulator wire waveguides," *Japanese journal of applied physics*, vol. 45, no. 8S, p. 6589, 2006.

[2] Y. Xing, J. Dong, U. Khan, and W. Bogaerts, "Capturing the effects of spatial process variations in silicon photonic circuits," *ACS Photonics*, 2022.

[3] Wikipedia, "Bang-bang control." https://en.wikipedia.org/wiki/Bang%E2%80%93bang_control [Accessed: (28/06/2023)].

[4] S. Bennett, "Development of the pid controller," *IEEE Control Systems Magazine*, vol. 13, no. 6, pp. 58–62, 1993.

[5] theengineeringconcepts.com, "Pid controller." https://www.theengineeringconcepts.com/pid-controller/ [Accessed: (28/06/2023)].

[6] C. Li, R. Bai, A. Shafik, E. Z. Tabasy, G. Tang, C. Ma, C.-H. Chen, Z. Peng, M. Fiorentino, P. Chiang, *et al.*, "A ring-resonator-based silicon photonics transceiver with bias-based wavelength stabilization and adaptive-power-sensitivity receiver," in *2013 IEEE International Solid-State Circuits Conference Digest of Technical Papers*, pp. 124–125, IEEE, 2013.

[7] C. Li, R. Bai, A. Shafik, E. Z. Tabasy, B. Wang, G. Tang, C. Ma, C.-H. Chen, Z. Peng, M. Fiorentino, *et al.*, "Silicon photonic transceiver circuits with microring resonator bias-based wavelength stabilization in 65 nm cmos," *IEEE journal of solid-state circuits*, vol. 49, no. 6, pp. 1419–1436, 2014.

[8] S. Saeedi and A. Emami, "Silicon-photonic ptat temperature sensor for micro-ring resonator thermal stabilization," *Optics express*, vol. 23, no. 17, pp. 21875–21883, 2015.

[9] W. A. Zortman, A. L. Lentine, D. C. Trotter, and M. R. Watts, "Bit-error-rate monitoring for active wavelength control of resonant modulators," *IEEE Micro*, vol. 33, no. 1, pp. 42–52, 2012.

[10] C. T. DeRose, M. R. Watts, D. C. Trotter, D. L. Luck, G. N. Nielson, and R. W. Young, "Silicon microring modulator with integrated heater and temperature sensor for thermal control," in *Conference on Lasers and Electro-optics*, p. CThJ3, Optica Publishing Group, 2010.

[11] K. Padmaraju, D. F. Logan, T. Shiraishi, J. J. Ackert, A. P. Knights, and K. Bergman, "Wavelength locking and thermally stabilizing microring resonators using dithering signals," *Journal of Lightwave Technology*, vol. 32, no. 3, pp. 505–512, 2013.

[12] S. Lin, X. Zheng, P. Amberg, S. S. Djordjevic, J.-H. Lee, I. Shubin, J. Yao, Y. Luo, J. Bovington, D. Y. Lee, *et al.*, "Wavelength locked high-speed microring modulator using an integrated balanced homodyne cmos control circuit," in *Optical Fiber Communication Conference*, pp. Th3J–4, Optica Publishing Group, 2016.

[13] J. A. Cox, A. L. Lentine, D. C. Trotter, and A. L. Starbuck, "Control of integrated micro-resonator wavelength via balanced homodyne locking," *Optics express*, vol. 22, no. 9, pp. 11279–11289, 2014.

[14] C. Sun, M. Wade, M. Georgas, S. Lin, L. Alloatti, B. Moss, R. Kumar, A. H. Atabaki, F. Pavanello, J. M. Shainline, *et al.*, "A 45 nm cmos-soi monolithic photonics platform with bit-statistics-based resonant microring thermal tuning," *IEEE Journal of Solid-State Circuits*, vol. 51, no. 4, pp. 893–907, 2016.

[15] S. Agarwal, M. Ingels, M. Pantouvaki, M. Steyaert, P. Absil, and J. Van Campenhout, "Wavelength locking of a si ring modulator using an integrated drop-port oma monitoring circuit," *IEEE Journal of Solid-State Circuits*, vol. 51, no. 10, pp. 2328–2344, 2016.

[16] I. The MathWorks, "pade." https://ch.mathworks.com/help/control/ref/dynamicsystem.pade.html [Accessed: (20/06/2023)].

[17] D. Liu, H. Xu, Y. Tan, Y. Shi, and D. Dai, "Silicon photonic filters," *Microwave and Optical Technology Letters*, vol. 63, no. 9, pp. 2252–2268, 2021.

[18] D. Liu, M. Zhang, Y. Shi, and D. Dai, "Four-channel cwdm (de) multiplexers using cascaded multimode waveguide gratings," *IEEE Photonics Technology Letters*, vol. 32, no. 4, pp. 192–195, 2020.

[19] M. Georgas, J. Leu, B. Moss, C. Sun, and V. Stojanović, "Addressing link-level design tradeoffs for integrated photonic interconnects," in *2011 IEEE Custom Integrated Circuits Conference (CICC)*, pp. 1–8, 2011.

[20] P. Dong, R. Gatdula, K. Kim, J. H. Sinsky, A. Melikyan, Y.-K. Chen, G. de Valicourt, and J. Lee, "Simultaneous wavelength locking of microring modulator array with a single monitoring signal," *Opt. Express*, vol. 25, pp. 16040–16046, Jul 2017.

Chapter 5

Polarization management

5.1 Motivation

The system concept of a SiPh based data link for HEP applications is shown in Fig. 5.1. As was already mentioned, this system differs from typical telecom, datacom and co-packaged optics systems. One of its more important particularities is that the lasers that are required for providing the optical input to the RMs need to be placed far away from the RMs (more than 100 m), at the back-end and be connected to the RMs through long SMFs. This is necessary due to the high power consumption and low radiation tolerance of available laser technologies that would render their integration in the FE impossible. The lasers would not survive the radiation levels and they would increase the power consumption of the FE TRx that much that SiPh would no longer offer an advantage as a technology platform compared to already existing solutions.

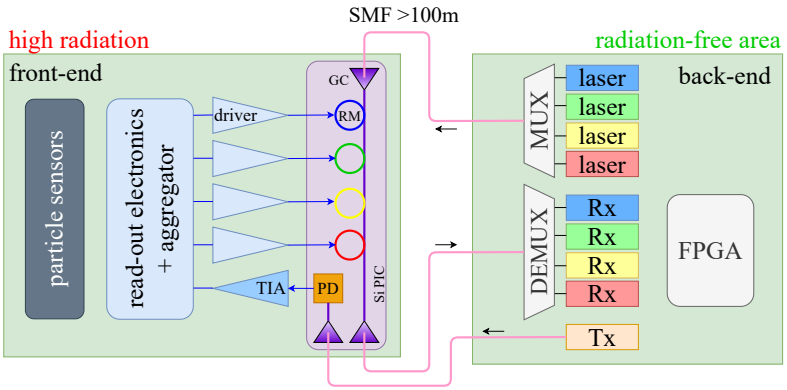

Figure 5.1. *System concept of a SiPh based optical data link for HEP experiments.*

Although the decoupling of the optical sources from the modulators and their placement in the BE offers a very convenient solution to this problem, it comes at the cost of complicating the link and introducing the need for polarization management. This is generated from the fact that the SiPh PIC can only operate for a specific polarization of the light while SMFs do not maintain the polarization. As a result, a polarization diversity scheme is required for effective coupling of the light from the lasers to the Si PICs. Without such a scheme, depending on the architecture of the link, either the input power to the RMs will fluctuate or multiple polarization states will be excited in the Si PIC leading to spatial broadening of the optical pulses and degradation of the optical signal. Both effects are unwanted and prohibitive for the successful operation of such links. It is important that the power budget of the link remains stable during operation to achieve high quality modulation and compatibility with the BE Rx sensitivity and of course the broadening of the pulses may result in excessive increase of the transmission errors and limit the achievable data rate. In the rest of this section the polarization of the light in SMFs and is the Si waveguides will be explained.

5.1.1 Polarization in SMFs

SMFs, as their name suggests, only support the fundamental hybrid mode HE_{11}. HE_{11} consist of two orthogonal polarization modes. As a convention we can consider they have their electric fields predominantly polarized along that x and y axis of the fiber respectively (the direction of propagation is along the z axis). These two polarization modes are denoted as E_x and E_y and the corresponding spatial variation of the electric fields as $E_x(x, y)$, $E_y(x, y)$. In a lossless fiber, the electric field vector of any wave propagating along the z-direction can then be described by a linear superposition of these two modes according to:

$$E(x, y, z) = [C_x E_x(x, y) + C_y E_y(x, y)]e^{-i\omega t} \tag{5.1}$$

where $C_j = c_j E^{i\beta j z}$ are complex coefficients describing the amplitudes and phases of the modes, $E_i(x, y)$ describe the spatial variation of the electric fields, $k_0 = 2\pi/\lambda_0$ is the wavenumber in free space for a given frequency of light, $\beta_j = k_0\ n_j$ are the propagation constants of the polarization modes, λ_0 is the free-space wavelength, and n_j are the effective indices of the modes [1]. Monochromatic propagation is assumed in 5.1. All polarization effects arise because of these two modes.

The state of polarization of the modes is described by the average direction of their electric field vector. The complex ratio C_x/C_y then describes the polarization state of the propagating wave. In ideal fibers with perfect rotational symmetry, the two modes are degenerate with $\beta_x = \beta_y$ and any polarization state injected into the fiber would propagate unchanged. However, real fibers have imperfections such as core deformations, bends, twists, inner stress, asymmetrical lateral stress, etc. These imperfections break the circular symmetry of the ideal fiber and lift the degeneracy of the two modes. The two modes will therefore propagate with different phase velocities and consequently have different effective refractive indices $n_{eff_x} \neq n_{eff_y}$.

This property of SMFs, the difference between the effective refractive indices of modes $E_x(x, y)$, $E_y(x, y)$, in other words the dependence of the refractive index on the polarization state, is defined as the fiber birefringence $\Delta n = n_y - n_x$ or equivalently $\delta = k_0(n_y - n_x)$. Here, E_x is considered as the fast mode. The so-called slow mode is the component for which the material has the higher effective refractive index (slower phase velocity), while the fast mode is the one with a lower effective refractive index.

Due to the birefringence, if light is injected into the fiber so that both modes are excited, one will slip in phase relative to the other as they propagate. This effect is called polarization mode dispersion (PMD) [2]. PMD is a type of modal dispersion that appears in waveguiding media where different polarization modes that would ideally travel with equal group velocities, have different speeds due to asymmetries and imperfections. This causes the spreading of the optical pulses and unless compensated it limits the transmission data rate and causes degradation of the optical signal. A schematic representation of PMD in SMFs is shown in Fig. 5.2.

At the same time, due to the birefringence and the consequent phase difference between the two polarization modes, the electric field of the light (the superposition of the $E_x(x, y)$, $E_y(x, y)$ components), will no longer have a specific direction but will rather rotate. This

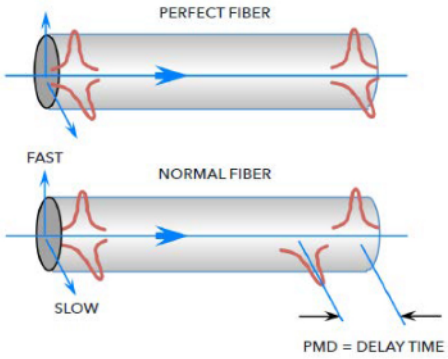

Figure 5.2. *Schematic representation of polarization mode dispersion in SMFs. Source:[3]*

continuous change of the direction of the electric field signifies that the polarization of light evolves through a sequence of states as it propagates though an SMF. Power will inevitably couple from one polarization mode to the other. As a result, the polarization at the output of the fiber will be different than the one injected. Since the fiber imperfections are caused also by external factors like stress or temperature changes that are unknown, random and continuously changing, the birefringence will be present in unknown numbers, strengths, and distributions along the fiber and will be time-variant as well. Therefore, the polarization along and at the output of an SMF will be unknown, random and unstable.

To summarize, SMFs do not maintain the polarization of light. Due to birefringence, PMD and the broadening of the optical signal is caused. At the same time the polarization of light transmitted though an SMF will be random and unstable. It is therefore necessary to adopt a polarization diversity scheme to compensate for the PMD and adjust the polarization at the SMF output.

5.1.2 Polarization in Silicon PICs

As was described in Sec. 2.2.1, planar waveguides support TE and TM modes. Also, hybrid modes can also be supported. These modes are denoted as HE or EH and they have both magnetic and electric field components along the direction of propagation.

Planar waveguides in low-index contrast platforms tend to exhibit negligible longitudinal components and therefore usually only support the TE and TM modes. On the contrary, in waveguides with tight confinement the relative strengths of the polarization of the optical field changes in the waveguide compared to what is typically observed in less confined waveguides [4]. This means that photonic devices one high-contrast platforms like SiPh have guided modes that are inherently hybrid in nature. They have all field components ($E_x, E_y, E_z, H_x, H_y, H_z$) to be non zero. However, there is a dominant E and H component for all the modes in general. Such modes are referred to as quasi-TE (qTE) and quasi-TM (qTM) modes [5].

In the SiPh platform that shows an ultra high index contrast between the Si and the SiO_2/air cladding, qTE and qTM modes are supported. For consistency with low-index platforms we refer to these modes as TE and TM, given the dominant component of the electric field in each case has TE or TM polarization respectively. Typical Si waveguides

in the 220 nm SOI platform with widths of 450 nm and 380 nm for the C-band and O-band respectively are designed to be single mode meaning the only support the fundamental TE and TM modes, TE_0 and TM_0. However, a direct consequence of the high index-contrast between the silicon core and the cladding is that SOI waveguides generally have a considerable birefringence [6], as seen also in SMFs. This birefringence introduces significant polarization dependence to SOI PICs and causes PMD. If both modes are excited in a Si waveguide they will accumulate a phase difference that will distort the optical signal. Also, if interfacing with SMFs that have random polarization, the signal-to-noise ratio will degrade seriously after it goes through a polarization-sensitive PIC. Another factor that adds to the polarization sensitivity is that many components of the SiPh platform (e.g. grating couplers, MMIs) only work for a specific polarization.

Given the previous it is evident that operation with a single polarization, either TE_0 or TM_0 is required for our SiPh chips. As happens in most telecom and datacom systems, we have chosen to work with TE_0 polarization. This prevailed for a number of reasons. First of all, TE_0 has a higher n_{eff} than TM_0 and therefore lower group velocity. The means that TE_0 is less affected by material dispersion, making it more suitable for high-speed data transmission. Another aspect of having a high n_{eff} is that it enables a stronger confinement of the electric field in the core of the waveguide, which results in a smaller mode size and lower propagation loss. This means that more of the optical power is transmitted through the waveguide rather than being absorbed or scattered. Another factor is related to the tolerance to process variations. If changing the waveguide size, TM and higher order modes are more affected than TE_0. Hence, TM mode has a higher sensitivity to waveguide geometry variations, which can cause a larger propagation loss and a lower tolerance to fabrication variations. The TM mode also has a more complex field distribution that can make it more difficult to efficiently couple to other optical devices. Because of its simpler field distribution, the TE_0 mode is generally easier to couple to other optical devices, such as SMFs, which is important in practical applications. That is why components like grating couplers that are designed for TM operation have in principle higher losses compared to the ones designed for TE operation, further increasing the losses of the link in the case of TM polarization.

Having described the polarization, birefringence and PMD in SMFs and Si chips it is now easier to explain the complication related to the use of SMFs that needs to be addressed. A technique is necessary to couple the randomly polarized light from the SMFs to TE polarized light in the Si PICs, and also compensate for the PMD in the fiber. This is necessary to ensure constant power coupling to the Si PIC irrespective of the random polarization rotation the light will experience in the SMF. If no polarization management scheme is employed, then two scenarios are possible. In the first case that 1D-GCs are used for coupling between the fiber and the PIC, only the TE component will be coupled to the PIC and the power of the link will fluctuate, from maximum coupling to zero coupling in the two extreme cases, leading to decrease in the OMA or complete loss of modulation. In the second case where a polarization insensitive coupling mechanism is adopted (edge coupling) all power will be coupled in the PIC but both TE and TM modes will be excited in the Si waveguide leading to extra losses, PMD and the consequent signal distortion. It

becomes therefore evident that a polarization diversity scheme is mandatory for the stable operation of a SiPh based data link in HEP applications. In the next section, the different available schemes will be analyzed.

5.2 Polarization recovery techniques

The polarization management schemes can be divided in two categories: the off-chip and the on-chip methods. In the first case the polarization control happens off-chip, along the fiber or at its output so that the light arrives at the PIC input with the correct TE-equivalent polarization. Such solutions involve the use of polarization maintaining fibers or polarization controllers. In the second case, the light arrives at the Si PIC with random polarization and the rotation and PMD compensation happens on-chip. This type of methods include the use of 2D-GCs or integrated polarization splitters and rotators.

5.2.1 Off-chip methods

Polarization maintaining fibers

Most commercially available laser sources provide a linearly polarized optical output with TE equivalent polarization. Therefore, if it were possible to connect the laser output to the Si PIC input with a fiber that maintains the polarization, there would be no need for extra polarization control.

This type of fibers exist and are called polarization maintaining fibers (PMFs). A PMF is an optical fiber designed to preserve the linear polarization of light. When correctly launched into the fiber the light maintains its polarization and exits the PMF with a specific linear polarization state (TE-polarization equivalent for our case). In PMFs there is little or no cross-coupling of optical power between the two polarization modes, making them ideal for applications that require the preservation of polarization. This is achieved through different mechanisms.

PMFs are constructed with a high degree of birefringence, which means that the refractive index of the fiber material varies for different polarization directions. This birefringence arises from the fiber's geometric and stress-induced asymmetries. By carefully engineering the fiber structure, the birefringence can be enhanced, leading to a greater difference in refractive index between the two orthogonal polarization states. To this end, PMFs often incorporate stress elements into their structure, such as stress rods or elliptical cores that induce anisotropic changes in the refractive index, causing a differential phase delay between the two orthogonal polarization states (stress-induced birefringence). This differential delay helps maintain the polarization state of the light by constraining it to one polarization axis. PMFs are often coated with a stress-applying material or packaged in a way that preserves the stress-induced birefringence and protects the fiber from external stresses that could otherwise cause depolarization or perturb the polarization state. At the same time, the specific geometry of PMFs (the core and cladding regions are asymmetrically shaped, as shown in Fig. 5.3 left) allows to induce birefringence and guide the

light along the desired polarization direction given that the input polarization is already aligned with the preferred polarization axis [7, 8].

Most laser sources are usually supplied with a polarization maintaining output patch cord that can be used to directly connect them to the 1D-GCs. Alternatively, a PMF can be used between the laser and the Si PIC. This solution is often adopted in co-packaged optics systems with patch cords of less than 1 m length. It is also a very convenient solution for lab testing for our Si PICs because in the lab they are placed close to the laser sources. However, in the final system as it has already been described the laser sources will be placed in the BE, more than 100 m away from the SiPh TRx. Therefore, fibers of around 100 m long will be required to connect them. This makes the use of PMFs non realistic because of their very high cost, especially for such a long link with many channels. At the same time there are not many studies about the radiation hardness of PMFs and whether they could be placed inside the CERN experiments. Therefore, although convenient for lab testing, PMFs are not suitable for the adoption in out final system implementation, at least with current technology.

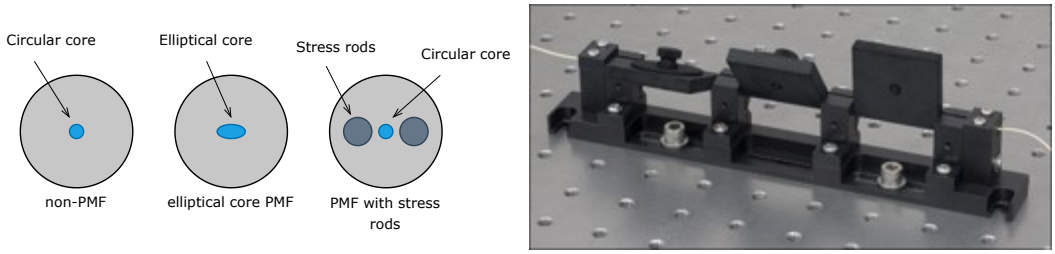

Figure 5.3. *Left: cross section of three different fiber types. The first is a standard SMF with circular core, that does not maintain the polarization. The second is an elliptical core PMF that maintains the polarization by introducing a core asymmetry. The third is a PMF with stress rods that maintains the polarization by applying an internal stress to the fiber. Right: picture of a manual polarization controller form our lab. The polarization in changed by applying mechanical stress to the fiber through by rotating the three handles.*

Polarization controllers

If we abandon the PMF solution, standard SMFs have to be used in the SiPh data link. However, as it was described in detail SMFs do not maintain the polarization. Active polarization control is therefore necessary. On way to achieve this is using off-chip polarization controllers, shown in Fig. 5.3 right. Polarization controllers are optical devices that allow to control the polarization of the light. Usually they are manual, motorized or electrically driven. The manual version rotates the polarization by applying mechanical stress on the fiber and is operated by rotating some rods by hand. The motorized and electrically driven devices are controlled through a computer/controller manually and use stress-induced birefringence to again control the polarization. They are all bench-top instruments and can be placed along the SMFs or between the SMF output and Si PIC input. Proper operation allows to rotate the polarization and ensure the we arrive at the PIC input with TE equivalent polarization. Of course, since the polarization along the fiber randomly and continuously changes the polarization controllers also need to be ad-

justed continuously to ensure stable power coupling. This solution is compatible with the use of 1D-GCs that are polarization sensitive. As with PMFs we often use polarization controllers in the lab for testing our PICs since they offer an easy, quick and effective solution for polarization management. However, as a system becomes more complex with many fibers and connection points polarization controllers become less convenient. Any small change in the position of the fibers or temperature will affect the polarization state therefore continuous adjustment is necessary. The manual solution is no longer viable. Especially for the final systems that will include many channels and fibers in would be impossible to control the polarization in such a way. Overall, polarization controllers are convenient for the lab testing of simple links but their adoption in the final system would be unsuitable.

5.2.2 On-chip methods

The aforementioned polarization management schemes were off-chip solutions and although convenient for lab testing, they are not suitable for the final system implementation. There, it is better to adopt an on-chip polarization diversity technique. With such techniques, the light arrives at the PIC-SMF interface with random polarization and then the polarization handling and rotation happens on chip. Two main categories of on-chip polarization handling solutions exist: based on the use of 2D-GCs and based on polarization splitters and rotators. These solutions will be analyzed here.

2-dimensional grating couplers

Principle of operation As it was described in Sec. 2.2.1, the 2D-GCs are components that couple the light from an SMF to the Si PIC while simultaneously splitting and rotating the polarization. A schematic of a 2D-GC is shown in Fig. 5.4.

The power splitting ratio of a 2D-GC among its two output waveguides (ΔP) depends on the polarization state at the input of the 2D-GCs (polarization at the SMF output) and will be random and unstable. At the same time, there will be a phase difference between the two output waveguides of the 2D-GC ($\Delta\varphi$) as a result of the PMD in the SMF. This phase difference will also be random and unstable. Therefore, some extra functionality is then required to compensate for PMD and the random splitting ratio and constructively recombine the light from the two output waveguides into a single waveguide, before it can be directed to the RMs. The 2D-GC with this extra logic consist a complete solution for on-chip polarization control. It is a simple method that can easily be implemented since all of the necessary components are available from our foundry's PDK. However, this solution has some important drawbacks. Most important is the high IL of the 2D-GCs in the technology that we are using, that is much higher than the 1D-GC IL. Also, from the foundry we are working with, only C-band 2D-GCs are available at the moment. Last but not least, GCs are in principle narrow-band components and although they are compatible with DWDM grids they cannot be adopted in WDM systems with CWDM grids. Nevertheless, since they consist of a simple solution for polarization control we have further investigated, designed and tested such components. Advances in the available technology will hopefully improve

their performance and allow their adoption also in O-band WDM systems in the future.

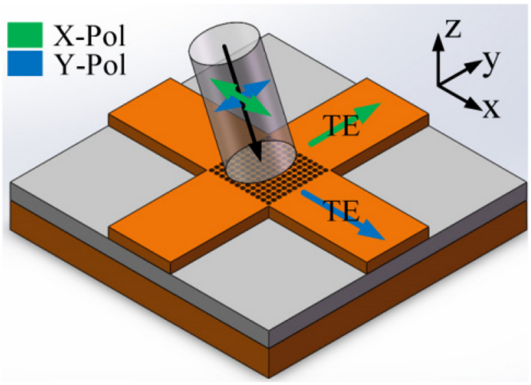

Figure 5.4. *Schematic of a 2D-GC. Source:[9].*

Proposed circuit - Simulation and design We have simulated and designed a polarization recovery circuit based on 2D-GCs. A schematic of the proposed circuit is shown in Fig. 5.5. The circuit comprises a 2D-GC whose output waveguides are connected to a 2x2 MZI [10]. The MZI includes phase shifters (PS) on each arm and at its input ports. The MZI employs 2x2 MMIs as power splitters, whose output ΔP and $\Delta\varphi$ depends on the input ΔP and $\Delta\varphi$. The use of directional couplers instead of MMIs would alternatively be possible, however we chose MMIs because they are less sensitive to the input laser wavelength and therefore more broadband. As phase shifters we use integrated Tungsten heaters.

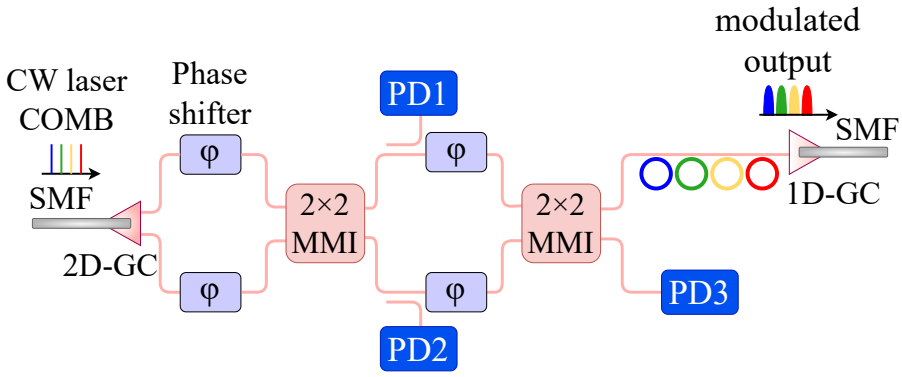

Figure 5.5. *A schematic diagram of the designed polarization recovery circuit based on 2D-GCs and a double MZI architecture.*

This circuit resembles the building block of programmable photonics circuits: the 2x2 analog optical gate. A 2×2 optical gate projects the light from two input waveguides onto two output waveguides as a linear combination [11]. The most common on-chip implementation is a MZI which needs at least two adjustable parameters p1 and p2 to independently control the power splitting ΔP and the relative phase delay $\Delta\varphi$ between the output ports. This can be achieved with two optical phase shifters placed in different locations within the MZI. In our circuit the principle of operation is the same. However, instead of implementing variable power splitters we target the constructive recombination of the power of

the 2D-GC output arms in a single waveguide (where the RMs are connected), irrespective of their ΔP and $\Delta\varphi$.

To verify the functionality of this circuit we have simulated it with the Interconnect simulator software by Ansys Lumerical. Fig. 5.6 show the simulation results. In all three plots the y-axis is the $\Delta\varphi$ in degrees between the two input ports of the MMI and the x-axis is the power in a.u. at the top input port of the MMI (P_{in1}). This is equivalent to the power difference (ΔP) or ratio of the power between the two input ports. The total power $P_{in} = P_{in1} + P_{in2}$ equals 1 (in a.u.), therefore the x-axis value that varies between 0 and 1 expresses the percentage of P_{in} in the top input port. When P_{in1}=1 all input power is a the top input port, while when P_{in1}=0 all power is distributed at the bottom input port. Fig. 5.6a shows the power in a.u. at the top output port (P_{out1}) of a 2x2 MMI (with the color scale) varying the power and $\Delta\varphi$ of its two input ports. In Fig. 5.6b we see the power in a.u. at the bottom output port (P_{out2}) of a 2x2 MMI (with the color scale) varying the power and $\Delta\varphi$ of the input ports. It can be observed that P_{out1}+P_{out2}=1. Finally, in Fig. 5.6c we see the $\Delta\varphi$ between the two output ports of the 2x2 MMI in degrees (with the color scale) varying the power $\Delta\varphi$ of the input ports. The different input $\Delta\varphi$, ΔP combinations (x and y axis values) represent the different input polarization conditions, since ΔP depends on the input polarization state and $\Delta\varphi$ on PMD. As expected, it is evident from the plots that the power splitting ratio and the phase difference between the output ports of the MMI depend on the ΔP and $\Delta\varphi$ of its input ports.

The circuit works as follows: The PSs at the first stage of the circuit (output of 2D-GC) are used to compensate for the PMD in the fiber and to ensure that the two arms have $\Delta\phi = 0°$ (or 180°) at the input of the first MMI. In this case, the first MMI will split the power equally at its two output ports, independently of the ΔP at the input ports. This condition is highlighted by the pink boxes in Fig. 5.6a. However, the $\Delta\varphi$ at the MMI output depends on the ΔP at the input, and will therefore be random since input ΔP is also random. This is shown in Fig. 5.6c. In the second MMI stage, when power is now split 50-50 in the two arms of the MZI, condition marked with the black vertical line in Fig. 5.6a, the PSs of the MZI are used to adjust the random $\Delta\varphi$ and ensure that $\Delta\phi = 270°$ at the second MMI input so that all power is directed to its top output port, where the RMs are connected (condition marked with the green rectangle in Fig. 5.6a). This way all power is constructively combined in the waveguide that is directed towards the RMs, irrespective of the ΔP and $\Delta\varphi$ at the 2D-GC output.

To ensure the continuous and stable operation of this circuit at the optimal point where all power is constructively recombined in the top output arm, a feedback closed loop control loop will be necessary. This is because the polarization in the fiber is unstable and will change with time as it was already explained. Therefore, the phase shift required for compensating for the PMD in the first stage and adjusting the $\Delta\varphi$ in the second stage will also change. Hence, real time monitoring of a feedback signal is necessary to verify if the target operational condition has been achieved or adjustments in the PSs are necessary. As feedback signal, the output power of the two MMIs can be used. An easy and convenient way to acquire this signal is by placing monitoring Ge PDs at the MMI outputs. The PDs can be connected at waveguides coupled close to the circuit waveguide that will tap a small

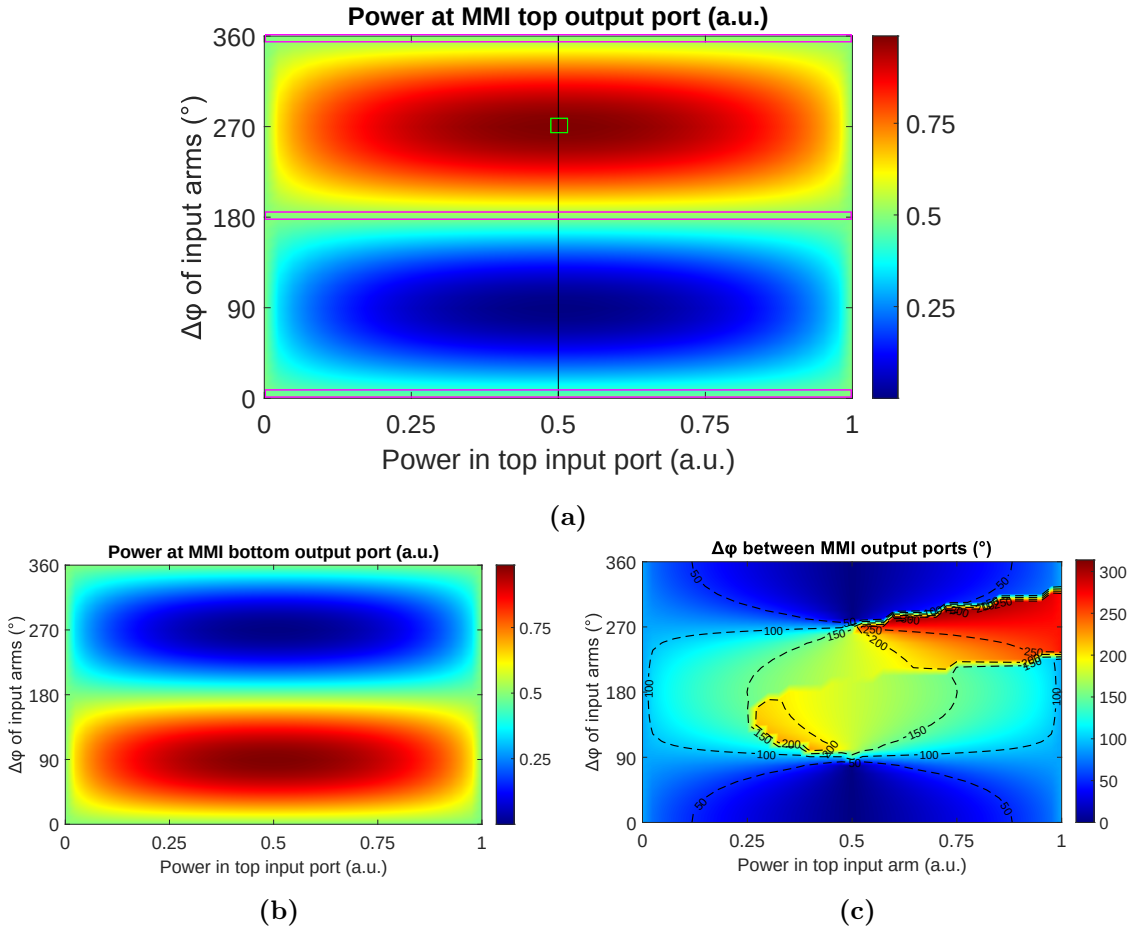

Figure 5.6. *Simulated output of the 2x2 MMI used in the polarization recovery circuit. In all plots the y-axis is the $\Delta\varphi$ in degrees between the two input ports of the MMI and the x-axis is the power in a.u. at the top input port of the MMI. (a) The power at the top output port in a.u. (b) The power at the bottom output port in a.u. (c) The $\Delta\varphi$ between the two output ports of the in degrees.*

percentage of the power, as shown in Fig. 5.5. PD_1 and PD_2 can be used for controlling the first part of the circuit, meaning the voltage applied to the PSs at the 2D-GC output. When the photocurrents at the outputs of PD_1 and PD_2 are equal it means that the phase was properly adjusted, the PMD was compensated and the power is split 50-50 in the MZI arms. Then PD_3 is employed to measure the power at the bottom output port of the second MMI. At the optimal condition when all power is directed to the RMs, this should be 0. While a value other than 0 is measured it means that the PSs of the MZI arms require further adjustment.

Having defined the feedback signal and acquisition method, it is simple to then design a complete feedback control loop. This control loop can be very similar to the one implemented for controlling the RM resonance. It can be based on the same sensor-controller-actuator architecture, where the PDs are used as the sensor and the phase shifters (heaters, either Tungsten or doped-Si) as the actuators. A PI controller would again be a reasonable choice. By properly designing the phase shifters (material and geometrical dimensions so that their sheet resistance is low) a low voltage and low power solution can be achieved.

All the components required to make this circuit are already available to us from our foundry's library. Therefore to realize this circuit no extra simulation and design work was necessary in the component level. It was enough to carry out the circuit level simulations with Interconnect to verify its operation, as it was already presented. The complete circuit has been included in a chip submission as part of the the version 3 of the PIC designed at CERN (PICv3) in October 2022. However, due to the long turnaround times of the foundries the fabricated chip in not yet available for testing. However, PICv2 included part of this circuit. In the next paragraph we present this partial circuit and its experimental characterization, that although only tests part of the functionality it is very crucial for the whole investigation of on-chip polarization management solutions.

Partial design for PMD compensation and WDM compatibility verification PICv2 includes a part of the proposed polarization recovery circuit. More specifically it includes a simplified version of the circuit comprising the 2D-GC, the phase shifters and the output waveguides of the 2D-GC, a 2x1 MMI and a 1D-GC connected at its output. This partial circuit is shown in Fig. 5.7.

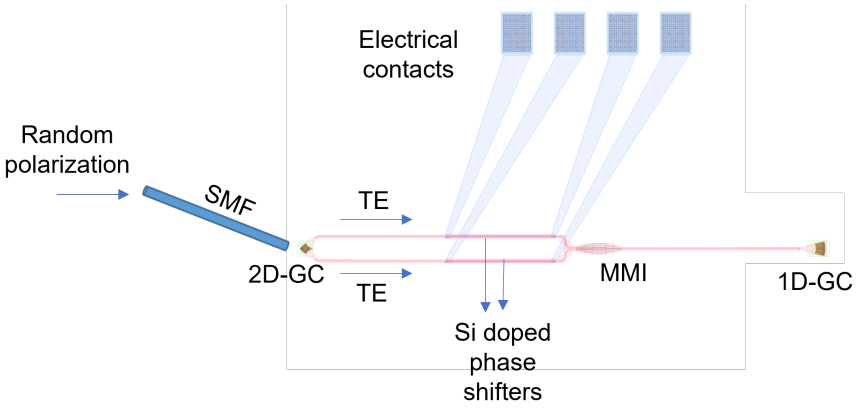

Figure 5.7. *The partial 2D-GC based polarization recovery circuit that is integrated on PICv2. In includes the first part of the complete design presented on Fig. 5.5, namely the 2D-GC, a 2x1 MMI and an 1D-GC at the output. The two input ports of the MMI include doped-Si phase shifters that can be biased through their electrical contact.*

This simplified version is not a complete solution for polarization recovery. Lacking the second stage it can only operate in the optimal regime and recombine constructively the power of the two output waveguide of the 2D-GC to the single output of the MMI when the splitting ratio of the 2D-GC is 50/50. This can be observed in Fig. 5.8 that shows the simulated output power in a.u. of the 2x1 MMI of the circuit, varying the ΔP and $\Delta\varphi$ at its input. It is evident that the output power becomes maximum (dark red regions of the plot) only when the top input port has power of 0.5 (meaning the bottom input port has also equal power of 0.5). In all other cases we lose part of the power. Of course to achieve this optimal condition apart from equal power at the two input ports, $\Delta\phi = 0°$ is also required. However, this input $\Delta\varphi$ can be controlled with the available phase shifters, allowing for PMD compensation in the circuit.

Even though the circuit in not a complete polarization management solution, it allows

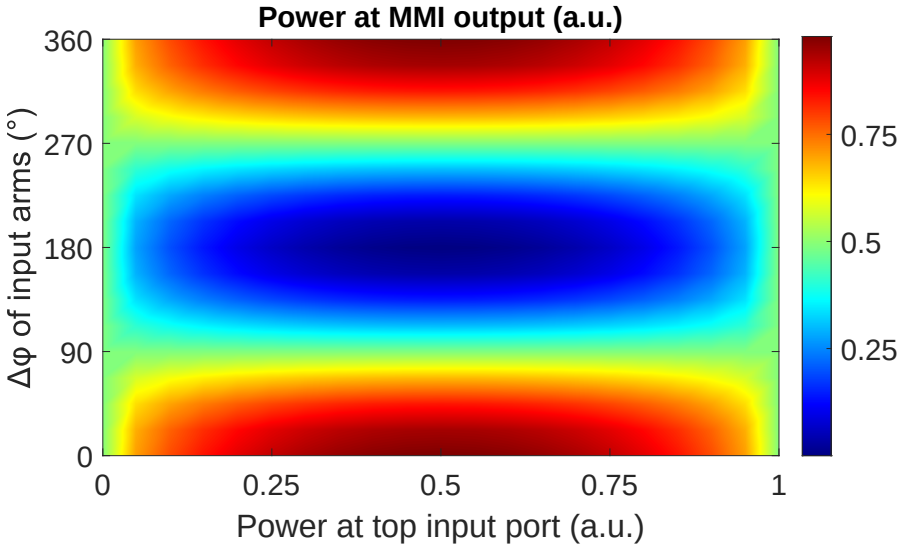

Figure 5.8. *Simulated output power in a.u. of the 2x1 MMI used in the partial polarization recovery circuit from PICv2. The y-axis is the $\Delta\varphi$ in degrees between the two input ports of the MMI and the x-axis is the power in a.u. at the top input port of the MMI.*

for experimentally testing the PMD compensation functionality, which is half of the functionality of the complete circuit. At the same time it allows for investigating the WDM compatibility of such a circuit. When multiple wavelengths will be coupled in the same fiber, it is not evident if their polarization will rotate the same way and if the will undergo the same PMD, accumulating the same $\Delta\varphi$ when they arrive on the chip. If that is not the case and every wavelength undergoes a different polarization change and PMD then such a polarization management solution is not suitable for WDM systems. Since all of the wavelengths will be multiplexed in the same fiber and then coupled to a common bus waveguide, the same phase shifters placed around the waveguide have to be used for adjusting the phase of all wavelengths simultaneously. If different $\Delta\varphi$ is required for every wavelength (resulting in different bias voltage for the phase shifters), this circuit cannot compensate for PMD for all wavelengths at the same time. Optimal operation might be ensured for only one of them, while the rest might end up in an intermediate condition, where some power is constructively recombined at the output port but not all of it, resulting in fluctuation of the output power of the link.

In fact, the compatibility with WDM operation is critical not only for polarization management schemes based on 2D-GCs, but for all on-chip methods, like the ones based on PSRs. These methods will be analyzed in the next section, but it is worth to mention here that they will also require a similar functionality with phase shifters and MMIs for PMD compensation, power recombination and phase alignment. This is required because PSRs will also eventually split the power originating from the two fiber polarization in different waveguides. Since the PMD is inherent at links that involve fibers, its compensation will also be necessary, requiring phase shifters. Then, the recombination of the power from two waveguides in a single one will require further phase adjustment. The question therefore remains: will the different wavelengths undergo the same PMD and polarization rotation in the fibers, and will a single circuit be able to ensure optimal operation for all wavelengths

simultaneously? It is critical to answer this question as the outcome will define if on-chip polarization management schemes, that seem to be the only suitable way to address the polarization challenge in our application, are indeed compatible with WDM schemes.

Experimental characterization To test the WDM compatibility of the partial circuit from PICv2, a test board has been assembled that includes the circuit under test, as shown in Fig. 5.7, and the necessary electrical and optical connections. The optical input is provided by fiber arrays attached to the PIC on top of the 2D-GC and 1D-GC, as shown in Fig. 5.9a, b. The electrical contacts of the phase shifters are wire bonded to electrical connectors on the test board, highlighted in Fig. 5.9c.

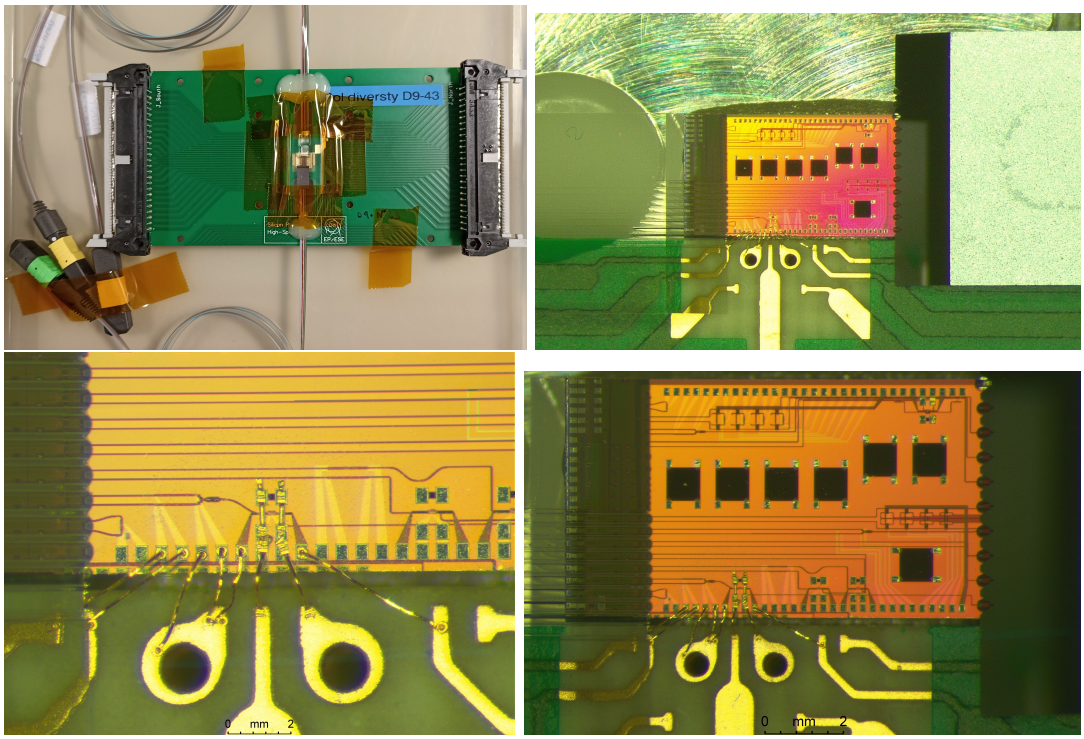

Figure 5.9. *Test board assembled for the testing of the partial polarization recovery circuits. The pictures show (a) the complete test-board with the attached SMFs, as well as (b), (c), (d) some zoomed-in views on the structures and the wire-bonds.*

The complete test setup is shown in Fig. 5.10. It includes a laser source for the optical input connected to a bench-top polarization controller for controlling the input polarization. At the output a power meter records the optical power. The phase shifters (denoted with φ) are biased with the help of a bench-top power supply.

The first test that was performed was aiming to verify if the designed circuit can effectively compensate for the PMD in the SMF. For this reason the input polarization was adjusted with the polarization controller so that at the 2D-GC we arrive with 50% of the power in fiber mode E_x and the other 50% in mode E_y. This ensures that the 2D-GC with equally split the power in its two output waveguides and the circuit is operated at the desired point. It is useful to remind that this is a partial circuit that cannot compensate for the unequal splitting ration of the 2D-GC. That is why we manually set this condition. However, although we adjust the polarization so that the 2D-GC has splitting ration of

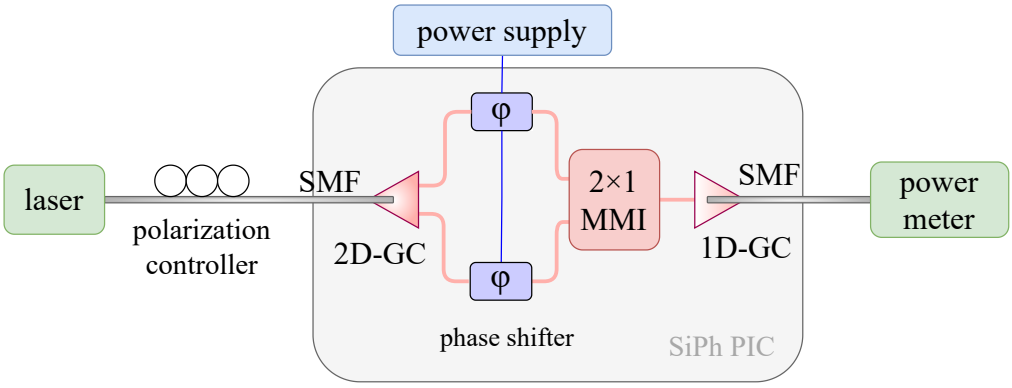

Figure 5.10. *A schematic of the full test setup of the partial polarization recovery circuit from PICv2. The structure described in 5.7 is situated on the SiPh PIC. The optical input is provided by an external laser and its polarization is controlled with the help of a manual polarization controller. The output is recorded by a power meter. The phase shifters are controlled by an external power supply.*

50-50, the PMD still remains random so the 2D-GC outputs will still have an unknown $\Delta\varphi$.

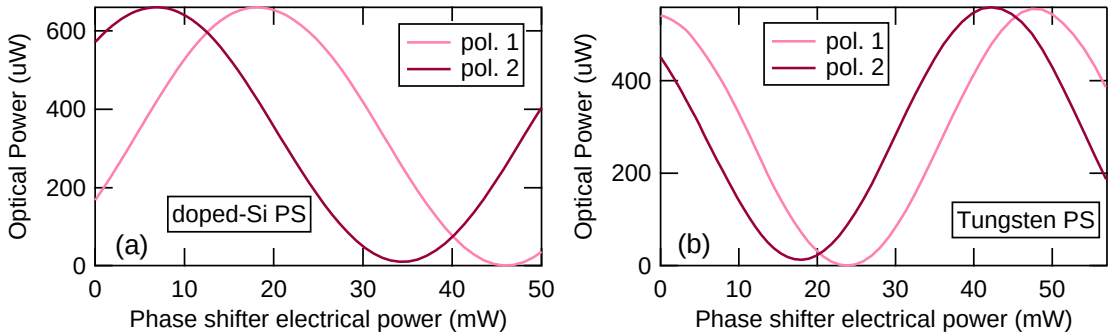

Figure 5.11. *The optical power at the output of the polarization recovery circuits from PICv2 varying the phase shifter electrical power for two different input polarization states at the fiber that induce different PMD (a) when a doped-Si phase shifter is used and (b) when a Tungsten phase shifter is used. In both cases the polarization is adjusted so that at the 2D-GC we arrive with 50% of the power in fiber mode E_x and the other 50% in mode E_y. This ensures that the 2D-GC with equally split the power in its two output waveguides.*

Once we were at this point, we then scanned the electrical power dissipated in the phase shifter (P_{PS}) from zero the the maximum power (around 50 mW). This results in a consequent scan of the $\Delta\varphi$ of the two input ports of the MMI. We expected then to see the optical power at the output to become maximum for a specific value of P_{PS} that corresponds to $\Delta\phi = 0°$ and minimum for another value of P_{PS} that corresponds to $\Delta\phi = 180°$ (see Fig. 5.8). This is confirmed from the measurements that are shown in Fig. 5.11a and b for the case of doped-Si and Tungsten phase shifter respectively. As expected from the simulation, the power at the output changes in a sinusoidal way with P_{PS} and consequently with the $\Delta\varphi$ ($\Delta\varphi$ is analogous to P_{PS} as described previously in the characterization of available phase shifters) and becomes max and min for two specific P_{PS}. In the plots we show the results for two different input polarizations that correspond

to two different PMDs. In all cases we can identify the P_{PS} that will result in the optimal condition where the MMI output becomes max. This is a proof of concept that such a circuit can effectively compensate for the PMD in the SMFs. Moreover it is shown that the available electrical power gives enough margin to do a complete scan of the $\Delta\varphi$ (since we see almost the complete sine) and compensate for PMD in all cases of input polarization.

Once we showcased that our circuit can effectively compensate for the PMD in the case of a single wavelength, the next step was to test what happens to the polarization and PMD in the case of multiple wavelengths. As a first step we used the same setup as before and a tunable laser as optical source. Setting a first wavelength λ_1 we adjusted the polarization at the fiber to get 50-50 splitting ration at the 2D-GC and then also adjusted the phase shifter to reach the optimal condition where at the output power meter we record maximum power. Then we changed the input wavelength with the tunable laser to another value λ_2. If the system stays at optimum point for the same phase shifter power (we can use the maximum or minimum output power as reference, after repeating the phase shifter power scan for the new wavelength) it means that both wavelengths undergo the same polarization change at the SMF and the two polarization states of λ_1 and λ_2 undergo the same $\Delta\varphi$. This was verified for $\Delta\lambda$ up to 15 nm, for λ between 1545 nm and 1560 nm. We also repeated the test using SMFs of different lengths to investigate whether chromatic dispersion becomes important for lengths close to the target length of the final system (expected to be maximum 200 m long). For SMF of 50 m and 100 m the results were okay for $\Delta\lambda$ up to 15 nm. Note that some small fluctuation is expected due to the wavelength dependence of the 2D-GC response. The fluctuations observed were small and near optimal condition was maintained during the measurements. A 3 km long SMF was also tried. In that case a small change in the phase shifter voltage was required indicating that the chromatic dispersion becomes important. However, for lengths comparable to the final system requirements, these measurements serve as a first proof of concept that the different wavelengths undergo the same polarization rotation and $\Delta\Phi$ as they propagate through the system.

To further investigate what happens when multiple wavelengths are multiplexed in the link and verify the compatibility of the circuit with WDM schemes, the previous setup was adjusted. As shown in Fig. 5.12, we added another laser at the input, and then multiplexed both laser sources in a common fiber with the help of a MUX (optical filter). At the output side a DEMUX (optical filter) was added with its two outputs going to two different power meters for recording the output power in each wavelength separately.

We then repeated the same test as before. Since two laser sources were used we needed three polarization controllers instead of one. As a first step we adjusted PC1 and PC2 so that the polarization between the two lasers was aligned at the MUX output. The third PC (PC3) was then placed along the fiber to adjust the polarization at the 2D-GC input, so that the 2D-GC will equally split the power in its two output waveguides. This adjustment was done while monitoring the two output power meters. Part of the test was to verify if this adjustment can be performed for both wavelengths at the same time, meaning if the polarization state changes for both wavelengths simultaneously. We verified that using a common PC along the common SMF, as long as the polarizations of the two lasers are

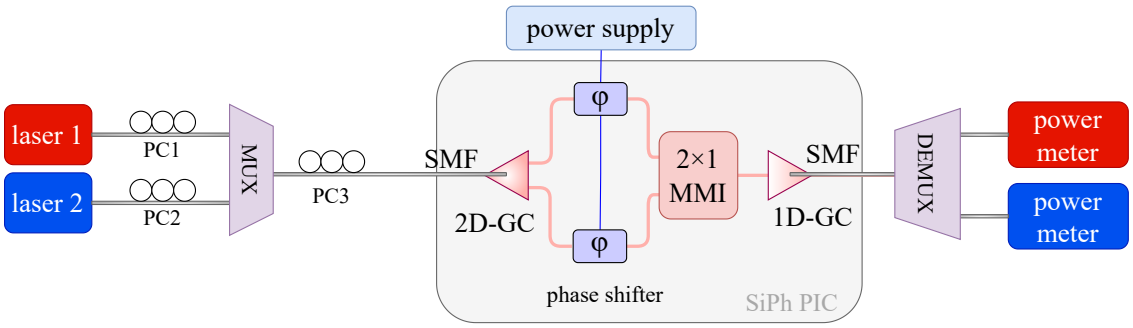

Figure 5.12. *The modified test setup of the partial polarization recovery circuit from PICv2, adjusted for testing its WDM compatibility. Instead of a single laser, two laser sources are used as input, multiplexed in the common fiber with the help of a MUX. At the output two power meters monitor the different wavelengths after they are demultiplexed with a DEMUX.*

aligned at the MUX output, we can achieve almost 50-50 splitting ratio at the 2D-GCs output for both wavelengths. This is another indication that both wavelengths undergo the same polarization rotation along the fiber.

Once we reach this optimal splitting ration of the 2D-GC, we then perform the phase shifter power scan while monitoring the power at the two output power meters. This is to verify if both wavelengths will experience the same PMD, and if they can both be operated at the optimal point with a single phase shifter. This measurement was repeated for the different types of lasers at the input: DFB lasers (FLD5F15CX) and the tunable lasers. This was done because the tunable lasers we use in the labs for testing are very good quality lasers with very narrow linewidth of 100 kHz [12]. However, the commercial lasers that will be eventually used for the optical input are expected to have bigger linewidths. That is why we also did the test using DFB lasers that have a linewidth of 5 MHz [13]. We also tested different channel spacings ($\Delta\lambda$) between the two wavelengths to verify if the wavelength grid choice is important. In the case of the DFB laser $\Delta\lambda = 9$ nm and in the case of the tunable lasers $\Delta\lambda = 1.6$ nm. Last, different SMFs with lengths of 100 m and 200 m were tested.

The results are shown in Fig. 5.13. The different subplots represent the different laser devices, channel spacing and SMF length combinations, to investigate the influence of these parameters that might vary in the real system. Fig. 5.13a and b show the results using DFB lasers with $\lambda_1 = 1550.9$ nm and $\lambda_2 = 1559$ nm, $\Delta\lambda = 9$ nm and SMF of 100 m and 200 m long respectively. Fig. 5.13c and d show the results when using tunable lasers with $\lambda_1 = 1549.32$ nm and $\lambda_2 = 1550.92$ nm, $\Delta\lambda = 1.6$ nm and SMFs 100 m and 200 m long respectively. In all the cases we see that both wavelengths require almost the same phase shift to achieve optimal operation. This is a successful demonstration of the collective tuning approach for polarization and PMD. It indicates that different wavelengths will experience the same polarization rotation and PMD as they propagate through our link, for channel spacing of up to 10 nm, SMF length of up to 200 m and even when lasers have linewidths up to some nm. Therefore, our proposed solution for polarization recovery based on 2D-GCs is compatible with WDM schemes. This is also true for other on-chip

polarization recovery methods that require similar logic with power splitters and phase shifters.

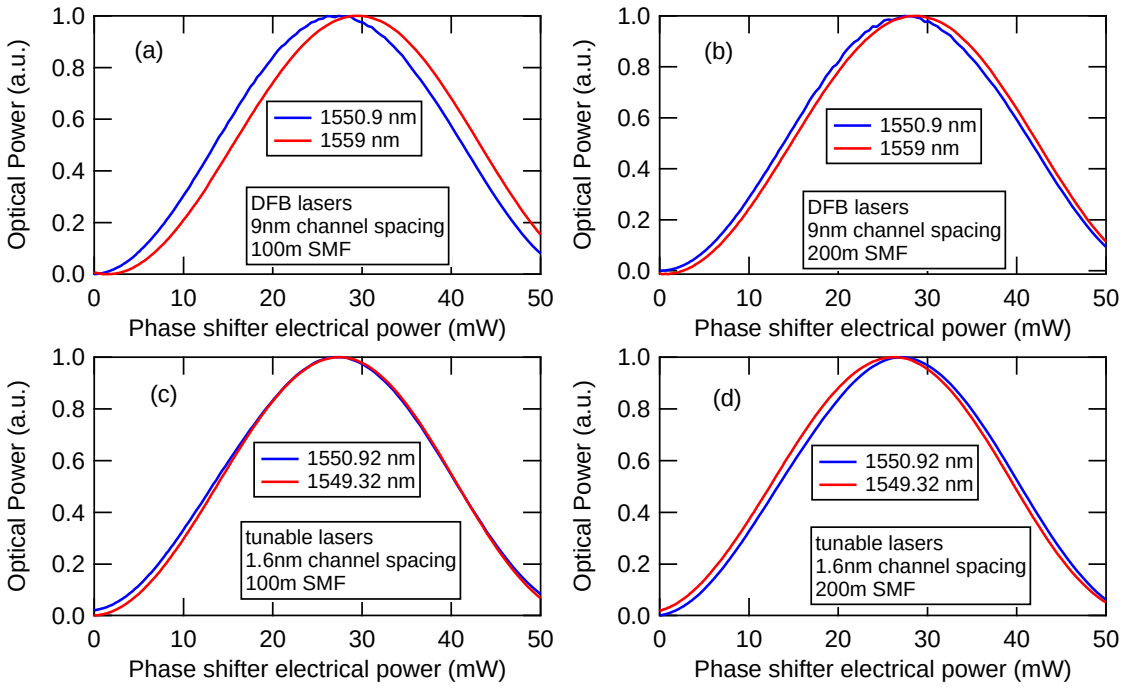

Figure 5.13. *Normalized optical power as recorded by the power meters, varying the phase shifter electrical power, when two wavelengths are multiplexed in the system. The different plots represent different laser devices, channel spacing and SMF length combinations: (a) DFB lasers with* $\lambda_1 = 1550.9\,\text{nm}$ *and* $\lambda_2 = 1559\,\text{nm}$*, channel spacing of* $9\,\text{nm}$ *and an SMF of* $100\,\text{m}$*. (b) DFB lasers with* $\lambda_1 = 1550.9\,\text{nm}$ *and* $\lambda_2 = 1559\,\text{nm}$*, channel spacing of* $9\,\text{nm}$ *and an SMF of* $200\,\text{m}$*. (c) Tunable lasers with* $\lambda_1 = 1549.32\,\text{nm}$ *and* $\lambda_2 = 1550.92\,\text{nm}$*, channel spacing of* $1.6\,\text{nm}$ *and an SMF of* $100\,\text{m}$*. (d) Tunable lasers with* $\lambda_1 = 1549.32\,\text{nm}$ *and* $\lambda_2 = 1550.92\,\text{nm}$*, channel spacing of* $1.6\,\text{nm}$ *and an SMF of* $200\,\text{m}$*.*

It is useful to note that in Fig. 5.13a the two lines do not overlap as well as in Fig. 5.13b that was measured with a longer fiber. One would expect the opposite. However this is a measurement artifact. To perform this test the polarization at the input needs to be aligned very carefully and even small movements of the fiber might cause deviation from the optimal condition. This is probably why we notice this difference between the two subplots. Probably some environmental fluctuation caused the offset noticed in Fig. 5.13a.

Circuit with partial design and RM PICv2 also includes a circuit that comprises the partial polarization recovery circuit for PMD compensation and a RM connected between its output and the input 1D-GC. A picture of the circuit is shown in Fig. 5.14. This circuit was also tested in high speed operation to verify the compatibility of the polarization recovery circuit with the RM. As before, a polarization controller was used at the input to adjust the 2D-GC splitting ration to 50-50. Then the $\Delta\Phi$ of the two input ports of the MMI was adjusted using the phase shifters. This way operation at the optimal condition was ensured. The constructively recombined power at the output of the MMI was then

directed to the RM that was driven with a high-speed signal at 25 Gbit s^{-1} provided by an external pattern generator. They eye diagram at its output was recorded with the help of a high-speed scope and is shown in Fig. 5.15. They eye is open with low noise and jitter like previously recorded with Tx characterization test board. This high-speed measurement shows that no filtering effect is induced by the polarization recovery circuit and that it is compatible with the high speed operation of the RM.

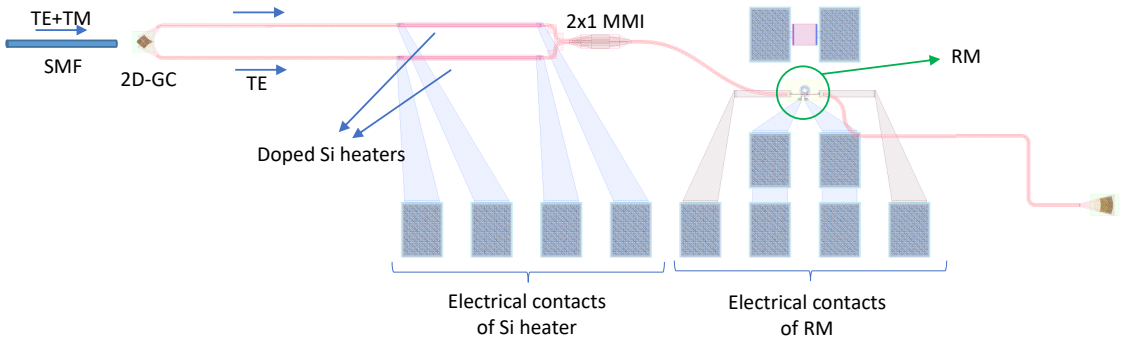

Figure 5.14. *Mask layout from PICv2 of the circuit that comprises the partial polarization recovery circuit for PMD compensation and a RM connected between its output and the input 1D-GC.*

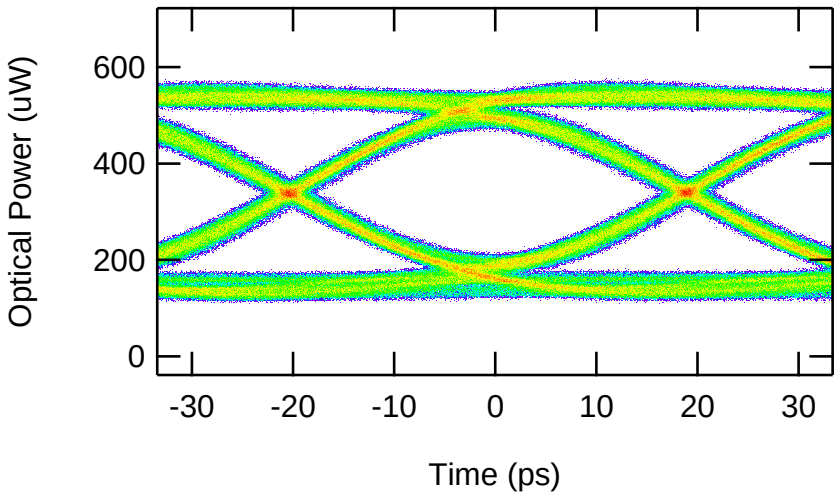

Figure 5.15. *The eye diagram recorded at the output of the circuit presented in Fig. 5.14, as recorded at* 25 Gbit s^{-1} *with the help of a high-speed scope.*

Polarization splitters and rotators

The most common solution for on-chip polarization management involves the use of polarization beam splitters (PBS) and polarization rotators (PR). Alternatively, instead of the combination of a PBS and PR a single component can be employed for polarization control, namely a polarization splitter and rotator (PSR). The principle of operation of these components was described in Sec. 2.2.1.

Proposed circuit For our application the use of a PSR or a PBS along with a PR is an interesting alternative to the use of 2D-GCs for on-chip polarization management. To this end, we have simulated and designed components necessary for the realization of such a circuit, based on the use of polarization splitters and rotators. A schematic diagram of the general structure and concept of the proposed PSR-based polarization recovery circuit is presented in Fig. 5.16. First of all such a circuit will take care of both the polarization splitting and rotation, therefore it can handle an input with both TE and TM polarizations. Of course in this case 1D grating couplers should not be used for the coupling. GCs will only couple into the PIC the percentage of the power of the SMF that has TE polarization and the rest will be lost. GCs require off-chip polarization management. To effectively couple all the power from the SMF to the PIC without dealing with its polarization we need to use edge couplers. Edge couplers will couple all the power from the SMF (both E_x and E_y polarization components) to the PIC with TE and TM polarization respectively. The percentage of the power with TE and TM polarization will be random depending on the random polarization at the SMF. After we have coupled the light in the PIC a polarization splitter is required, to split the power in two separate waveguides, one with TE polarization and the other with TM. The power will be therefore separated in two waveguides (with random splitting ration). The part with TM polarization then needs to go through a polarization rotator that will effectively rotate it to TE at its output. In the end, the process is the following: the input with both TE and TM polarization is split in two output waveguides, both with TE polarization.

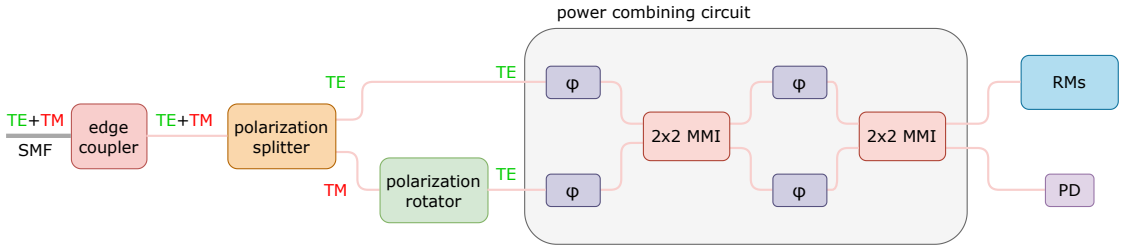

Figure 5.16. *A schematic diagram of the general structure and concept of the proposed PSR-based polarization recovery circuit.*

Then we have reached a state that is equivalent to the output of the 2D-GC as it was presented before in paragraph 5.2.2. The power at the two waveguides will be random and unknown, reflecting the random polarization at the SMF that will define the on-chip TE and TM components. Also, the $\Delta\varphi$ between the two waveguides will be random and unknown due the SMF PMD, Si waveguide PMD and the different paths that the two beams will travel after being split. To constructively recombine the power in a single waveguide before it can be directed towards the RMs the same circuit presented for the 2D-GCs solution can be employed. It comprises the phase shifters and MMIs, as before, and it will serve the same purpose: to combine in a single output waveguide the power from two input waveguides with random $\Delta\Phi$ and power splitting ratio.

Having defined the concept of a PSR-based circuit for polarization recovery, it remains to design it in practice. The study for the power combining circuit has already been

carried out as part of the 2D-GC solution and as it was previously mentioned all necessary components are already available form the foundry's library. The same is true for the edge couplers. However, no polarization splitting and rotation components, other than the 2D-GCs, are provided by the foundry. This signifies that the components would have to be designed by us. To this end, a research was carried out to define what the requirements for the polarization splitter and rotator would be for our application, followed by an extensive literature review of available solutions already proposed.

Regarding the requirements, first of all we care about the operational wavelength. For the moment most devices included on PICv2 are designed for the C-band. However we want to follow the market tendency to migrate towards the O-band in the next 10-20 years. This also concerns the commercial components that will be required for the operation of the link, and especially the transceivers and laser sources at the BE in the case a WDM scheme will be adopted. The latter only now will start to become available and it looks like they will be designed for the O-band. Therefore, we are interested in PSRs that work in the C-band as for now our devices operate in the C-band, but most importantly we are interested in O-band components since eventually we will also migrate towards the O-band for compatibility with commercially available components and emerging standards.

For the realization of a WDM transmitter we have designed and included in PICv3 an O-band WDM circuit. This circuit is compatible with the CWDM4 MSA 100G standard [14] that we are planning to align with. A PSR compatible with this circuit would not only need to operate at the O-band, but also be broadband and cover a BW of at least 80 nm from 1260 nm up to 1340 nm.

At the same time, for the moment we are fabricating the PICs using DUV lithography. Therefore our designs need to have low fabrication complexity and be fully compatible with DUV lithography. This means that single etch depth is preferred and complex structures like bends, slanted waveguides, multiple etch depths or small features cannot be realised. Moreover, the component needs to have adequate tolerance to fabrication imperfections that might be induced by the lithography process. Usually, variation across a few nm of the actual dimensions of the fabricated devices, compared to the specified ones, is observed [15]. If the device is not tolerant to these variations its performance might be compromised after fabrication. Of course, the performance itself is an important parameter. We need efficient PSRs that show low losses so that their use is compatible with power budget of the link and offers advantages compared to the 2D-GC solution.

In the case of a PSR, another important parameter is the PDL of the component. Low PDL means that the efficiency of our design will be constant independently of the input polarization state. In the opposite case the efficiency of the PSR will depend on the input polarization and will fluctuate as the random polarization in the SMF changes, leading to non-constant power coupling to the RMs. However the goal of polarization diversity is to achieve constant and stable power coupling to the RMs, therefore PDL should be as low as possible.

After an extensive literature review it was observed that, to the best of our knowledge, none of the proposed components meet all the above requirements. Most PSRs proposed in literature are designed for the C-band, leaving very few choices for the O-band. Also,

the components that show good performance require complex fabrication, are not tolerant or not broadband. For this reason it was necessary to simulate and design a custom polarization splitter and rotator that could be fabricated and would have adequate performance for our needs. To this end we simulated and designed two different components. The first one is a thermally tunable PR for the C-band, that can effectively rotate TM mode to TE. It is based on mode hybridization and is shaped as a single-stair waveguide with double etch depth [16]. The second component is a broadband O-band PSR based on mode conversion and phase matching that implements the TM_0-TE_1-TE_0 mode conversion in a structure that consists of an adiabatic taper and an asymmetric directional coupler (ADC) with one tapered arm, employing air as top cladding [17]. Both components are fully compatible with DUV lithography MPW processes and have been included in the PICv3 chip submission. As was explained before due to the large turnaround times of the foundries the components are not yet available for testing. In the following paragraphs we present the simulation and design process for both of them.

Polarization splitter-rotator - simulation and design The proposed O-band PSR is designed on the 220 nm SOI platform and the effective refractive indices for Si and SiO_2 are $n_{Si} = 3.504$ and $n_{SiO_2} = 1.4469$ at 1300 nm respectively. Fig. 5.17 shows a top-view of the proposed structure with all the design parameters noted (waveguide widths, lengths of the different sections and coupler gap). The device consists of two sections, the adiabatic taper section highlighted with light purple and the asymmetric directional coupler (ADC) section highlighted with light green color [18,19]. The two sections are connected to the input and output waveguides that have nominal for the O-band widths of $w_0 = w_{out} = 380$ nm. The component has a single input waveguide where the input light with both TE and TM polarization is launched, and two output waveguides denoted as cross port and through port, where the two polarizations will be rotated and split. Therefore, the input power will be split in the two output waveguides, both with TE polarization. The principle of operation of the PSR is based on mode conversion ($TM_0 \rightarrow TE_1$) in the taper and mode coupling due to phase matching ($TE_1 \rightarrow TM_{0\text{-cross}}$) in the coupler. The TE_0 at the input propagates unchanged through the PSR to the through port, while TM_1 is rotated to TE_0 at the cross port. This is illustrated in Fig. 5.18 that shows how the optical power propagates through the PSR for the cases of TE and TM input.

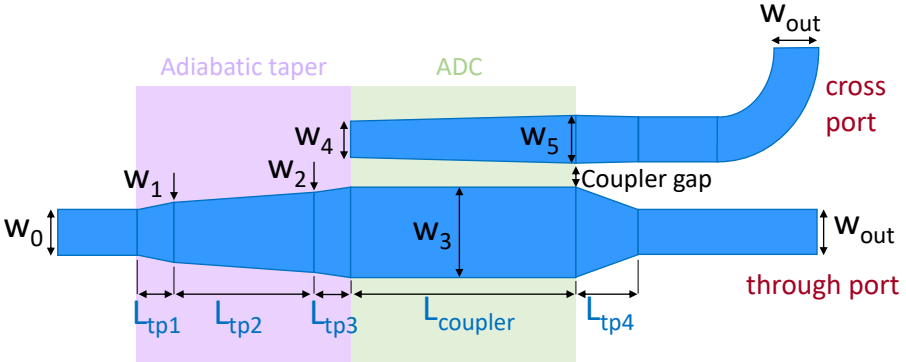

Figure 5.17. *Top view of the geometry of the proposed PSR.*

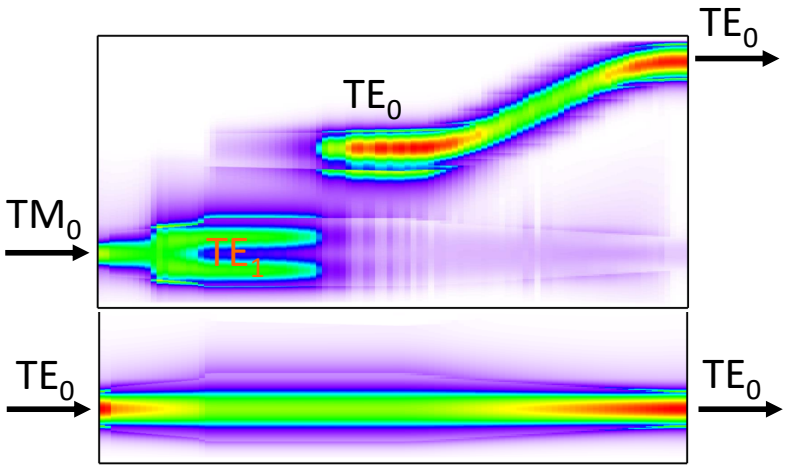

Figure 5.18. *Top view of the simulated light propagation along the PSR with TE_0 input mode (at the top) and TM_0 input mode (at the bottom).*

To achieve the mode conversion and mode coupling, a vertical asymmetry needs to be introduced in the component. To avoid the use of complex structures like bi-level tapers, bends, waveguides with cut-corners or stacked waveguides, that require complex fabrication we decided to use a different material for the top and bottom cladding. Since we work in the SOI platform our waveguides are made of Si and the bottom cladding is SiO_2. Possible solutions for the top cladding could be materials like SiN or air. Unfortunately, with the current technology we have access to, SiN is not an available option, so we have chosen to employ air as top cladding. This is achieved by etching the SiO_2 that is deposited during the process as top cladding, leaving the waveguide structures exposed to air. This way we achieve having a different material and therefore different effective indices in the vertical axis ($n_{eff_{SiO_2}} = 1.4469$ at the bottom cladding and $n_{eff_{air}} = 1$ at the top cladding). Therefore the vertical symmetry is broken and mode conversion and coupling can be achieved.

Fig. 5.19 shows the n_{eff} of the eigenmodes of the Si waveguide varying its width, as calculated using the FDE solver by Lumerical. Due to the vertical asymmetry introduced by the air top-cladding, for a critical width of around 590 nm, we cannot distinguish the polarization between eigenmodes the TM_0 and TE_1 because the modes are hybridized. When a mode is hybridized, its E_x and E_y electric field components (we consider z as the direction of propagation) will become comparable. Also, in the region where the two modes are hybridized they have comparable electric field components with each other and are not distinguishable. Therefore, this mode hybridization will lead to mode conversion if the light propagates along an adiabatic taper. This would not have been possible if a uniform cladding was used (e.g. SiO_2). In that case, as it is illustrated in Fig.5.20 the lines corresponding to the different modes are crossing, meaning the modes are purely polarized and no coupling is possible.

Concerning the principle of operation of the ADC region, as it was already mentioned the mode coupling due to phase matching happens between TE_1 and $TE_{0\text{-cross}}$. This is illustrated in Fig. 5.19 with dashed light blue lines. For some specific waveguide widths

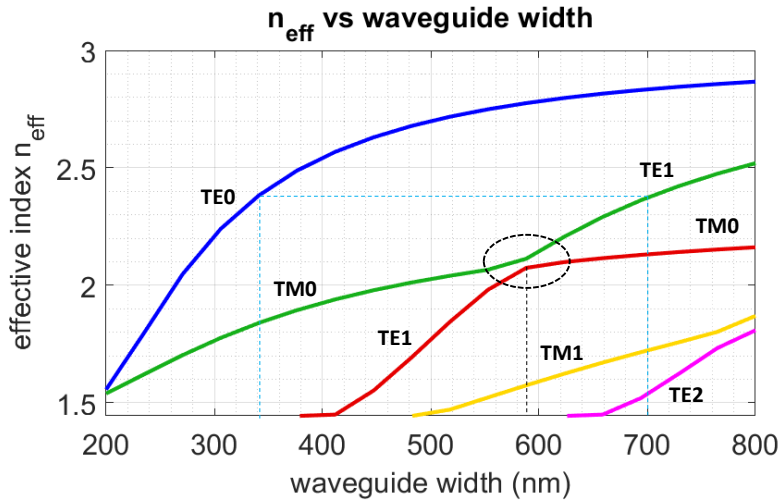

Figure 5.19. *The calculated effective indices of the eigenmodes of a Si waveguide with air top-cladding and Si height of* 220 nm *varying the waveguide width. The coupling region where mode conversion happens between TM_0 and TE_1, around* 590 nm, *is highlighted with the dashed black circle. The waveguide widths for which the phase matching condition is satisfied for modes TE_1 and TE_0 is marked with the light blue dashed lines.*

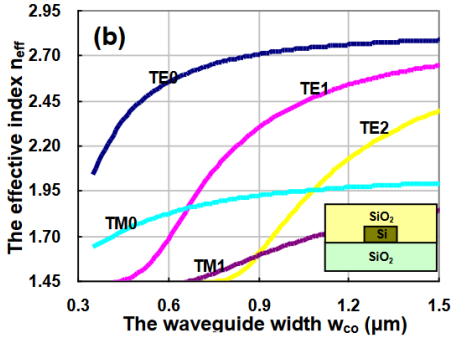

Figure 5.20. *The calculated effective indices of the eigenmodes of a Si waveguide with SiO_2 top-cladding and Si height of* 220 nm *varying the waveguide width. Source: [18]*

the two modes have equal n_{eff}, meaning the phase matching condition is satisfied and the two modes will couple to each other if the ADC is appropriately designed. For a vertically symmetrical waveguide TM_0 cannot be converted to any other mode as was explained before, but at the same time it cannot couple to TE_0 in an ADC structure since the phase matching condition is not satisfied for any waveguide, as shown in Fig. 5.20 ($n_{eff_{TM_0}}$ is always smaller than $n_{eff_{TE_0}}$).

Having defined the structure of the PSR and its principle of operation, then the exact geometrical parameters of the structure (widths, segment lengths and coupler gap) need to be defined. These geometrical parameters are shown in Fig. 5.17. A series of simulation were performed to calculate them, as will be presented here.

For selecting the taper dimensions, the results of Fig. 5.19 were used as calculated using the FDE solver by Lumerical. For a critical width of around 590 nm the TM_0-TE_1 modes are hybridized and therefore mode conversion is achieved around this region. The taper widths are selected so that the taper input (w_0) is single mode, while its output (w_3)

also supports mode TE_1. As w_0 the nominal waveguide width is selected ($w_0 = 380\,\text{nm}$). w_3 is selected to be larger than the critical width so that the whole hybridization region is included in the taper ($w_3 = 750\,\text{nm}$). To achieve adiabatic mode conversion with high efficiency and short length, a three-segment taper approach is employed. The middle segment (L_{tp_2}) is where the mode conversion happens. It should include the critical width for all operation wavelengths and should have a very small taper angle to be adiabatic. The first and third segments (L_{tp_1}, L_{tp_3}) can have steeper slopes to ensure a short taper, without compromising the efficiency. We choose $w_1 = 500\,\text{nm}$ and $w_2 = 670\,\text{nm}$ ($w_1 < 590\,\text{nm} < w_2$). The lengths of the three segments are optimized with the EigenMode Expansion (EME) propagation solver by Lumerical, to achieve maximum mode conversion efficiency (MCE) at 1300 nm. Fig. 5.21a shows the TE_0-TE_0 propagation efficiency and TM_0-TE_1 conversion efficiency varying the middle segment length. The optimal length is calculated to be $L_{tp_2} = 170\,\mu\text{m}$, where the TM_0-TE_1 mode conversion efficiency is 97%. We also calculate $L_{tp_1} = 7\,\mu\text{m}$ and $L_{tp_3} = 11\,\mu\text{m}$. No coupling occurs for TE_0 in this region, therefore TE_0 propagates unchanged through the taper with efficiency of almost 100%.

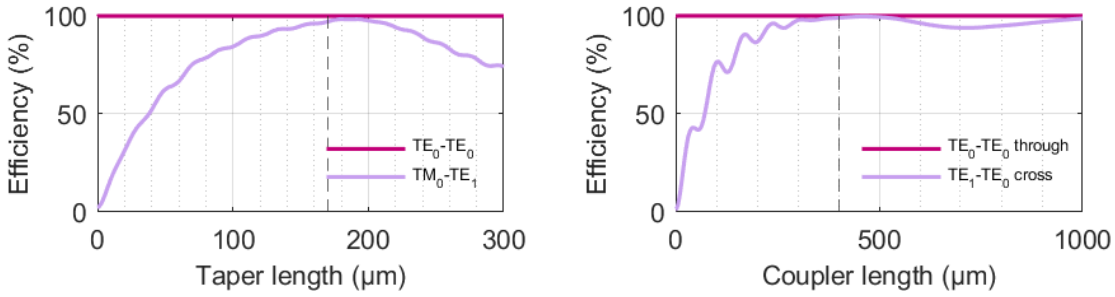

Figure 5.21. *(a)TM_0-TE_1 mode conversion efficiency and TE_0-TE_0 propagation efficiency varying the length of the taper section L_{tp2}, (b) TE_1-$TE_{0\text{-}cross}$ coupling efficiency and TE_0-TE_0 propagation efficiency varying the coupler length $L_{coupler}$.*

After converting TM_0 to TE_1, a narrow, tapered waveguide is placed next to the wide waveguide at the output of the taper section, to form an ADC. With correct choice of the waveguide widths of the ADC, the phase matching condition is satisfied, meaning $n_{eff_{TE_1}}$ at the wide waveguide is equal to $n_{eff_{TE_0}}$ at the narrow one. This way, TE_1 will be efficiently coupled to TE_0 at the cross waveguide. For $w_3 = 750\,\text{nm}$, this is satisfied for a width of around 265 nm for the narrow waveguide (highlighted in Fig. 5.19 with dashed light blue lines). In the case of a cross waveguide with uniform width, the latter would have to be chosen with nm accuracy and any deviation induced by fabrication would cause the breaking of the phase matching condition. By making it tapered, the fabrication tolerance of the design is improved, since even if the final dimensions deviate from the specified ones, the phase matching condition will be met at some point along the taper. Also, the bandwidth of the design is enlarged, since the phase matching points are slightly different for the various O-band wavelengths, but they can always be found along the coupling region. Eventually, we choose $w_4 = 340\,\text{nm}$ and $w_5 = 390\,\text{nm}$ (around the 365 nm phase

matching point for 1300 nm). Also, the coupler gap is chosen to be $\geq$ 180 nm ensuring low fabrication complexity. Then, the length of the coupler is optimized using the EME solver to maximize the coupling efficiency. The simulation results are shown in Fig. 5.21b. The optimal length is found to be $L_{coupler}$ = 400 µm wielding a TE_1-$TE_{0\text{-cross}}$ coupling efficiency of 99% at1300 nm. For the TE_0 at the wide waveguide in the coupling section, no phase matching condition is satisfied, so TE_0 will propagate straight to the through port with very small cross-talk at the cross port and negligible losses.

Having defined all the geometrical parameters of taper and ADC section, the performance of the complete design was verified with EME simulations. Fig. 5.18 shows the light propagation across the device for TE and TM input and indicates that the device works as designed: for TE_0 input all power propagates to the through port (with TE polarization), whereas for TM_0 input the mode is rotated to TE_1 and is then coupled to TE_0 at the cross-output port. The transmission and crosstalk varying the wavelength across the O-band as simulated with the Lumerical EME solver are shown in Fig. 5.22a and 5.22b respectively. The TE_{in}-$TE_{out\text{-}through}$ insertion loss is almost 0 dB across the O-band, while the TM_{in}-$TE_{out\text{-}cross}$ conversion loss is <0.5 dB, making the design highly efficient and broadband. The cross-talk for both TE and TM input is <-85 dB across the O-band. The PDL is <0.5 dB in the O-band.

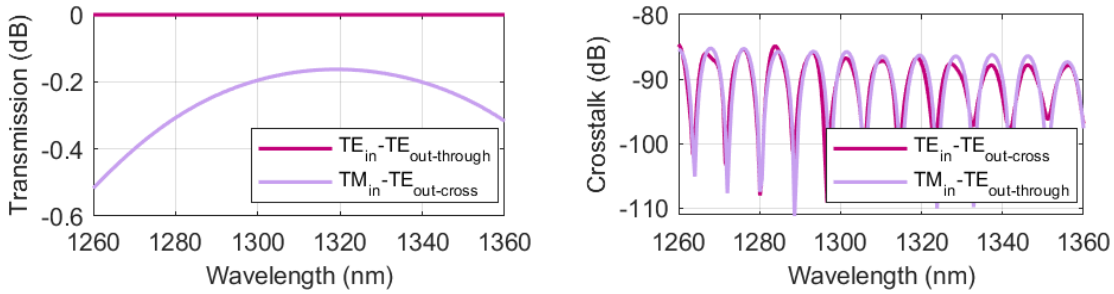

Figure 5.22. *Simulated wavelength characteristics of the proposed PSR. (a) The TE_0-TE_0 and TM_0-TE_0 transmissions, showing the simulated BW of the device. (b) The cross-talk.*

Since this is an on-chip PSR that will be connected at its input and output with standard waveguides with SiO_2 top cladding, the EME solver was used to simulate the interface. It was thus verified that no losses are introduced because of the different cladding, and coupling efficiency is almost 100% for both propagation directions.

As it was already explained, this designed PSR should be tolerant to fabrication imperfections that are expected in the DUV fabrication process. This was an important requirement that was taken into consideration during the design process, and it is part of the reason for making the ADC tapered. To verify with simulations the tolerance of the complete design to fabrication imperfections, a tolerance study was carried out. The goal was to investigate the effect of the variation of the two most important parameters of the PSR on its performance. These two parameters are the waveguide width (Δw) and the SOI wafer height (Δh). The waveguide width variation is induced by variations of the lithography process itself and is typically limited to 5 nm for DUV lithography [20]. The

SOI height will also show a variation both within the same wafer and between different wafers, depending on the wafer quality. Typically Δh is limited to 2 nm. In both cases we varied Δw and Δh in a wider range than what is expected for certainty. The results are reported in Fig. 5.23a and Fig. 5.23b respectively. Polarization conversion loss for TM_0 input remains below 0.5 dB for $\Delta w = 10$ nm and below 1.5 dB for $\Delta h = 5$ nm. This showcases a very good tolerance to fabrication imperfections and full compatibility with MPW services. This is very important for real applications that require reliable, efficient and broadband PSRs, without having access to more advanced and expensive fabrication techniques. In this regard, the design has been included in PICv3 that was submitted for fabrication in October 2023. It is currently under fabrication so no experimental characterization is available yet.

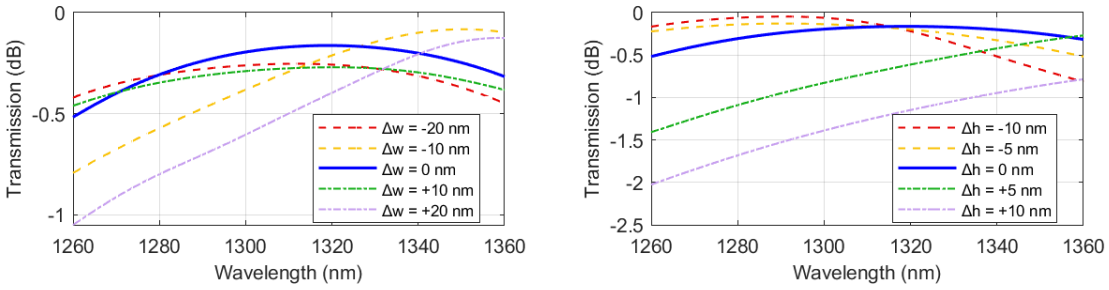

(a) **(b)**

Figure 5.23. *Process variation study results for the PSR. TM_{0in}-$TE_{0cross\text{-}out}$ transmission varying (a) the width of the PSR and (b) the height of the SOI wafer.*

To conclude, in this paragraph we presented a novel broadband PSR element designed for the 220 nm top SOI integration platform. The design has a length of 610 µm. Simulations show a TE-TE efficiency of >99% across the O-band, and TM-TE MCE of 96% at 1310 nm and >89% across the O-band. The simulated PDL is < 0.5 dB across the O-band and < 0.4 dB in the 100G CWDM grid, adhering to the low PDL requirements of the designed PSR. The simulated crosstalk is < 85 dB in the O-band. The novelty of the design is built upon a mode hybridization taper and tapered ADC for the mode coupling, resulting in low fabrication complexity, low loss and broadband O-band operation, while showcasing increased tolerance to fabrication imperfections. It employs a single etch depth and is fully compatible with DUV lithography MPW processes, meeting all the design requirements.

Thermally tunable polarization rotator - simulation and design The proposed PR is designed on the 220 nm SOI platform with 2 µm BOX and operates in the C-band. It consists of an intermediate rotator segment, shaped as a single-stair waveguide, connecting an input and an output wire waveguide, as shown in Fig. 5.24. The PR implements the TM_0-TE_0 mode conversion. This is achieved by breaking the symmetry of the waveguide cross-section, in which case the supported propagation modes are hybridized. By then appropriately choosing the rotator segment length (L) the state of the polarization at the output waveguide can be selected, so that it is TE.

The principle of operation if based on mode hybridization. The rotator segment sup-

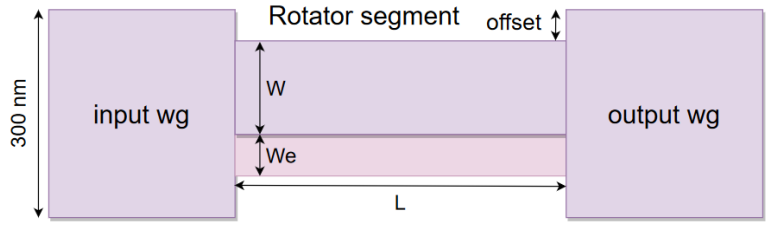

Figure 5.24. *Top view of the geometry of the proposed PR*

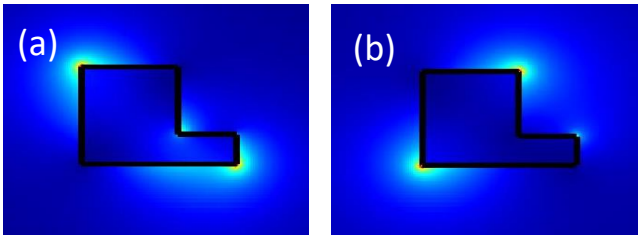

Figure 5.25. *Cross section of the rotator segment of the proposed PR showing the profiles of (a) the first and (b) the second hybrid mode that are supported.*

ports two hybrid modes. Their profiles at a cross section of the rotator segment are shown in Fig. 5.25a and Fig. 5.25b respectively. The two supported hybrid modes have optical axes perpendicular to each other. The optical axis is calculated in 5.2:

$$tan\theta = \frac{\iint_\Omega n^2(x,y) \cdot H_x^2(x,y)dxdy}{\iint_\Omega n^2(x,y) \cdot H_y^2(x,y)dxdy} \tag{5.2}$$

where $n(x,y)$ is the refractive index distribution profile, while $H_x(x,y)$ and $H_y(x,y)$ are the x- and y- components, respectively, of the magnetic field of the hybrid mode.

Since the two hybrid modes have different effective indices and therefore different propagation constants (β_1 and β_2), while they propagate in the rotator segment they accumulate a phase difference ($\Delta\varphi$). For $\Delta\phi = \pi$ rad polarization rotation is achieved. This condition is fulfilled for rotator segment length equal to the conversion length, given by 5.3.

$$L_\pi = \frac{\pi}{\beta_1 - \beta_2} \tag{5.3}$$

The rotator segment can be characterized by the polarization conversion efficiency (PCE), given by Eq. 5.4

$$PCE = 4\, sin^2\theta\, cos^2\theta\, sin^2(\frac{\pi L}{2L_\pi}) \times 100\% \tag{5.4}$$

where ϑ is the optical axis of the first hybrid mode, L_π is the conversion length and L the actual length of the rotator segment. PCE represents the percentage of the power that when launched at the PR rotator segment input with TM polarization will be rotated to TE at its output. To achieve maximum PCE three requirements must be met. Firstly, the hybrid modes should be equally TE and TM polarized, thus their optical axes need to

be near 45°. Secondly, both hybrid modes are targeted to be equally excited by the input modes and finally the actual length L of the segment must be equal to L_π. Considering these requirements, simulations were performed to determine the optimal geometrical parameters of the rotator segment. The topview of the rotator is shown Fig. 5.24. The rotator segment single step is formed via etching part of the waveguide as shown in 5.24, where W is the width of the unetched part, and W_e is the width of the etched part of the waveguide (150 nm etch depth). FDE simulations varying a set of (W, W_e) pairs were performed, to optimize the intermediate segment rotation efficiency (the PCE). The calculated hybrid mode profiles are shown in Fig. 5.25a and Fig. 5.25b respectively. With the help of the simulation results, the theta angle (ϑ) of the optical axis and the PCE were calculated and plotted varying (W, We) pair values. The results are shown in Fig. 5.26 and Fig. 5.27 respectively.

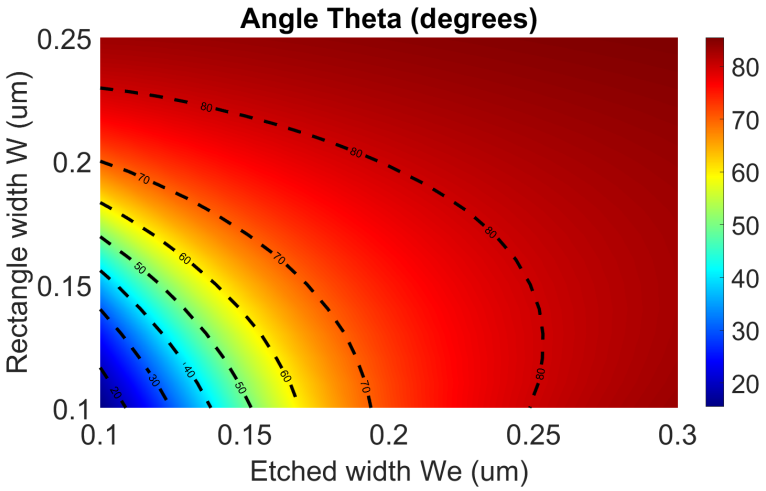

Figure 5.26. *Calculated optical axis angle theta of the PR rotator segment varying the W and W_e values for length L=L_π.*

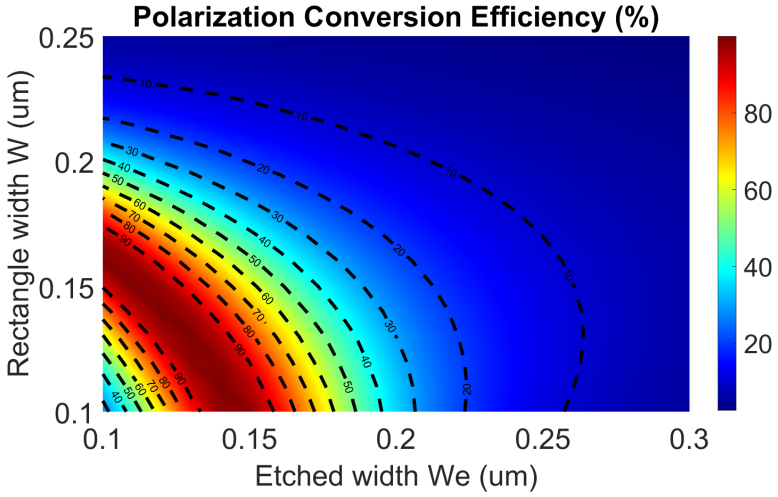

Figure 5.27. *Calculated PCE of the PR rotator segment varying the W and W_e values for length L=L_π.*

Note that the plotted ϑ corresponds to the first hybrid mode, however since the two modes are perpendicular it is enough to optimize the optical axis of the first mode. From these plots we can extract the (W, We) pairs for which the optical axis θ is close to 45° and the PCE near 100%. These value are shown with light green in the theta plot (Fig. 5.26) and in dark red in the PCE plot (Fig. 5.27). This is a first estimation of the values of (W, W_e) for achieving optimum performance.

As a next step, to calculate the overall component's efficiency, a set of EME propagation simulations were carried out considering the rotator segment and input/output waveguides. In these simulations, input/output waveguides width values as well as the lateral offset between them and the intermediate segment are optimized to achieve equal excitation of the two hybrid modes, and minimise the interface insertion losses. Having defined the optimum lateral offset and input/output waveguides width (in the range 300 nm - 400 nm), for each pair of (W, W_e) values, the TE efficiency (TM mode excited at input) and Polarization Extinction Ratio (PER) values are presented in Fig. 5.28 and Fig. 5.29 respectively, calculated via 3D-EME simulations. Both figures of merit characterise the performance of the complete component, including the input and output waveguides, meaning the take into account both the PCE of the rotator segment, as well as the losses at the interfaces between the rotator segment and the input/output waveguides. TE efficiency expresses the percentage of the input power at the input waveguide (considering TM input polarization) (TM_{in}) that is rotated to TE power at the output waveguide (TE_{out}). PER expresses the ratio of the output power that was rotated to TE polarization (TE_{out}) and the output power that remains TM polarized (TM_{out}). The goal is to maximize both the TE efficiency and the PER. High TE efficiency signifies low losses whereas high PER low crosstalk.

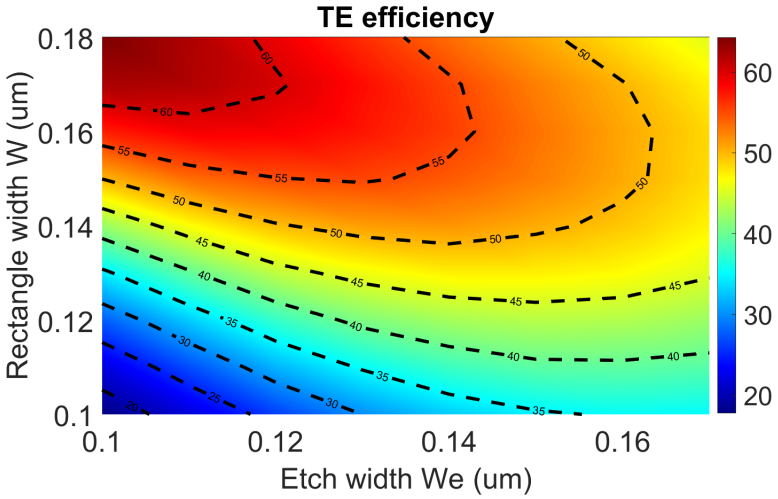

Figure 5.28. *Calculated TE efficiency at the PR output varying the W and W_e values for length $L=L_\pi$ and optimized lateral offset.*

From Fig. 5.28 W and W_e values that result in maximum TE efficiency, and the corresponding values of lateral offset, can be identified. Optimum geometrical characteristics can be found with dark red in Fig. 5.28 and 5.29.

The final design parameters deduced when taking into account all figures of merit,

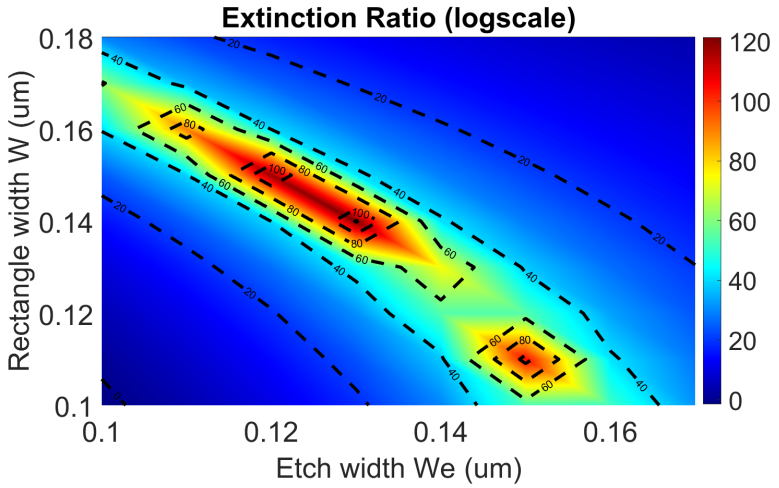

Figure 5.29. *Calculated PER at the PR output varying the W and W_e values for length $L{=}L_\pi$ and optimized lateral offset.*

namely the theta angle, PCE, TE efficiency and PER are $W = 170\,\text{nm}$, $W_e = 100\,\text{nm}$ and lateral offset$=-60\,\text{nm}$.

To verify the tolerance of the design to fabrication imperfections, a tolerance study was then carried out, investigating the effect of ±10% variation in the etch depth and waveguide height, around their nominal values of 150 nm and 220 nm respectively. The etch depth variation is induced by variations of the lithography process itself while the SOI height will also show a variation both within the same wafer and between different wafers. The results of the tolerance study are shown in Fig. 5.30a and Fig. 5.30b respectively. TE efficiency remains above 53% for up to ±15 nm etch depth variation (Fig. 5.30a), and above 50% for up to ±10 nm silicon waveguide height variation (Fig. 5.30a). These variations are an overestimation and in practice we expect that the actual variation will be much smaller. This showcases that the designed PR is tolerant to fabrication imperfections, has relaxed fabrication requirements and is fully compatible with fabrication in SiPh MPW services.

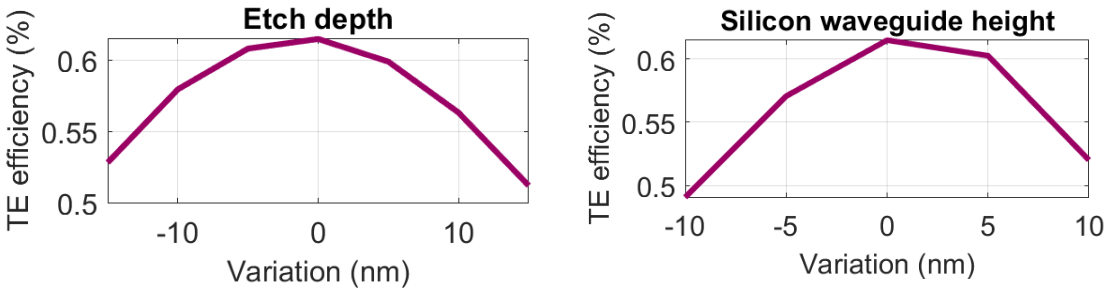

Figure 5.30. *Simulated output efficiency of the proposed PR versus (a) the etch depth variation and (b) the SOI wafer height variation for rotator segment length $L{=}L_\pi$.*

The spectral performance of the complete component, shown in Fig. 5.31, was calculated with 3D-EME simulations and was also validated with 3D-FDTD simulations. This validation step is important because the EME solver provides fast results, however it is not

very accurate since it is based on the modal decomposition of electromagnetic fields into a basis set of eigenmodes. EME simulations are usually used during the design process since they allow the quick and flexible simulation of the different design parameters. Then, when the size of the device under design allows it, it is also useful to validate its performance also through FDTD simulation. FDTD solves the Maxwell's equations, giving more accurate results, but is highly computationally intensive.

As shown in Fig. 5.31, the simulated TE efficiency, TM efficiency and PER value (right axis) reveal broadband operation centred around 1550 nm, where 62% TE efficiency and 30.5 dB PER is achieved. Over the entire C-band, TE efficiency remains above 59.5% and PER higher 13 dB is achieved.

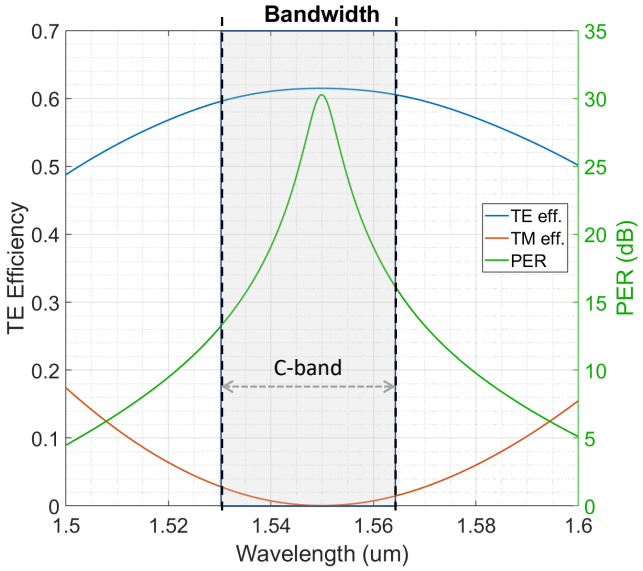

Figure 5.31. *The spectral performance of the PR showing the TE and TM efficiency and PER for input wavelengths from* 1500 nm *up to* 1600 nm.

In order to make the designed PR more versatile and suitable for applications with varying temperature or varying operational wavelength, a thermal tuning mechanism was also integrated of the PR. Thermal tuning of the component is achieved through a 1.5 µm wide metal heater wire placed 1 µm above the rotator segment waveguide. By applying a DC voltage, the rotator segment temperature can be adjusted allowing for tuning the refractive index by exploiting the thermo-optic effect. The thermo-optic coefficients used for Si and SiO_2 were 1.8×10^{-4} and 1×10^{-5} respectively, with reference temperature of 300 K. EME simulation results for TE efficiency and PER values, varying temperature from 27° to 227° (300 K to 500 K) are shown in Fig. 5.32a and Fig. 5.32b respectively. A 0.075 nm °C^{-1} central wavelength redshift is calculated for both TE efficiency and PER values, resulting in a 3.5 mW nm^{-1} power tuning efficiency. This low-power thermal tuning mechanism allows this polarization rotator to be used in applications under changing temperature environments where thermal tuning is necessary to ensure maximum PER in a specific wavelength. In addition, it can be deployed as a key element in elastic optical networks where wavelength tunability and high PER are indispensable requirements.

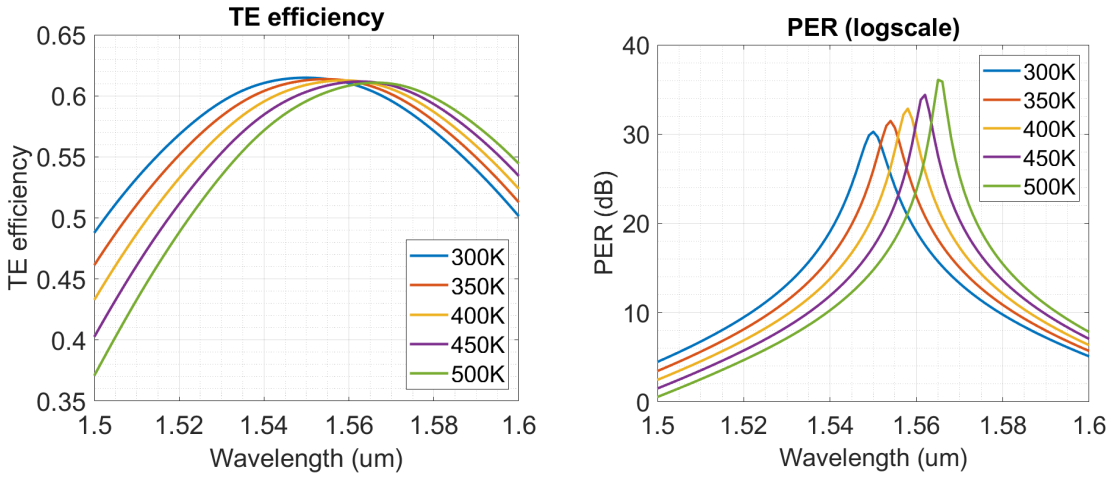

(a) (b)

Figure 5.32. *(a) The output TE efficiency and (b) the output PER of the PR varying the input wavelength, for various temperatures from* 300 K *up to* 500 K

To conclude, we have simulated and designed a novel broadband thermally tunable polarization rotator element for the 220 nm top SOI integration platform, based on mode hybridization. It is a compact component, having a short length of 15.5 µm, insertion loss of 2.25 dB and PER value above 13 dB across the entire C-band. By exploiting the thermal tuning mechanism, PER value higher than 30.5 dB over 15 nm range is achieved with 3.5 mW nm^{-1} tuning efficiency. The tuning mechanism presented requires low power and enables the integration of a high PER polarization rotator component in flex-grid DWDM systems, and in circuits with varying temperature operational requirements. The component has low fabrication complexity and is tolerant to fabrication imperfections, making it fully compatible with MPW services. In this regard, the design has been included in PICv3 that was submitted for fabrication in October 2023. It is currently under fabrication so no experimental characterization is available yet.

5.3 Conclusions

Comparison of 2D-GCs and PSR based solutions Compared to the 2D-GC based solution, the PSR circuit offers some important advantages. First of all it requires edge couplers instead of 2D-GCs. As already mentioned 2D-GCs have very high losses with the current technology that is available to us. Also, different designs reported in literature that might be compatible with our application in terms of material platform and fabrication complexity showcase losses of higher than 5 dB that can reach 7 dB [21]. On the other hand, edge couplers have much lower losses. In the technology available to us the losses are 2 dB in the O-band and 1 dB in the C-band. The PSR component will add some extra loss in the circuit, but it is possible to design PSRs with low losses of around 1 dB. In total, we might gain 2-4 dB if using PSRs instead of 2D-GCs. At the same time edge couplers are broadband components in contrast to GCs that usually have 3 dB bandwidths

of less than 50 nm. Although this might be compatible with DWDM schemes, it becomes a problem in the case of CWDM where the stable power coupling is required in a wider range of wavelengths. Moreover, 2D-GCs currently are only available for the C-band with the technology we are using, making PSRs the only choice for O-band circuits. It would be also worth to mention that for final system implementations, edge couplers are a better choice.

However, the use of PSRs has also some disadvantages. First, it requires the design of custom PSRs that meet the requirements of our application, since the components that have already been proposed in literature could not be adopted in our system for various reasons. This adds extra complexity and delays in the realisation of such a circuit. On the other hand all the components necessary for the 2D-GC based polarization recovery circuit are already available to us by our foundry's PDK. At the same time, with the technology we have access to, the edge coupling scheme requires coupling to 3 µm mode field diameter beam which in turn imposes the use of tapered or high numerical aperture fibers with tight alignment tolerances. However we except that in the future this problem will be addressed thanks to the advances of the technology, or the use of a different technology platform.

It is evident that each solution has its advantages and drawbacks, and compromises need to be made in any case. That is why we have been investigating both, and with time we expect to get a better idea about which one will eventually be better for our application, depending on the progress of available technology.

Bibliography

[1] S. Rashleigh, "Origins and control of polarization effects in single-mode fibers," *Journal of Lightwave Technology*, vol. 1, no. 2, pp. 312–331, 1983.

[2] S. Rashleigh and R. Ulrich, "Polarization mode dispersion in single-mode fibers," *Optics Letters*, vol. 3, no. 2, pp. 60–62, 1978.

[3] L. OFS Fitel, "Fiber optic dispersion and other non-linear effects." https://www.ofsoptics.com/fiber-optic-dispersion-and-other-non-linear-effects/ [Accessed: (12/05/2023)].

[4] J. B. Driscoll, R. M. Osgood, R. R. Grote, J. I. Dadap, and N. C. Panoiu, "Squeezing light in wires: fundamental optical properties of si nanowire waveguides," *Journal of Lightwave Technology*, vol. 33, no. 14, pp. 3116–3131, 2015.

[5] A. Kaushalram, G. Hegde, and S. Talabattula, "Mode hybridization analysis in thin film lithium niobate strip multimode waveguides," *Scientific Reports*, vol. 10, no. 1, pp. 1–13, 2020.

[6] D. Dai, L. Liu, S. Gao, D.-X. Xu, and S. He, "Polarization management for silicon photonic integrated circuits," *Laser & Photonics Reviews*, vol. 7, no. 3, pp. 303–328, 2013.

[7] I. Kaminow, "Polarization-maintaining fibers," *Applied Scientific Research*, vol. 41, pp. 257–270, 1984.

[8] J. Noda, K. Okamoto, and Y. Sasaki, "Polarization-maintaining fibers and their applications," *Journal of Lightwave Technology*, vol. 4, no. 8, pp. 1071–1089, 1986.

[9] J. Zou, Y. Yu, and X. Zhang, "Single step etched two dimensional grating coupler based on the soi platform," *Opt. Express*, vol. 23, pp. 32490–32495, Dec 2015.

[10] P. Velha, V. Sorianello, M. Preite, G. De Angelis, T. Cassese, A. Bianchi, F. Testa, and M. Romagnoli, "Wide-band polarization controller for si photonic integrated circuits," *Optics letters*, vol. 41, no. 24, pp. 5656–5659, 2016.

[11] W. Bogaerts, D. Pérez, J. Capmany, D. A. Miller, J. Poon, D. Englund, F. Morichetti, and A. Melloni, "Programmable photonic circuits," *Nature*, vol. 586, no. 7828, pp. 207–216, 2020.

[12] A. Technologies, "Agilent 81480a and agilent 81680a, 81640a, 81682a, 81642a, 81689a tunable laser modules user's guide." https://www.keysight.com/us/en/assets/9018-06520/user-manuals/9018-06520.pdf [Accessed: (31/05/2023)].

[13] E. D. Inc, "1,550nm continuous wave dfb laser." https://pdf.dzsc.com/200810211/200809251415472913.pdf [Accessed: (31/05/2023)].

[14] "Cwdm4 msa group." https://cwdm4-msa.org/ [Accessed: (02/06/2023)].

[15] Y. Xing, J. Dong, M. U. Khan, and W. Bogaerts, "Capturing the effects of spatial process variations in silicon photonic circuits," *ACS Photonics*, 11 2022.

[16] T. Prousalidi, G. Poulopoulos, C. Scarcella, H. Zervos, D. Bergin, A. Bulling, S. Detraz, M. Lalović, L. Marcon, L. Olanterä, U. Sandven, C. Sigaud, C. Soos, J. Troska, and H. Avramopoulos, "Thermally tunable silicon polarization rotator based on mode hybridization," in *Proceedings of the European Conference on Integrated Optics (ECIO 2022)*, (Milan, Italy), pp. 227–229, May 2022.

[17] T. Prousalidi, G. Poulopoulos, C. Scarcella, H. Zervos, S. Detraz, M. Lalović, L. Olanterä, A. Pandey, U. Sandven, C. Sigaud, C. Soos, J. Troska, and H. Avramopoulos, "Broadband, low-loss o-band silicon polarization splitter-rotator," in *Proceedings of the European Conference on Integrated Optics (ECIO 2023)*, (Enschede, The Netherlands), pp. 210–212, 2023.

[18] D. Dai and J. E. Bowers, "Novel concept for ultracompact polarization splitter-rotator based on silicon nanowires," *Optics express*, vol. 19, no. 11, pp. 10940–10949, 2011.

[19] Y. Yin, Z. Li, and D. Dai, "Ultra-broadband polarization splitter-rotator based on the mode evolution in a dual-core adiabatic taper," *Journal of Lightwave Technology*, vol. 35, no. 11, pp. 2227–2233, 2017.

[20] Y. Xing, J. Dong, U. Khan, and W. Bogaerts, "Capturing the effects of spatial process variations in silicon photonic circuits," *ACS Photonics*, 2022.

[21] R. Marchetti, C. Lacava, L. Carroll, K. Gradkowski, and P. Minzioni, "Coupling strategies for silicon photonics integrated chips," *Photonics Research*, vol. 7, no. 2, pp. 201–239, 2019.

Chapter 6

Silicon Photonics Receiver

6.1 Principle of operation

The SiPh Rx consists of a Ge PD with BW of 50 GHz and low dark current of around 10 nA at −1 V. Two different variations of the PDs were used for the Rx characterization, one with responsivity of 0.8 A W^{-1} and another with responsivity of 0.6 A W^{-1}. The PDs operate both at the C-band and the O-band with similar performance, however depending on the target operational wavelength the input waveguide width is chosen accordingly to match the nominal width of each band. The PD acts as a photodetector and is responsible for converting the optical data (configuration, trigger and timing data in our case) received from the BE to electrical, before they can then be transmitted to the FE electronics. The output of the Ge PD is a photocurrent (I_{PD}) whose value is proportional to the input optical power, according to the sensitivity of the PD. The I_{PD} then requires amplification, which is usually achieved with the help of a TIA. The TIA also converts the photocurrent to a digital voltage signal with appropriate levels that are compatible with the FE electronics input requirements.

Since we are trying to develop radiation hard components, the TIA that will be employed in this FE Rx also has to be radiation hard, therefore we cannot use a commercial component. Within CERN collaborations two different versions of radiation tolerant TIAs have been developed, the giga-bit TIA (GBTIA) [1] and low power GBTIA (lpGBTIA) [2]. The GBTIA is implemented in 130 nm CMOS process, requires supply voltage of 2.5 V and works at the nominal data rate of 4.8 Gbit s^{-1}. The lpGBTIA is implemented in 65 nm CMOS process, requires supply voltage of 1.2 V and works at 2.56 Gbit s^{-1}. Both ASICs were tested with the Ge PDs. Note that the GBTIA and lpGBTIA do not withstand the radiation levels of HL-LHC innermost regions and eventually will have to be replaced by a more radiation tolerant TIA. However, their use allows for the proof of concept of a SiPh based Rx.

The desired BW of the Rx is estimated between 2.56 Gbit s^{-1} and 5.12 Gbit s^{-1} for this application, a value sufficient for the transferring of the configuration data to the FE due to the asymmetrical nature of this link. Therefore, the BW of the Ge PD is more than sufficient for this purpose. The same is true for the BW of the GBTIA and lpGBTIA.

The optical coupling in the Rx between the SMFs and SiPh PIC can be achieved in two different ways, either with the use of a 2D-GC or the use of a 1D-GC. In the case of the 2D-GC [3] the IL of the link increases because of the higher IL of the 2D-GCs which is expected to be at least −6 dB in optimal conditions with perfect coupling between the SMF and the 2D-GC. On the other hand, the 2D-GCs are polarization insensitive, therefore they also act as the polarization diversity circuit. As it was already described in chapter 5, also for the case of the Rx a polarization diversity scheme is necessary to convert the random polarization of the SMF to TE polarization on the Si PIC. Unlike the Tx circuit, in the Rx circuit if 2D-GCs are used for coupling, the 2D-GCs are enough for the polarization recovery. No extra circuit is then necessary to recombine the power of the two output waveguides of the 2D-GC (that have random splitting ration and phase) in a single waveguide. The PD has two optical input ports that can be used simultaneously. As illustrated in Fig. 6.1b, the two output waveguides of the 2D-GC can be directly

connected in the two sides of the Ge PD. These two light beams arriving from both sides each generate a photocurrent. The total response of the PD is then given by adding the two photocurrents, according to the principle of superposition. Each incident light beam interacts with the material of the PD at a different region (at its two ends) both contributing in the total generated photocurrent.

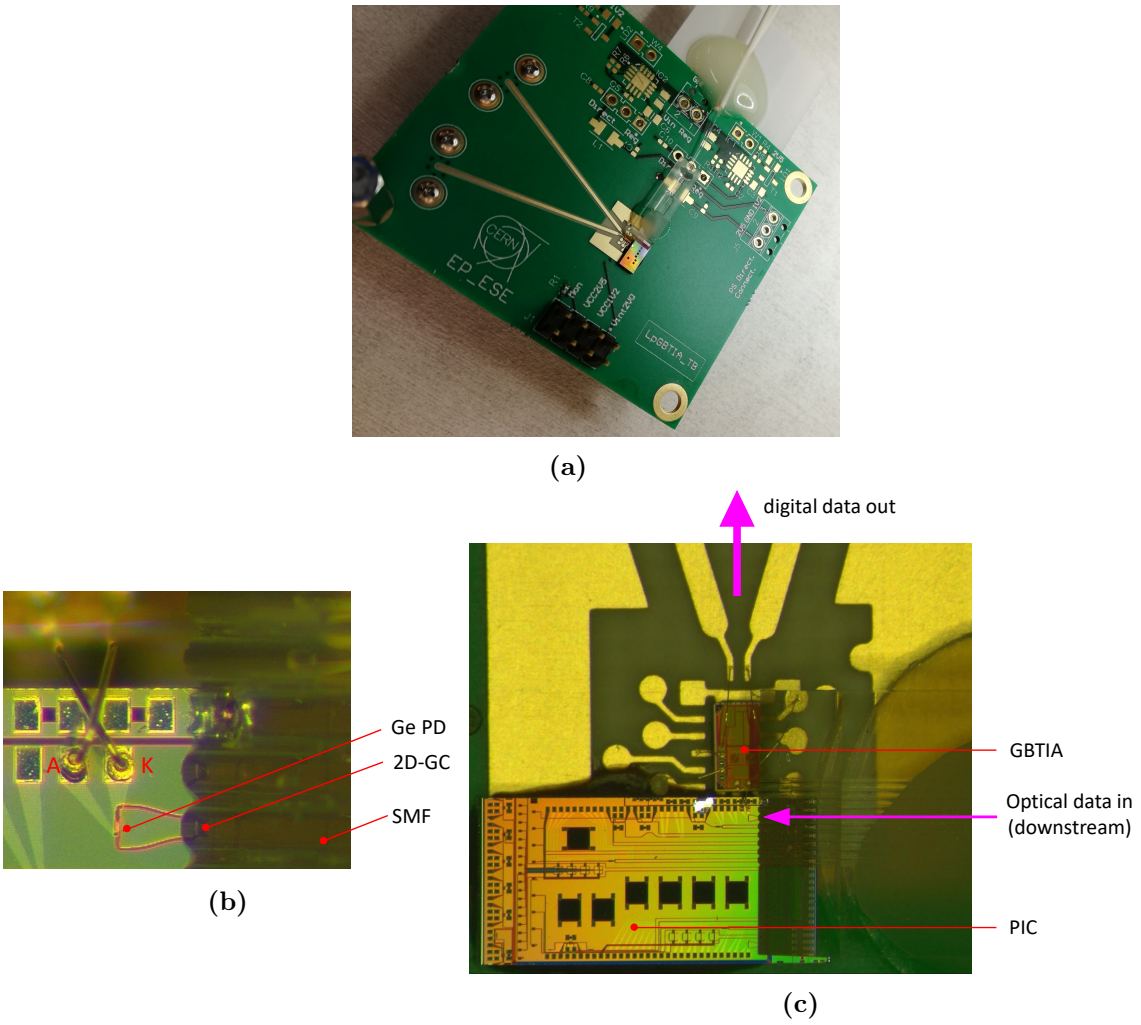

Figure 6.1. *(a) Picture of the Rx test board with the 2D-GC coupling scheme and GBTIA. (b) A zoomed-in picture of the board showing the fiber array, 2D-GC, Ge PD and electrical wire-bonds for connection with the GBTIA. (c) A zoomed in picture of the test board showing the SiPh PIC with the GE PD, the GBTIA, the fiber array for the optical data input, and the traces of the board for the digital data output.*

In the case a 1D-GC is used for the coupling, the IL of the link is expected to be smaller since the IL of the 1D-GCs is around −3 dB in optimal conditions with ideal fiber alignment. However in this case an external polarization controller is required since the 1D-GC do not work as polarization splitters and rotators. For this coupling scheme the 1D-GC single output waveguide is connected to one side of the PD. This is illustrated in Fig. 6.2b. On PICv2 we have included PDs with both coupling configurations, and as it will be described in the next section we have assembled two different test boards, one with each configuration.

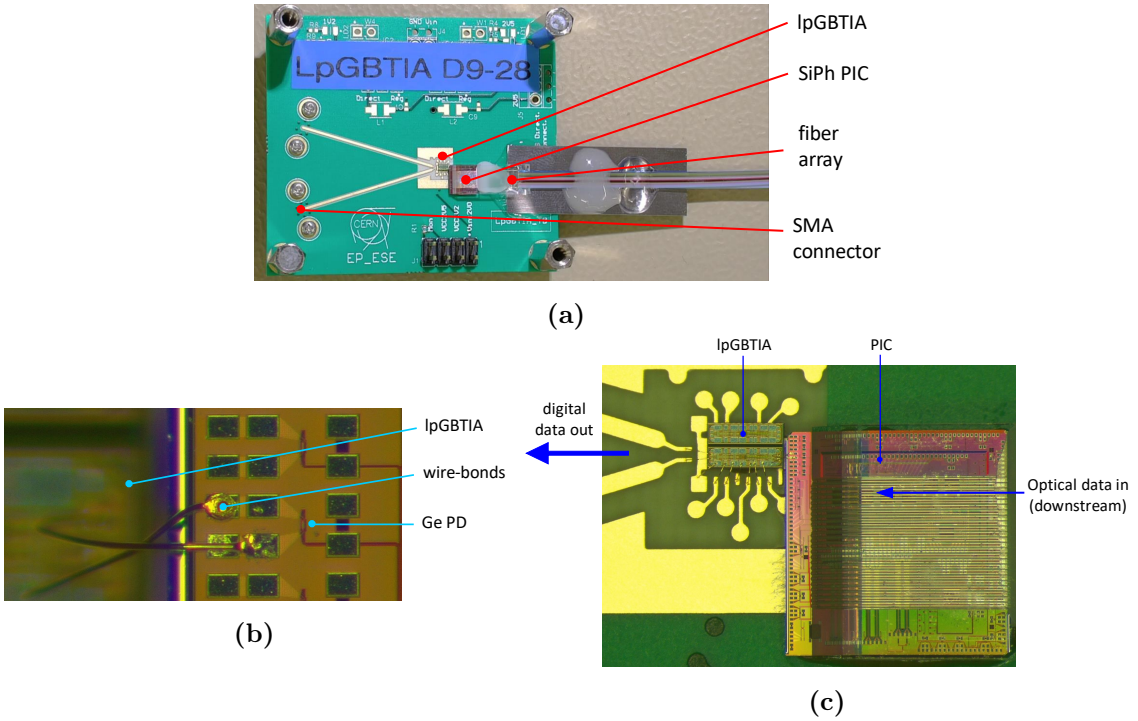

Figure 6.2. *(a) Picture of the Rx test board with the 1D-GC coupling scheme and lpGBTIA. (b) A zoomed-in picture of the board showing the Ge PD and electrical wire-bonds for connection with the lpGBTIA. (c) A zoomed in picture of the test board showing the SiPh PIC with the GE PD, the lpGBTIA, the fiber array for the optical data input, and the traces of the board for the digital data output.*

6.2 Receiver test-board

To characterize the Rx, two test board have been assembled, one including the GBTIA and high responsivity PD ($0.8\,\mathrm{A\,W^{-1}}$) and the other including the lpGBTIA and lower responsivity PD ($0.6\,\mathrm{A\,W^{-1}}$). A picture of the first test board with the GBTIA is shown in Fig. 6.1a. It includes the Si PIC and the GBTIA that are glued on the PCB as shown in Fig. 6.1c, and all the necessary optical and electrical connections. A PD that is connected at the output of a 2D-GC is used in this case. The optical input is provided by a fiber array (SMF) that is attached on top of the 2D-GC, as illustrated in Fig. 6.1b. The electrical output of the Ge PD is wire-bonded to the GBTIA input. The electrical output of the GBTIA is wire-bonded to the PCB traces that lead to SMA connectors that can be used to monitor the electrical output of the Rx. The GBTIA requires powering of 2.5 V that can be provided by an external power supply through the PIN connectors of the board.

The second test board that includes the lpGBTIA is shown in Fig. 6.2a. It includes the Si PIC and the lpGBTIA attached on the housing PCB, as shown in Fig. 6.2c. In this test board a PD from a different part of the PIC is employed, that is connected at the output of a 1D-GC. As before, the electrical output of the Ge PD is wire-bonded to the lpGBTIA input, as illustrated in 6.2b. The electrical output of the lpGBTIA is wire-bonded to the PCB traces that lead to SMA connectors. The lpGBTIA requires powering of 1.2 V that can be provided by an external power supply through the PIN connectors of this board.

6.3 Characterisation

The characterization of the Rx on the system level included two types of measurements: the high speed eye diagram measurements to evaluate the quality of the output signal and verify the compatibility of the Ge PD with the GBTIA and lpGBTIA, as well as the BER measurements to compute the margin of the system for error-less transmission.

A setup was put together to perform this characterization. A schematic of the setup is shown in Fig. 6.3. It includes the Rx test board with the Ge PD and rad-hard TIA. The required input in provided by a pattern generator (JBERT) at 5.12 Gbit s^{-1} and is converted to optical by a commercial transmitter working at 1550 nm, namely a Small Form-Factor Pluggable (SFP) module. The optical output of the SFP is then transmitted through a SFM to the Rx test-board input. The electrical output of the Rx board is recorded by a high-speed scope.

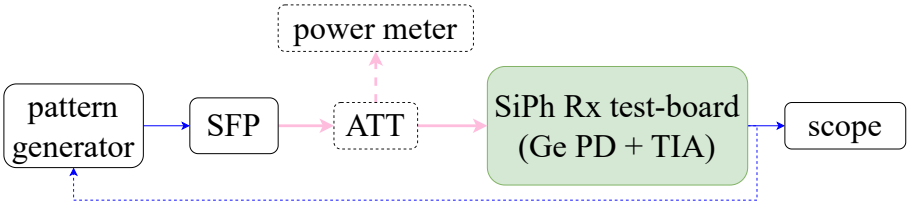

Figure 6.3. *The Rx characterization test setup. Electrical cables are marked with blue and SMFs with pink. The power meter, attenuator and electrical and optical connections that are added to the setup for the BER measurement are drawn in dashed lines.*

6.3.1 High-speed measurements

The aforementioned setup shown in Fig. 6.3 was used for the characterization of the Rx. The first measurements performed were the high speed eye diagram measurements, as recorded with the help of the scope. The measured optical eye diagram at the output of the SFP module (or equivalently input of the Rx board) and the corresponding electrical eye diagram at the output of the Rx board, at 5.12 Gbit s^{-1} are shown in Fig. 6.4a and Fig. 6.4b respectively. Although this is not illustrated in Fig. 6.3, the optical eye diagram at the SFP module output was also measured with the help of the scope and a high-speed photodetector interposed between the SFP and scope for the high-speed opto-electrical conversion of the signal.

6.3.2 BER tests

After the measurement of the high-speed eye diagrams, a BER test was also performed. With the BER test we can define the sensitivity of the Rx board. As sensitivity we define the minimum OMA that is required at the input of the Rx board for which error-less transmission is achieved ($BER \leq 10^{-12}$). Since the Ge PDs has a specific responsivity, the Rx sensitivity is mainly defined by the TIA that is used and the minimum OMA required at its input for which it gives a good enough eye diagram at the output with one and zero levels distinguishable and bigger than the noise. Normally, the electrical output of the

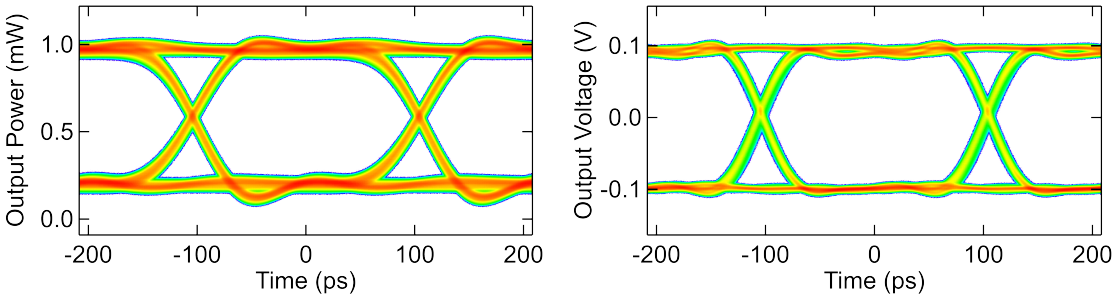

Figure 6.4. *(a) The optical eye diagram at the output of the SFP module and input of the Rx at* 5.12 Gbit s^{-1}*. (b) The corresponding electrical eye diagram at the output of the Rx at* 5.12 Gbit s^{-1}*.*

GBTIA and lpGBTIA has a voltage swing of 200 mV as imposed by the limiting amplifier they include. The lpGBTIA sensitivity has been previously measured around −17 dB, considering no coupling losses and a photodiode responsivity of 1 A W^{-1}. The GBTIA has also been measured at around −17 dB in same conditions. These numbers are useful to estimate the expected sensitivity of the SiPh Rx. Starting from the expected sensitivity of the TIA at around −17 dB, we need to add the expected IL in the case of the two coupling schemes in this Rx, that will reduce the sensitivity due to the extra loss they incure. This is minimum −6 dB and −3 dB for the case of 2D-GC and 1D-GC respectively. Therefore, sensitivity is expected to be at least −11 dB and −14 dB in optimal coupling conditions for the case of 2D-GC and 1D-GC respectively. Of course any fiber misalignment that is usually expected will further increase this number. The number might further be increased due to the reduced responsivity of the Ge PDs that is 0.8 A W^{-1} and 0.6 A W^{-1} for the two designs, compared to the value of 1 A W^{-1} that was used for the calculation of the TIA sensitivity.

To experimentally measure the BER of the Rx, the setup presented in Fig. 6.3 was adjusted. An attenuator was interposed between the SFP and the SiPh Rx that can be used to vary the input OMA of the Rx board by varying the attenuation. The attenuator used in this test had two output ports. The first output port with 90% of the output power was directed to the Rx input. The rest 10% from the second port was connected to a power meter that allowed to measure the average power (P_{AVG}) at the input of the Rx board. This P_{AVG} can be used along with ER at the SFP output to calculate the OMA at the Rx input, given Eq. 6.1 and 6.2

$$ER = \frac{P_1}{P_0} \tag{6.1}$$

$$P_{AVG} = \frac{P_1 - P_0}{2} \tag{6.2}$$

where P_1 and P_0 are the one and zero levels of the transmission respectively. This is because the ER of the SFP output is a characteristic value of the SFP module and even though P_1 and P_0 will vary along with the attenuation, their ratio is constant. The ER

can be easily calculated by measuring once the optical eye diagram at the output of the SFP. Therefore, knowing the ER and measuring the P_{AVG} it is easy to compute the P_1 and P_0 and from those calculate the OMA, according to Eq. 6.3.

$$OMA = P_1 - P_0 \tag{6.3}$$

It is worth noting that the OMA was not directly measured because as the attenuation increases, we reach OMA values as low as −15 dBm or equivalently 30 µW. This corresponds to eye diagrams with very small opening that cannot be recorded we the scopes we have available since they are comparable to the noise levels.

To perform the BER test, the electrical output of the Rx board is no longer connected to the scope, but it is connected in loop-back mode to the bit-error-rate tester (BERT). The BERT can then compare the Rx output signal with the provided input signal to calculate the BER. The BER measurement results for the two test boards are shown in Fig. 6.5. In both cases the measured sensitivity for $BER \leq 10^{-12}$ is around −11 dBm. These results are close to what we expected and within the error margin. The calculated values make sense, given that the GBTIA had higher IL but also higher PD sensitivity, while the lpGBTIA board had lower IL and also lower sensitivity. At the same time it is suspected that the fiber was well aligned in the case of the 2D-GC, and not so well aligned in the case of the 1D-GC, bringing the IL of the two boards closer. Indeed this was partially verified by measuring the coupling efficiency of the lpGBTIA board with the help of a shunt waveguide. The 1D-GC IL was measured at around −4.5 dB. Variations from the expected value are also attributed to the measurement error.

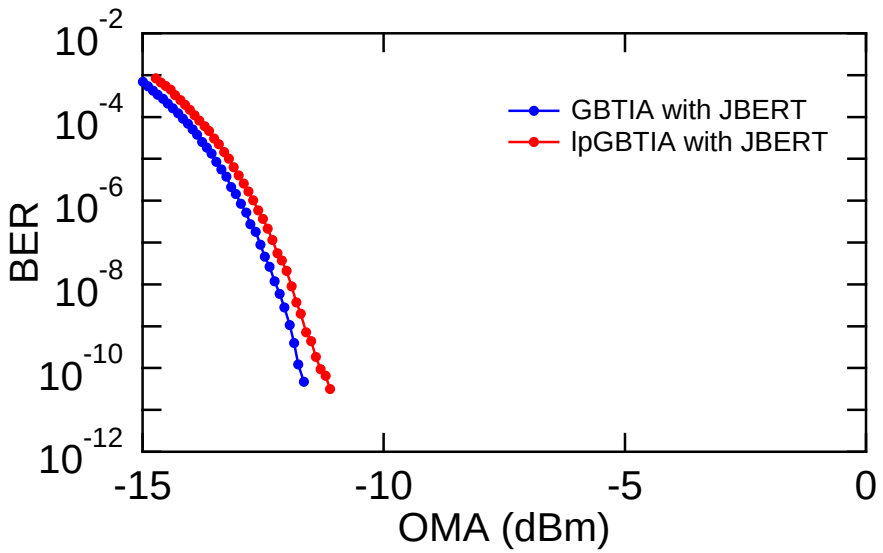

Figure 6.5. *BER test results of the Rx showing the BER vs. OMA for three different test setups. In blue the BER results for the GBTIA measured with the JBERT. In red the BER of the lpGBTIA measured with the JBERT. The measured sensitivity of the Rx is of about* −11 dBm.

6.4 Conclusions

In this chapter we have presented the SiPh Rx that has been developed, based on Ge PDs and radiation tolerant TIAs. The components characteristics were described. Two different Rx test boards have been assembled comprising of different variations of the PD, TIA and optical coupling scheme. Both test boards were experimentally evaluated. The high-speed operation of the PDs was verified with eye diagram measurements recorded at $5.12\,\mathrm{Gbit\,s^{-1}}$. The eye is open with low noise and jitter. This measurement also showcases the compatibility of the Ge PD with the available TIA. BER measurements revealed a Rx sensitivity for both system configurations of around $-11\,\mathrm{dBm}$. This value matches the estimated sensitivity.

The measured sensitivity of the SiPh Rx is a bit worse that what has been previously achieved with discrete components and free-space coupling in the VTRx+ system, with an InGaAs PD and the GBTIA, showing $-15\,\mathrm{dBm}$ of sensitivity [4, 5]. This penalty in performance is caused by the high IL of the GCs which was not optimised for this application. When 2D-GCs are employed the loss induced is of at least 6 dB. One way to address this is by using the 1D-GCs instead, which can have IL as low as 2 dB with current technology. However, in that case a polarization diversity scheme needs to also be included on chip that will also have some IL and will increase at the same time the power consumption. Another way to address the high IL of the 2D-GCs is by making use of improved 2D-GCs in future designs with better performance. However the computed $-11\,\mathrm{dBm}$ sensitivity is already a very good result for the Rx and gives enough margin for the system. The output of the SFP used for this test is 2 dBm. Eventually a similar component will be used in the BE providing a similar output. Between the SFP output and Ge PD a fiber of maximum 200 m will be interposed and then the GC. Maybe some extra connections will be required, but the losses will not be higher than 13 dB. Overall, the Rx has already adequate performance so no optimizations are necessary.

Bibliography

[1] M. Menouni, P. Gui, and P. Moreira, "The GBTIA, a 5 Gbit/s Radiation-Hard Optical Receiver for the SLHC Upgrades," in *Proceedings of the Topical Workshop on Electronics for Particle Physics (TWEPP 2009)*, (Paris, France), 2009.

[2] M. Menouni, R. Francisco, L. Olantera, J. Troska, C. Sigaud, S. Detraz, C. Soos, F. Vasey, and P. Moreira, "The lpGBTIA, a 2.5 Gbps Radiation-Tolerant Optical Receiver using InGaAs photodetector," *PoS*, vol. TWEPP2019, p. 030, 2020.

[3] R. Marchetti, C. Lacava, L. Carroll, K. Gradkowski, and P. Minzioni, "Coupling strategies for silicon photonics integrated chips," *Photonics Research*, vol. 7, no. 2, pp. 201–239, 2019.

[4] J. Troska, A. Brandon-Bravo, S. Detraz, A. Kraxner, L. Olanterä, C. Scarcella, C. Sigaud, C. Soos, and F. Vasey, "The VTRx+, an optical link module for data transmission at HL-LHC," *PoS*, vol. TWEPP-17, p. 048, 2017.

[5] T. Prousalidi, A. Bulling, M. Court, S. Detraz, M. Lalović, L. Marcon, L. Olanterä, S. Orfanelli, U. Sandven, C. Scarcella, C. Sigaud, C. Soós, and J. Troska, "Towards optical data transmission for high energy physics using silicon photonics," *Journal of Instrumentation*, vol. 17, p. C05004, may 2022.

Chapter 7

Conclusions and next steps

7.1 Conclusions

This thesis, as described in 1, targeted the progress in the development of a SiPh Tx and Rx as part of the new generation of optical links that are required in the future upgrades of the HEP experiments at CERN. In this Section we will summarize the work done during the PhD, as it was described in the thesis, and relative to the thesis objectives that were defined in chapter 1.

Concerning the SiPh Tx, we introduced the concept of a SiPh based transmitter that employed RMs for the high-speed modulation of light. The different test-boards that were assembled for the characterization of the RM and Tx are then presented. The RM was fully characterized with measurements of its output spectra and figures of merit. This work allowed to perform an extensive characterization of the Tx, that included both DC measurements with low and high input power, as well as high-speed measurements, and characterization of the self-heating effect and μ-heater. This validates the high-speed operation of the Tx and its performance characteristics that are well in agreement with the values extracted from simulations. The development of the SiPh Tx also includes the design and characterization of a 4-channel circuit based on 4 cascaded RMs that can be utilized in WDM schemes. As a first step, the DC and high-speed characterization of this 4-channel circuit was performed and validated its spectral characteristic and high speed operation. Overall, these measurements constitute a complete characterization of the SiPh Tx and its components. This was necessary first of all for understanding the SiPh platform limitations and performance and understand what optimizations and improvements are required from a design and fabrication process aspect, to meet the application requirements. This way the next PICs that were designed so far and will be designed in the future can take advantage of this valuable experience to improve the components. At the same time, the complete characterization of the Tx allowed to successfully operate the Tx test vehicles that enable further testing, characterization and development in higher levels. This opens the way to investigate system challenges that need to be addressed for such a SiPh TRx to operate, like the thermal tuning and the polarization management.

Concerning the thermal tuning, this constitutes one of the main system challenges that need to be addressed. It is required in all circuits that rely on RMs, since these devices are very sensitive to temperature and process variations, that result is continuous variation of their resonant wavelength. This can be solved by using an active thermal tuning mechanism that will counteract these external fluctuations and ensure the stable operation of the RMs at their optimal operating point. During this PhD, an extensive effort took place to realise a thermal tuning mechanism based on average power monitoring at the drop port. This effort included the design, tuning and implementation of a PI controller as part of the feedback control loop. After the PI controller was experimentally validated, two different versions were implemented, each one compatible with a different phase of the Tx development. The implemented control loop was successfully tested in single channel operation, managing to compensate both for temperature and external laser wavelength fluctuations. This is a milestone in the development of the SiPh Tx, since without the thermal tuning the stable operation of the Tx is not possible. The availability of a thermal tuning test setup

also also to perfect the tuning process, consisting of the power-up procedure and the PI operation, and adjust it for our system. As a second step, the thermal tuning control loop was adjusted for multi-channel operation. This was a very complex task and involves many complications, like the assembly and the scaling of the system, the required test-boards and the performance of the tests. However, we successfully demonstrated the operation of the thermal control loop in multi-channel operation, correcting for temperature variations. These results serve as a proof of concept of the compatibility of this solution with our system. However its adoption in a final WDM system implementation involve extra challenges that stem from the presence of multiple wavelengths in the system. The thesis aims to address the challenge, by proposing various solutions that include either use of drop-port filters or adoption of different system choices. Overall, the work that was done related to the thermal tuning control loop not only resulting in the implementation of a first thermal tuning system that allowed further testing and characterisation of the Tx both in single and multi channel operation, but at the same time it provides the methodology and research that will allow the implemented control loop to be adjusted for a different system or be improved for compatibility with the final system requirements.

The polarization management is another system challenge that requires careful investigation. It stems from a particularity of our system, that necessitates the remote placement of the lasers in the back-end, away from the front-end SiPh TRx. This in turns signifies that light has to be transferred form the lasers to the TRx through single mode fibers that do not maintain the polarization, and be coupled to the SiPh PIC that requires operation with TE polarization. Therefore, a polarization management scheme is necessary. Off-chip polarization diversity methods are suitable for lab testing but not compatible with the final system. Instead, an on-chip method will have to be adopted there. Two different on-chip methods are studied and proposed. The first one relies on the use of 2D-GCs that can simultaneously split and rotate the polarization. A circuit based on the 2D-GCs and a power combining circuit is simulated and designed, offering a complete solution for on-chip polarization management. Only part of the circuit was available for testing during this PhD. However, this allowed to verify the principle of operation, and its compatibility with WDM implementations. The second alternative solution involves the use of PSRs for the on-chip polarization management. These components can split and rotate the polarization efficiently and offer important advantages compared to the 2D-GCs: they are compatible with edge coupling schemes, have lower losses and higher BW and are also available both for the C-band and O-band, contrary to the 2D-GCs that for the moment only support C-band operation in the platform we are using. Nevertheless, such PSR components are not yet available for our foundry's PDK. Two custom components were therefore designed as part this thesis work. The first is a C-band thermally tunable PR. The second component is a broadband O-band PSR based on mode conversion and phase matching. The devices were designed to meet the application requirements and their performance was verified with simulations. Although both components were included in a PIC that is under fabrications through an MPW, the large turnaround times did not allow for their experimental characterization during this PhD. However, the research that has been carried out concerning the polarization management managed a thorough study of the subject and

has yielded a first characterization of the available on-chip methods as well as different alternative solutions, that can address the polarization diversity issue in different system architectures. The research has also resulted in designs that are under fabrication, allowing for the full characterization of the proposed solutions to be performed after the end of this PhD. In total this effort helped to move one step forward in the process of addressing this system challenge, that requires many design and fabrication cycles and could not be completed in three years.

Last but not least, part of the PhD work was also the characterization of the SiPh Rx. The Rx is based on Ge PDs and a TIA. Two Rx test-boards have been assembled, including different variations of the PDs, as well as the two different available radiation-hard TIAs, the GBTIA and lpGBTIA. High speed testing of the boards verified the high speed operation of the Rx and the compatibility between the Ge PDs and available TIAs. Also, BER measurements investigated the sensitivity of the Rx. It was thus verified that the Rx is fully compatible with power budget of the link, and no further optimization of the Rx is necessary.

To conclude, in this thesis we presented the modelling, testing and characterization of building blocks for the development of radiation tolerant SiPh Tx and Rx for HEP experiments, which is part of the feedback process that is required to make design, technology and architecture choices regarding the target system. We addressed the most important system challenges, namely the thermal tuning of RMs and polarization management. The above results are a proof of concept of a Si based Tx and Rx for HEP applications. This work has successfully contributed to move one step forward the effort to put together from the available components a SiPh Tx and Rx, and address the important system challenges, which will eventually lead to a first demonstration of SiPh TRx for HEP experiments. Given that the radiation tolerance of the individual components has already been verified, advances in the component level performance and system integration will allow the adoption of the presented devices in the next generation of optical links at CERN.

7.2 Next steps

Given the work presented in this thesis, in this Section we analyse some proposals and ideas about further research and improvements that would benefit this application.

7.2.1 Migration to the O-band

The market research we have done has revealed a tendency to migrate towards the O-band for the telecom and datacom systems [1]. This indicates that the commercial components that will be required for our optical link, like a 4-channel external laser source or BE SFPs, will be available possibly only in the O-band. Therefore, for compatibility with the commercially available components and emerging standards, we also plan to migrate towards the O-band. Between the emerging standards, the one that matches our system specifications (4-channel WDM inter data center links with bitrates of $25\,\mathrm{Gbit\,s^{-1}}$ per channel) and we estimate will dominate the market is the 100G CWDM4 MSA Ethernet

standard. Therefore, we try to align with this standard with the systems and components we design. This is true for the RMs, the polarization handling components, as well as the next generation of 4-channel WDM circuits and the components, like the drop-port filters, that need to be compatible with it. Therefore, from now on the PICs that will be designed will target O-band operation. This is also true for PICv3 that includes mostly O-band components. Part of the future work will be to repeat the characterisation process for the O-band components and adjust the thermal tuning control loop for O-band operation. However, the methodology and expertise we have gained from the work performed so far can be exploited.

7.2.2 Remote laser sources

As it was analyzed in the thesis, due to the unique environment of the CERN experiments, the FE components of the optical links need to be radiation tolerant and low power. This imposes the remote placement of the lasers in the BE, away from the FE modules. Therefore, external laser sources (ELS) will be used. In case a WDM scheme is adopted in the final system, we will need a laser source that is compatible with our system architecture and adopted standard. For the moment the emerging standard we are planning to align with is the 100G CWDM4 MSA Ethernet standard. The requirements for the laser source are high enough power (estimated value is 17 dBm with realistic assumption), 4-channels with the correct spacing of 20 nm and operation at the O-band. At the same time, even though these components will be placed in the BE, since hundreds of them will be deployed in the final system, reasonable size and power consumption are required. Having bulky laser sources that take up too much space and consume a lot of power will not allow their integration in the final system. Ideally, devices that come in a SFP module format will be preferred. The existing CW lasers developed for pluggable transceivers cannot meet the high output power requirement of our application, that shares a lot of commonalities with co-packaged optics. Although such components are not available right now, since there hasn't been interest from the datacom and telecom community, given the emerging standards it is expected that soon they will start to become commercially available. Standardization of ELS in OIF is underway and will accelerate the maturity of the technology, aiming to provide an External Laser Small Form-Factor Pluggable (ELSFP)[2].

7.2.3 Optimization of RM design

From the characterization of the SiPh Tx and the results presented so far, a limitation concerning the RMs and their performance arises. This concerns the TP of the RMs for voltage swing of 1 V. The TP of an RM depends on the Q-factor and the driving voltage. For voltage swing of 1 V, RMs with higher Q-factor present lower TP, while RMs with lower Q-factor present higher TP. At the same time, the Q-factor is inversely proportional to the RM BW. Therefore, a trade-off exists between the BW and the TP. The RMs from the PIC designed at CERN that have BW of 50 GHz show increased TP for voltage swing of 1 V with value around 15 dB. The RMs with lower BW of 25 GHz have better TP of around 10 dB for voltage swing of 1 V. The low TP for voltage swing of 1 V is a prerequisite in our

system due to the power and space limitations at the FE. The expected available voltage levels will likely be limited to 1 V of voltage swing. At the same time, given the current considerations of the link power budget, that estimate that the power per wavelength in the RM input of a 4-channel circuit will be around 5 dBm, there is no margin to address this problem by increasing the input power. It is also unlikely that the link losses will be reduced since the considerations we have made so far take into account the realistic conditions. Therefore, the solution that arises in this problem concerns the performance of the RMs. Although increasing the driving voltage to 1.5 V is being considered and will relax a bit the requirements compared to the 1 V case, this is still not enough. It becomes evident, then, that the RMs that will be employed need to have adequately low TP so that the produced OMA is detectable by the BE Rx, given the power budget of the link (OMA must be larger than the BE Rx sensitivity). One way to achieve this is by sacrificing a bit of the BW of the device. In any case, as it was analyzed in the thesis we estimate that the maximum required BW per RM will be of 25 GHz. However, even if we employ the 25 GHz RMs, we still require at least 2 dB of further improvement on the TP for voltage swing of 1 V. This can be addressed by designing RMs with higher Q-factor and therefore lower TP.

Several studies are done to optimize the waveguide geometry and doping profile of a PN doped waveguide. It is shown that the Q-factor of a depletion-mode waveguide can be increased using the following methods: a lower dopant concentration for the p and n regions, a lower ratio of slab thickness to rib height, or a bigger distance between highly doped region, p_{++}/n_{++}, and the edge of the waveguide (d_{++} as shown in Fig. 7.1). Increasing the doping levels in the silicon waveguide generally leads to higher carrier concentrations. Higher carrier concentrations can reduce the speed of the carrier recombination process, affecting the modulator's response time. While this may enhance the modulation efficiency, it can also introduce additional carrier-induced dispersion, potentially leading to increased signal distortion and TP. On the contrary, lower doping levels in the silicon waveguide can result in a lower concentration of free carriers. This can reduce free-carrier absorption and increase the Q-factor of the modulator and improve the TP [3]. However, usually it is not possible to change the doping levels, especially in MPW runs. Some fabs might offer different doping levels, like high, medium or low, but the exact numbers of the free carriers concentrations are not known and cannot be customized. Therefore, this approach cannot always be exploited, or it needs to be combined with other design solutions for efficient results. Concerning the ratio of slab thickness to rib height, reducing the ratio generally results in increased modal confinement within the waveguide core. This increased confinement can lead to a higher overlap between the optical mode and the active region of the modulator, which in turn means improved modulation efficiency and reduction in the transmission penalty [4]. Last, increasing the distance d_{++} can contribute to improved TP. As both the cavity photon lifetime and the electrical (i.e. the RC limited) bandwidth of carrier-depletion ring modulators are affected by d_{++}, due to the effect in the series resistance, and since d_{++} is not limited by the foundry, it can be used as a handle to further optimize ring modulator design [5]. Nevertheless, in all the aforementioned techniques there are trade-offs between the different FOMs, the BW and the TP, as well as the radiation

hardness. Hence, it is important to systematically study these design trade-offs to optimize the RM performance according to the application needs.

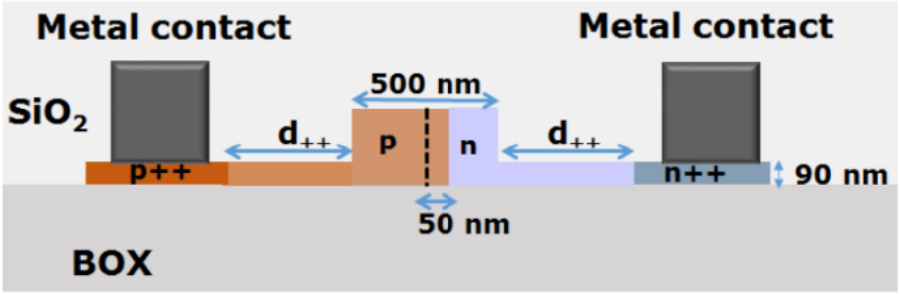

Figure 7.1. *Ring modulator waveguide cross-section. Source [5].*

7.2.4 Power consumption

A key performance metric for the successful adoption of SiPh based technology in HEP detectors will be sufficiently low electrical power consumption. This is a prerequisite to make the proposed TRx competitive compared to the current technology and other alternatives. This needs to be addressed in future work. For the moment, the exact system architecture is not known, therefore estimation of the overall power consumption are not possible. However, among the factors that will affect it are the following. First of all, it is a question of the system choices that will be made and concern the architecture of the FE Tx, the number of channels, the modulation scheme, the choice or not of a WDM implementation and the datarates. The SiPh components themselves do not require powering. It is the FE electronics that accompany the SiPh that contribute to the power consumption. These include first of all the electrical driver of the RMs. The design study has already started and the driving schemes and design choices are being investigated, to achieve a low power component that is compatible with the RMs. Then there is the thermal tuning controller and its blocks that need to be added to the FE, like the DAC, ADC and some ASIC for the PI functionality. Similarly, the electronics department at CERN has already started investigating possible ways to implement the thermal control loop. However, its power consumption will mostly depend of the SiPh design, the required thermal tuning range and power consumption of the μ-heaters, they so far require more than 60 mW to scan a full FSR. There are however ways to reduce this number. One approach would be for example to add thermal insulation trenches, including an undercut of the silicon substrate in the RM region, to minimize unwanted leakage of heat. The heaters with thermal insulation trenches and undercut are 10-20 times more efficient than without [6]. Another aspect to consider for the power consumption would be polarization diversity technique that is adopted. As it was described in Chapter 5, in the on-chip methods extra phase shifters are required, and possibly even a feedback mechanism similar to that of the thermal tuning, to verify if the polarization has been successfully rotated, or if further adjustment of the phase shifters in necessary. Once it is known which scheme will be eventually adopted, and what the design choices will be, it will become easier to make estimation on the power consumption overhead it will impose. Apart from these

design choices, other key elements to reducing the overall power consumption within the detector are the remote placement of the source laser and achieving sufficient high levels of integration between the FE electronic and the photonic circuits. The latter will be affected both by the technology advances in the next years, as well as the choice of the photonic-electronic integration that will be possible (e.g. hybrid vs monolithic, placement of electrical drivers relative to RMs and the electrical connections between them).

7.2.5 Characterization and evaluation of on-chip polarization diversity circuits

As it was explained in Chapter 5, two different solutions for on-chip polarization diversity have been proposed: the first based on the use of 2D-GCs, and the second is based on PSRs. For both alternatives, a complete circuit has been simulated and designed. Both proposed circuits have been included in a PIC submission that is under fabrication through an MPW. However, due to the long turnaround times of the fab, the designs were not available for testing and characterization before the end of the PhD. This did not allow to experimentally verify the principle of operation, especially for the case of the PSR based solution that is being investigated for the first time within this project. As a next step, the characterization of the designed PSR and PR is required. This will first of all allow to measure the performance of the components and verify whether they have low IL, low PDL and high PER. This information is important to realize if this approach is compatible with our application. Moreover, since the characterization of these components requires edge coupling, these tests offer an excellent opportunity to investigate for the first time edge coupling schemes and solutions. So far, we have only used GCs for the coupling of light between PICs and SMFs. However, PICv3 that includes the polarization structures also includes edge couplers for their testing. The CERN lab is planning to buy the necessary equipment to attach fibers in edge coupling schemes. For the moment, this approach requires coupling to 3 µm mode field diameter beam which in turn imposes the use of tapered or high numerical aperture fibers with tight alignment tolerances. However, we believe that after proper training and experimentation it will be possible to implement this idea, which is not only necessary to test the polarization diversity circuits, but it also very useful for the whole project, as the edge coupling scheme will be eventually the one used in the final system. Further advances in the available technology are expected to simplify the edge coupling in the future, making this solution even more appealing.

Concerning the polarization diversity circuit based on 2D-GCs, only its partial characterization was possible. Its testing once PICv3 is available will allow to verify the performance of the 2D-GCs, their IL as well as the verification of the principle of operation. It will also allow to test the second part of the circuit that performs the power recombination from the 2 output arms of the 2D-GCs in a single waveguide, after properly adjusting their phase. This part of the circuit can be a standalone component that is required also in the PSR-based solution, so verifying its operation is important for all polarization management approaches. Eventually, the comparison of the two approaches will also help to decide which one in more compatible with our system, and make the corresponding design

choices in future work.

Bibliography

[1] "CW-WDM MSA Technical Specifications." Accessed: 07/12/2023.

[2] OIF, "Physical and Link Layer Working Group/Physical Layer User Group Working Group." Accessed: 07/12/2023.

[3] B. Pile and G. Taylor, "Small-signal analysis of microring resonator modulators," *Opt. Express*, vol. 22, pp. 14913–14928, Jun 2014.

[4] H. Jayatilleka, W. D. Sacher, and J. K. Poon, "Analytical model and fringing-field parasitics of carrier-depletion silicon-on-insulator optical modulation diodes," *IEEE Photonics Journal*, vol. 5, no. 1, pp. 2200211–2200211, 2013.

[5] S. Karimelahi, W. Rahman, M. Parvizi, N. Ben-Hamida, and A. Sheikholeslami, "Optical and electrical trade-offs of rib-to-contact distance in depletion-type ring modulators," *Opt. Express*, vol. 25, pp. 20202–20215, Aug 2017.

[6] A. Masood, M. Pantouvaki, G. Lepage, P. Verheyen, J. Van Campenhout, P. Absil, D. Van Thourhout, and W. Bogaerts, "Comparison of heater architectures for thermal control of silicon photonic circuits," in *10th International Conference on Group IV Photonics*, pp. 83–84, IEEE, 2013.

List of Abbreviations

7.3 List of abbreviations

1D-GC	One-dimensional Grating Coupler
2D-GC	Two-dimensional Grating Coupler
λ_{laser}	laser wavelength
λ_{res}	resonant wavelength
µ-heater	micro heater
ADC	Analog to digital converter
ADC	Asymmetric Directional Coupler
ALICE	A Large Ion Collider Experiment
APD	Avalanche Photodiode
ASIC	Application-Specific Integrated Circuit
ATLAS	A Toroidal LHC ApparatuS
AWG	Arrayed Waveguide Grating
BE	back-end
BER	Bit Error Rate
BERT	Bit Error Rate Tester
BHL	Balanced Homodyne Locking
BW	Bandwidth
CE	Coupling Efficiency
CERN	European Organization for Nuclear Research
CLEAR	CERN Linear Electron Accelerator for Research
CMOS	Complementary Metal-Oxide Semiconductor
CMS	Compact Muon Solenoid
COTS	Commercial off-the-shelf
CT	Continuous Time
CWDM	Coarse Wavelength Division Multiplexing
D	Derivative
DAC	Digital to analog converter
DC	Directional Coupler
DD	Displacement Damage
DEMUX	Demultiplexer
DFB	Distributed feedback

DP	Drop Port
DSP	Digital Signal Processing
DUV	Depp Ultra Violet
DWDM	Dense Wavelength Division Multiplexing
EDG	Echelle Diffraction Gratings
ELS	External Laser Sources
ELSFP	External Laser Small Form-Factor Pluggable
EME	EigenMode Expansion
EMI	Electromagnetic Interference
ER	Extinction Ratio
FCA	Free Carrier Absorption
FDE	Finite Difference Eigenmode
FDTD	Finite-Difference Time-Domain
FE	Front-end
FEC	Forward Error Correction
FOM	Figures of Merit
FPGA	Field Programmable Gate Array
FPR	Free Propagation Regions
FSR	Free Spectral Range
FWMH	Full Width at Half Maximum
GBTIA	Gigabit Transimpedence Amplifier
GC	Grating Coupler
Ge	Germanium
HEP	High Energy Physics
HL	High Luminosity
HL-LHC	High Luminosity Large Hadron Collider
I	Integral
IC	Integrated Circuit
IL	Insertion Loss
IM/DD	Intensity Modulation / Direct Detection
InGaAs	Indium Gallium Arsenide
IP	Intellectual Property
I_{ph}	Photocurrent
IV	Current-Voltage
L3	LINAC 3
L4	LINAC 4
LDD	Laser Diode Driver
LEIR	Low Energy Ion Ring
LIDAR	Light Detection and Ranging
LINAC	Linear Accelerator
LHC	Large Hadron Collider

LHCb	Large Hadron Collider beauty
LNOI	Lithium Niobate on Insulator
LS1	Long Shutdown 1
lpGBT	Low Power Gigabit Transceiver
lpGBTIA	Low Power Gigabit Transimpedence Amplifier
LTI	Linear time invariant
MCE	Mode Conversion Efficiency
MFD	Mode Field Diameter
MIR	Mid Infra Red
MMI	Multi Mode Interference
MPW	Multi-Project Wafer
MRR	Micro Ring Resonator
MSA	Multi-Source Agreement
MSM	Metal-Semiconductor-Metal
MUX	Multiplexer
MWG	Multimode Waveguide Grating
MZI	Mach–Zehnder Interferometer
MZM	Mach–Zehnder Modulator
n_{eff}	effective refractive index
N_i	Nitride
NIEL	Non-Ionizing Energy Loss
NIR	Near Infra Red
NRZ	Non-Return to Zero
OMA	Optical Modulation Amplitude
OSA	Optical Spectrum Analyzer
P	Proportional
PAM4	Pulse Amplitude Modulation, 4 Levels
PBS	Polarization Beam Splitter
PC	Personal Computer
PCB	Printed Circuit Board
PCE	Polarization Conversion Efficiency
PD	Photodiode
PDK	Process Design Kit
PDL	Polarization Dependent Loss
PER	Polarization Extinction Ratio
PhC	Photonic Crystall
PI	Proportional-Integral
PIC	Photonic Integrated Circuit
PICv2	Photonic Integrated Circuit version 2
PID	Proportional-Integral-Derivative
PM	Polarization Maintaining

PMD	Polarization Mode Dispersion
PMF	Polarization Maintaining Fiber
Q-factor	Quality Factor
PR	Poalrization Rotator
PS	Phase Shifter
PSB	Proton Synchrotron Booster
PSR	Poalrization Splitter Rotator
qTE	quasi Transverse Electric
qTM	quasi Transverse Magnetic
RM	Ring Modulator
RR	Ring Resonator
Rx	Receiver
SEE	Single Event Effect
Ser/Des	Serializer/Deserializer
SFP	Small Form-Factor Pluggable
Si	Silicon
SiPh	Silicon Photonics
SMA	SubMiniature version A
SMF	Single-Mode Fiber
SNR	Signal-to-Noise Ratio
SOI	Silicon-on-Insulator
SPP	Surface Plasmon Polariton
SPS	Super Proton Synchrotron
SWG	Sub-wavelength grating
TE	Transverse Electric
TF	Transfer Function
TIA	Transimpedence Amplifier
TID	Total Ionizing Dose
TIR	Total Internal Reflection
TM	Transverse Magnetic
TO	Thermo-optic
TOC	Thermo-optic coefficient
TOE	Thermo-optic effect
TP	Transmission Penalty
TPA	Two Photon Absorption
TRx	Transceiver
Tx	Transmitter
VCSEL	Vertical-Cavity Surface-Emitting Laser
V_{heater}	Heater Voltage
VL+	Versatile Link plus
V_{mod}	Modulation Voltage

VTRX+	Versatile Transceiver plus
W	Tungsten
WDM	Wavelength-Division Multiplexing